ALMA MATER STUDIORUM
UNIVERSITÀ DI BOLOGNA

DOTTORATO DI RICERCA IN ASTROFISICA

Ciclo XXXVII

Settore Concorsuale: 02/C1 - ASTRONOMIA, ASTROFISICA, FISICA DELLA TERRA E DEI PIANETI

Settore Scientifico Disciplinare: FIS/05 - ASTRONOMIA E ASTROFISICA

The chemical inventory of peculiar globular clusters: a divergence from the norm

Presentata da:

Deimer Antonio Alvarez Garay

Coordinatore Dottorato

Prof. Andrea Miglio

Supervisore

Prof. Alessio Mucciarelli

Co-supervisori

Prof. Francesco R. Ferraro

Dr. Livia Origlia

Esame Finale Anno 2025

A aquél niño enamorado de las estrellas.

"*Il che vuol dire, in fondo, che noi anche oggi crediamo che la luna non stia per altro nel cielo, che per farci lume di notte, come il sole di giorno, e le stelle per offrirci un magnifico spettacolo. Sicuro. E dimentichiamo spesso e volentieri di essere atomi infinitesimali per rispettarci e ammirarci a vicenda, e siamo capaci di azzuffarci per un pezzettino di terra o di dolerci di certe cose, che, ove fossimo veramente compenetrati di quello che siamo, dovrebbero parerci miserie incalcolabili.*"

Luigi Pirandello
Il fu Mattia Pascal

Abstract

This PhD Thesis was aimed at obtaining a chemical characterization of the stellar populations of three peculiar stellar systems, namely ω Centauri, Liller 1, and M 54. Historically these systems were classified as globular clusters due to their morphology, but nowadays it is widely recognized that they are actually more complex systems than previously believed.

- ω Centauri is the most massive system among the globular clusters, but with a wide metallicity spread that is not usually observed in *genuine* globulars. Moreover, ω Centauri displays the typical features of globular clusters, i.e. the anticorrelations among light-elements. In this Thesis I investigated the role of the complete MgAl burning chain in shaping the stellar populations of ω Centauri. From this work I found that ω Centauri displays a very extended Mg-K anticorrelation, suggesting a prominent role of the asymptotic giant branch stars at the origin of the observed chemical anomalies, at least in those systems very massive and/or metal-poor.
  I also detected extended Mg-Al and Mg-Si anticorrelations, which show different shapes and extensions as a function of the metallicity. This result demonstrates the different efficiency of the MgAl burning chain as function of the metallicity, with the burning chain being less and less efficient at [Fe/H] > -1.3 dex.

- Liller 1 is a massive and metal-rich stellar system located in the Bulge of the Milky Way. Very recently it was found to host two different populations of stars: an old and metal-poor subpopulation (13 Gyr and [Fe/H]$= -0.3$ dex) and a young and metal-rich one ($\sim$ 2 Gyr and [Fe/H] $= +0.3$ dex). Thanks to its peculiar properties Liller 1 was suggested to be a remnant of the early epoch of Bulge formation. In this Thesis I presented a complete chemical characterization of the Liller 1 populations, finding that its stars follow the same chemical pattern of the Bulge field, with the metal-poor stars being enhanced in [α/Fe] and the metal-rich stars having solar scaled [α/Fe]. Moreover, no evidence of the typical Na-O anticorrelation is present in Liller 1. These findings strongly suggest that Liller 1 formed and evolved within the Bulge and probably is a fossil fragment of the Bulge formation.

- M 54 is a massive globular cluster located at the center of the remnant of the Sagittarius dwarf galaxy, that akin to ω Centauri displays a wide metallicity spread. It is considered to be part of the nuclear star cluster of the Sagittarius galaxy. In this Thesis I analyzed the largest high-resolution spectroscopic dataset obtained so far of M 54 members, finding evidence that the complete MgAl burning chain was active in this cluster. Indeed, M 54 presents all the Mg-Al, Mg-Si, and Mg-K anticorrelations. Moreover, I presented the first distributions of Ba and La for M 54, finding no evidence of significant increase of Ba and La abundances as a function of the metallicity. However, the stars at [Fe/H] > -1.5 dex display an increase in the scatter of both Ba and La abundances. This suggests that the contribution from low-mass asymptotic giant branch stars to the chemical enrichment in this system was poorly efficient.

Publications

1. *The Mg-K anticorrelation in ω Centauri*
   Alvarez Garay, D. A., Mucciarelli, A., Lardo, C., Bellazzini, M., & Merle, T., 2022 ApJL, 928, L11

2. *The MgAl burning chain in ω Centauri*
   Alvarez Garay, D. A., Mucciarelli, A., Bellazzini, M., Lardo, C., & Ventura, P., 2024 A&A, 681, A54

3. *X-shooter spectroscopy of Liller 1 giant stars*
   Alvarez Garay, D. A., Fanelli, C., Origlia, L., Pallanca, C., Mucciarelli, A., et al., 2024 A&A, 686, A198

4. *Multi-iron subpopulations in Liller 1 from high-resolution H-band spectroscopy*
   Fanelli, C., Origlia, L., Rich, R. M., Ferraro, F. R., Alvarez Garay, D. A., et al. 2024 A&A, 690, A139

5. *Chemical inventory of a peculiar ω Centauri giant star*
   Alvarez Garay, D. A, Bonifacio, P., Mucciarelli, A., in preparation

6. *Chemical abundances of M 54 giant stars from high-resolution spectroscopy*
   Alvarez Garay, D. A, Mucciarelli, A., in preparation

Contents

List of Figures

List of Abbreviations

AGB	Asymptotic Giant Branch
BFF	Bulge Fossil Fragment
BHB	Bright Horizontal Branch
BP	Blue Plume
BSS	Blue Straggler Star
ChM	Chromosome Map
CMD	Color-Magnitude Diagram
DM	Distance Modulus
DR	Data Release
ESO	European Southern Observatory
EW	Equivalent Width
FDU	First Dredge Up
FG	First Generation
FHB	Faint Horizontal Branch
FRMS	Fast Rotating Massive Star
GC	Globular Cluster
GMM	Gaussian Mixture Modeling
HB	Horizontal Branch
HBB	Hot Bottom Burning
HR	High Resolution
HST	Hubble Space Telescope
IMF	Initial Mass Function
JWST	James Webb Space Telescope
LPV	Long Period Variable
MDF	Metallicity Distribution Function
M-int1	Metal-intermediate1
M-int2	Metal-intermediate2
MP	Metal-Poor
MPs	Multiple Populations
MR	Metal-Rich
MS	Main Sequence
NGC	New General Catalogue
NIR	Near InfraRed

NLTE	Non-Local Thermal Equilibrium
NSC	Nuclear Star Cluster
OC	Open Cluster
ODF	Opacity Distribution Function
OP	Old Population
RGB	Red Giant Branch
RV	Radial Velocity
SAGB	Super-Asymptotic Giant Branch
SFH	Star Formation History
SG	Second Generation
SGB	Sub Giant Branch
Sgr dSph	Sagittarius dwarf Spheroidal
SgrN	Sagittarius Nucleus
SMS	Super Massive Star
SNe	Supernovae
SNR	Signal-to-Noise Ratio
SSP	Simple Stellar Population
TO	Turn-Off
VLT	Very Large Telescope

CHAPTER 1

The stellar populations of the globular clusters

Globular clusters (GCs; Herschel, 1789) are among the first structures in the Universe that were discovered and studied. The German amateur astronomer Johann Abraham Ihle is credited with the discovery of the first known globular cluster, M 22, which he found in 1665 when observing Saturn in Sagittarius (Lynn, 1886). In 1764 Charles Messier was the first astronomer able to resolve individual stars in the GC M 4[1]. In 1771 Charles Messier published the first version of his famous catalog in which were contained numerous GCs, while the final version of the catalog was published in 1781 (Messier, 1781). Another collection of these systems was carried out by Herschel (1789), who coined the term "globular cluster".

Later, several astronomers studied and examined in detail these systems to unveil their nature, and the catalog of GCs was continuously updated with both Galactic and extragalactic GCs. Nowadays we can count on catalogs that contain more than 150 GCs belonging to our Galaxy (Harris, 2010; Baumgardt & Hilker, 2018).

Historically, GCs were considered to be the nearest example to the concept of Simple Stellar Population (SSP), i.e. stellar systems formed by stars with the same age and chemical composition (Renzini & Buzzoni, 1986). Among the GCs under analysis, for a long period of time only ω Centauri was considered as a noticeable exception due to the fact that its stars displayed a large spread in metallicity and other chemical elements (Cannon & Stobie, 1973; Freeman & Rodgers, 1975; Dickens & Bell, 1976; Butler et al., 1978; Norris, 1980; Persson et al., 1980).

Nevertheless, in the last three decades the situation has drastically changed thanks to the advent of increasingly high-resolution photometric and multi-object spectroscopic analysis. Indeed, even though GCs are still considered the best approximation of SSP, last decades of

[1] Numerous GCs today are known by both their names NGC or M that stands for "Messier".

analysis revealed the presence of multiple populations (MPs) of stars chemically distinct from each other within the same GC. Today, it is widely recognized that the majority, if not all, GCs have experienced multiple episodes of star formation, leading to a distinctive pattern of self-enrichment in terms of chemical composition. From a chemical point of view, GCs exhibit significant variations in the abundances of light elements such as He, Li, C, N, O, F, Na, Mg, Al, Si, and K (Kraft, 1994; Gratton et al., 2004; Martell & Smith, 2009; Carretta et al., 2009a,b; Pancino et al., 2010; Gratton et al., 2012; Mucciarelli et al., 2012; Mészáros et al., 2015; Pancino et al., 2017; Mészáros et al., 2020).

Previously, the observed large intrinsic spreads in light elements were mainly thought to be associated with significant variations in iron abundance only in a small subset of the entire GC population (e.g., ω Centauri, M 54, Terzan 5, and Liller 1; Norris & Da Costa, 1995b; Sarajedini & Layden, 1995; Ferraro et al., 2009; Crociati et al., 2023). However, recent photometric and spectroscopic studies have found evidence suggesting that small-to-moderate iron spreads (from less than 0.05 up to 0.3 dex) may be relatively common in massive clusters (Legnardi et al., 2022; Lardo et al., 2022, 2023; Lee, 2022, 2023).

Furthermore, these kind of inhomogeneities in the chemical abundances are observed not only in the Galactic GCs, but also in extragalactic clusters such as the GCs present in M 31 (Andromeda galaxy; Colucci et al., 2009), Large Magellanic Cloud (Johnson et al., 2006; Mucciarelli et al., 2009), and Fornax (Letarte et al., 2006).

Therefore, the presence of chemical anomalies within the stars of a given GC (Galactic or extragalactic) is not anymore a pure quirk of some clusters, but it is an intrinsic feature that emerges from the analysis of these systems.

Nowadays, the understanding of the formation and evolution of MPs and, more broadly, of GCs, is one of the most intriguing topics of astronomy. Many studies, both from the theoretical and observational points of view, are aimed at explaining the still elusive phenomenon of GCs formation, which is of great importance for many astrophysical issues. Its understanding would allow to put constraints on stellar evolution and nucleosynthesis, to probe star formation in the early Universe, unveil the role of stellar dynamics in dense environments, and understand the connections between these systems and their parent galaxies.

16. Of Globular Cluster of Stars

The objects of this collection are of a sufficient brightness to be seen with any good common telescope, in which they appear like telescopic comets, or bright nebulae, and under this disguise, we owe their discovery to many eminent astronomers; but in order to ascertain their most beautiful and artificial construction, the application of high powers, not only of penetrating into space but also of magnifying are absolutely necessary; and as they are generally but little known and are undoubtedly the most interesting objects in the heavens..."

Herschel, W. 1814, Philosophical Transactions, 104, 248

1.1 General properties

It was demonstrated that the majority of stars in the Universe form in star clusters, where stars are bound together by gravity (Lada & Lada, 2003). Historically, these star clusters are divided into open clusters (OCs) and GCs. The latter systems, GCs, are much more dense than OCs and can contain up to millions of stars.

In this Section I will describe the major features of the systems we call GCs, which make these structures among the most fascinating astrophysical objects.

GCs are usually considered as an homogeneous class of objects; however, they can display different morphologies as shown from Fig. 1.1.

Within the Milky Way, GCs are considered to be among the oldest objects with ages between $\sim$ 10 and 13 Gyr[2] (Marín-Franch et al., 2009) and Turn Off masses of $\sim$ 0.8 $M_\odot$. GCs are used to study the infancy of our Universe because they possess stellar fossils that are used to uncover the history of primordial Universe through observations of the Local Universe (Frebel & Norris, 2015). Moreover, the study of the properties of stars inside GCs allows to accurately determine many of the fundamental parameters of these systems like distances, ages, metallicities, sizes and masses.

GCs are very compact and dense systems, with half-light radius ($r_{h,l}$) up to a few tens of pc with more typical values of $\sim$ 3 to 5 pc and densities in their central regions up to 10^6 stars pc^{-3} (Baumgardt & Hilker, 2018). Moreover, these systems are very bright, with mean absolute magnitudes in the visible domain $M_V \sim -7$ (Harris, 2010).

GCs have present-day masses in the range $\sim$ 10^4 up to $\sim$ 10^6 $M_\odot$ (Baumgardt & Hilker, 2018), with an average mass for a GC of $\sim 2\times10^5$ $M_\odot$. However, these masses may be largely different from the original mass of GCs, because the clusters have a substantial dynamical

[2] It is noteworthy that younger GCs are found in Magellanic clouds (Gatto et al., 2020) and in the Andromeda galaxy (Wang et al., 2021).

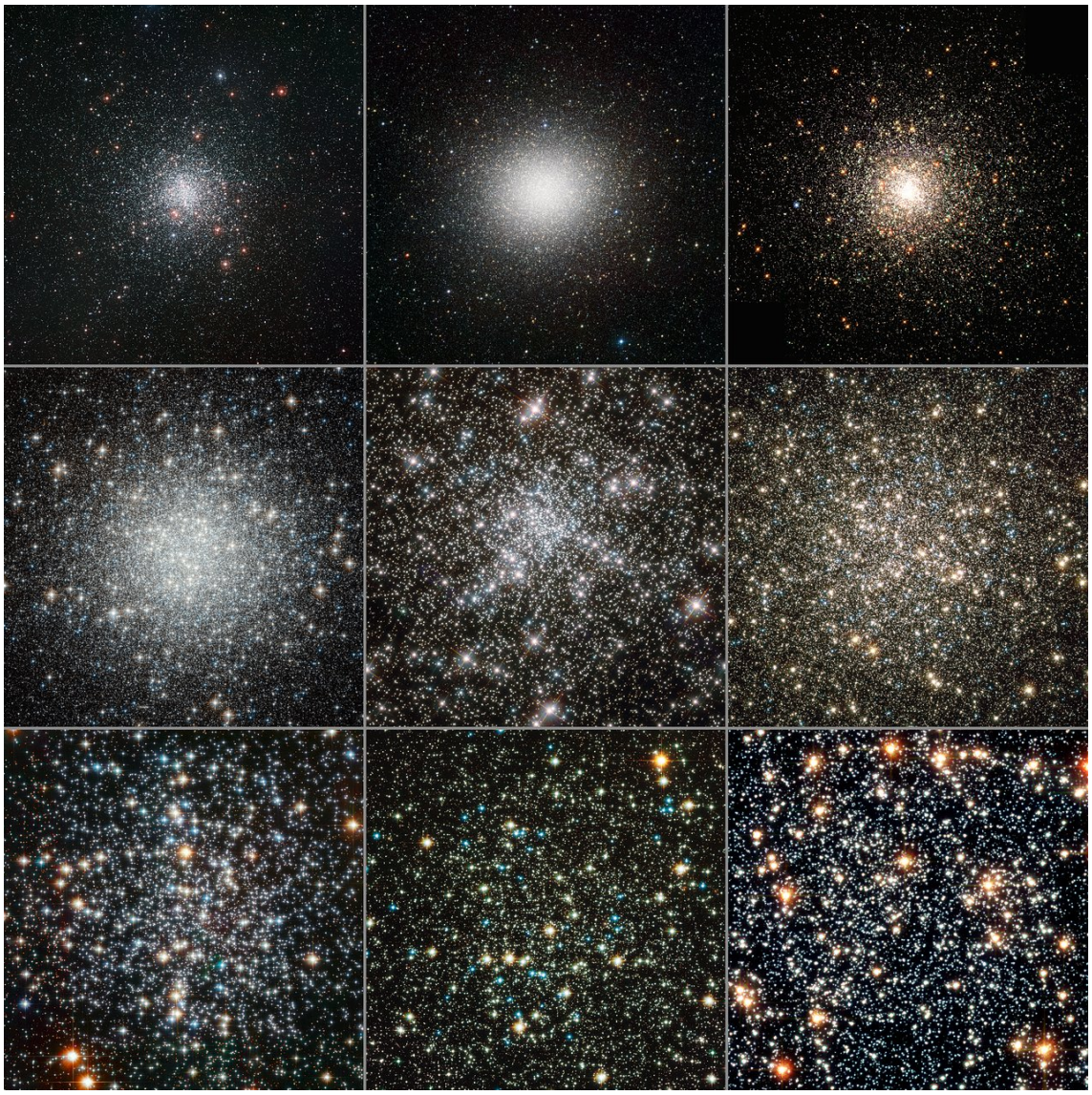

FIGURE 1.1: Example of some Galactic GCs. From left to right and top to bottom: M 4, ω Centauri, M 80, M 53, NGC 6752, M 13, M 4, NGC 288, 47 Tucanae. Credits: ESO.

evolution, and several attempts were performed in the past to better estimate original masses. Very recently, Baumgardt et al. (2019) published new estimates for the present-day and initial mass of Galactic GCs based on extensive comparisons between observational data for the surface luminosity and internal velocity distribution and N-body computations. This is the first attempt to account how the dynamical evolution of the last Gyr affected the mass loss process occurring in GCs.

As highly compact objects, GCs are challenging to observe at large distances. Indeed, beyond the Milky Way, there is evidence of GCs existing within the Local Group up to a maximum distance of 800 kpc in the galaxy M 31.

Within our Galaxy, there are more than 150 GCs, located in the regions of the Galactic Bulge, Halo, and thick disk (Harris, 2010; Baumgardt & Hilker, 2018). The clusters in our Galaxy are systems characterized by low metallicity, with iron abundances [Fe/H][3] ranging from ~ -2.5 up to ~ 0.0 dex and a typical value centered at [Fe/H] ~ -1.5 dex (see Fig. 1.2), even though some Bulge GCs are slightly more metal-rich (e.g., Ferraro et al., 2009, 2021).

Nevertheless, the traditional definition of GCs appears somewhat ambiguous, with numerous objects being classified as GCs based on only a subset of these criteria (being old, compact, bright, metal-poor, etc.). In recent times, Carretta et al. (2010a) introduced a novel definition of GCs, focusing on the chemical inhomogeneities that distinguish these systems from the less massive systems such OCs. In this new definition, a GC is a stellar system characterized by the presence of anticorrelations among light elements in its stars, with the Na-O anticorrelation that represents the prominent and prevalent manifestation of this features. The presence of anticorrelations in GCs are widely recognized as the result of a self-enrichment process happened within the GCs during their early evolution, where different episodes of star formation happened. This scenario has lead to the notion that GCs are constituted by MPs, one with field-like composition and a second with *anomalous chemistry* unique to GCs. In the following of this Thesis, I will refer to the stars having field-like abundances as primordial or first generation (FG) and the stars with peculiar chemical composition as enriched or second generation (SG). It is important to note that in many GCs the MPs are constituted by more than two populations (e.g., Milone et al., 2015b; Bellini et al., 2017b). In those GCs, the stars with field-like chemical composition are the FG stars, while all the other populations (the enriched ones) are the SG stars, divided according to the degree of chemical variations. Many different scenarios were proposed in the last decades, all aiming to explain the origin

[3]Metallicity is defined as follows:

$$[\mathrm{Fe/H}] = \log\left(\frac{\mathrm{Fe}}{\mathrm{H}}\right)_{\star} - \log\left(\frac{\mathrm{Fe}}{\mathrm{H}}\right)_{\odot}$$

The iron abundance is usually used as indicator of the stellar metallicity.

of MPs in GCs. In Sect. 1.4 I will go in detail through the different proposed models.
Although the classification of GCs based on this criterion remains imperfect, it offers us the advantage to put the attention on critical aspects of these systems such as their intricate formation and evolution processes. Indeed, while the mechanisms governing the formation of GCs and their initial phases remain subjects of intense debate, theoretically exists the possibility to separate chemically, and occasionally dynamically, rather pure populations (FG and SG) within GCs. These populations share remarkably similar chemical characteristics that reflects effects of a single nucleosynthesis process. Therefore, in GCs different populations of stars form with different chemical composition, that are not observed in the main population of galaxies, where a blend of diverse nucleosynthesis processes typically prevails.
The detection and the study of single populations inside GCs are based on both photometric and spectroscopic analysis. In particular, the first hints of the presence of distinct populations in GCs came out from intermediate band photometry and low-resolution spectroscopy in the early 1970s (see Kraft, 1979 for a review of the very early results). Nowadays, thanks to the use of of high-quality spectroscopic data for large samples of stars within numerous individual GCs, facilitated by multi-fiber high-resolution spectrographs on 8-meter class telescopes, along with the exceptional photometric capabilities of the Hubble Space Telescope (HST) and James Webb Space Telescope (JWST), a significant advancement in the comprehension of GCs was obtained. This progress shed light on the recognition that the observed chemical inhomogeneities GCs are attributable to a different chemical evolution occurring within these systems, which appear to be distinguished by the presence of MPs of stars.

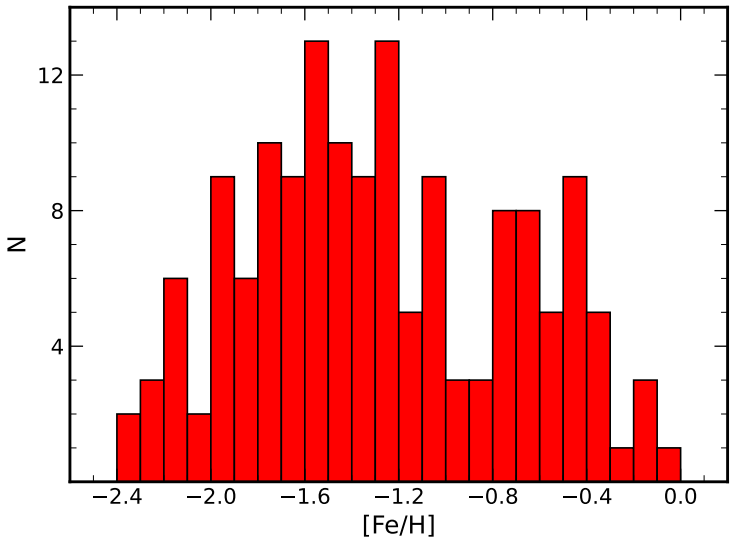

FIGURE 1.2: Metallicity distribution for the GCs belonging to the Milky Way. Data from Harris (2010).

1.2 Multiple populations from a photometric point of view

The first detection of some quirks in GCs is reported by Lindblad (1922), when they reported giant stars of NGC 6205 (M 13) with anomalously weak CN bands. Since then, observations searching for abundance variations in GCs were conducted using either spectroscopic or photometric methods. Spectroscopy is the privileged approach, given that the nature of MPs lies on the abundance differences. However, photometry across various wavelength bands can be considered akin to low-resolution spectroscopy, offering the advantages of accessing large samples in short observing time and facilitating improved management of densely populated regions near the cluster's center.

The photometric methodology involves tracking abundance variations by observing their effects (flux variations) in specific bandpasses that enclose molecular features of CNO. In this context, wide-field photometry can be considered as spectroscopy at an extremely low-resolution. The exploration of MPs can be achieved using various photometric systems with filters positioned in the UV/blue spectral regions, covering relevant molecular bands such as CN, NH, OH, and CH.

Also He abundances and variations are mainly detected by using the photometric approach. Indeed, a direct determination of He abundances through spectroscopy is limited by the lack of photospheric He lines in cool stars. Only a small number of giant stars have He abundances determined from the near-IR line at 10830 Å. Moreover, this line originates in the upper chromosphere under Non-Local Thermal Equilibrium (NLTE) conditions, necessitating for the use of chromospheric models. The analysis also requires consideration of the spherical geometry of the atmosphere (Pasquini et al., 2011; Dupree & Avrett, 2013). The only other direct determinations of He come from the faint He I triplet at 5875.6 Å, first identified in the spectra of late-type stars by Wilson & Aly (1956). This line disappears in stars cooler than ∼8000 K and cannot be reliably used above 11500 K. As a consequence, He is directly measured solely in Horizontal Branch (HB) stars within this limited range of temperature (e.g., Villanova et al., 2009; Gratton et al., 2014), while its abundance and variation in GCs is predominantly inferred through indirect estimations based on photometry.

A range of photometric systems including broad-band filters (e.g., Yong et al., 2008; Lardo et al., 2011; Monelli et al., 2013; Piotto et al., 2015) were employed to identify variations in the abundances of light element in GCs, distinguish between different populations on color-magnitude diagrams (CMDs), and map their radial distribution with the benefit of large statistical samples enabled by photometry.

Distinction between low and high resolution also applies to photometric observations, as for example the dense GC cores can only be resolved using space-based photometry techniques.

The recent advancements in astronomical observations, facilitated by the remarkable capabilities of the HST, JWST, the deployment of 8 meter class telescopes, and the widespread use of U-band filter observations, enabled very precise photometric analyses. These investigations unveiled surprisingly complex CMDs in numerous GCs. Indeed, variations from star to star in light- and α-element abundances, along with differences in age and metallicity, can lead to the emergence of multimodal or broad sequences within the CMDs of Galactic and extragalactic GCs (e.g., Milone et al., 2012, 2018, 2023; Larsen et al., 2014; Dalessandro et al., 2016; Dondoglio et al., 2022; Cadelano et al., 2024).

In this context, ω Centauri (NGC 5139) represents the most famous GC with photometric evidence of MPs. Indeed, in its CMD can be observed multiple sequences along different evolutionary stages (see Figs. 1.3 and 1.4). Are present multiple Main Sequences (MSs, Bedin et al., 2004; Bellini et al., 2017b; Latour et al., 2021), Sub-Giant Branches (SGBs, Pancino et al., 2000; Bellini et al., 2010), and Red Giant Branches (RGBs, Pancino et al., 2000; Nitschai et al., 2024). Moreover, ω Centauri is characterized by the presence of a very extended HB (Villanova et al., 2007; Bellini et al., 2010).

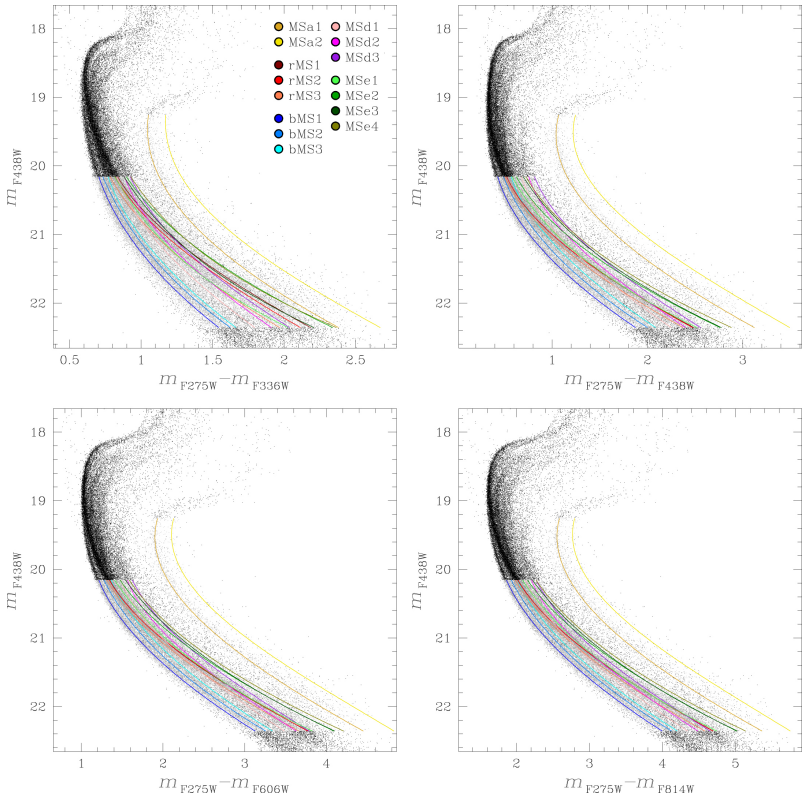

FIGURE 1.3: CMD of ω Centauri based on different combination of HST filters and centered around the MS and SGB. From the MS are recognized a total of 15 subpopulations in ω Centauri. Figure from Bellini et al. (2017b).

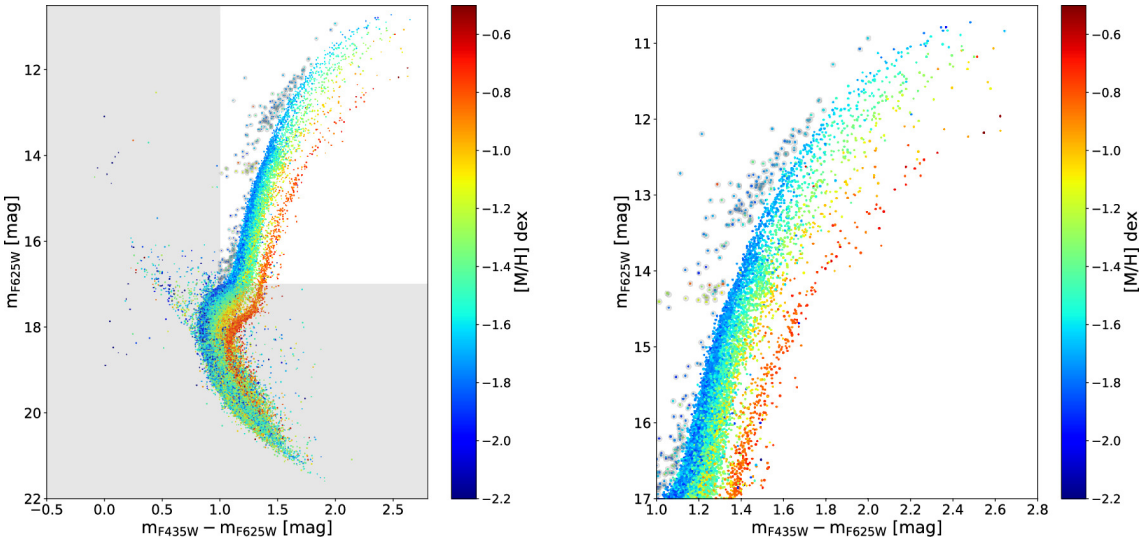

FIGURE 1.4: CMD of ω Centauri. On the left is displayed the full CMD, while in the right a zoom-in on the RGB. The stars are color-coded according to their metallicity [M/H]. Figure from Nitschai et al. (2024).

The observed complexity in the CMD of ω Centauri is due not only to the presence of MPs with different content in light elements. Indeed, ω Centauri covers a large metallicity range, $-2.2 \lesssim$[Fe/H]$\lesssim -0.5$ dex (e.g., Norris & Da Costa, 1995b; Johnson & Pilachowski, 2010; Alvarez Garay et al., 2024). This multi-modal iron distribution lead to the conclusion that ω Centauri underwent multiple episodes of star formation (e.g., Romano et al., 2010; Villanova et al., 2014). The most common interpretation is that ω Centauri is not a genuine GC, but the remnant of disrupted dwarf galaxy (Bekki & Freeman, 2003; Bekki & Tsujimoto, 2019). I will discuss in detail the complex system ω Centauri in Sect. 2.1.

Therefore, the multiple sequences observed in ω Centauri along the different evolutionary stages are due to a combination of different chemical composition in terms on light elements, different metallicity and possibly different ages.

Nevertheless, in the following I will show that the presence of MPs arise naturally in all GCs, in all different evolutionary stages if the correct combination of photometric filters are employed.

1.2.1 Main Sequence

The detection of multiple sequences along the MS of GCs is possible thanks to the advent of very deep CMDs obtained with HST and JWST photometry. This feature seems to be something common among GCs. Multimodal MSs are observed in a plethora of Galactic and extragalactic GCs, including NGC 2808, NGC 6341, NGC 104, NGC 6440, NGC 6752, NGC 2210 (Piotto et al., 2007; Ziliotto et al., 2023; Milone et al., 2023; Cadelano et al., 2024;

Milone et al., 2019; Li et al., 2023). This is just a small subset of GCs in which this phenomenon was observed. In Fig. 1.5 can be clearly observed the presence of two different MSs in the Bulge GC NGC 6440. This cluster is known to have no intrinsic metallicity spread (Muñoz et al., 2017), therefore the most plausible interpretation is that the observed split in the MS between magnitude 19 and 22 is caused by a significant difference in the He mass fraction (Y) between the two subpopulations. At magnitudes fainter than 22 (i.e. $m_{F115W} > 22$) there is another bimodal pattern, that in this case is probably due to variations in the abundance of O on the surfaces of the stars. Indeed, the JWST F200W filter is particularly sensitive to O abundance variations since it covers a wavelength range where molecular absorptions due to the water molecule reside (Salaris et al., 2019).
Thus, the presence of multiple MSs in GCs is interpreted as the result of the presence of MPs with different content in terms of He and light elements.

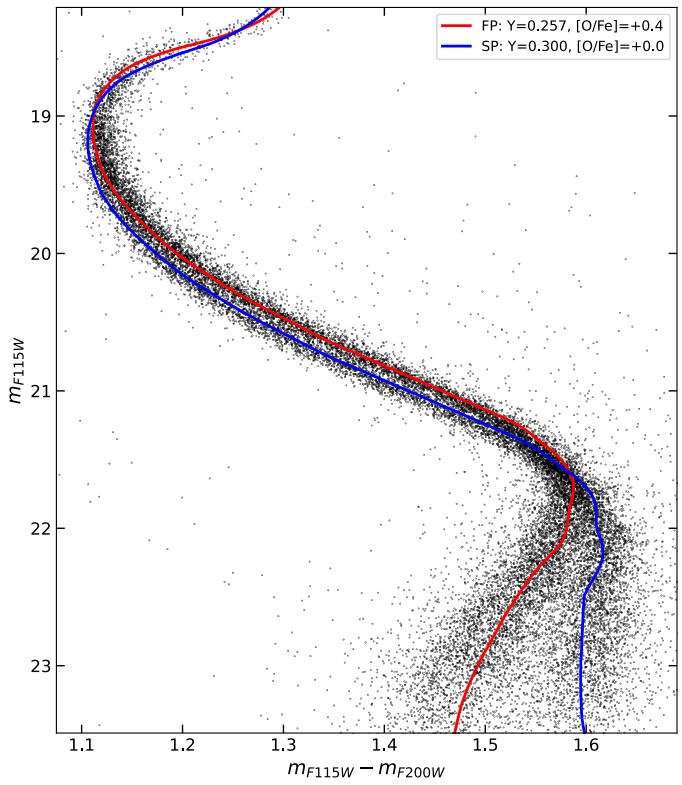

FIGURE 1.5: JWST CMD of the Bulge GC 6440. The red curve represents a 13 Gyr BaSTI isochrone reproducing a $[\alpha/\mathrm{Fe}] = +0.4$ stellar population with a metallicity $[\mathrm{Fe/H}] = -0.6$ dex and a He fraction Y = 0.257. The blue curve represents an isochrone computed at the same age and metallicity as the red one, but with a He fraction Y = 0.3 and a solar-scaled chemical mixture ($[\alpha/\mathrm{Fe}]$ = 0.0 dex). Figure from Cadelano et al. (2024).

1.2.2 Sub Giant Branch

Multimodal sequences are observed also along the SGB stage of numerous GCs, thanks to the analysis coming from very precise photometry. The most famous cases of GCs with multiple SGBs are NGC 1851 (Milone et al., 2008; Zoccali et al., 2009; Han et al., 2009; Lardo et al., 2012; Piotto et al., 2012a; Dondoglio et al., 2023), NGC 6388 (Moretti et al., 2009; Piotto et al., 2012a; Bellini et al., 2013), NGC 6656 (Piotto, 2009; Marino et al., 2012a; Piotto et al., 2012a), NGC 6715 (Piotto, 2009), NGC 362, NGC 5286, and NGC 7089 (Piotto et al., 2012a).

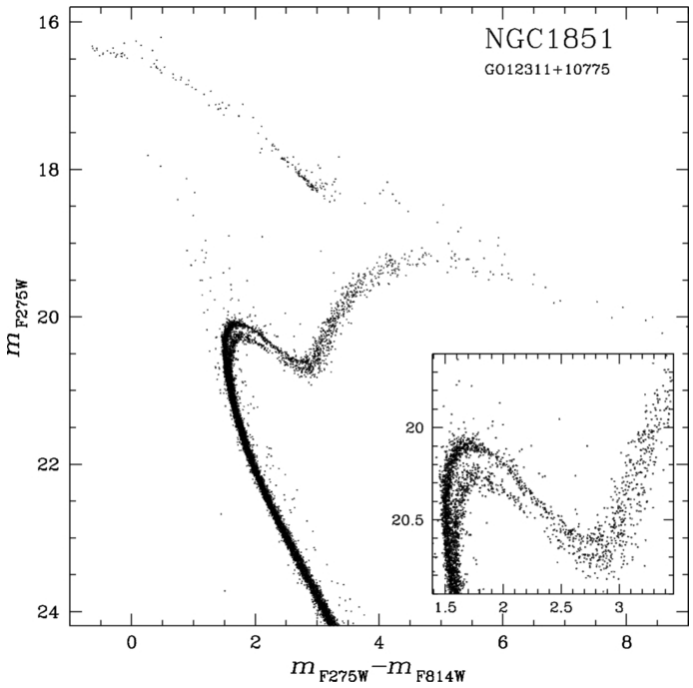

FIGURE 1.6: HST CMD of NGC 1851 obtained from ACS/WFC/F814W and WFC3/UVIS/F275W photometry. The inset on the bottom-right side displays the SGB double sequence of NGC 1851. Figure from Piotto et al. (2012b).

Among them, one of the best studied systems is NGC 1851. In Fig. 1.6 can be observed the presence of a double SGB. These two sequences of SGB, the fainter and brighter ones, are photometrically connected with the RGB sequence. Indeed, Han et al. (2009) and Lardo et al. (2012) found that the fainter SGB is connected with the red RGB population, while the brighter SGB is linked to the blue RGB population. The studies conducted by these authors demonstrated that the double SGB can be explained by two populations of stars with either an age difference of $\sim$ 1 Gyr or with distinct overall abundances of C, N, and O. In particular, according to Lardo et al. (2012) appears that on average the brighter SGB stars are more N-poor than then fainter SGB stars. Assuming that in NGC 1851 is present the classical N-O

anticorrelation, the stars located along the brighter SGB should also be O-rich, while the stars along the fainter SGB should be O-poor.
To conclude, the presence of multiple sequences of stars along the SGB in GCs are really good indicators of chemical differences in light elements.

1.2.3 Red Giant Branch

The presence of multiple sequences of stars along the RGB is an evidence observed in almost all GCs where photometric observation with a good signal-to-noise were performed (e.g., Grundahl et al., 2000; Yong et al., 2008). The detection of multiple RGBs in GCs is made easier by the fact the RGB are the brightest stars present in a GCs and therefore not so deep photometric observations are required to sample with high accuracy this evolutionary stage.

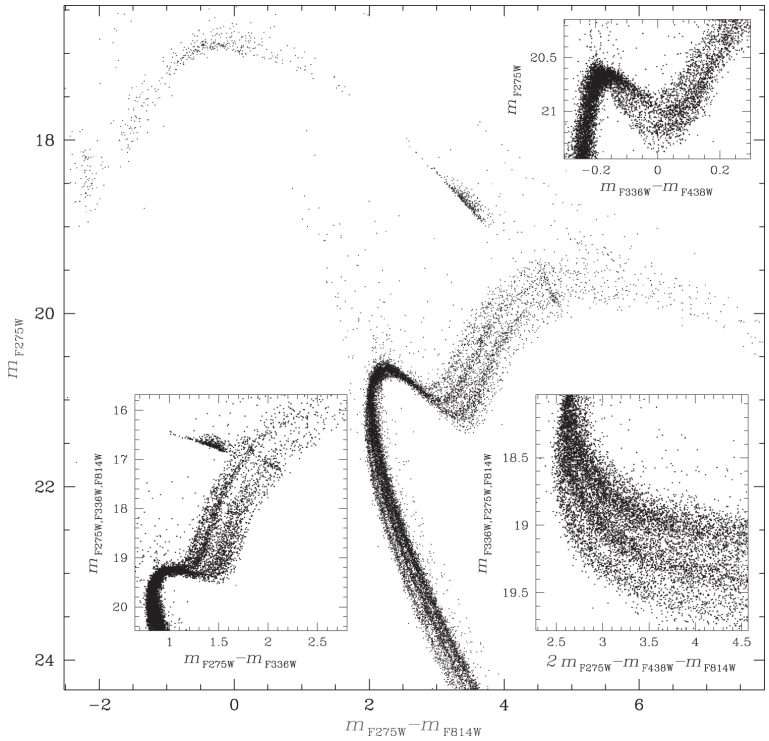

FIGURE 1.7: HST CMD of NGC 2808. Can be seen the multiple RGB sequences in the central figure, while the insets show the same sequences in the MS, SGB and RGB. Figure from Milone et al. (2015b).

As a pure examples, in Figs. 1.7 and 1.8 are reported the HST CMDs of two clusters, namely NGC 2808 and NGC 5286, where multiples RGBs are clearly visible (Milone et al., 2015b, 2017a). This kind of separation is present in a different set of photometric bands. For example, in the work by (Yong et al., 2008) they used the Strömgren photometry to reveal the presence of noticeable spreads along the RGBs of numerous GCs (NGC 288, NGC 362, NGC 5904, NGC 5272, NGC 6205, NGC 6341, NGC 6397, NGC 6752, and NGC 7078).

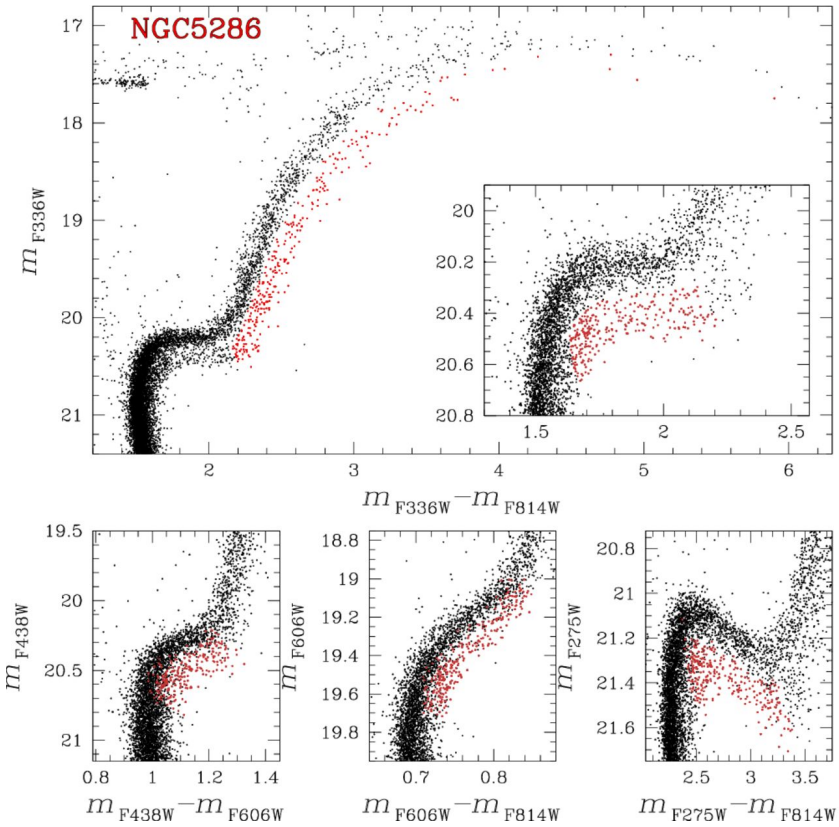

FIGURE 1.8: HST CMD of NGC 5286. It can be clearly recognized the presence of two different RGBs, photometrically connected with the SGB. Figure from Milone et al. (2017a).

Also in this case, the presence of different sequences of stars along the RGBs of GCs is related to variations in the abundances of light elements. However, not only variations in light elements are responsible for the split along the RGB, but also variations in heavier elements. Indeed, the red RGB is usually associated with an enhancement in s-process elements such as Ba and La, while the blue RGB is associated with a depletion in these elements (e.g., Lardo et al., 2012; Marino et al., 2015). These differences in the content of s-process elements are coupled with differences in the overall content of the C, N, O abundances between the red and the blue, with the red RGB enriched in the overall CNO abundance (C+N+O) with respect to the blue RGB (Cassisi et al., 2008; Milone et al., 2017a). Finally, the split along the RGB is influenced also by variations in the abundances of other elements such as Ca, Si, and Ti (e.g., Han et al., 2009). This is particularly evident in NGC 1851, where Han et al. (2009) demonstrated that the red RGB is enhanced in Ca by $\sim$ 0.15 dex with respect to the blue RGB.

1.2.4 Horizontal Branch

At odds to the other evolutionary stages, the HB is rarely used to derive accurate determinations of the stars belonging to different populations with different chemical composition, but it is very useful to obtain information on the MPs present in GCs.
It is widely accepted that the HB morphology in GCs is mainly determined by the metallicity, with the metal-rich GCs stars that preferentially populate the red side of the RR-Lyrae instability strip (the red HB) while metal-poor GC stars tend to stay on the blue HB (Arp et al., 1952). As an example of the different morphology of the HB, in Fig. 1.9 are reported the CMDs of NGC 6637 and NGC 6388 from the work by Dondoglio et al. (2021). NGC 6637 is characterized only by a red HB, while NGC 6388 has an extended HB with a blue tail.

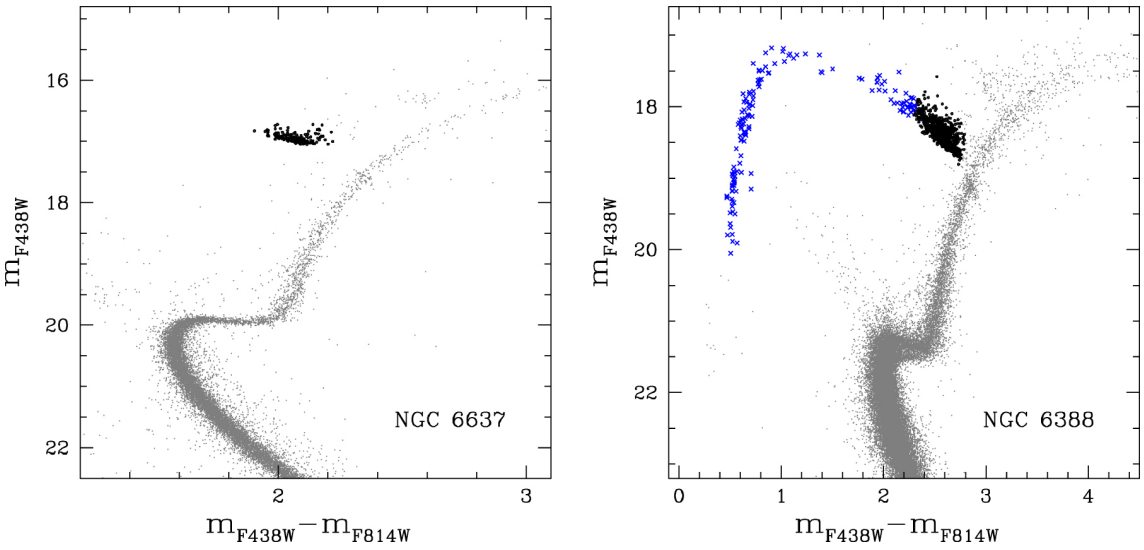

FIGURE 1.9: HST CMD of NGC 5637 (left panel) and NGC 6388 (right panel). The HB of the two clusters is highlighted. Figure from Dondoglio et al. (2021).

In GCs where only the red HB is present, can be found different populations with different abundances in light elements. Indeed, Norris & Freeman (1982) measured the strengths of CN and CH bands in the spectra of 14 HB stars belonging to NGC 104 and found a dichotomy for the analyzed stars. In particular they found that the CN-weak stars (tracer of the N abundance) are on average ~ 0.04 mag brighter in V magnitude than CN-strong stars. Similar results were found also for NGC 6838 by Smith & Penny (1989). Both these clusters are classified as metal-rich GCs (Harris, 2010).
For GCs where also a blue HB is present, also differences in the abundances of light elements are detected between the blue and red HB. Indeed, in GCs such as NGC 6121 and NGC 2808 the HB stars display different content in Na depending on their position in the CMD, with blue HB stars having higher Na than red HB stars (Marino et al., 2011b, 2014).

Moreover, the presence of a blue HB is usually associated with an enhancement in the He abundance with respect to the red HB. Indeed, the main effect of increased He is to increase the temperatures, making all colors bluer. This is suggested by stellar evolutionary models that indicate that bluer sequences have higher He content than redder ones (e.g., D'Antona et al., 2005; Piotto et al., 2007; D'Antona et al., 2022; Li et al., 2023; Cadelano et al., 2023).

1.2.5 Asymptotic Giant Branch

The presence of MPs with different chemical abundances along the asymptotic giant branch (AGB) was detected photometrically in several GCs (Monelli et al., 2013; Nardiello et al., 2015; Milone et al., 2015a,b), by using a combination of $(U-B)$ and $(B-I)$ colors. Indeed, the combination $C_{UBI} = (U-B)-(B-I)$ is very effective to separate different populations of stars in the $V - C_{UBI}$ diagram in both RGB and AGB stages, producing multimodal or broad sequences (Milone et al., 2013; Monelli et al., 2013).
In a recent work by Lardo et al. (2017), they found that the AGB stars of NGC 6121 exhibit a broad distribution across a wide range of C_{UBI} values. This pattern closely mirrors the observations for the RGB stars, for which MPs where confirmed both photometrically and spectroscopically (Marino et al., 2008). Therefore, this result indicates that MPs are present within the AGB of NGC 6121 as well.
Same results about the MPs along AGB sequence were presented for a total of 58 Galactic GCs in a very recent work by Lagioia et al. (2021).

1.2.6 The role of Chromosome Maps

In the last decade a new kind of photometric diagrams were introduced to study and disentangle MPs with different chemical abundances in much more detail. They are known as Chromosome Maps (ChMs) and were firstly used by Milone et al. (2015b) to study the MPs of NGC 2808 along the MS and RGB. However, for this new diagram the name *Chromosome Map* was firstly used by Renzini et al. (2015). ChMs are a pseudo-two-color diagrams built to study separately the diverse evolutionary stages (MS, RGB, AGB, etc.) and are constructed using colors that are particularly responsive to specific compositions of stars within GCs, with the objective of enhancing the separation among the different populations present. The most used filters are the HST F275W, F336W, F438W, and F814W. In particular, ChMs are built by combining the color $(m_{F275W} - m_{F814W})$, which predominantly reflects He variations, with the pseudo-color $C_{F275W,F336W,F438W}$[4] primarily indicative of N abundance variations.

[4]The pseudo-color C is defined as follows:

$$C_{F275W,F336W,F438W} = (m_{F275W} - m_{F336W}) - (m_{F336W} - m_{F438W})$$

It is worth noting that Milone et al. (2013) introduced for the first time the pseudo-color C, with the filter F410W instead of F438W, to study MPs in NGC 6752.
Obviously, other ChMs are built from the combination of optical ($m_{F606W} - m_{F814W}$) and near-infrared (NIR, $m_{F110W} - m_{F160W}$) HST photometry to distinguish populations with different O content (Milone et al., 2017b). Recently also ChMs including the filter F280W were introduced to study MPs as this filter is sensitive to Mg variations (Milone et al., 2020). Also ground-based photometry in U, B, and I bands is used to build ChMs.
In ChMs, FG of stars are identified as those ones at nearly constant $\Delta_{C,F275W,F336W,F438W}$ departing from the origin of the reference frame, that is situated at $\Delta_{C,F275W,F336W,F438W} = \Delta_{F275W,F814W} = 0$. Therefore, SG stars are those ones located in the steep branch of the diagram, at high values of $\Delta_{C,F275W,F336W,F438W}$. As an example of the usefulness of the ChMs to distinguish MPs, in Fig. 1.10 is reported the ChM of NGC 104 for the MS, RGB, and AGB sequences (Milone & Marino, 2022). Can be clearly noted the presence of different populations of stars in the three sequences.

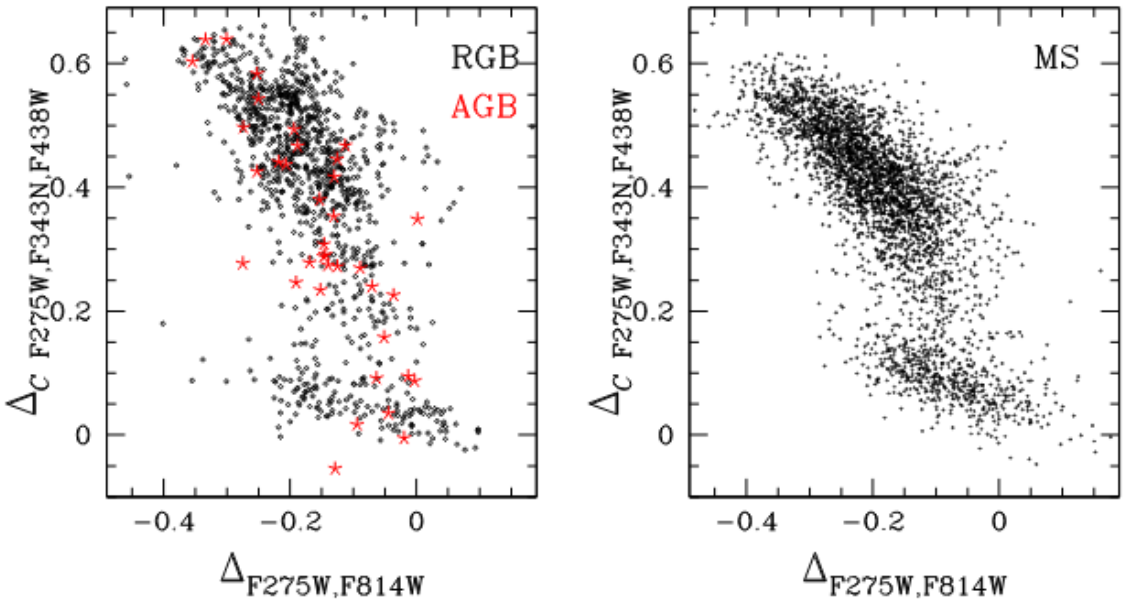

FIGURE 1.10: ChM of NGC 104 for different evolutionary stages. Figure from Milone & Marino (2022).

Milone et al. (2017a) analyzed a total of 57 GCs through the ChMs and found that in the majority of GCs is possible to identify easily the MPs. These clusters were classified as type I clusters. They are characterized by having similar metallicity, but different content in terms of light elements, that are the responsible for the MPs in the ChMs. However, in some of them the separation between FG and SG is quite ambiguous or in some cases not possible at all such as in the cases of NGC 5927, NGC 6304, and NGC 6441.

Among the analyzed GCs exist some that exhibit very complex ChMs, with additional SG (NGC 1851) or split in both the FG and SG sequences (NGC 6934). These GCs were classified as type II clusters. In Fig. 1.11 can be observed the ChMs of two cluster classified as type I (NGC 6723) and type II (NGC 1851), respectively.

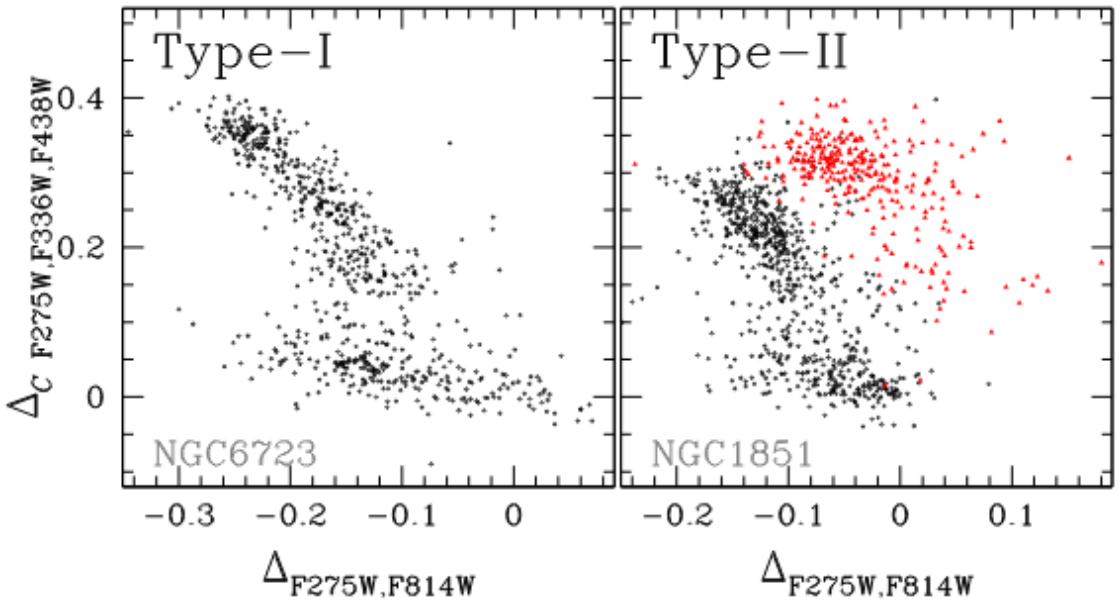

FIGURE 1.11: ChMs for the type I GC NGC 6723 (left-panel) and for the type II GC NGC 1851 (right panel). Figure from Milone & Marino (2022).

According to Milone & Marino (2022), the type II account for $\sim 15 - 20\%$ of the entire Milky Way population of GCs studied through the ChMs, and are characterized by at least one of the following properties:

1. The presence of two or more sequences in the ChM, with the existence of at least and additional sequence on the red part of the ChM.

2. UV and optical CMDs characterized by split or broad SGBs, with the faint SGB that evolves in a redder RGB sequence with respect to the bright SGB.

3. The presence of significant variations in terms of metallicity, or in the overall C+N+O content, or in the content of s-elements (such as Ba and La), or a combination of these effects.

These characteristics of type II GCs could be connected each other and could be key features in the comprehension of formation and evolution of these kind of systems.

1.3 Multiple Populations from a spectroscopic point of view

The first spectroscopic evidence of chemical inhomogeneity among the stars in GCs came out more than fifty years ago (Osborn, 1971) from the study of CN spectral features in RGB stars. Since then an incredible number of spectroscopic evidence of chemical differences in the stars of all GCs were collected. These chemical differences involve the majority of light elements (He, Li, C, N, O, Na, Mg, Al, Si, and K) and are structured as correlations and anti-correlations among these elements. The presence of these patterns in GCs are so important that their presence is one of the key features that define whether a stellar system is classified as GC or not (Carretta et al., 2009a). The authors concluded about the Na-O anticorrelation that *"is present in all clusters studied to date, so it must be fundamentally related to the mechanisms of formation and early evolution of GCs"*.
The most common idea is that within a GC exist at least two different populations of stars with different chemical composition. The FG is characterized by field-like chemical composition, while the SG is enhanced in some light elements such as N, Na, and Al and depleted in others such as C, O, and Mg. The presence of SG stars is generally explained by the existence of some massive stars of the FG (called polluters) that process the material in their interiors through the hot H burning and then eject this material into the intracluster medium. From this processed gas new generations of stars form, with the signatures of the hot H burning. I will discuss in detail the different candidate polluters in Sect. 1.4.
In the following I will present in detail the main spectroscopic evidence of MPs present in GCs. In particular, I will focus on the main anticorrelations observed, including the historical C-N, and I will discuss their possible origin in terms of nuclear reactions.

1.3.1 Helium abundances

The difficulties in the direct He measurements from spectroscopy were already explained in Sect. 1.2. He enhancement among GC stars can be inferred from **(1)** direct measurements of He abundance, **(2)** splits or spreads of the MS in optical CMDs, and **(3)** the HB morphology in the CMD of the clusters. In the following of this Thesis I will refer to He in terms of its mass fraction Y and indicate the He variations among different populations as $\Delta Y = Y - Y_p$, where Y_p represents the initial He mass fraction $Y_p = 0.244$ (Cassisi et al., 2003).
Direct measurements of He can be obtained only along the HB of stars in the temperature range 8000 $\lesssim$ T $\lesssim$ 11500 K. Marino et al. (2014) determined the He content in SG stars of NGC 2808 from the analysis of the He triplet at 5875.6 Å, finding a mean enhancement $\Delta Y \sim 0.09$. However, for these stars the strong effects of atomic diffusion can affect the

final values (Behr, 2003), even though variations are clearly present.
Mucciarelli et al. (2014) measured the content of He along the HB of two metal-poor GCs, namely NGC 7099 and NGC 6397, from the He I line present at 4771 Å. They found small spread of the Y distributions fully compatible with the values expected from the observed MS splitting.
High He enhancements were found also in massive systems such as ω Centauri ($\Delta Y \geqslant 0.14$, Norris, 2004; Piotto et al., 2005; Moehler et al., 2007; Dupree & Avrett, 2013; Bellini et al., 2017b), NGC 6641 ($\Delta Y \sim 0.15$, Caloi & D'Antona, 2007), and NGC 2419 ($\Delta Y \sim 0.11 - 0.18$, di Criscienzo et al., 2011). In all cases such high He enhancements are necessary to explain the blue MS or the blue HB.

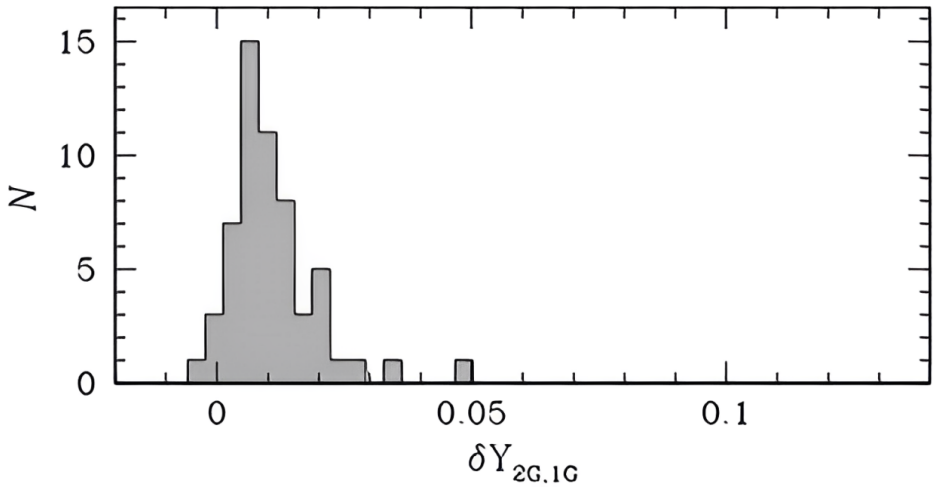

FIGURE 1.12: Histogram distribution of the derived values for the He differences between SG and FG stars for 57 GCs. Figure from Milone et al. (2018).

In the majority of other GCs, the He differences between FG and SG stars were determined through the comparison of multiwavelength HST photometry with synthetic spectra with different chemical composition (e.g., Milone et al., 2018). From the analysis of 57 galactic GCs Milone et al. (2018) found that SG stars are typically more He-rich than FG stars. The median He enhancement for the SG stars is $\Delta Y = 0.01$ (see Fig. 1.12). Noticeably, the two main populations of many GCs are consistent, within the measurement errors, with constant He content but in none of the analyzed systems the FG is more He-rich than the SG. The average He enhancement of SG stars never exceeds 0.05.
He could have enhancements up to at maximum $\Delta Y \sim 0.20$, in some of the most massive GCs, while in other systems the enhancement is usually much lower. Therefore, this quantity serves to put an important constraint on the models for the formation of MPs. Indeed, the He in SG stars usually never exceeds $Y \sim 0.40$ and the yields of the models have to take into account this limit value (see Sect. 1.4).

1.3.2 Lithium abundances

Li represents a fundamental element while searching for the possible polluters responsible for the formation of MPs in GCs. Indeed, Li is rapidly destroyed in proton capture reactions at temperatures exceeding $\sim 2.5 \times 10^6$ K. Such temperature is much lower than the one required to activate the hot H burning (NeNa and MgAl chains, see Sects. 1.3.4 and 1.3.5) at the origin of the light elements anticorrelations. Thus, if SG stars with high values of N, Na, and Al are present within a GC they should be depleted in Li.

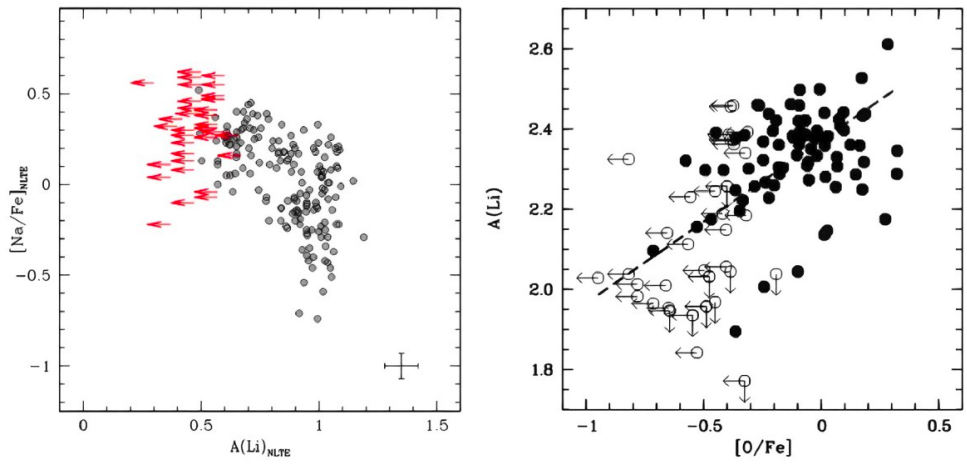

FIGURE 1.13: Left panel: Na-Li anticorrelation for ω Centauri RGB stars (Mucciarelli et al., 2018a). Right panel: Li-O correlation for NGC 6752 (Shen et al., 2010).

Different studies, based on high-resolution spectroscopy, found anticorrelation between Li and Na and Al (and correlation with O), as expected (see Fig. 1.13; Pasquini et al., 2005; Lind et al., 2009; Shen et al., 2010; Monaco et al., 2012; D'Orazi et al., 2015; Mucciarelli et al., 2018a; D'Antona et al., 2019). On the other hand, other studies found no Li variations between FG and SG stars (Mucciarelli et al., 2011; D'Orazi et al., 2010, 2014, 2015).
The presence of Li in SG stars, at the same levels of FG, can be explained in two ways:

- The ejecta of the FG stars (which are Li-free) mix with unprocessed material (which is Li-rich) and from this mixed gas SG stars are formed.
- Li is produced within AGB stars through the Cameron-Fowler mechanism (Cameron & Fowler, 1971) and is ejected into the intracluster medium where SG stars can form with high content of Li.

The case of the dilution model with pristine gas presents some difficulties, as outlined by Salaris & Cassisi (2014). Due to the fact that the processed material should be Li-free and depleted on O, the spread in Li should always be larger than the spread in O. However, for

example in the case of NGC 6752 the spread in Li is smaller than the spread in O. The second hypothesis put strong constraints on the models responsible for the origin of MPs.

1.3.3 C-N anticorrelation

The first hint of the presence of MPs within a given GC came from the analysis of the CN (tracer of N abundance) in the RGB stars of two GCs, namely NGC 5904 and NGC 6254 (Osborn, 1971). They found two stars, one in NGC 5904 and one in NGC 6254, with the CN band strengths anomalously strong with respect to other cluster stars in the same evolutionary stage (see Fig. 1.14).

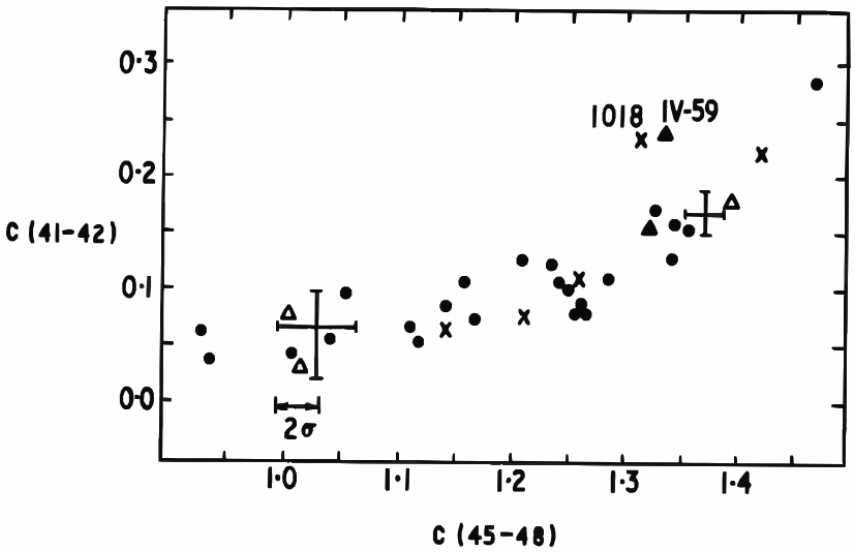

FIGURE 1.14: C(41-42) as a function of C(45-48) for the stars in NGC 5904 (triangles), NGC 6254 (crosses), and other GC stars (circles). The C(41-42) color index is an indicator of the strength of the CN band. The two stars of NGC 5904 (IV-59) and NGC 6254 (1018) display anomalously strong C(41-42) compared with the other stars. Figure from (Osborn, 1971).

Later on Bell & Dickens (1980) and Norris et al. (1981) discovered that the CN bands were anticorrelated with the CH bands (tracer of the C abundance) in RGB stars of the GCs NGC 5272, NGC 6205, and NGC 6752. These clusters present a bimodal distribution of the CN strength (see Fig. 1.15) with the stars divided in CN strong and CN weak. This feature was swiftly identified as a defining characteristic of stars within GCs. Indeed, field and OC stars display weak CN and strong CH bands (Smith & Norris, 1984; Gratton et al., 2004; Martell & Smith, 2009; Carrera & Martínez-Vázquez, 2013).

In normal conditions of equilibrium, the CNO cycle favors the conversion of both C and O into N (see Fig. 1.16). In these conditions, the observed CN strong RGB were interpreted as stars with the presence of CNO processed material in their atmospheres. Indeed, when a

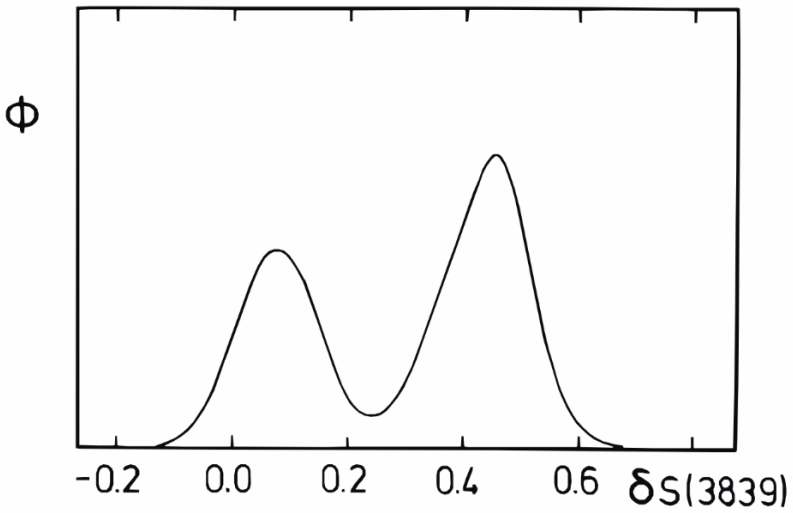

FIGURE 1.15: Distribution of the CN for 49 RGB stars in NGC 6752. Can be noted the bimodality of the distribution. The index S(3839) is an indicator of the CN band. Figure from Norris et al. (1981).

star evolves from MS to ascend along the RGB, as the envelope expands outward, convection delves into regions that previously underwent partial CN processing, where abundances of light elements were altered by proton-capture reactions. As convection penetrates these regions, it dredges up material towards the stellar surface, with the final result of the presence in the atmosphere of the features of the H burning. In particular, the $^{12}C/^{13}C$ and C/N ratios are lowered (Langer, 1985; Charbonnel, 1994; Gratton et al., 2000). This phenomenon is known as first dredge-up (FDU, Iben, 1964). As a consequence, the CNO cycle and the mixing mechanisms responsible for transporting processed material to the surface of the star during the RGB were promptly put forward as a plausible explanation for the observed C-N anticorrelation. Nevertheless, this mixing hypothesis faced challenges due to the advent of new observational evidence. Specifically, the FDU cannot account for the presence of C-N anticorrelation **(1)** in low metallicity stars, in which the convective envelopes will never penetrate deep enough to touch the H burning shell and therefore bring processed material to the surface during the entire RGB evolution of these stars (Gratton et al., 2004), and **(2)** in other evolutionary stages such as the MS (Suntzeff & Smith, 1991; Cannon et al., 1998; Cohen et al., 2002; Grundahl et al., 2002; Ramírez & Cohen, 2002).

The general consensus during this first period of *"chemical anomalies"* observations was that the mixing process occurring during the RGB should take a role, but that mixing alone was not the final answer. Indeed, alongside to the C-N anticorrelation other chemical anomalies started to emerge from the spectroscopic analysis. In particular, Cottrell & Da Costa (1981) observed that the CN strong stars in NGC 6752 were enhanced in both Na and Al with respect to the CN weak stars. These authors proposed that since Na and Al are not produced

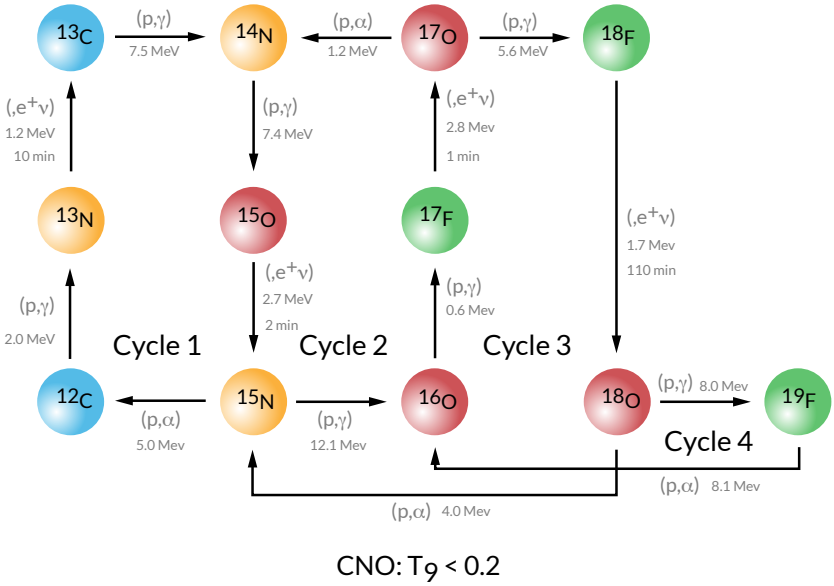

FIGURE 1.16: CNO cycle nuclear reactions. This cycle use the C, N, and O as catalysts to convert ^{1}H into ^{4}He. Figure from the website `https://cococubed.com/code_pages/burn_hydrogen.shtml` by Professor Francis Timmes.

during the evolution of low-mass stars, the observed enhancements in these elements in the CN strong stars cannot be due to the mixing process. Cottrell & Da Costa (1981) concluded that *"massive stars that form in the protocluster gas evolve rapidly and enrich the remaining gas with the products of supernova explosions. Subsequent star formation then yields the CN-strong population of each cluster"*. Even though the proposed responsible for the observed anomalies were massive stars, this is the first time in which MPs are suggested to exist within GCs.
In the subsequent decades, thanks to the advent of higher resolution spectra and deeper observations, many other anticorrelations in all the evolutionary stages were found in GCs.

1.3.4 Na-O anticorrelation

The Na-O anticorrelation is probably the most known chemical anomaly present in a GC. This anticorrelation is widely observed in almost all GCs and is considered as the key feature to define a stellar system as a GC (Carretta et al., 2009a).
The first evidence of the presence of variations in the abundances of O and Na was found by Cohen (1978) from the analysis of red giants in M 3 and M 13 (see Fig. 1.17). The authors concluded that is not possible to explain the measured scatters in O and Na abundances by convective mixing and that the most likely explanation is that the primordial gas from which the stars of these two clusters formed was not chemically homogeneous.

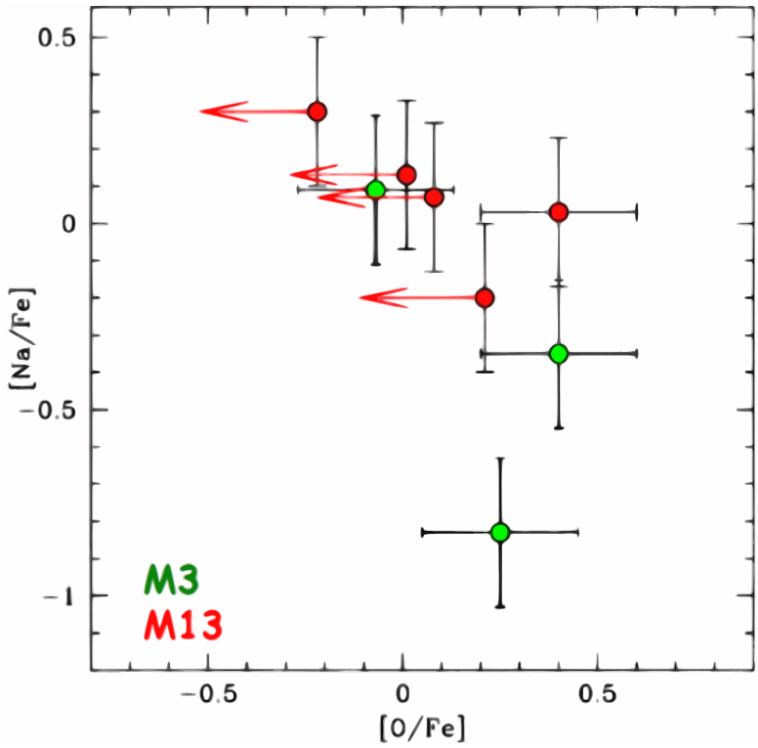

FIGURE 1.17: Na-O anticorrelation for the GCs M 3 and M 13. Figure adapted from Cohen (1978).

This anticorrelation was then observed in an increasing number of GCs and stars (see Fig. 1.18) from the analysis of higher resolution spectra (see Kraft, 1994; Gratton et al., 2004, 2012; Carretta et al., 2009a,b; Bragaglia et al., 2017, for a complete summary of all the observed Na-O anticorrelations in GCs.). Moreover, the Na-O anticorrelation was detected also in other evolutionary phases than RGB such as MS, HB or AGB (D'Orazi et al., 2010; Marino et al., 2011b; Lapenna et al., 2016). These findings lead to the conclusion that the observed anticorrelations among GC stars are the effects of a primordial phenomenon and not due to mixing mechanisms during the RGB phase. Indeed, low mass MS stars are not hot enough for the required set of nuclear reactions that are able to produce the observed chemical variations. In addition, stellar models do not predict any physical mechanism able to transfer processed material from the core of these stars to the surface.

The secondary NeNa chain of the hot CNO cycle (see left part of Fig. 1.19) is considered the responsible for the observed Na-O anticorrelation among the GC stars (Denisenkov & Denisenkova, 1989; Langer et al., 1993; Arnould et al., 1999; Prantzos et al., 2007). This nuclear reaction takes place at temperatures higher than the CNO cycle that cannot be reached during the MS or RGB phase of low-mass stars. During this nuclear reaction, at temperatures $T \geqslant 4 \times 10^7$ K ^{23}Na can be produced at expense of ^{22}Ne through the reaction ^{22}Ne(p,γ)^{23}Na in the same regions where O is depleted by the ON branch of the CNO cycle.

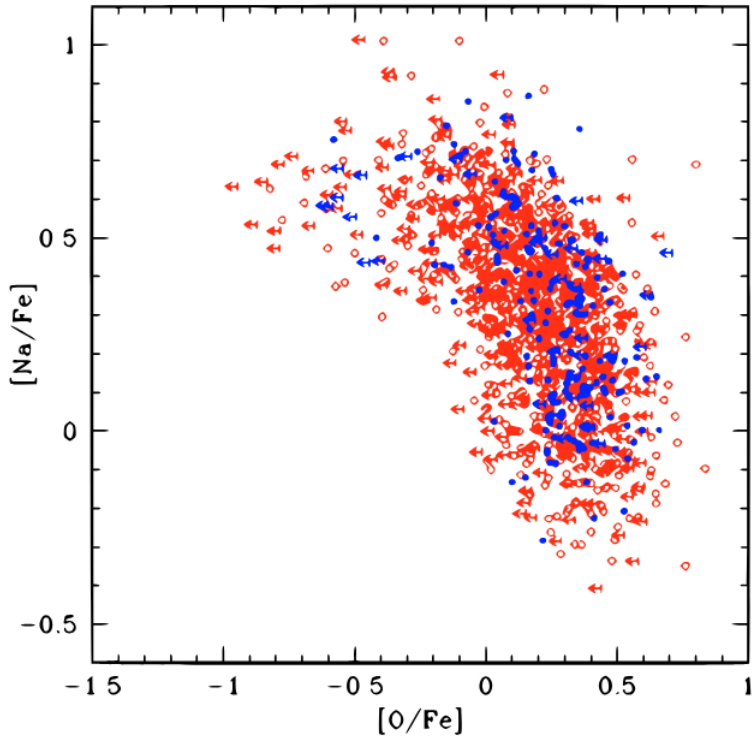

FIGURE 1.18: Na-O anticorrelation for the 19 GCs. A total of 1958 stars are represented. Figure from Carretta et al. (2009a).

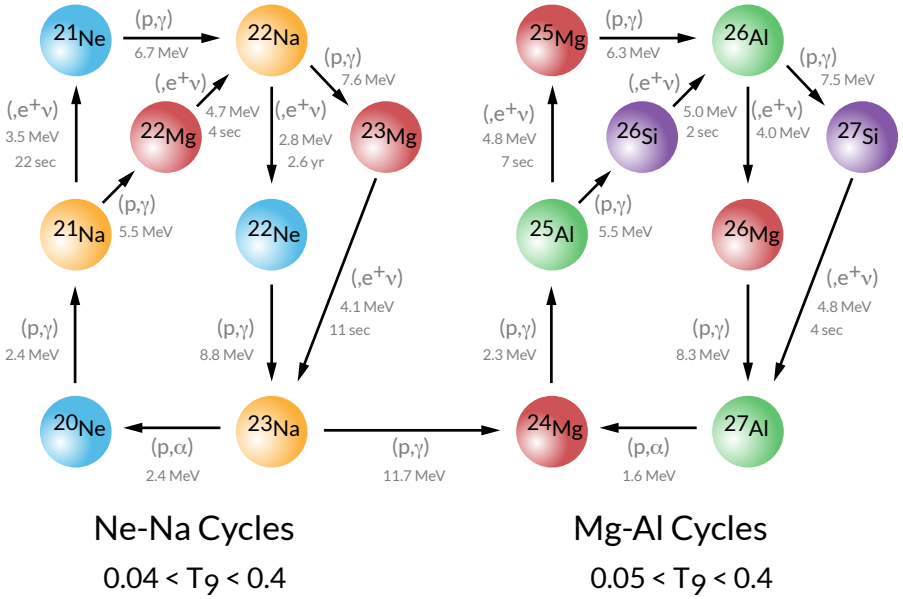

FIGURE 1.19: On the left part is represented the NeNa burning chain, while on the right the MgAl one. Figure from the website `https://cococubed.com/code_pages/burn_hydrogen.shtml` by Professor Francis Timmes.

The presence of the Na-O anticorrelation is related also to the C-N anticorrelation. Indeed, Na is correlated with N, while O is anticorrelated with N abundances (e.g., Cottrell & Da Costa, 1981; Sneden et al., 1992; Marino et al., 2012b).

1.3.5 Mg-Al anticorrelation and beyond

Mg-Al anticorrelation originates from the MgAl chain of the CNO cycle at very high temperatures (T$\geqslant 6 \times 10^7$ K, see e.g., Langer et al., 1993; Arnould et al., 1999; Denissenkov & Tout, 2000; Prantzos et al., 2007). In this nuclear reaction the ^{27}Al is produced by proton captures on the nuclei of the different isotopes of Mg (^{24}Mg, ^{25}Mg, and ^{26}Mg, see right part of Fig. 1.19).

A part from the first evidence of an enhancement of Al in the CN strong stars in NGC 6752 reported by Cottrell & Da Costa (1981), the other evidence coming from this burning chain reported the existence of very large Al variations that were correlated with the Na and anticorrelated with O abundances (Drake et al., 1992; Shetrone, 1994; Norris & Da Costa, 1995b). However, the first evidence of a clear Mg-Al anticorrelation among GC stars is reported by Shetrone (1996) that studied the clusters NGC 5904, NGC 6205, NGC 6341, and NGC 6838. Subsequent studies showed that Mg-Al anticorrelation is present not in all GCs, at odds with the Na-O one, but only the most massive and metal-poor ones (Gratton et al., 2001; Mészáros et al., 2015, 2020; Pancino et al., 2017; Masseron et al., 2019). In particular, Mg depletion and consequent Mg-Al anticorrelation is observed in only $\sim$ 40% of Galactic GCs and is more extended in most massive and metal-poor ones. In Fig. 1.20 is displayed the Mg-Al anticorrelation for a set of GCs studied by Masseron et al. (2019). The majority of GCs are characterized by the presence of a Mg-Al anticorrelation or by a large Al abundance variations, while in some GC (M 107 and M 71) none of these two features are present. These two GCs are the most metal-rich existing in the sample analyzed by these authors. The presence of Mg-Al and Na-Al (anti)correlations in some GCs is the manifestation of the two CNO secondary chains NeNa and MgAl that are operating in a very large range of temperatures.

Among the GCs in which is present the Mg-Al anticorrelation exists a small subsample in which also a Mg-Si anticorrelation is observed (Masseron et al., 2019; Mészáros et al., 2020; Baeza et al., 2022). At temperatures higher than 8×10^7 K the previously produced ^{27}Al is efficiently transformed into ^{28}Si by the nuclear reaction ^{27}Al(p,γ)^{28}Si (Arnould et al., 1999; Prantzos et al., 2007), thus originating the Mg-Si anticorrelation. Indeed, in the absence of this nuclear reaction a correlation between Mg and Si should be present since both are $\alpha-$elements (see Fig. 1.21). This is clear in the analysis by Mészáros et al. (2020) of the Mg-Si anticorrelation in GCs at different metallicities.

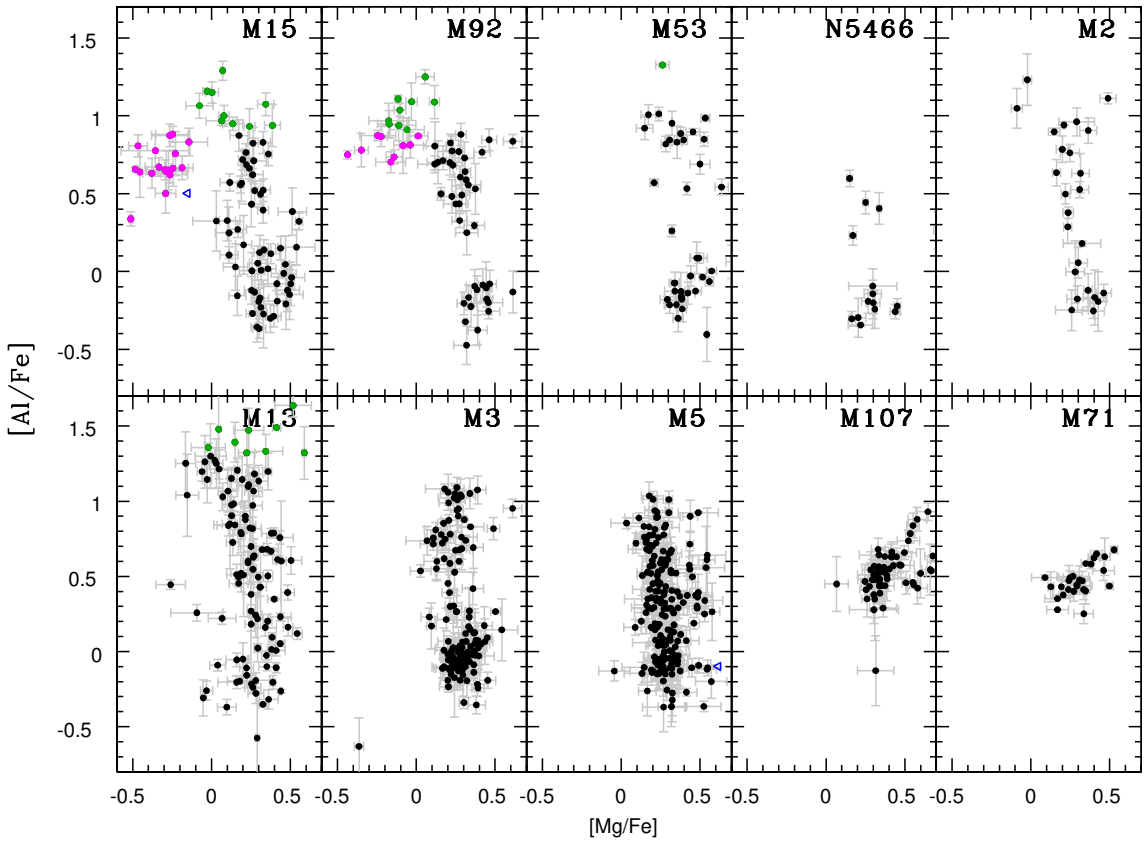

FIGURE 1.20: Mg-Al anticorrelation for 10 GCs. The cluster are sorted by increasing metallicity from left to right and from top to bottom. Figure from Masseron et al. (2019).

More recently another chemical anomaly involving Mg was found among GCs, that is the Mg-K anticorrelation (Mucciarelli et al., 2012, 2015; Cohen & Kirby, 2012; Carretta, 2021, 2022). Such anticorrelation is observed only in an handful of GCs, that are NGC 2419, NGC 2808, NGC 4833, and NGC 6715. However, the presence of an extended Mg-K anticorrelation, associated with large depletion of Mg, is observed only in NGC 2419, NGC 2808 that are among the most massive and/or metal-poor GCs known.

K is produced in a very high temperature regime ($T > 1.5 \times 10^8$ K) through the reaction chain ^{36}Ar(p,γ)^{37}K(β^+)^{37}Ar(p,γ)^{38}K(β^+)^{38}Ar(p,γ)^{39}K (see Ventura et al., 2012; Prantzos et al., 2017).

The presence of all these chemical anticorrelations (C-N, Na-O, Mg-Al/Si/K) shows not only the effects of the complete CNO burning cycle, but also that all the secondary chains of proton capture reactions NeNa and MgAl were active at least in the most massive and/or metal-poor GCs. Moreover, these anticorrelations are observed also in unevolved phases of GC stars. All these evidence exclude the mixing mechanisms as the responsible for the observed chemical differences and point forward to a primordial origin as firstly proposed by Cottrell & Da Costa (1981). Indeed, the presence of anticorrelations linked to the NeNa and

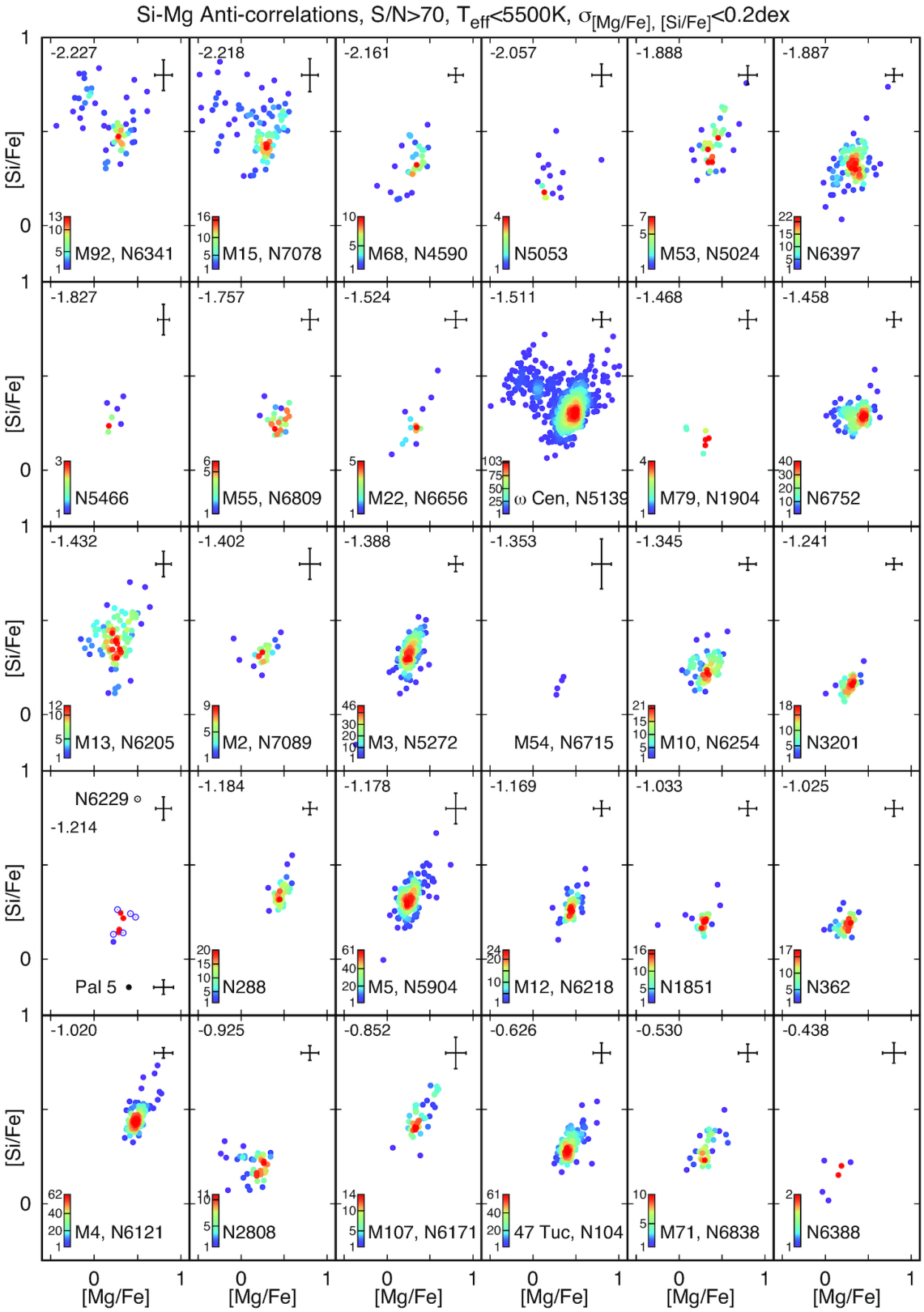

FIGURE 1.21: Mg-Si anticorrelation for 30 GCs. The cluster are sorted by increasing metallicity from left to right and from top to bottom. clear Mg-Si anticorrelation is observed only in M 15, M 92, and ω Centauri. Figure from Mészáros et al. (2020).

MgAl chains exclude the fact that these anomalies could have originated inside the currently living stars due to the fact that they have low masses and their temperatures are too low to activate the proton capture reactions through the NeNa and MgAl chains (Prantzos et al., 2007, 2017). Additionally, the detection of anticorrelations with similar extensions in both dwarf and giant stars rules out any possibly mixing mechanism at the origin of the observed differences because in MS stars the convection is negligible and thus not able to bring material to the surface of the star. Moreover, in MS the H burning mode is dominated by the p-p reactions and not by the CNO cycle (see Gratton et al., 2019).
Therefore, the most likely explanation for the observed chemical anticorrelations is that within GCs exist multiple stellar populations, with the presence of at least two different populations. The first population (or generation) of stars is characterized by the same chemical composition of population II field stars at similar metallicity, while the second population (or generation) of stars is usually enhanced in terms of He, N, Na and in some cases also in Al, Si, and K, while they are depleted in C, O, Ne, and Mg. This second generation of stars thus arises from the ashes of nuclear reactions that happen in some stars of the first generation, called also polluter stars, that eject the processed material through the complete CNO cycle into the intracluster medium allowing then new episodes of star formation.
In the next section I will explore in detail the most likely candidates to be the polluter stars and which are the pros and cons of each of them.

1.4 Polluter stars

In this section I will discuss about the different candidate polluter stars responsible for the formation of MPs in GCs, because the most likely explanation is that MPs are the result of a self-enrichment process within the clusters where material processed through the hot CNO cycle and its secondary NeNa and MgAl chains (e.g., Langer et al., 1993; Arnould et al., 1999; Prantzos et al., 2007) is incorporated in a subsequent generation of stars. Indeed, the majority of theoretical models for the formation of MPs involve the occurrence of two or more episodes (in some clusters only two main populations are detected) of star formation where CNO-enriched stars (SG) were formed out of matter polluted by massive stars with field-like composition (FG) within the first 100-200 Myr of the cluster life.
With this scenario in mind, I would like also to remind that the material that gave rise to the FG of stars was not pristine but was previously enriched by the remnants of several supernovae, predominantly Supernovae (SNe) Type II, as no known GC has a metallicity [Fe/H] $\leqslant -2.5$ dex (see Fig. 1.2) and most of them is defined as α-enhanced ([α/Fe]$\geqslant +0.2$ dex).

During the decades many candidate polluters were proposed to explain the MPs phenomenon in GCs. Given the physical properties of GCs and the observational constraints coming from the chemical anticorrelations, whatever the polluter stars is, it must have the following properties:

- Be able to produce significant variations only in the light elements without producing major variations in heavy elements such as Fe. Indeed, recently it was found that small-to-moderate variations in Fe (from 0.05 up to 0.3 dex) could be quite common in massive GCs (Legnardi et al., 2022; Lardo et al., 2022, 2023; Lee, 2022, 2023; Monty et al., 2023). However, these Fe variations are smaller than those in light elements. In some among the most massive GCs large Fe spreads were found: ω Centauri (Pancino et al., 2000; Johnson & Pilachowski, 2010; Mészáros et al., 2021), M 54 (Bellazzini et al., 2008; Carretta et al., 2010b), M 22 (Marino et al., 2009, 2011a), NGC 1851 (Yong & Grundahl, 2008; Tautvaišienė et al., 2022), M 2 (Lardo et al., 2013; Yong et al., 2014), NGC 5286 (Marino et al., 2015), NGC 6273 (Johnson et al., 2015), Terzan 5 (Ferraro et al., 2009; Origlia et al., 2011; Massari et al., 2014), and Liller 1 (Ferraro et al., 2021; Crociati et al., 2023). These systems probably experienced more complex histories of formation and evolution than the so called *genuine* GCs.

- Be able to activate the complete CNO cycle, including the NeNa and MgAl chains at least on those GCs where the entire set of anticorrelations are observed.

- Be able to eject the processed material into the intracluster medium at low velocity ($\sim$ 10 km s^{-1}) in order to avoid this material to escape from the cluster potential well.

With these ingredients in mind, here are the candidate polluters proposed during the years to explain MPs in GCs.

1.4.1 Asymptotic Giant Branch stars

AGB stars were among the candidates proposed to explain the chemical anomalies observed early in the eighties (Dantona et al., 1983; Renzini, 1983; Iben & Renzini, 1984) and then as the polluters of the FG responsible for the observed patterns of anticorrelation in GCs (Ventura et al., 2001, 2012, 2013; D'Ercole et al., 2008, 2010). The AGB stars in the range of masses between $\sim$ 3M$_\odot$ and $\sim$ 8M$_\odot$ experience a burning phase called hot bottom burning (HBB) in which they can reach very high temperatures (T$>$ 10^8 K) at the base of the convective envelope (see Ventura et al., 2022, and references therein). This mass range can be extend up to $\sim$ 10M$_\odot$ to include the so-called super-AGB (SAGB) stars. In this regime of temperature the proton capture reactions can happen very efficiently through the CNO cycle and NeNa

and MgAl chains.

It is worthy to mention that the maximum temperature that can be reached at the base of the convective envelope is a function of the AGB star mass: in a 3 $M_\odot$ the temperature at the base of the envelope is $\sim 8 \times 10^7$ K, while in a 7.5 $M_\odot$ is $\sim 1.4 \times 10^8$ K (Ventura et al., 2013). In this scenario, a GC experience a major episode of star formation that leads to the formation of FG stars. In the first Myr the feedback from high-mass stars and the associated SNe clean the intracluster medium from the enriched material. This effect is required to avoid large Fe spreads. Then, after $\sim$ 30 Myr the stars of the FG start to evolve through the AGB phase, and their winds due to their low velocity ($\sim 10 - 30$ km s^{-1}; Loup et al., 1993), are not able to escape from the cluster. Thus a reservoir of processed material begins to form into the intracluster medium. This material cools and sinks toward the cluster center, and once a critical density is reached, a SG of stars begins to form out of this material (D'Ercole et al., 2008; Bekki, 2017). However, in order to reproduce the observed Na-O anticorrelation the ejecta of the AGB stars should mix together with pristine material left by the FG star formation before forming the SG.

The dilution of the processed material with gas sharing the same chemical composition of the FG stars is a crucial point of the AGB scenario. Indeed, the yields of all the AGB models produce a Na-O correlation instead of the observed anticorrelation. In Fig. 1.22 can be seen the yields of the AGB stars of different metallicities and masses (see the caption for details). All the models predict a Na-O correlation, with larger correlation at lower metallicity. Thus, in order to obtain a Na-O anticorrelation from the yields of the AGB stars Ventura & D'Antona (2009) proposed a dilution of the ejected material with pristine matter at the level of $\sim$ 50%. However, the amount of dilution between processed material (AGB yields) and diluting material (FG gas composition) varies from star to star depending on its position on the anticorrelation plane.

On the other hand, when Mg and Al (and in some cases also Si) abundances are considered the yields of AGB stars naturally predict depletion of Mg and enhancement of Al/Si (see Fig. 1.23), thus originating a Mg-Al/Si anticorrelation. In particular, the extension of the anticorrelation is metallicity dependent, with larger extensions in a lower metallicity regime that is perfectly in agreement with the currently observations in GCs.

AGB yields are also able to explain, at least qualitatively, the presence of the last outcome of the MgAl chain, that is the Mg-K anticorrelation observed in some GCs. Indeed, when Mucciarelli et al. (2012) and Cohen & Kirby (2012) found the presence of a Mg-K anticorrelation among the stars of NGC 2419 with [K/Fe] enhanced up to $\sim$ 2 dex and [Mg/Fe] depleted down to ~ -1 dex, AGB and specially SAGB stars were proposed as valuable polluters responsible for the formation of SG stars with the observed K and Mg abundances

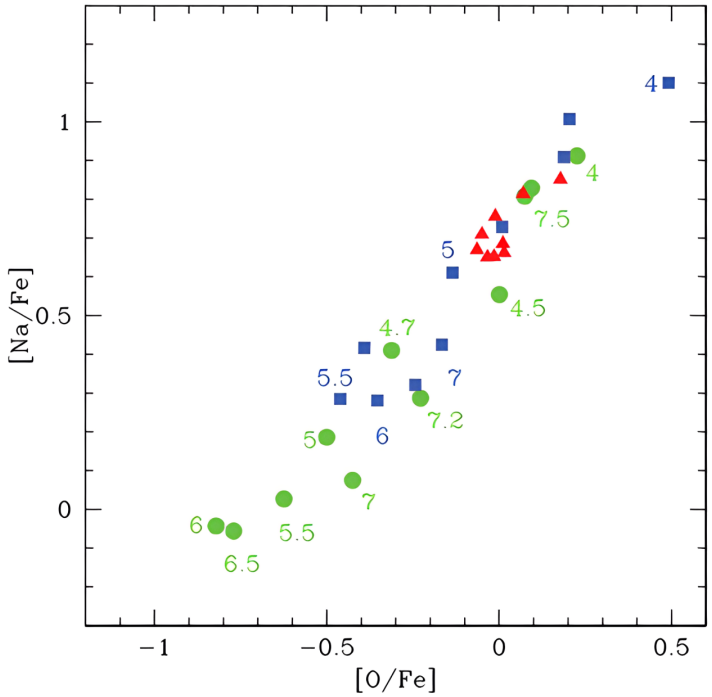

FIGURE 1.22: Yields of AGB of different metallicities in the O–Na plane. Green points: $Z = 3 \times 10^{-4}$; blue squares: $Z = 10^{-3}$ models by Ventura & D'Antona (2009, 2011); red triangles: $Z = 8 \times 10^{-3}$. Numbers close to the points indicate the values of the initial mass. Figure from Ventura et al. (2013).

(Ventura et al., 2012). Ventura et al. (2012) proposed that the AGB and SAGB stars in the low metallicity regime of NGC 2419 experienced a very strong HBB phase, especially around $\sim 6M_{\odot}$, allowing for strong depletion in Mg. The production of K at the observed levels in these stars can happen by proton capture on Ar nuclei, but only if the reaction cross section ^{38}Ar(p,γ)^{39}K is increased by a factor of 100 with respect to the standard rate or if the temperatures at the base of the convective envelope exceed $\sim 1.5 \times 10^8$ K. The SG of stars then formed directly from the ejecta of AGB and SAGB with little or even no dilution with pristine material present in the cluster (di Criscienzo et al., 2011; Di Criscienzo et al., 2015). In those clusters where Mg-K anticorrelation is observed, at the temperatures needed to produce K ($T > 1.5 \times 10^8$ K) the light elements participating the NeNa and MgAl chains disappear because at so high temperatures elements such as Na and Al are destroyed more efficiently than they are produced (see Prantzos et al., 2017 for a detailed discussion). Thus, no Na-O or Mg-Al anticorrelations should be present, which is at odds with the observations. Therefore, the contribution of the yields of AGB stars at different masses as well different degrees of dilution are required to account for the observational evidence.

A major problem affecting the AGB models is the necessity for a dilution to explain the anticorrelations. Indeed, is not clear where gas with FG chemical composition is stored in the

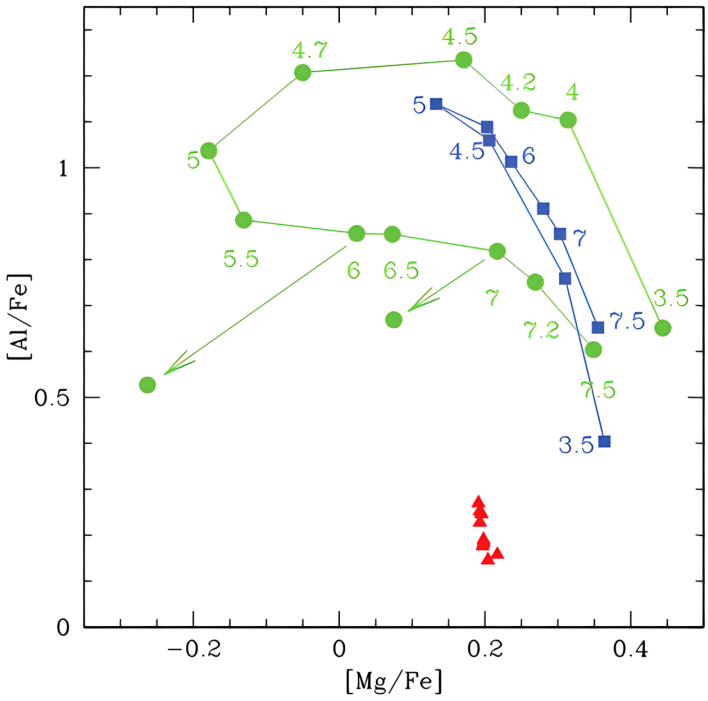

FIGURE 1.23: Yields of AGB of different metallicities in the Mg-Al plane. Green points: $Z = 3 \times 10^{-4}$; blue squares: $Z = 10^{-3}$ models by Ventura & D'Antona (2009, 2011); red triangles: $Z = 8 \times 10^{-3}$. Numbers close to the points indicate the values of the initial mass. The two arrows indicate the results from $Z = 3 \times 10^{-4}$ models of initial mass 6 and 7 $M_{\odot}$ calculated with a smaller rate of mass loss. Figure from Ventura et al. (2013).

meantime of the AGB evolution, and how this gas is not contaminated by the ejecta of FG SNe. In the model proposed by D'Ercole et al. (2008) the AGB ejecta is able to cool very rapidly, likely mix with pristine material, fall at the center of the cluster, and form a SG of stars. However, if there is the presence of heating of a population of X-ray binaries the gas is not able to cool down, but is swept out from the cluster (see Bastian & Lardo, 2018 for a discussion). Another problem comes out from the fact that in the AGB model by Doherty et al. (2014) the sum C+N+O does not remain constant for any AGB polluter star, which is in contrast to the observations for the majority of GCs where the abundances of C, N, and O are available[5]. In the models by Ventura & D'Antona (2009, 2011); Ventura et al. (2013) this effect is mitigated by the fact that in massive AGB progenitors the nuclear reactions are not notably affected by the third dredge-up, which is responsible for the increasing sum C+N+O in the model by Doherty et al. (2014).

[5]Only some GCs such as NGC 1851, M 22, and ω Centauri display increasing sum of C+N+O (Yong et al., 2009; Marino et al., 2011a, 2012b). Again, these clusters are among those suspected to have experienced complex histories of formation and evolution.

1.4.2 Fast Rotating Massive Stars

Fast Rotating Massive Stars (FRMSs) during their MS phase were proposed as candidate polluters for the formation of the SG stars in GCs. Indeed, these kind of stars undergo the H burning in their cores during the MS phase and therefore are, in principle, able to provide the enriched material for the formation of SG stars. Firstly, Wallerstein et al. (1987) proposed that the fast winds coming from the Wolf-Rayet stars could be part of the solution for the observed chemical anomalies in GCs. Later on, Prantzos & Charbonnel (2006) proposed a qualitatively model in which the winds of massive stars (in the mass range $10 - 100\ M_{\odot}$) can provide the enriched material necessary for the formation of SG stars. The stellar winds, enriched with products of H burning, particularly if the stars are rotating, gradually disperse into the surrounding interstellar medium, exerting pressure that creates circumstellar cavities. These winds eventually mix with untouched pristine gas remaining in the system after the formation of FG stars. When this mixed gas encounter the boundaries of these cavities, the shock waves from subsequent SN explosions trigger the formation of new stars. The high-temperature ejecta from SNe within these shock waves primarily expand along the previously carved cavities by the winds of massive stars, ultimately escaping the cluster entirely.
The first quantitatively model based on FRMS was proposed by Decressin et al. (2007a,b). This scenario is similar to the AGB one, because the enriched material produced by FG stars is used to form SG, but this phenomenon happens when the cluster is very young (just $\sim 10-20$ Myr after the FG formation). Also in this case some degree of dilution of the ejected material with pristine gas is needed in order to match the observed patterns of anticorrelations. At odds with the AGB scenario, the FRMSs ejecta naturally originate a Na-O anticorrelation. Also large amounts of He are produced in these stars, thus easily explaining the large spreads of He observed in clusters such as NGC 2808. Nevertheless, the high He yields could be a challenge for those GCs that exhibit small He variations (Chantereau et al., 2016). However, the temperatures necessary for the activation of the MgAl chain in FRMSs can be achieved only at the end of the MS phase, in an environment that have produced large amounts of He, much larger than the inferred values in GCs. Similar results are relative to the Si production. The only way to match the observed MgAl anticorrelation in GCs is to increase the $^{24}\mathrm{Mg}(p,\gamma)$ reaction rate by a factor up to ~ 1000 at $\sim 5\times10^{7}$ K with respect to the nominal rate reported in literature (Iliadis et al., 2001). Finally, no K can be produced in these stars, since they are not able to reach the temperatures needed to burn Ar. Thus, FRMSs models are challenging for those GCs where clear Mg-K anticorrelations are observed. This first model based on FRMSs was further refined in Decressin et al. (2010).
Based on the ideas proposed in Decressin et al. (2007b, 2010), the FRMSs model was further

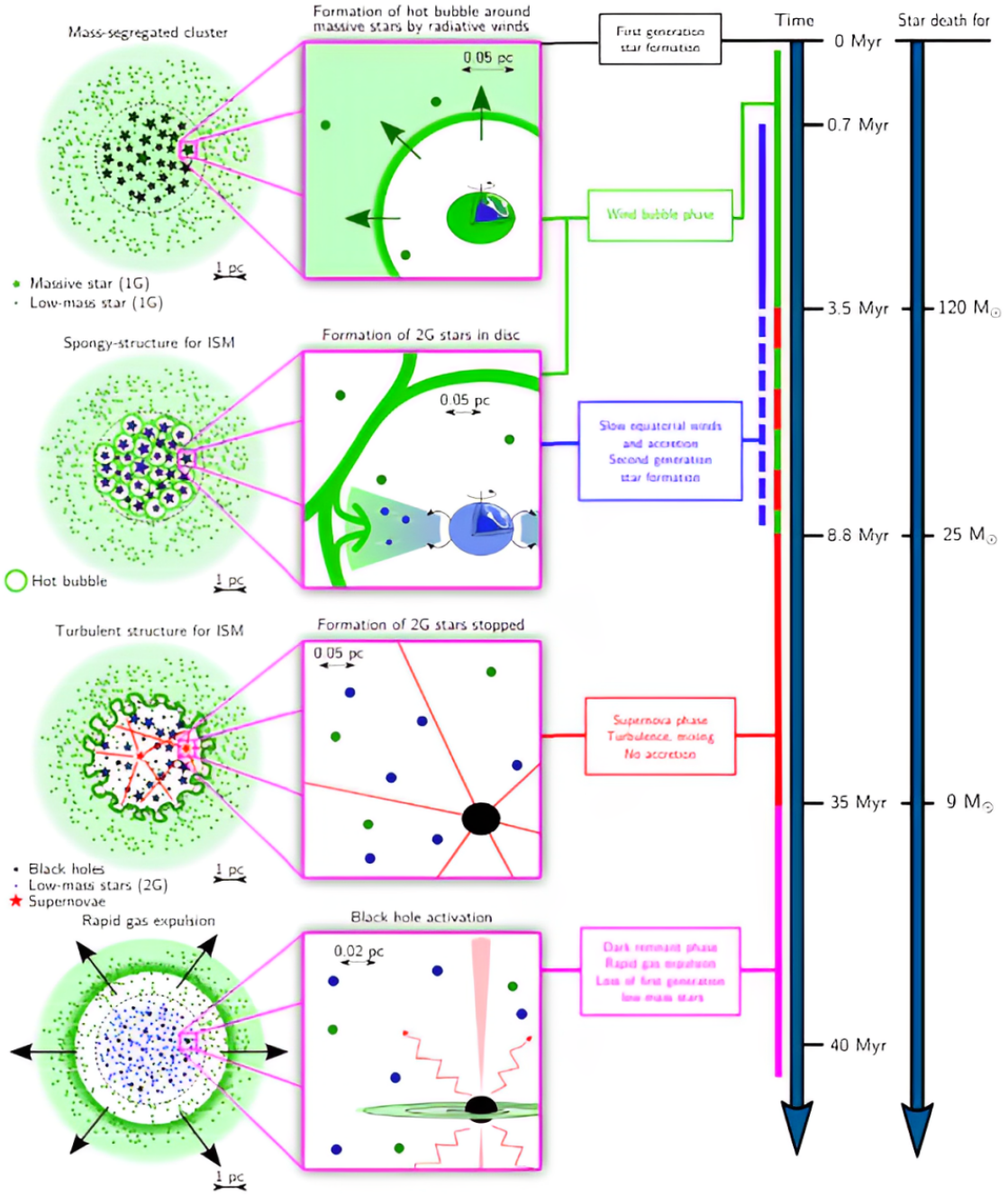

FIGURE 1.24: Sketch of the FRMSs model for the first 40 Myr of evolution of a two population GC together with the global timeline (from top to bottom) and the associated time when the stellar life ends for selected stars on the right. The complete description of the model is in the text. Figure from Krause et al. (2013).

developed by Krause et al. (2013) by considering the case in which the former GC is able to retain the remaining gas from the formation of FG stars, also in the presence of SNe. The model follows the GC evolution over a period of $\sim$ 40 Myr in which the different populations within the cluster form (see Fig. 1.24). In the first column from the left can be seen the entire GC, while the second column shows a zoom-in on a FRMS. The rows (from top to bottom) show four important steps of these model. *First row*: first, a mass-segregated proto-cluster is formed with all FRMS inside the half-mass radius (dashed line) and with the pristine gas (light pistachio-green shade) remaining after the first episode of star formation. Each massive star (the blue interior signifies the convective hydrogen burning core, the bright green envelope depicts the convective envelope, which still has the pristine composition at this stage) creates a hot bubble around it. The corresponding wind shell is represented in a darker shade of green than the uncompressed gas. *Second row*: all hot bubbles connect and create a spongy structure in the center of the cluster. At the same time, slow mechanical winds around the FRMSs create a disk around them. The outer envelope of the FRMS is now blue to denote that it was contaminated by hydrogen-burning products. In the interaction between the ejected disc (blue) and the accreting pristine gas (green), a second generation of chemically different stars is born (blue filled circles). *Third row*: SNe (red stars with straight lines) fail to eject the gas but create a highly turbulent convection zone. Additional accretion onto the remaining FRMSs discs is inhibited. The equatorial ejections also end around this time and the formation of the SG stars is completed by about 10 Myr on the global time axis. *Fourth row*: subsequently, high-velocity gas expulsion takes place and removes the remaining gas together with the majority of the less tightly bound FG stars out of the cluster potential well. Such a rapid gas expulsion is likely to be caused by the activation of black holes by accretion of matter.
Finally, Charbonnel et al. (2014) proposed a variation of the FRMSs model.
A potential problem affecting this scenario is that after $\sim 3-8$ Myr core collapse SNe start to explode and the retention of just a small amount of their material would result in large Fe spreads that are not usually observed in GCs (see e.g., Renzini, 2008; Renzini et al., 2015).

1.4.3 Massive interacting binaries

Massive interacting binaries were proposed as valuable polluters able to release enriched material into the intracluster medium of GCs (de Mink et al., 2009). The authors modeled the binary interaction between a 15 and 20 $M_{\odot}$ and studied the yields of the ejected material. In the interaction they considered the effects of non conservative mass and angular momentum transfer and of rotation and tidal interaction. From the evolution of the model emerges that

the system eject ~ 10 $M_\odot$, that is nearly the entire envelope of the primary star. The ejecta are enriched in He, N, Na, and Al and depleted in C and O, similar to the abundance patterns observed in GC stars. However, Mg is not significantly depleted in the ejecta of this model (see Fig. 1.25) because the temperatures reached are high enough to activate proton capture onto ^{25}Mg and ^{26}Mg, but not onto the most abundant isotope ^{24}Mg. This has an effect on the Al abundances that are enhanced just by a factor of two. In this model the sum C+N+O is expected to be constant, according to the observations in most GCs. The ejected material of these stars has low velocity and thus it remains inside the potential well of the GC and becomes available for the formation of the SG stars. This model works well within the assumption that the majority of massive stars in the proto-cluster are members of interacting binary systems.

In this model the precise yields are contingent on many factors such as the time of interaction, the total stellar mass, and the mass ratio. As a result, massive interacting binaries offer a potential explanation for the different amounts of abundance variations from cluster to cluster.

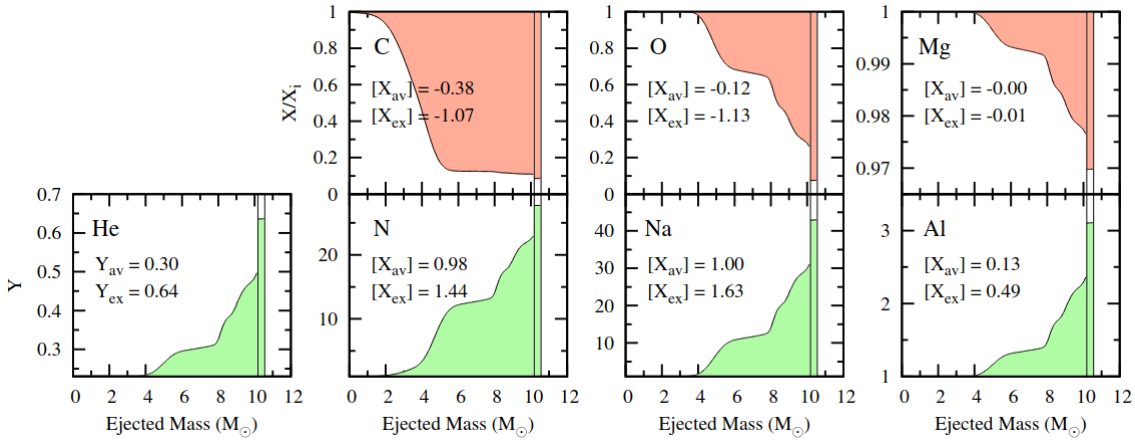

FIGURE 1.25: Composition of the low-velocity ejecta of the considered binary system as a function of the ejected amount of mass. The mass fraction X of the main stable isotope of each element is given relative to the initial mass fraction X_i, except for Mg where all its isotopes were added together. The average X_{av} and the most extreme mass fraction X_{ex} are expressed on a logarithmic scale: $[X] \equiv \log_{10}(X/X_i)$. For He is shown the absolute mass fraction Y. Mass ejected during the different mass transfer phases is separated by a thin vertical line. Figure from de Mink et al. (2009).

1.4.4 Cool Supergiants

Another type of proposed polluters within GCs are the cool red supergiants in the range mass $\sim 150 - 600$ $M_\odot$ (Szécsi et al., 2018). In this model, star-forming shells around cool supergiants could form the SG low-mass stars in Galactic GCs. The cool supergiants in general

have a convective envelopes because of their low surface temperatures (T$<$ 10^4 K). Thus, envelope convection mixes nuclear products from the burning regions of the core or shell to the surface. Hence, the wind of the cool SG stars contains the products of nuclear burning that is happening in the deeper regions of these stars. In particular, in case of H burning in the core of these supergiants, the nuclear products of the winds are hot H burning products. Indeed, due to the high core temperatures of these stars, they are able to activate also the MgAl chain very efficiently, without increasing artificially the reaction rate of the MgAl chain as required for FRMS and interacting binaries (see Decressin et al., 2007b; de Mink et al., 2009). The ejecta are naturally enriched in Na and Al and depleted in O and Mg, with the caveat that in order to explain extreme depletion/enhancement of Mg/Al deeper layers of the supergiants should be lost.

The material processed by the cool supergiants is ejected via strong but slow winds into the intracluster medium and could eventually mix with pristine gas and form the SG stars in shells around the supergiants. However, as for the other models based on massive stars, the model based on cool supergiants can only explain the Na-O and Mg-Al anticorrelations together with high He abundances, much higher than the observed values. This issue is generic to all models, as both the NeNa and the MgAl chains are side reactions of hot H burning and H burns into He.

Finally, an issue of this model is that is expected to operate at low metallicity. Indeed, in the metal-rich regime the very massive stars (M $>$ 150 $M_\odot$) do not become cool supergiants because their mass-loss is very high and so they become hot Wolf–Rayet stars instead. No shells are expected to form around these hot stars. Thus, if cool supergiants were effective polluters for the SG stars in GCs, they were active in the subsample of low-metallicity GCs.

1.4.5 Supermassive Stars

Supermassive Stars (SMSs) represent another type of proposed polluters within GCs that could be responsible for the formation of SG stars with abundance variations compared with FG stars. Denissenkov & Hartwick (2014); Denissenkov et al. (2015) proposed a model where within a proto-cluster the most massive stars sink to the center by dynamical friction and coalesce together, forming SMSs of $\sim 10^4$ $M_\odot$. The model was refined by Gieles et al. (2018) who proposed the concurrent formation of GC and SMSs (M$\gtrsim 10^3 M_\odot$) to address the origin of the observed chemical patterns in GCs. In this scenario GCs form in converging gas flows and accumulate low-angular momentum gas, which accretes onto protostars. This leads to an adiabatic contraction of the cluster and an increase of the stellar collision rate, which

can produce a SMS through runaway collisions if the cluster reaches sufficiently high density before two-body relaxation halts the contraction. An object of this kind would be fully convective, with a luminosity close to or exceeding the Eddington luminosity, hence would lose mass at high rate. Since full convection makes the SMS chemically homogeneous, as it evolves its winds would be progressively enriched in He, in the products of CNO cycle and proton capture reactions. This is exactly the gas chemical composition necessary to form SG stars.

Gieles et al. (2018) showed that a minimum SMS mass of $\sim 5 \times 10^3 M_\odot$ is required to reach the Mg-burning temperatures ($\geqslant 7.5 \times 10^7$ K). Finally, SMSs do not reach the temperatures needed to produce K (Prantzos et al., 2017). As for other proposed model, also in this case the processed material could mix with pristine gas present in the proto-cluster.

The process of gas ejection from SMSs goes on until they burn out or potentially explode owing to instabilities within the stars. Moreover, due to the fact the SMSs can be rejuvenated many times through stellar collisions, the amount of processed material ejected by these stars could be an order of magnitude higher than the maximum mass of the stars.

One important point of this model is linked to the fact that the central temperature strongly increases at the end of the MS (where He mass fraction Y = 0.8), up to values where Na and Al are efficiently destroyed through proton capture. Therefore, if SMSs played a role in the GC pollution, they must have ejected processed material at the beginning of the MS, before starting to destroy the previously produced Na and Al. Albeit this process leads to MPs of stars within the cluster, the expected age spread between different populations would be less than $\sim$ 3 Myr, in order to avoid the Fe contamination coming from the explosion of first core collapse SNe (see e.g., Renzini, 2008; Renzini et al., 2015).

In Fig. 1.26 is depicted the general interaction between a SMS and the proto-cluster.

According to this model at lower [Fe/H] the SMSs are hotter, which predicts that the extension of the Mg-Al anticorrelation is larger at lower metallicity. Also a strong correlation between the mass of the SMSs and GC mass comes from the model, which naturally translate into the fact that preferentially massive and metal-poor GCs contain more pronounced Mg–Al anticorrelations. This is in agreement with the current observations (Mészáros et al., 2015; Pancino et al., 2017).

However, one of the major flaws of the model is that SMSs are still only theoretical, although Gieles et al. (2018) perform numerical simulations showing that under specific conditions runaway collisions are likely to take place, even when considering two-body relaxation and the strong stellar mass loss of these stars due to their winds.

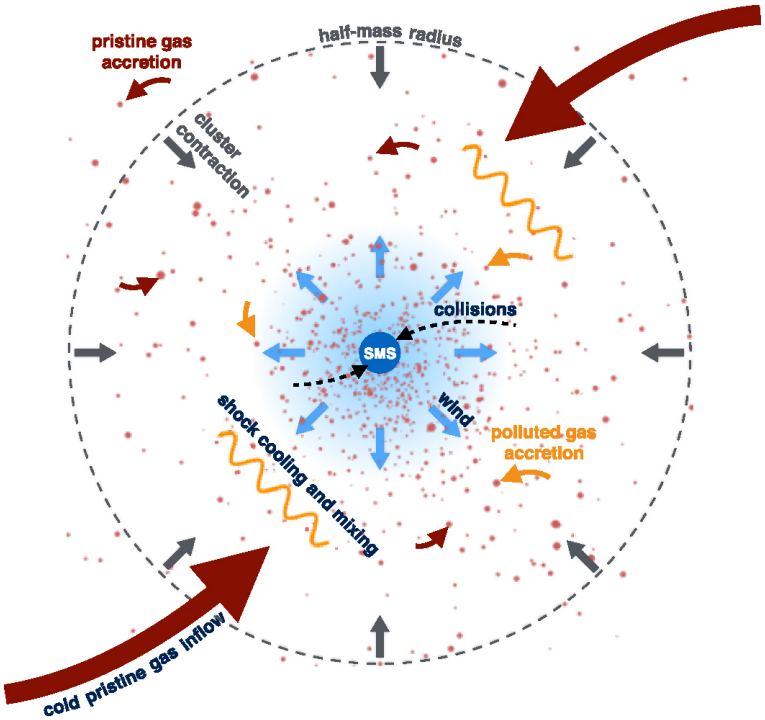

FIGURE 1.26: Picture of the enrichment scenario due to a SMS. Cold, pristine gas accretes onto the cluster, causing the cluster to contract. The higher stellar density results in stellar collisions, generating a SMS in the cluster center. The SMS eject winds enriched in hot H products, which interacts and mixes with the accreting gas. This material serves as a reservoir of gas for the formation of SG stars. Figure from Gieles et al. (2018).

1.4.6 Novae

Maccarone & Zurek (2012) studied the possible contribution of classical and recurrent novae from isolated white dwarfs accreting from the intracluster medium to the abundances of SG stars present in GCs. In this model, the authors find that $\sim 8\%$ of the initial mass of the FG stars ends up as white dwarfs. Maccarone & Zurek (2012) evaluated the amount of material that a white dwarf can process before the formation of SG stars and found that an average white dwarf is able to process about its own mass. This material, enriched in He and some light elements, is then lost through the nova shell and injected into the intracluster medium and becomes available to form SG stars. The model assumes that a large amount of gas is still available in the cluster after the white dwarfs start to form.

The yields of He and metals and the ejected masses seem to depend only weakly on the composition of the white dwarf, while the specific composition of the metals in the ejecta can depend strongly on whether the white dwarf is a CO white dwarf or a NeOMg white dwarf (see Yaron et al., 2005). The set of parameter values for which nova yields were calculated was steadily expanding over the last decades, but is still not detailed enough to account for

a precise amount of metals produced by novae. Therefore, the nova model can satisfactorily explain only the observed He abundances in GCs.
Theoretical investigations showed that the nova outburst is a multi-parameter phenomenon, depending on the mass, temperature and composition of white dwarfs (José, 2017), therefore is not straightforward to perform simulations of the nova nucleosynthesis. However, simulations suggest that peak temperatures up to 4.5×10^8 K can be reached during the nova outburst (Yaron et al., 2005; Denissenkov et al., 2014), allowing production of elements up to K. The problem with the yields is that in all cases elements lighter than K such as Na, Al, Si are overproduced with respect to the observed patterns.

1.5 Constraints on the formation scenarios

All the aforementioned scenarios apart from be able to explain the chemical anticorrelations have also to reproduce a large number of observational constraints coming from both the old Galactic GCs, but also from younger GCs present in the Magellanic Clouds. In this Section, I will list the main observational constraints that all the described scenarios have to reproduce in order to be considered as feasible models.

1.5.1 Mass-budget problem

It is well known that within GCs the fraction of enriched stars, i.e. the SG stars are equal or even larger than the primordial population FG (e.g., Renzini et al., 2015; Bastian & Lardo, 2018). In particular, in the central regions of GCs SG stars can constitute up to $\sim 70\%$ of total stars, as the case of NGC 2808 (Milone et al., 2015b). In the case in which a standard initial mass function (IMF) is adopted for both the FG and SG stars, the quantity of processed material by FG stars and from which SG formed would not be enough. This phenomenon is known as the mass-budget problem[6]. The mass-budget problem in its simplest form is the following: the SG that is born in the cluster should contain as much (50:50) mass as the FG. For example, in the case in which the AGB are the polluter stars and adopting a standard IMF (e.g., Prantzos & Charbonnel, 2006), only $\sim 7\%$ of the total FG mass is in the AGB stars. Assuming that 100% of the mass of every AGB star is used to form SG stars (which is not reliable) and that also the SG has a standard IMF, AGB stars can only account for $\sim 4-5\%$ of the population of SG stars. Also in the case in which is assumed that, on average, 50% of the mass of each SG star is given by pristine gas diluted with ejecta, AGB stars can account

[6]According to Prantzos & Charbonnel (2006) stars are formed in the range $0.1 - 100$ $M_\odot$. However, also adopting the IMF by Kroupa (2001) which is in the range $0.1 - 120$ $M_\odot$ the mass-budget problem persists.

for $\sim 8 - 10\%$ of the total SG stars.
The mass-budget problem is faced also by massive polluters such as FRMS, massive interacting binaries, and cool supergiants.
Different solutions were proposed to solve or alleviate the mass-budget problem. In particular:

- D'Ercole et al. (2010) proposed a truncated IMF for the SG stars. In particular they proposed that all the SG stars are less massive than ~ 8 $M_{\odot}$.
- The number of FG stars was much larger when the cluster formed, and that $\sim 90\%$ of them were lost during the evolution of the cluster. These lost stars would then populate the field of the host galaxy. Therefore, at the epoch of formation GCs were substantially more massive than their present-day GC progeny, with a strict lower limit of a factor of ~ 5.
- The ejecta of the polluters mix with large amounts of pristine gas left in the cluster after the FG star formation or that is accreted by the interstellar medium (e.g., Conroy & Spergel, 2011). This provides a natural explanation for the approximately equal number of first- and second-generation stars in GCs, but at the cost of having fewer chemically peculiar SG stars than are observed.

All the proposed solutions suffer for different problems. For example, for the AGB scenario D'Ercole et al. (2008) and Conroy (2012) estimated that GCs were at least $10 - 20$ times more massive than today. In the FRMS scenario, GCs were expected to be $8 - 25$ more massive than today. In a recent study, Cabrera-Ziri et al. (2015) discussed the mass-budget problem in detail finding that under more realistic assumptions this problem could be $2 - 3$ times worse, implying that GCs at their birth were up to 60 times more massive than today. Therefore, the standard solution proposed to overcome this problem is the assumption that GCs were $10 - 100$ times more massive at birth than they are currently, and that, because the SG stars are thought to be born more centrally concentrated, a large fraction of the FG stars were lost during their evolution.
Kruijssen (2015) estimated the total amount of mass lost from GCs forming and evolving in a cosmological context and found that massive GCs (initial mass $> 5 \times 10^5$ $M_{\odot}$) are only expected to lose a relatively small fraction of their initial masses, thus being at their birth just a factor $2 - 4$ more massive than today. Therefore, no final solution for the mass-budget problem exists, independently for the adopted model.

1.5.2 Specificity

The existence of SG stars within GCs that are characterized by their peculiar chemical composition made of (anti)correlations is common in almost all these systems, but not in other environments such as the Milky way field or OCs. Still, in the field of Milky Way exist stars with the chemistry of GC SG stars, but they are few and thought to be lost by the clusters through tidal interaction with the Galaxy (Vesperini et al., 2010; Martell et al., 2011). Therefore, the environment conditions of the proto-clusters were very *specific*, allowing to form stars (SG) with peculiar chemical compositions that are not observed in stars present in other environments.
Young massive clusters, with masses up to $\sim 10^8$ $M_\odot$ are occasionally forming in the local Universe, but do not appear to be forming stars with the chemistry typical of SG (Bastian et al., 2013). This seems to be an hint of the special conditions present in the early Universe at the epoch of GCs formation.

1.5.3 Ubiquity and variety

The presence of MPs is an evidence that was found in (almost) all GCs and their existence is demonstrated both from a photometric and spectroscopic point of view. This suggests that the production of MPs is an inevitable outcome of the early formation process of GCs. Indeed, MPs are nearly *ubiquitous* in old massive GCs, independent of their formation environment (formed within the Galaxy or elsewhere) or metallicity. Thus, any GC formation scenario have to account for the formation of MPs.
There is evidence that each GC studied has its own specific pattern of MPs. In some cases just two different populations are present among a GC, while in other many different populations coexist within a GC such as in NGC 2808 where seven different populations where recognized (Milone et al., 2015b). Moreover, each GC with MPs shows a different degree of depletion/enhancement among its stars according to different parameters such as the cluster mass or metallicity. All these evidence call for a high degree of *variety* among the MPs of GCs. It can therefore be inferred that there will be considerable differences between the manner in which material from the FG stars are incorporated into SG stars and the chemical composition of these material.

1.5.4 Discreteness

A significant attribute of MPs is that within each GC, they can be well separated into *discrete* sequences in both CMDs and ChMs (see Fig. 1.27), as opposed to a continuous distribution.

The utility this property offers in differentiating between different scenarios is considerable, particularly given the challenges encountered in reproducing discrete populations by some of them. The issue mainly concerns scenarios invoking a single star formation episode, where the FG stars are accreting material with a peculiar chemical composition, thereby becoming SG stars. In order to account for the observed discreteness, the most likely explanation is that GCs experienced several star formation episodes that created different populations. Indeed, individual bursts of star formation had a finite duration, hence stars formed at different phases of the burst were made of material with slightly different composition, as indeed the composition of the intracluster medium was continuously changing, being the medium continuously fed by the polluter stars of the FG. This is a feasible assumption in the AGB scenario, but it is more complicated to apply to scenarios involving disks around massive stars, such as the FRMSs and the massive interacting binaries. For these latter scenarios there is still the possibility to produce discrete populations under the assumption that massive star feedback leads to multiple episodes of star formation.
The presence of discrete MPs in GCs is easily detectable through different photometric diagrams (CMD and ChMs), while in many cases it appears that from a spectroscopic point of view (in the abundance planes of anticorrelations) the MPs have a continuous distribution. This continuous distribution in the anticorrelation planes is mimed by abundance measurement errors, which blur the underlying discreteness. Indeed, from a spectroscopic analysis in NGC 2808, Carretta (2015) were able to find five distinct populations in the Mg-Na plane. NGC 2808 is not the only case in this sense.

1.5.5 Supernova avoidance

In the majority of GCs the MPs display significant variations in their light elements with extended (anti)correlations, while their content of Fe is almost the same with small to moderate variations (at maximum 0.3 dex, see Legnardi et al., 2022; Lardo et al., 2022, 2023; Lee, 2022, 2023; Monty et al., 2023). These kind of GCs are known as type I GCs according to their ChMs (Renzini et al., 2015; Milone et al., 2017a). This evidence has a strong implication for the early evolution of these systems. Indeed, core collapse SNe belonging to both first- and second-generation stars, whose ejecta are enriched in Fe, should give little or no contribution at all to the formation of the SG. This problem is known as *supernova avoidance*. All the proposed models for the formation of MPs should somehow take into account the fact that the majority of the gas coming from the core collapse SNe is sweep out, allowing the cluster to retain only the gas processed through hot H burning. The situation is even more complicated when the dilution with pristine gas is considered. Indeed, is not clear how the

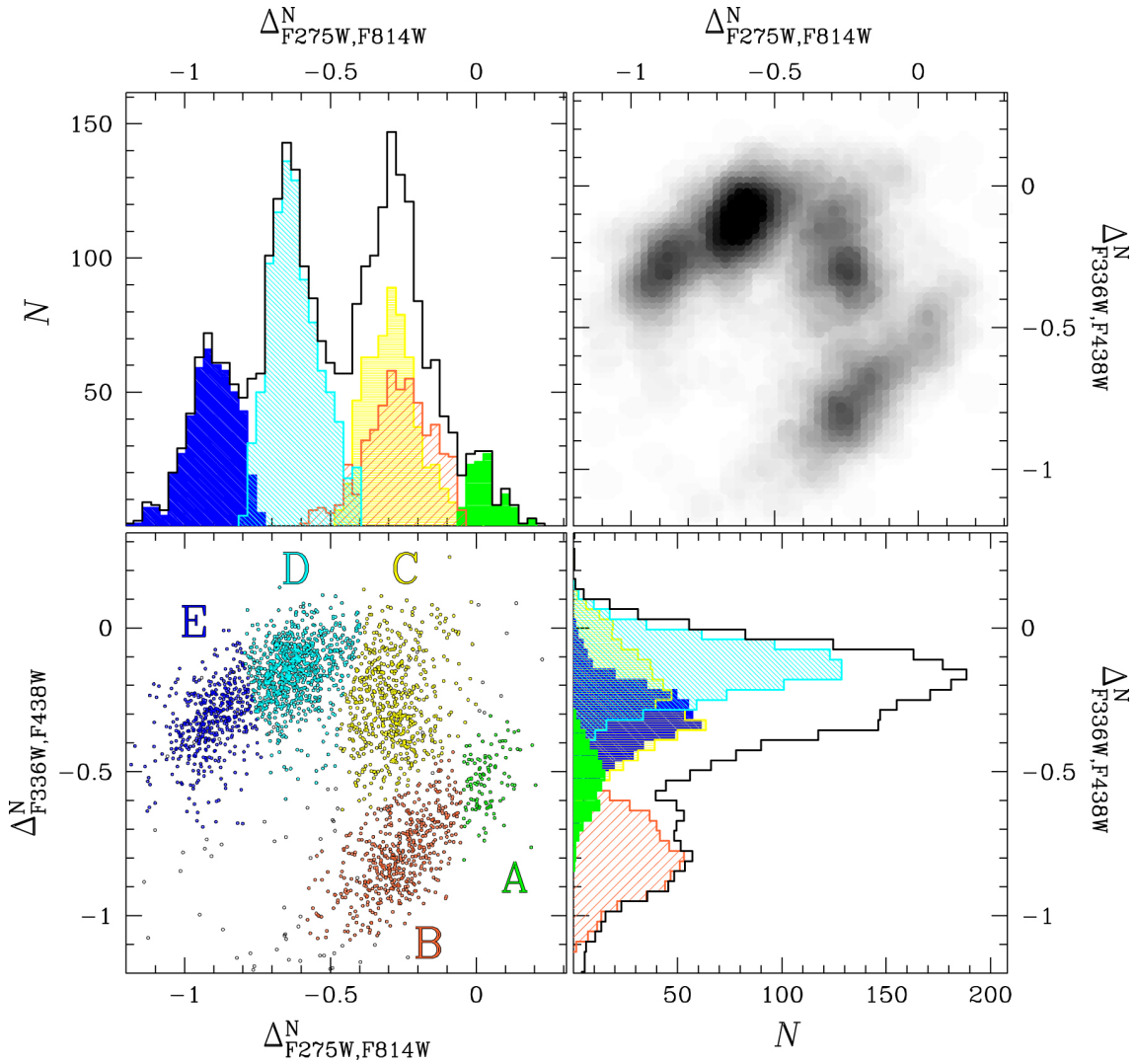

FIGURE 1.27: The ChM of NGC 2808. Stars in the groups A, B, C, D, and E are colored in green, orange, yellow, cyan, and blue, respectively (lower-left panel). The corresponding Hess diagram is plotted in the upper-right panel. The histograms of the normalized $\Delta_{F275W,F814W}$ and $\Delta_{F336W,F438W}$ distributions for all the stars are plotted in black in the upper-left and lower-right panels, respectively. The shaded colored histograms show the distributions for each of the five populations defined in the lower-left panel. Figure from Milone et al. (2015b).

unprocessed material is able to remain into the intracluster medium and is not swept out by the SNe explosions. The proposed solutions to avoid the recycling of the SNe ejecta into the intracluster medium are the following:

- SG stars must be formed in a very short amount of time (Wirth et al., 2021). In the majority of cases the authors found that the star formation ends after $\sim$ 6 Myr. This scenario disfavors models of polluters that require longer times to evolve, such as the AGB model.

- Stars more massive than 8 $M_\odot$ do not form and thus no core collapse SNe are present within the cluster. In the model by D'Ercole et al. (2010) this problem is alleviated, since the IMF of the SG is truncated at 8 $M_\odot$, therefore no core collapse SNe of SG exist in their model.

- The ejecta of core collapse SNe are fully released in the medium surrounding the cluster (Tenorio-Tagle et al., 2015, 2016). Such events lead then to no contamination of the gas left over from the formation of a FG stars.

- Massive stars collapse directly into a black hole without exploding as core collapse SNe. This was postulated by Krause et al. (2013) to ensure the supernova avoidance for the FRMSs. The authors proposed that stars more massive than $\sim$ 25 $M_\odot$ would collapse to a black hole without noteworthy energy and material release into the intracluster medium. This hypothesis is supported by independent arguments (Sukhbold et al., 2016; Adams et al., 2017; Eldridge & Stanway, 2022). However, all the stars in the range $8 - 25$ $M_\odot$ still have the possibility to explode as core collapse SNe. Thus, the problem persists.

The exception to the *supernova avoidance* seem to be represented by the GCs that exhibit large Fe spreads, with ω Centauri being the most emblematic case. These systems are the so-called type II GCs. Nonetheless, also in the case of ω Centauri to enrich SG stars to their observed Fe content it is sufficient that only $\sim$ 2% of the Fe ejecta of the core collapse SNe from the FG were retained and incorporated into SG stars, while 98% of such ejecta were lost by the system (Renzini, 2013). Indeed, the main SG component of this system contains only $\sim$ 25 $M_\odot$ more Fe than the FG component (Renzini, 2008). The core collapse SNe from the FG of $\sim 2 \times 10^6 M_\odot$ at origin have instead produced $\sim 10^3$ $M_\odot$ of Fe, with most that was ejected. As quoted by Renzini (2008) this estimate is just an upper limit and thus smaller fractions than 2% would be sufficient to enrich the SG. Therefore, in all GCs both type I and II, SG stars have experienced very little contamination by SNe explosions, or none at all, with only a very small fraction of such products integrated into SG stars. Every scenario for

the formation of GCs has to take into account the *supernova avoidance*.
Since a single model fails in reproducing all the observed chemical patterns and all the required constraints here described it was proposed that mixed contributions from different polluters can represent a valuable explanation for MPs (e.g., Sills & Glebbeek, 2010). While one particular class of polluters can be the dominant source for the processed material, it is very probable that several mechanisms are active at the same time during the early evolution of the GCs (Valcarce & Catelan, 2011). Indeed, if the protocluster at its birth formed stars with a standard IMF (e.g., Kroupa, 2001), different type of candidate polluters were present (i.e. AGB, FRMS, interacting massive binaries, etc.), with one class being probably the dominant source of enriched material.

CHAPTER 2

Among us: stellar systems disguised as GCs

It is widely recognized that (almost) all the Galactic GCs are characterized by the presence of MPs with different chemical composition. In particular, the FG is characterized by stars with primordial or field-like chemical composition, while the SG hosts stars with the chemical signatures of the material processed in the interiors of FG polluters. On the other hand, the majority of GCs are characterized by small or moderate Fe variations. In particular, Legnardi et al. (2022) measured the Fe spread among FG stars in 55 Galactic GCs finding that the metallicity spread ranges from less than [Fe/H] $\sim$ 0.05 dex up to 0.30 dex, with an average value of $\sim$ 0.1 dex. This spread is mildly correlated with the GC mass, implying that more massive cluster have larger Fe variations (see Fig. 2.1).

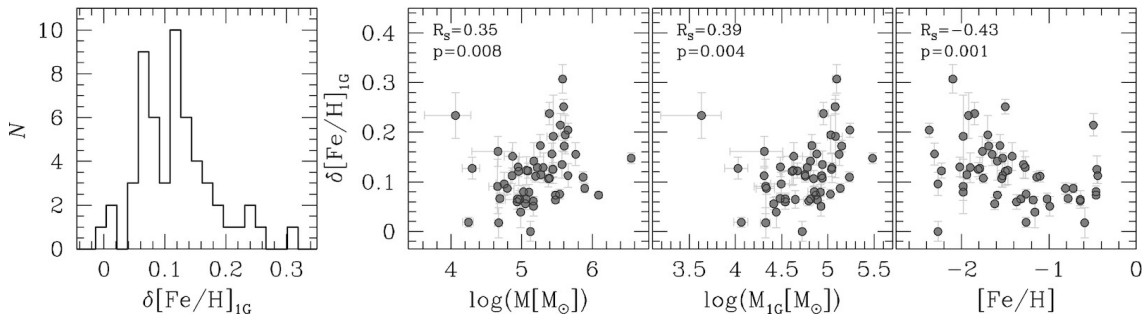

Figure 2.1: Histogram distribution of Δ[Fe/H] of the FG for 55 Galactic GCs (left). The relations between Δ[Fe/H] of the FG stars and cluster mass, FG mass, and [Fe/H] are plotted in the other three panels. Figure from Legnardi et al. (2022).

All the GCs with these characteristics, i.e. MPs with chemical variations and small-to-moderate Fe variations, can be classified as type I GCs according to their ChMs (see e.g., Renzini et al., 2015; Milone et al., 2017a). These systems are also known as *genuine* GCs.

On the other hand, exist a subset of GCs with the presence of MPs and with well recognized large and intrinsic Fe spreads. In the ChMs they are classified as type II GCs and apart from the Fe variations, spectroscopically are characterized by variations in the overall C+N+O

content, or by variations in the elements produced via slow neutron capture reactions (*s*-elements) such as Ba and La (e.g., Milone & Marino, 2022). However, not all the GCs with the described properties were studied through ChMs. In particular, for those systems located in the Bulge such as Terzan 5 and Liller 1 no ChMs exist due to the difficulties in UV/blue observations of regions with very high extinction.

Among the GCs with large Fe spreads, the most famous are NGC 1851 (Yong & Grundahl, 2008; Tautvaišienė et al., 2022), M 22 (Marino et al., 2009, 2011a), M 2 (Lardo et al., 2013; Yong et al., 2014), ω Centauri (Pancino et al., 2000; Johnson & Pilachowski, 2010; Mészáros et al., 2021), M 54 (Bellazzini et al., 2008; Carretta et al., 2010b), Terzan 5 (Ferraro et al., 2009; Origlia et al., 2011; Massari et al., 2014), and Liller 1 (Ferraro et al., 2021; Crociati et al., 2023). All these complex systems are stellar systems disguised as GCs and from a chemical perspective, they are situated in the middle between *genuine* GCs, the typical Type I GCs, and more massive systems such as dwarf galaxies with which they share the enrichment in metallicity. Historically these systems were classified as GCs due to the fact that they are (like *genuine* GCs) old, bright, compact and in the range of masses of GCs. However, during the decades high-resolution photometric and spectroscopic analysis revealed that these systems probably had different histories of formation compared with *genuine* GCs.

Nowadays is generally accepted that these complex GCs do not constitute an homogeneous class of objects, but rather each of them experienced its own complex history of formation and evolution. Today they are observed as GCs with chemical differences in light and heavy elements, signatures of their particular history.

In the following I will discuss in detail some of these complex GCs, that are the systems I characterized during my PhD work. I will describe each of them separately, according to the most common accepted scenario for their formation and evolution history.

2.1 ω Centauri: remnant of a disrupted galaxy

ω Centauri, also known as NGC 5139, is the most studied and at the same time the most complex stellar system among the Galactic GCs.

Historically, ω Centauri was classified as a GC due to its morphology (see Fig. 2.2). Dunlop (1828) described ω Centauri as a *"beautiful large bright round nebula, about 10' or 12' diameter, easily resolvable to the very centre; it is a beautiful globe of stars very gradually and moderately compressed to the centre; the stars are rather scattered preceding and following, and the greatest condensation is rather north of the centre; the stars are of slightly mixed magnitudes, of a white colour. This is the largest bright nebula in the southern hemisphere"*. From this note can be observed that ω Centauri was distinguished as a GC since its first observations due to its nature of bright and

compact object. Studies performed during the last 50 years demonstrated that ω Centauri behaves like a GC, with the presence of MPs with different chemical composition. However, the most astonishing characteristic of this system is its metallicity distribution that spans almost 2 dex, with the presence of different peaks of metallicity. From this point of view, ω Centauri could be considered a *bridge* between the *genuine* GCs, which display large variations in light elements and small variations in heavy elements, and the dwarf galaxies, which are the least massive self-enriching systems containing complex stellar populations with large Fe spreads (see Fig. 2.3; Tolstoy et al., 2009; Willman & Strader, 2012). It is interesting to observe that ω Centauri has a spread in Fe comparable to that of dwarf galaxies at similar absolute magnitude, reinforcing its possibly conjunction between GCs and dwarf galaxies.

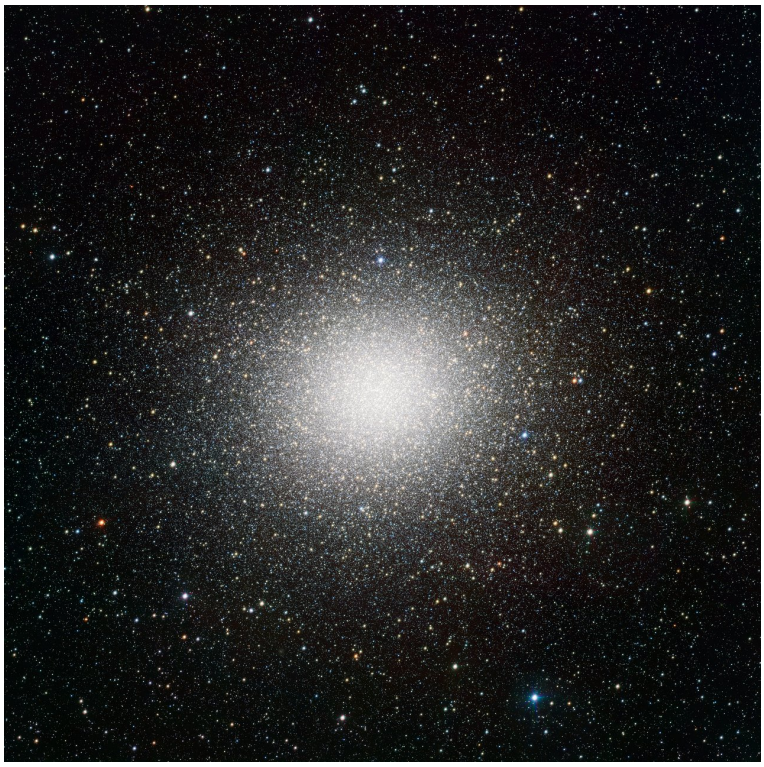

FIGURE 2.2: ω Centauri image acquired with the VST OmegaCAM. Credits: ESO/INAF-VST/OmegaCAM.

In the following Sections of this Thesis I will try to briefly review and summarize the vast literature of observational evidence, both photometric and spectroscopic, collected about ω Centauri. I will outline the different results and shortly mention the possible explanations. Also, I will try to explain why this system still deserves to be studied in detail through high-resolution data.

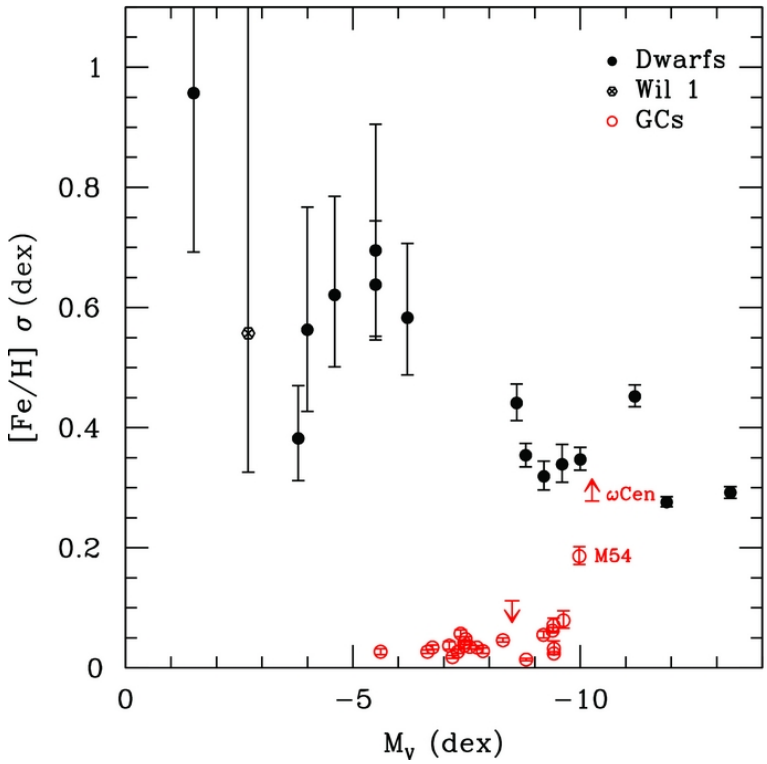

FIGURE 2.3: Dispersion in [Fe/H] measured for Milky Way dwarf galaxies (black filled) and GCs (red open) as a function of the absolute magnitude, calculated assuming an underlying Gaussian distribution. Figure from Willman & Strader (2012).

2.1.1 Structural properties

In this Section I will briefly review all the general properties concerning ω Centauri.

ω Centauri is the brightest system among GCs, with an absolute magnitude in the V-band $M_V = -10.17$ (Baumgardt et al., 2020). Shapley & Sawyer (1927) made a visual estimate of 3 for the integrated photographic magnitude of ω Centauri, finding that this cluster was the brightest among those they analyzed. Moreover, ω Centauri is the most massive Galactic GC with a mass $M = (3.94 \pm 0.02) \times 10^6\ M_\odot$ (Baumgardt & Hilker, 2018). Poveda & Allen (1975) first estimated that ω Centauri should be more massive than $3.3 \times 10^6\ M_\odot$, resulting in a mass-to-light ratio $M/L_V > 3.0$. Such value of mass, agrees very well with the current value of mass for ω Centauri, while the present value of mass-to-light ratio is quite smaller, being $M/L_V = 2.80 \pm 0.10$ (Baumgardt et al., 2020). In Fig. 2.4 are represented the absolute magnitude and mass distributions for the Galactic GCs. From these data, the average values for the absolute magnitude and masses for GCs are $M_V \sim -7$ and $M \sim 2 \times 10^5\ M_\odot$, respectively. In this sense, ω Centauri is the GC with utmost properties.

ω Centauri is clearly visible in the southern sky with the naked eye, due to its equatorial coordinates (RA J2000 = 201.°69699 ; Dec J2000 = −47.°47947, Goldsbury et al., 2010).

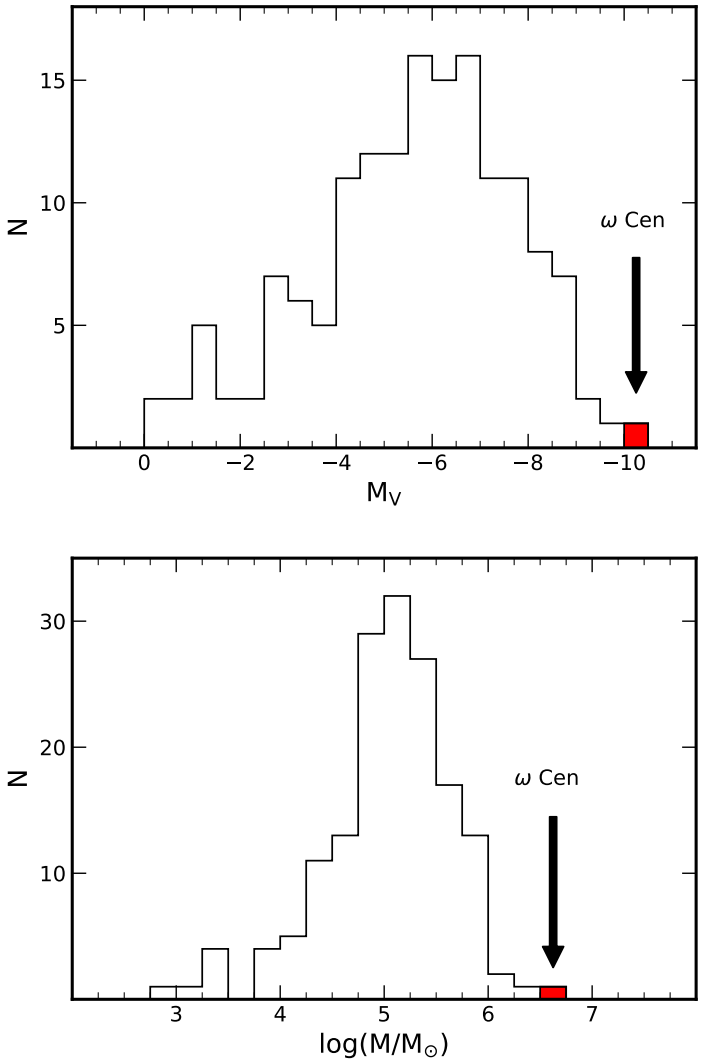

FIGURE 2.4: Histograms of absolute magnitudes, M_V (top panel), and masses, $\log(M/M_\odot)$ (bottom panel) for all the Galactic GCs. The position of ω Centauri, at the extreme of the distributions, is marked by an arrow and a red bin. Data from Baumgardt & Hilker (2018); Baumgardt et al. (2020); Baumgardt & Vasiliev (2021).

ω Centauri is located in the Halo of the Milky Way, at 5.43 ± 0.05 kpc from the Sun and at 6.50 ± 0.01 kpc from the Galactic center (Baumgardt & Vasiliev, 2021). Table 2.1 reports the main information about position, proper motions, and distances for ω Centauri.

Several studies showed that ω Centauri moves on a strong retrograde orbit (e.g., Dinescu et al., 1999; Majewski et al., 2000), but essentially confined within the Galactic plane with a $z_{max} = 1.40$ kpc and an apocentric radius of 6.95 ± 0.03 kpc (Baumgardt & Hilker, 2018). Therefore, given its proximity to the Galactic plane during the orbit, ω Centauri is subject

Table 2.1. Main properties of ω Centauri.

RA J2000	201.°69699	Goldsbury et al. (2010)
Dec J2000	−47.°47947	Goldsbury et al. (2010)
$\mu_\alpha \cos\delta$	-3.2510 mas yr^{-1}	Häberle et al. (2024)
μ_δ	-6.7398 mas yr^{-1}	Häberle et al. (2024)
Galactic latitude	309.°1020	Goldsbury et al. (2010)
Galactic longitude	14.°9683	Goldsbury et al. (2010)
Distance from Sun	5.43±0.05 kpc	Baumgardt & Vasiliev (2021)
Distance from Galactic center	6.50±0.01 kpc	Baumgardt & Vasiliev (2021)

to a strong dynamical interaction with the Galaxy. In particular, disk shocks and tidal interaction can produce loss of the most external stars of ω Centauri, forming the so-called tidal tails. These stars cannot be considered bound to the system anymore, since they are located much more outside the tidal radius, but they are relatively close to the cluster and share some characteristics with cluster member stars such as velocity and metallicity. Meylan et al. (2000) and Leon et al. (2000) for the first time suggested the presence of tidal tails around ω Centauri, with an extension to $\sim$ 5 tidal radii. These authors estimated also that during the last disk shocking ω Centauri lost about 0.6 to 1% of its mass. More recently Ibata et al. (2019a), used N-body simulations to show that the *Fimbulthul* structure (Ibata et al., 2019b) is the long hunted tidal stream of ω Centauri, extending up to 28° from the cluster. The presence of such tidal tails was confirmed also by a more recent work by Youakim et al. (2023).
ω Centauri has a core radius $r_c = 4.30$ pc, a projected half-light radius $r_{h,l} = 7.56$ pc, an half-mass radius $r_{h,m} = 10.42$ pc, and a tidal radius $r_t = 208.60$ pc (Baumgardt & Hilker, 2018). The resulting concentration index $c = \log(r_t/r_c) = 1.69$ implies that ω Centauri is relatively loosely bound. This relatively low value, combined with its small distance from us allows to observe individual stars over almost the entire extent of the cluster, including the central parts. All these information are summarized in Table 2.2.
I want to highlight the fact that all the reported information about the general properties of ω Centauri such as mass, kinematics, shape, structure, etc. are referred mainly to the most updated results. However, it is important to remember that systematic studies about this stellar system started early in the sixties (for some properties also before) and are still ongoing, resulting in hundreds and hundreds of publications that are impossible to cite.

Table 2.2. Structural values of ω Centauri.

Core radius r_c	4.30 pc	Baumgardt & Hilker (2018)
Half-light radius $r_{h,l}$	7.56 pc	Baumgardt & Hilker (2018)
Half-mass radius $r_{h,m}$	10.42 pc	Baumgardt & Hilker (2018)
Tidal radius r_t	208.60 pc	Baumgardt & Hilker (2018)
Concentration c	1.69	Baumgardt & Hilker (2018)

2.1.2 Photometry of ω Centauri

The first pioneering photometric study of ω Centauri was performed by Belserene (1959), who found that the RGB stars along the $(B-V), V$ CMD *"scatter widely instead of defining what might properly be called a branch"*. Later on, Woolley (1966) produced more than $\sim$ 6500 magnitudes and $\sim$ 4500 proper motions in the B and V bands for bright stars in ω Centauri in a distance from 3′ to 22′ from the cluster center. This study was followed by other studies by Dickens & Woolley (1967) and Dickens & Carey (1967) who found the same result of a large spread of the RGB stars along the CMD. However, in all these cases the associated uncertainties to the magnitudes were large (larger than 0.1 mag and for the fainter stars larger than 0.3 mag). Cannon & Stobie (1973) analyzed the UBV data for a total of 126 bright stars of ω Centauri (V$<$ 16.5), finding a large spread along the RGB stars. They concluded that the exceptionally large scatter observed can be only in part attributed to photometric errors, presence of field stars, and differential reddening. The authors concluded suggesting to perform several observational programmes, in order to confirm if the RGB scatter was intrinsic. As suggested by Cannon & Stobie (1973), in the following years a series of studies of ω Centauri were carried on by different authors. In particular, Freeman & Rodgers (1975) first suggested that the observed spread could be due to variations in the chemical abundances among the ω Centauri giant stars. This finding was demonstrated by later studies both spectroscopic and photometric that reached magnitudes fainter than the MS Turn-Off (TO) and mapped the whole extension of the system (e.g., Alcaino & Liller, 1987; Noble et al., 1991). Alcaino & Liller (1987) found a V magnitude at the MS TO V$=$ 18.3 $\pm$ 0.15 and also large scatter among the MS stars.

Lee et al. (1999) and Pancino et al. (2000) through a wide-field photometry discovered the presence of a new anomalous branch along the RGB, which appears to be well separated from the bulk of the RGB stars and characterized by redder color. Sollima et al. (2005a) from a high-resolution photometric analysis in the BVI filters confirmed the existence of multiple

branches along the RGB. Moreover, thanks to the high precision of the dataset, the authors were able to conclude that the RGB does not present a smooth and continuous distribution, but shows a discrete structure (see Fig. 2.5).

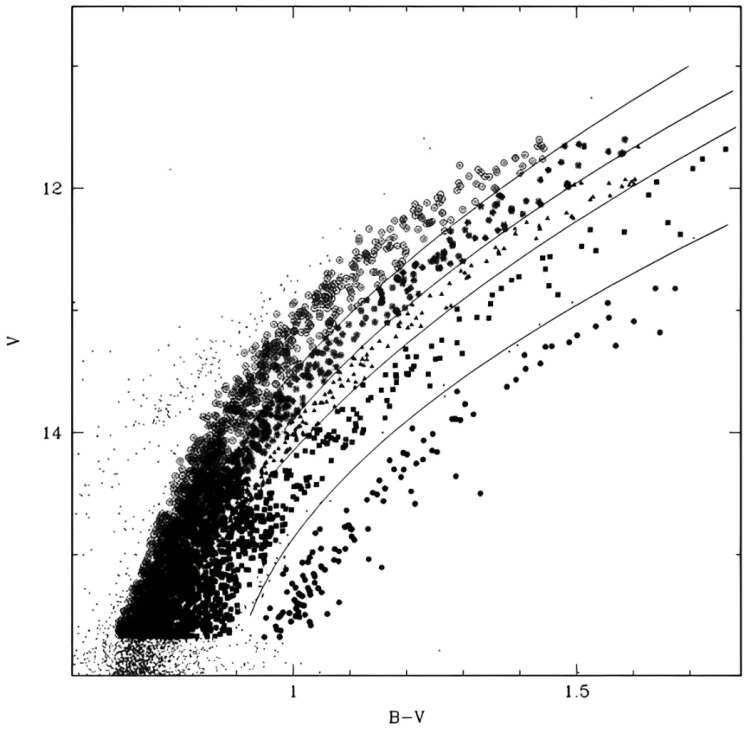

FIGURE 2.5: CMD of the RGB stars in ω Centauri. The stars are coded with different symbols according to their group. Figure from Sollima et al. (2005a).

In parallel to the wide-field photometry, the advent of the HST revolutionized the photometric studies for all the stellar systems. First studies with HST data in the V and I bands for ω Centauri were carried on by Elson et al. (1995) and Anderson (1997). These new studies were able to reach magnitudes as faint as I$\sim$ 26 allowing to obtain very precise luminosity functions, and mass functions down to M $\sim$ 0.2 $M_{\odot}$. Very recently, thanks to the HST catalog of the ω Centauri core Bellini et al. (2017b) presented a study to detail the MS into its different populations. To this purpose, the authors used the filters F275W, F336W, F438W, F606W, and F814W and developed a strategy to identify color systems where different populations stand out most distinctly. In this way, they were able to identify 15 different populations along the MS (see Fig. 2.6). These findings show that the stellar populations and star formation history of ω Centauri are even more complex than inferred previously.

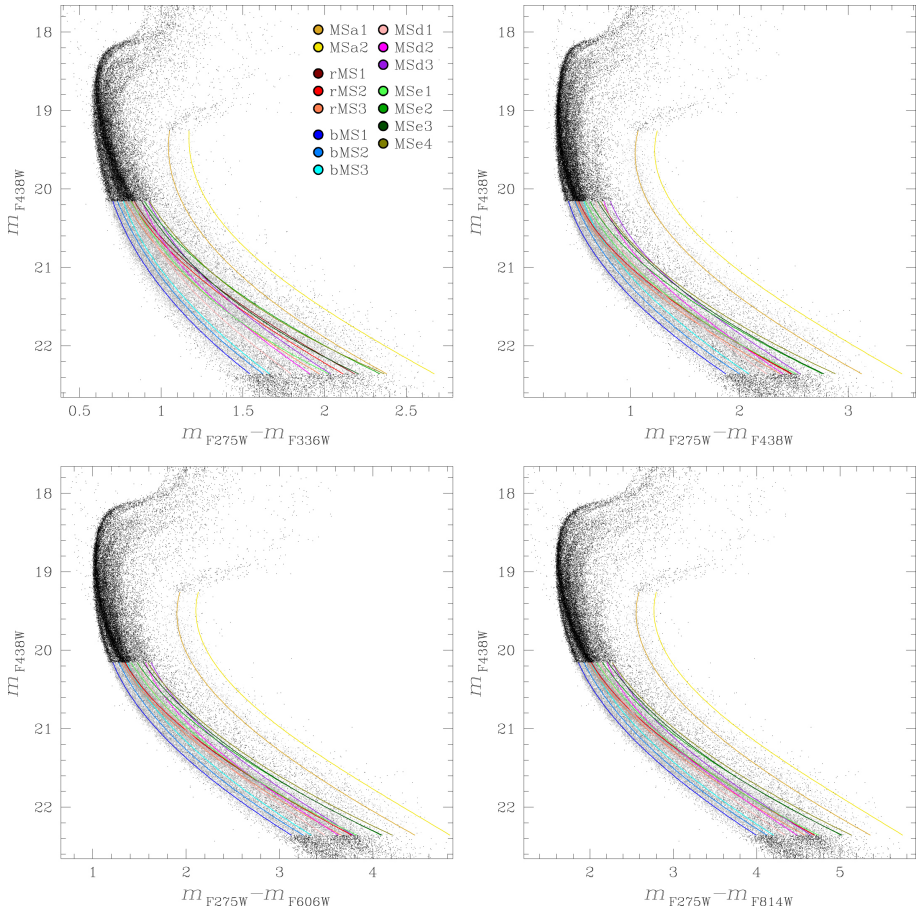

FIGURE 2.6: CMD of the MS stars in ω Centauri from different combination of HST colors and magnitudes. Fiducial lines for each of the 15 subpopulations are color-coded accordingly to the each subpopulation. Figure from Bellini et al. (2017b).

2.1.3 Metallicity and age distribution of ω Centauri

The most outstanding feature of ω Centauri is its wide metallicity spread, when compared to the other systems classified as GCs. Indeed, with some particular exceptions already discussed in previous Chapter, typical GCs have small or null Fe spreads. ω Centauri instead has a spread in Fe of almost 2 dex, a value comparable to that of dwarf galaxies (Willman & Strader, 2012).

The first spectroscopic study where a chemical inhomogeneity was found performed by Freeman & Rodgers (1975). From the analysis of the Ca II K line in 25 RR Lyrae stars these authors found values of [Ca/H] ranging from −1.6 up to −0.4 dex, with errors associated with the measurements of the order of 0.2 dex. Thus, such large spread could not be due to the measurement errors. Moreover, this spread cannot be associated to a strong differential reddening in ω Centauri. Newell et al. (1969) found that a maximum of 0.03 of differential

reddening in $E(B-V)$[1] is present in ω Centauri.
The first spectroscopic study where [Fe/H] was determined in ω Centauri stars was performed by Butler et al. (1978), who analyzed a large number of RR Lyrae stars, finding that [Fe/H] ranges from ~ -2.2 up to ~ -0.6 dex. The authors concluded that the observed spread is real and is very close to the range spread requested to explain the width of the RGB found by authors such as Cannon & Stobie (1973).
Since then, several different spectroscopic studies were performed in ω Centauri. Among them, here I cite Cohen (1981); Gratton (1982); Norris & Da Costa (1995a,b); Suntzeff & Kraft (1996); Smith et al. (2000); Pancino et al. (2002); Johnson & Pilachowski (2010); Marino et al. (2011c); Mészáros et al. (2021). All these studies point out to a mean metallicity of ω Centauri of ~ -1.5 dex, when the entire metallicity distribution is considered. However, when the entire distribution is analyzed in detail, at least four different groups emerge. In particular, according to the results by Johnson & Pilachowski (2010):

- There is a metal-poor subpopulation, with a peak at [Fe/H] ~ -1.75 dex, that constitutes the majority of the entire population.
- There is a first metal-intermediate subpopulation, with a peak at [Fe/H]~ -1.5 dex, that makes roughly 25% of the entire population.
- There is a second metal-intermediate subpopulation at higher metallicity, with a peak at [Fe/H]~ -1.1 dex, which makes the 10% of the population.
- Finally, there is a extended metal-rich tail that comprises only the 2% of the entire population and has a peak at [Fe/H]~ -0.75 dex.

These results are all summarized in Fig. 2.7, where the metallicity distribution of ω Centauri is displayed. The general results about the presence of at least four different subpopulations, a wide spread in metallicity covering almost 2 dex from ~ -2.2 up to ~ -0.5 emerge from all the spectroscopic studies performed in ω Centauri.
The presence of such wide metallicity range in the ω Centauri stars demands that in the past it was more massive than today, in order to retain SNe ejecta at very high velocity, allowing for multiple bursts of star formation, with each generation becoming progressively enriched in Fe (e.g., Lee et al., 1999).
Due to the wide spread in metallicities, which indicates a complex assembly history for ω Centauri numerous efforts were carried on to measure stellar ages and determine its star

[1] Nowadays is known that in the core of ω Centauri a maximum of $\sim$ 0.01 of differential reddening in $E(B-V)$ is present (Bellini et al., 2017a).

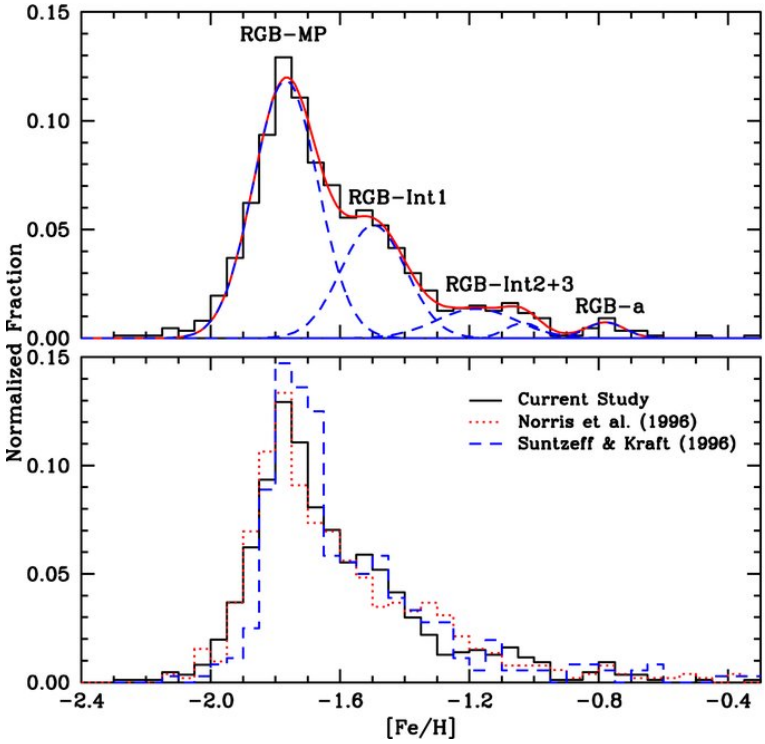

FIGURE 2.7: Top panel: metallicity distribution of the ω Centauri giant stars studied by Johnson & Pilachowski (2010). The dashed blue lines represent the Gaussian fits for the different subpopulations of ω Centauri, while the red line is the fit of the entire distribution.
Bottom panel: metallicity distributions by Johnson & Pilachowski (2010, solid black line), Norris et al. (1996, dotted red line), and Suntzeff & Kraft (1996, dashed blue line). Figure from Johnson & Pilachowski (2010).

formation history. For example, Lee et al. (1999) estimated that the most metal-rich population in ω Centauri is some 2 Gyr younger than its most metal-poor population. Similar results were found also by Villanova et al. (2014), who studied the SGB in ω Centauri. Taking advantage of the age sensitivity of the SGB, the authors found that exists an age spread of at least 2 Gyr between the most metal-rich and most metal-poor subpopulations.
On the other hand, different studies found a smaller age spread for the formation of the entire population of ω Centauri. Sollima et al. (2005b) from the analysis of SGB stars found a total age spread of ~ 0.5 Gyr between the most metal-rich and the most metal-poor subpopulations. These results impose severe constraints on the timescale of the enrichment process of ω Centauri, excluding the possibility of an extended star formation period. Same results were obtained by Tailo et al. (2016), who found a spread of 0.5 Gyr among the different populations in ω Centauri, assuming that the most metal-rich subpopulation is enhanced in He at the level of ~ 0.37 and is enhanced also in the C+N+O content with respect to the most metal-poor one. Lee et al. (2005) based on similar considerations on the He content of the different populations obtained an age spread of ~ 1.5 Gyr.

It is not a surprise that the literature provides disparate results on the intrinsic age spread. Indeed, populations in ω Centauri are uniquely complex, and large chemical variations are observed not just over metallicity but also in the other elements of stars at a given metallicity. All the peculiar physical properties possessed by ω Centauri, such as a very flattened shape for a GC, the multimodal metallicity distribution, stellar populations with different spatial distributions (Ferraro et al., 2002), a possibly age spread among different populations (see discussion above), and a retrograde orbit with respect to the Galactic rotation (Dinescu et al., 1999) suggest that there are remarkable differences in star formation histories, chemical enrichment processes and structure formation between ω Centauri and other Galactic GCs. The most common interpretation is that ω Centauri is the remnant of an old nucleated dwarf galaxy that the Milky Way accreted in the past (Bekki & Freeman, 2003; Bekki & Tsujimoto, 2019). In their model Bekki & Freeman (2003) demonstrated that the stellar envelope of the nucleated dwarf can be nearly completely stripped by the strong tidal field of the first generation of the Galactic thin disc, whereas the central nucleus can remain intact owing to its compactness. In this scenario, a large amount of metal-rich gas can be deposited into the nucleus of a gas-rich nucleated dwarf and within the nucleus can therefore occur multiple episodes of star formation with increasing metallicity. Moreover, the recent discovery of a stellar stream kinematically associated with ω Centauri (Ibata et al., 2019b), favors this proposed scenario. In the model proposed by Bekki & Tsujimoto (2019), ω Centauri forms within $\sim$ 300 Myr, a timescale that is much shorter than the age spread found by some authors such as Lee et al. (1999) or Villanova et al. (2014).

2.1.4 Multiple populations in ω Centauri

Although the observational scenario appears far more complex than for *genuine* GCs, ω Centauri also displays the key chemical signatures of (anti)correlations typical of presence of MPs. These chemical variations were detected among all the evolutionary phases of ω Centauri, from the MS up to the AGB phase. Moreover, once that the entire population is divided into different subpopulations according to their metallicity emerges that each subpopulation displays its own patterns of anticorrelations (e.g., Marino et al., 2011c; Mészáros et al., 2021). ω Centauri displays a clear Li-Na and Li-Al anticorrelations (see Fig. 2.8), as found by Mucciarelli et al. (2018a). The A(Li) distribution in ω Centauri is more complex than what is observed in other GCs, reflecting the peculiar chemical evolution of this system. *Genuine* GCs are dominated by FG and SG Li-normal stars, with the presence of a minor component of stars enriched in Na and depleted in Li. In the case of ω Centauri the fraction of SG stars

depleted in Li is $\sim$ 30%, that is unusually high with respect to the other GCs, where this fraction is less than $\sim$ 5%.

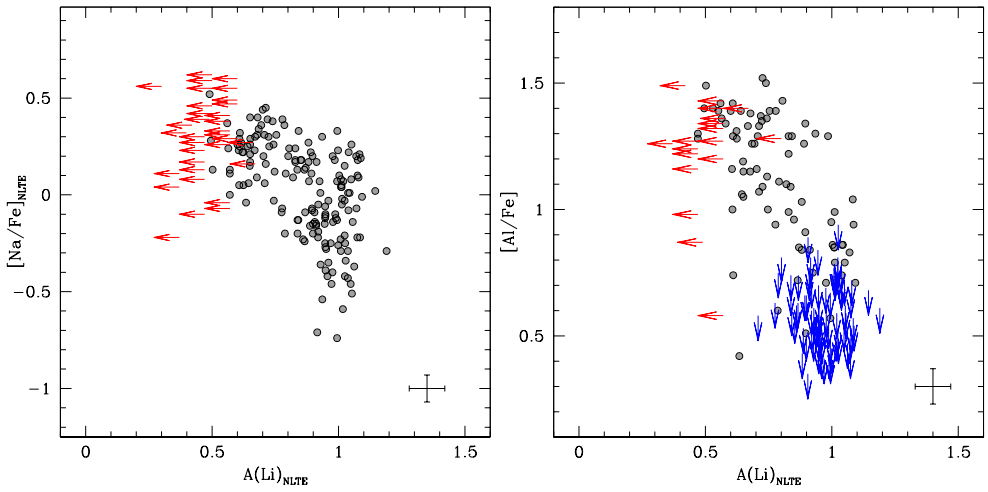

FIGURE 2.8: Left panel: Li-Na anticorrelation in ω Centauri. The red arrows represent upper limits for the abundances A(Li).
Right panel: Li-Al anticorrelation in ω Centauri The red arrows represent upper limits for the abundances A(Li), while blue upper limits for [Al/Fe]. Figure from Mucciarelli et al. (2018a).

ω Centauri displays also the most classical Na-O anticorrelation. The first clear detection of this chemical feature was obtained by Norris & Da Costa (1995a) from the analysis of high-resolution spectra for a total of 40 RGB stars. Same results were obtained also by Smith et al. (2000) from a smaller sample, but again located along the RGB. More recently, the high-resolution spectral analysis of a sample of 855 giants by Johnson & Pilachowski (2010) and 300 giants by Marino et al. (2011c) revealed with more clarity a very interesting peculiarity about the Na-O anticorrelation in ω Centauri. indeed, the Na-O anticorrelation exhibits variations in shape and extension as a function of metallicity. In particular, the Na-O anticorrelation becomes more extended as the metallicity increases, and disappears for the most metal-rich subpopulation ([Fe/H] $\gtrsim -1.3$ dex). In Fig. 2.9 is summarized the behavior of the Na-O anticorrelation over the entire metallicity range of ω Centauri as found by Marino et al. (2011c). The presence of such peculiar Na-O anticorrelation is relevant for an understanding of the formation of the different stellar populations in ω Centauri. In light of this chemical pattern, D'Antona et al. (2011) discussed the formation of MPs in ω Centauri using the AGB stars as a reference model.
ω Centauri displays also the anticorrelations related to the MgAl burning chain. Indeed, presence of enhancement in Al in ω Centauri was firstly reported by Cohen (1981). Later on, Norris & Da Costa (1995b) found a clear enhancement in Al, that was correlated with the

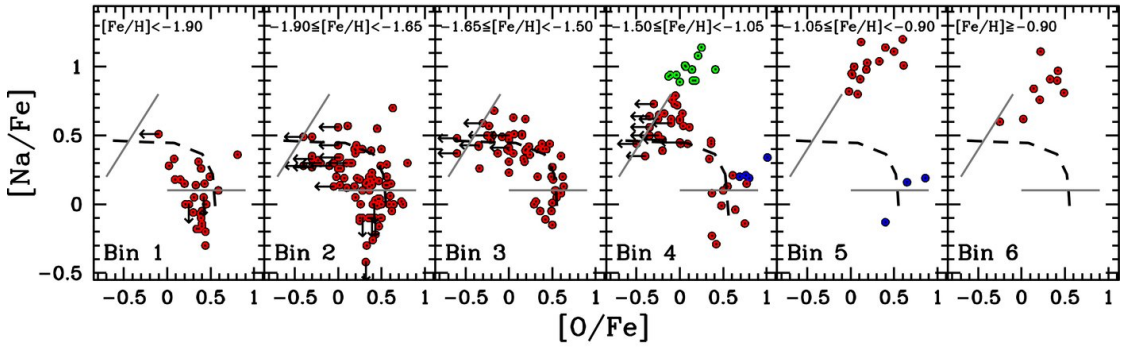

FIGURE 2.9: Na-O anticorrelation in ω Centauri for each metallicity group identified by Marino et al. (2011c). Figure from Marino et al. (2011c).

abundances of O and Na. Indeed, they found evident Na-Al correlation and O-Al anticorrelation. The first Mg-Al anticorrelation in ω Centauri was reported by Smith et al. (2000) from the analysis of 10 RGB stars. Within the survey of the southern GCs, Mészáros et al. (2020) presented the largest study to the date on the abundances of the elements linked to the MgAl chain. The authors analyzed a sample of $\sim$ 900 stars in ω Centauri and found clear evidence of Mg-Al anticorrelation. Following these results, Mészáros et al. (2021) performed a dedicated analysis of ω Centauri based on $\sim$ 1000 high-resolution, high signal-to-noise spectra collected within the APOGEE survey (Majewski et al., 2017), finding all the (anticorrelations) linked to the MgAl chain (see Fig. 2.10). The authors found that ω Centauri exhibits the most complex Mg-Al anticorrelation among all the GCs, with the shape and extension of the anticorrelation that varies with the metallicity. Moreover, it was found that the stars with the lowest content of Mg in ω Centauri have lower Al content than what is expected from the traditional shape of the Mg-Al anticorrelation, while they are also the most enriched in Si within the cluster. Therefore, a turnover in the Mg-Al plane is present and a Mg-Si anticorrelation naturally arises in ω Centauri. Masseron et al. (2019) explained the shape of Mg-Al anticorrelation by suggesting that Al was partially depleted in the polluter stars by very hot proton capture reactions occurring at temperatures higher than 8×10^7 K. In this regime part of the synthesized Al goes into Si through the ^{26}Al(p,γ)^{27}Si(e$^-$,ν)^{27}Al(p,γ)^{28}Si. Without this leakage, a simple correlation between Mg and Si should be present since they are both α-elements. Also a Al-Si correlation is evident among the ω Centauri stars.

The presence of correlations arising from the MgAl chain in ω Centauri, from a theoretical point of view for MPs favors the models able to activate this chain such as the AGB and SAGB scenario. Obviously, due to the peculiar nature of ω Centauri, multiple mechanisms could be responsible for the MPs in this system.

Mészáros et al. (2020, 2021) claimed also for a hint of Mg-K anticorrelation in ω Centauri,

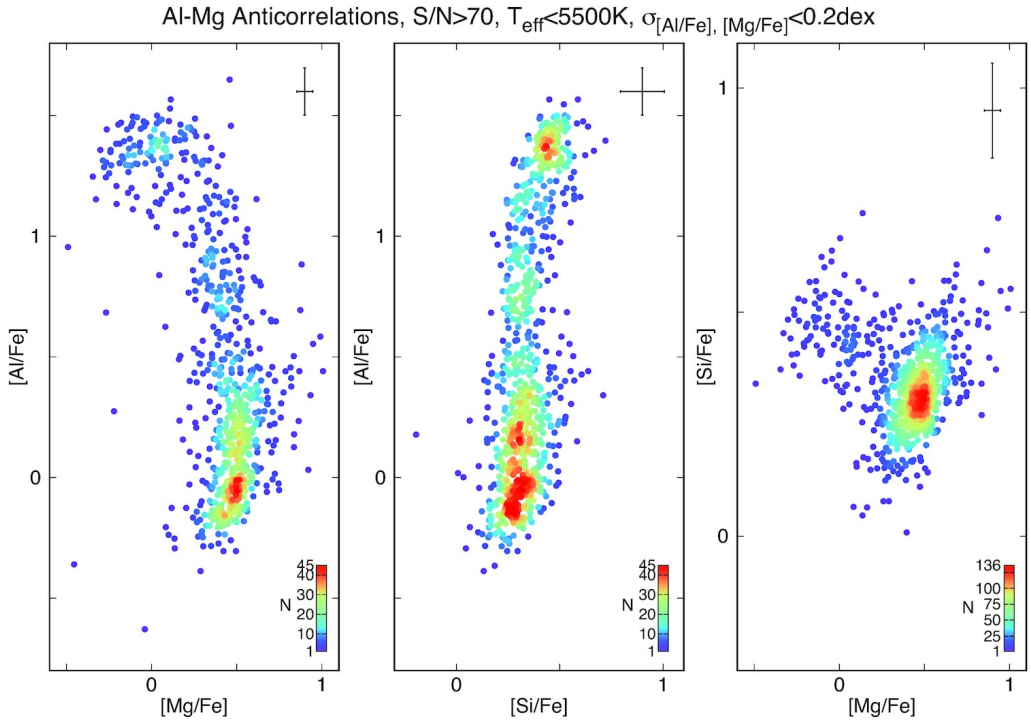

FIGURE 2.10: Mg-Al (left panel), Si-Al (central panel), and Mg-Si (right panel) (anti)correlations from the APOGEE survey for ω Centauri. Figure from Mészáros et al. (2021).

even though the stars with measured abundances are few and the K lines in the IR band used by these authors are weak and blended with other lines. Considering these issues, the conclusion was that the discovery of a K enhancement of the Mg-poor stars in ω Centauri cannot be convincingly claimed from the analysis by Mészáros et al. (2020, 2021).

Therefore, further studies are needed in order to confirm the presence of chemical anomalies involving also the K in ω Centauri. Indeed, the presence of a Mg-K anticorrelation is interpreted as the result of the extreme H burning through the MgAl chain (Ventura et al., 2012). For this reason, an accurate determination of K abundances and a confirmation of its link with the other light elements in terms of chemical correlations would support the notion of an extreme self-enrichment process in ω Centauri, where all the CNO secondary chains were very efficient. This finding would shed light on the nature of polluter stars responsible for the formation of MPs in this very intricate stellar system, where several mechanisms were active simultaneously during its early evolution.

2.2 Liller 1: fragment of the Bulge formation?

2.2.1 A new class of stellar systems

Most of the stellar mass in the Universe is contained within spheroids (Fukugita et al., 1998). Among these structures, the Galactic Bulge, the central region of the Milky Way, is the only spheroid where individual stars can be resolved and extensively studied. Understanding the origin and evolution of this stellar structure is a key point for modern astrophysics.
The Bulge constitutes $\sim$ 20% of the total mass of the Galaxy (Zoccali & Valenti, 2016), but due to the large and spatially variable extinction obscuring this region (Gonzalez et al., 2012) its study resulted to be very challenging, specially in the optical band. However, thanks to the recent introduction of NIR facilities, the exploration of the Bulge was facilitated, and now the advent of large spectroscopic and photometric studies are providing a comprehensive view of the stellar populations constituting the Bulge with exceptional precision. These results, enabled the investigation of the link among the stellar properties such as chemistry, kinematics, spatial distribution, etc., in order to refine (and exclude) models related to the Bulge formation. This would help, in a more general context, to understand the formation of galaxies in the Universe.
The general picture of bulges formation in galaxies is still highly debated in the literature. Among all the proposed models, three main scenarios emerge: **(1)** dissipative collapse (Ballero et al., 2007; McWilliam et al., 2008), with possibly an additional component formed with a time delay of a few Gyr (Grieco et al., 2012; Tsujimoto & Bekki, 2012), **(2)** dynamical secular evolution of massive and unstable disks (Combes & Sanders, 1981; Raha et al., 1991; Saha & Gerhard, 2013), **(3)** and merging of substructures either of primordial galaxies embedded in a dark matter halo (Scannapieco & Tissera, 2003; Hopkins et al., 2010), or massive clumps generated by early disk fragmentation (Immeli et al., 2004; Carollo et al., 2007; Elmegreen et al., 2008).
In this context, the detection of the so-called *"clumpy or chain galaxies"* (see Fig. 2.11) observed at high-redshift (Carollo et al., 2007; Elmegreen et al., 2009; Guo et al., 2015; Shibuya et al., 2016) suggests that the coalescence of primordial substructures is a promising channel that could have played a relevant role in the assembly process of galactic bulges. Indeed, numerical simulations (e.g., Immeli et al., 2004; Elmegreen et al., 2008; Bournaud & Elmegreen, 2009; Bournaud, 2016) demonstrated that primordial massive clumps with masses of 10^{8-9} $M_{\odot}$ can form from violent disk instabilities and eventually migrate to the center and dissipatively coalesce generating the bulge, within a $\sim$ 1 Gyr for a Milky Way-like galaxy. Simulations also predict not only that the massive clumps are able to migrate to the center, but that some

of them are also able to survive the total disruption and generate stellar clusters (Bournaud, 2016; Dekel et al., 2023), that are the *fossil fragments* of the Bulge formation. These relics should be located within the Bulge with the actual appearance of massive GCs. However, due to their peculiar origin they should manifest well-defined features:

- At odds with *genuine* GCs, these systems were able to retain the iron-enriched ejecta of the SNe explosions, and they likely experienced more than one burst of star formation. Therefore, these peculiar GCs should host multi-iron and multi-age subpopulations.
- Considering that these giant clumps would have formed stars rapidly and with very high star formation rate (similarly to the Bulge), a fraction of the stellar population of the fossil fragments should be composed of old stars characterized by the same chemistry (in terms of both α-elements and iron) as that observed in the Galactic Bulge.

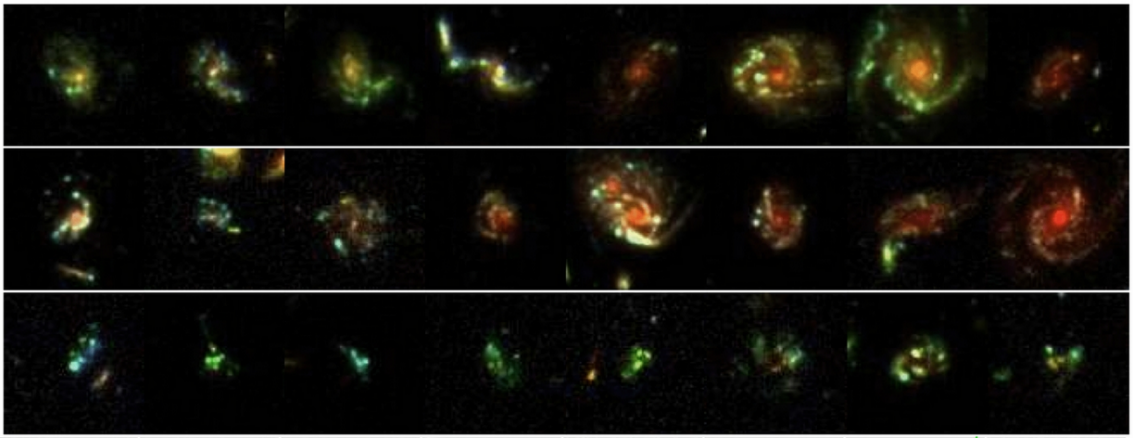

FIGURE 2.11: Example of *clumpy* galaxies as identified by Guo et al. (2015) in the redshift range $0.5 \leqslant z \leqslant 3$ from the HST survey CANDELS/GOODS. Figure from Guo et al. (2015).

Therefore, finding stellar systems with these specific properties would provide a strong observational support to the merging scenario for Bulge formation. Until few years ago, no evidence of the presence of such kind of systems was available. However, everything changed when Ferraro et al. (2009) found that Terzan 5, a stellar systems classified as GC, has exactly the described characteristics of the *fossil fragments*. Terzan 5 is a massive stellar system (M$= 2 \times 10^6$ M$_\odot$, Lanzoni et al., 2010), dynamically classified as an in-situ system belonging to the Bulge (Massari et al., 2019; Baumgardt et al., 2019; Callingham et al., 2022). It is located in the inner region of the Bulge at distance of 6.62 ± 0.15 kpc from the Sun and at 1.65 ± 0.13 kpc from the Galactic center (Baumgardt & Vasiliev, 2021). The high extinction in its direction, $E(B-V) = 2.38$ (Valenti et al., 2007), hampered for a long time the proper study of its stellar content. However, Ferraro et al. (2009) performed the first high-resolution

and NIR photometric observations of Terzan 5, coupled with high-resolution optical images acquired with HST. This allowed to discovery multi-age and multi-iron stellar populations coexisting within this stellar system. The authors detected two well-defined red HB clumps along the CMD of Terzan 5: a bright HB (BHB) and a faint HB (FHB). Moreover, they analyzed three stars in each clump finding a difference in the Fe content of $\sim$ 0.5 dex, with the FHB having [Fe/H] $= -0.20$ dex, and the BHB stars having [Fe/H] $= +0.30$ dex. In the CMD the observed clumps can be reproduced by two populations characterized by the observed metallicities and two different ages: $t = 12$ Gyr for the FHB and a significantly younger age of $t \sim 5$ Gyr for the BHB. The same separation is present also in the MS-TO as found by Ferraro et al. (2016). This latter study allowed to refine the ages of the two populations: 12 ± 1 Gyr for the old and metal-poor one, 4.5 ± 0.5 Gyr for the young and metal-rich one. Moreover, the authors found that the metal-rich subpopulation of Terzan 5 is more radially concentrated compared to the metal-poor ones.
Later spectroscopic studies of stars selected along the different red clumps and based on high-resolution spectra confirmed the presence of multi-iron populations in Terzan 5 (Origlia et al., 2011, 2013, 2019; Massari et al., 2014). In particular, Origlia et al. (2013) detected the presence of a third component, characterized by [Fe/H] ~ -0.8 dex, and α-enhanced. The result was confirmed by Massari et al. (2014), based on a larger spectroscopic dataset. These findings are summarized in Fig. 2.12. According to Ferraro et al. (2016), the emerging scenario is the following:

- There is a dominant old population ($t = 12$ Gyr) formed on a short timescale, from gas rapidly enriched by core collapse SNe with subsolar metallicity ([Fe/H] $= -0.3$ dex) and enhanced [α/Fe] abundance ratio.
- There is a younger population ($t = 4.5$ Gyr) formed from gas characterized by supersolar metallicity ([Fe/H]$= +0.3$ dex) and solar-scaled [α/Fe] abundance ratio.
- There is a smaller and much more metal-poor component, with [Fe/H] ~ -0.8 dex and enhanced in [α/Fe] at the same level of the dominant population.

The [α/Fe] vs [Fe/H] pattern of Terzan 5 is surprisingly akin to that of Bulge stars and totally incompatible with what is observed in the Milky Way outer disk and halo or in local dwarf galaxies. Indeed, the observed specific chemical pattern is distinctive of massive and dense environments that experienced star formation at very high rates, like the Galactic Bulge.
Recently, Romano et al. (2023) in their model for the chemical enrichment of Terzan 5 showed that is possible to reproduce the mass, metallicity distribution function, and chemical abundance patterns measured by assuming a chemical evolution model driven by self-enrichment.

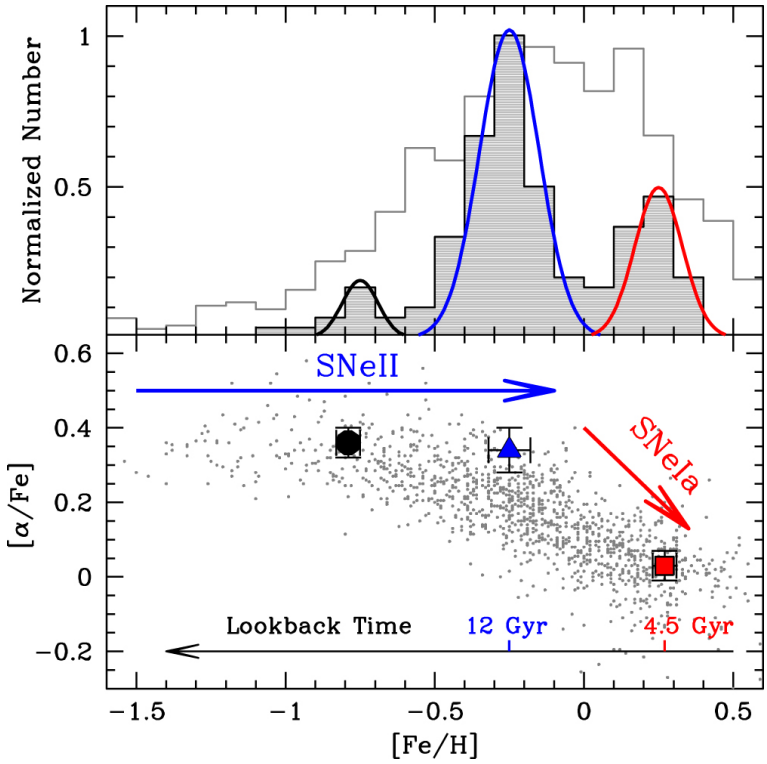

FIGURE 2.12: Top panel: Fe distribution of the three subpopulations of Terzan 5 (gray filled histogram and colored black, blue, and red lines, Massari et al., 2014) compared to that of the Galactic Bulge field stars from the literature (gray empty histogram, Ness et al., 2013, Johnson et al., 2014).
Bottom panel: [α/Fe] vs [Fe/H] distribution of the three subpopulations of Terzan 5 (extreme metal-poor: black circle; subsolar: blue triangle; supersolar: red square) compared to that of the Bulge field stars from the literature (gray dots). The formation epoch of the two major Terzan 5 subpopulations is also highlighted. Figure from Ferraro et al. (2016).

In order to reproduce the observed properties, the progenitor gas clump should have been more massive than the present-day Terzan 5, with a mass of $\sim 10^7$ $M_\odot$. The idea is that Terzan 5 is the relic of a gaseous clump that originated from the fragmentation of an early disk.

All the characteristics of Terzan 5 point out to the conclusion that this systems is the surviving fragment of the early formation of the Bulge. These fragments are called *Bulge Fossil Fragments* (BFF).

2.2.2 Liller 1: a new candidate

A paramount condition to prove the validity of the BFF scenario, suggested by the peculiar properties observed in Terzan 5, is the detection other similar complex stellar systems hidden in the Galactic Bulge with the appearance of massive GCs. This seems to be the case for

Liller 1, another Bulge stellar system (Callingham et al., 2022), apparently a GC, but that is largely unexplored.

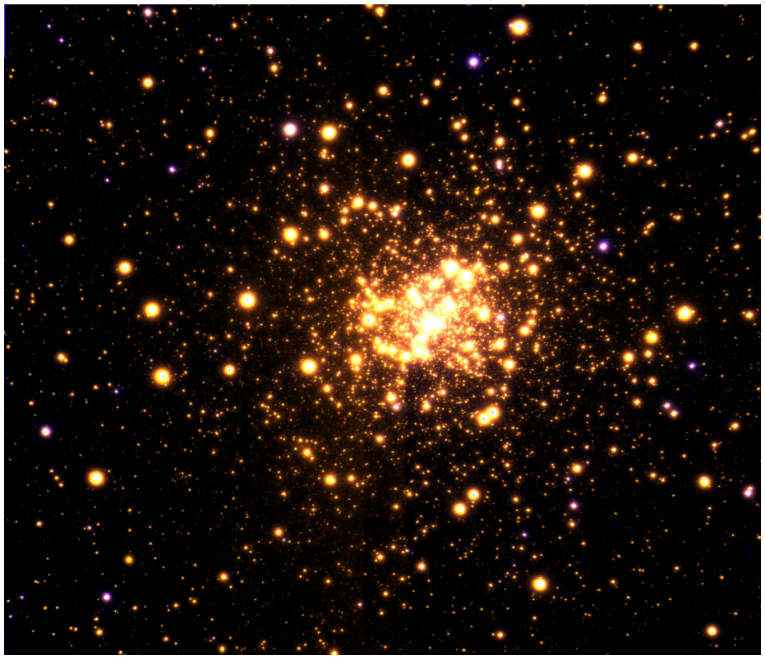

FIGURE 2.13: False-color image of Liller 1 obtained by combining GEMINI observations in the NIR bands. Figure from Saracino et al. (2015).

Liller 1 (see Fig. 2.13), a stellar system located in the inner region of the Milky Way was discovered quite recently (Liller, 1977). This system is located at a distance of 8.06 ± 0.34 kpc from the Sun (Baumgardt & Hilker, 2018). This value agrees very well with the previous value reported by other authors that placed Liller 1 at a distance between 7.9 and 8.1 kpc from the Sun (Harris, 1996; Ortolani et al., 2007; Valenti et al., 2010; Saracino et al., 2015). Liller 1 is located at 0.74 ± 0.07 from the Galactic center (Baumgardt & Vasiliev, 2021), in a region strongly affected by foreground extinction. Indeed, this system has a very large color excess, $E(B-V)$ larger than 3, that produces an extinction of $\sim$ 10 magnitudes in the optical band toward the cluster. Thus, for a long time the observations of Liller 1 were hampered, specially in the optical bands. Before proceeding further, I want to spend some words about the correct value for $E(B-V)$. The correct determination of this value is very important in order to obtain a precise CMD where the existence of different populations can be recognized. The early studies performed by different authors estimated a value $E(B-V)$ in the range from about 3.00 to 3.13 (Frogel et al., 1995; Ortolani et al., 1996; Barbuy et al., 1998; Ortolani et al., 2001; Valenti et al., 2010). Moreover, Ortolani et al. (2001) found evidence of significant differential reddening. More recently, Saracino et al. (2015) from the analysis of high-resolution IR images derived a value of $E(B-V) = 3.30 \pm 0.20$. However,

Table 2.3. Main properties of Liller 1.

RA J2000	263.°35233	Saracino et al. (2015)
Dec J2000	−33.°38956	Saracino et al. (2015)
$\mu_\alpha \cos\delta$	-5.403 mas yr^{-1}	Vasiliev & Baumgardt (2021)
μ_δ	-7.431 mas yr^{-1}	Vasiliev & Baumgardt (2021)
Galactic latitude	354.°840	Harris (1996)
Galactic longitude	−0.°161	Harris (1996)
Distance from Sun	8.06±0.34 kpc	Baumgardt & Vasiliev (2021)
Distance from Galactic center	0.74±0.16 kpc	Baumgardt & Vasiliev (2021)
Mass M	$\sim 1-2\times10^6$ M$_\odot$	Saracino et al. (2015)
Core radius r_c	0.21 pc	Saracino et al. (2015)
Half-mass radius $r_{h,m}$	1.20 pc	Saracino et al. (2015)
Tidal radius r_t	11.74 pc	Saracino et al. (2015)
Concentration c	1.74	Saracino et al. (2015)

this value turned out to be still incorrect. The most updated value of $E(B-V)$ to now was obtained by Pallanca et al. (2021) that by using optical and IR images obtained with HST and GEMINI South Telescope were able to build a high-resolution extinction map in the direction of Liller 1. The authors found a mean value $E(B-V) = 4.52 \pm 0.10$ and a differential reddening $\delta E(B-V)$ covering ~ 0.9 mag.

Liller 1 is a very massive system, with a total mass M $= 2.3\times10^6$ M$_\odot$ estimated by Saracino et al. (2015) by using a Salpeter IMF, while by using a Kroupa IMF the mass turn to be of 1.5×10^6 M$_\odot$. These values are good in agreement with the mass found by Baumgardt & Hilker (2018), who estimated a mass of $(1.01\pm0.16)\times10^6$ M$_\odot$ for Liller 1. This value places Liller 1 among most massive GCs in the Galaxy, together with systems such as ω Centauri and Terzan 5.

Liller 1 is a quite compact system, with a $r_c = 0.21$ pc, a $r_{h,m} = 1.20$ pc, and a $r_t = 11.74$ pc (Saracino et al., 2015). The resulting concentration is $c = 1.74$. All these values are different from the previous values reported in literature (Harris, 1996), resulting in the fact that Liller 1 is less concentrated and extended than previously thought, and with a larger core radius. All the describe properties of Liller 1 are reported in Table 2.3.

2.2.3 Photometry of Liller 1

The first photometric studies on the population of Liller 1 were carried out by Frogel et al. (1995) and Ortolani et al. (1996), who produced the first CMDs in the IR and optical bands by using images obtained at the duPont telescope and the ESO New Technology Telescope (ESO-NTT), respectively. However, due to the high extinction of this system, they were able to sample only the brightest part of the RGB. Deeper studies were performed by Davidge (2000) and Ortolani et al. (2001) by using the Canadian-France-Hawaii Telescope and HST, respectively. In particular, Davidge (2000) were able to reach $K \sim 18$. However, these studies were not deep enough to characterize the MS-TO of Liller 1. A more recent photometric study was performed by Valenti et al. (2010), who studied the brightest part of the RGB reaching the red clump of Liller 1 ($K_S \sim 14$), by using NIR SOFI imager mounted at the ESO New Technology Telescope. The first study of the Liller 1 population down to the MS-TO was obtained very recently by Saracino et al. (2015), based on NIR GEMINI observations. The dataset was used to determine the physical properties described above. However, the data did not allow to determine the age of the system, or to detect the presence of different populations.
The very first deep observations of Liller 1 were carried out by Ferraro et al. (2021), who combined observations in the V and I band made with HST, with NIR images in the J and K bands obtained with GEMINI. These data allowed to study in detail the populations of Liller 1. The $(I - K), I$ CMD, showed in Fig. 2.14 and properly corrected for the differential reddening by using the extinction map obtained by Pallanca et al. (2021), revealed the presence of some intriguing features:

- There is a dominant population typical of an old stellar system, consisting of cool and bright stars in the red part of the CMD, at $(I - K) \sim 6.5$, connecting to a populous MS extending to $I \sim 26$.
- There is a bluer component, denoted as Blue Plume (BP), located at $(I - K) \sim 5.8$, appearing as an extension of the old MS.

While the dominant component shows the properties typical of and old and metal-rich population (called Old Population, OP), with a well populated RGB extending for more than 6 magnitudes and a well-defined red clump, the surprising result is the presence of a populous BP, extending over a range of ~ 4 magnitudes. Such BP is not expected to be present in an old GC. Ferraro et al. (2021) performed different test to assess if this population belong to Liller 1. They determined the density profiles and performed a proper motion analysis of the Liller 1 stars finding that the BP persists indicating that this population really belongs to

Liller 1. Moreover, the BP is more radially concentrated with respect to the OP. The authors considered also the possibility that the BP could be composed by Blue Straggler Stars (BSSs), because the BP lies on the CMD region usually occupied by BSSs. However, this possibility was excluded by the fact that the BSSs is a sparse and small population, while the BP is as numerous as the OP in the same magnitude range. Ferraro et al. (2021) therefore, concluded that the morphology of the BP is more suggestive of a coherent and recent episode of star formation. From the isochrone fitting of the two populations it was derived that:

- The MS-TO and SGB of the OP are well fitted by an isochrone of $t = 12.0 \pm 1.5$ Gyr and a global metallicity [M/H] $= -0.3$ dex, thus confirming the presence of a very old stellar population in Liller 1.
- The BP is better reproduced by younger and metal-rich isochrones from 1 to 3 Gyr and [M/H] $= +0.3$ dex (right panel of Fig. 2.14) with respect to a younger but metal-poor (at the level of the OP) isochrones (left panel of Fig. 2.14), even though a proper determination of the metallicity of the stars in the BP is missing.

The conclusion claimed by Ferraro et al. (2021) is that Liller 1 is a complex stellar system hosting multi-age (and possibly multi-iron) subpopulations. This result collocates Liller 1 in the group of the non-*genuine* GCs, as happened for Terzan 5. The similar age and metallicity of the old populations of Terzan 5 and Liller 1 strongly suggests that formed in the early epoch of Galaxy formation from gas cloud with very similar chemistry. The high metallicity of the old populations suggests that Terzan 5 and Liller 1 formed from metal-rich gas, a characteristic expected in in the environment where the proto-bulge formed. On the other hand, the properties of the younger populations, which appear to be likely more metal-rich and centrally concentrated than the old populations, point out to the idea that these systems were massive enough in the past to retain the SNe ejecta and experienced new bursts of star formation in later epochs. These massive primordial systems could have contributed to form the Bulge $\sim$ 12 Gyr ago and survived disguised as GCs until now. Thus, Liller 1 seems to be the second BFF found after Terzan 5.
Moreover, the high-quality CMD obtained by Ferraro et al. (2021) was also used as reference to model the Liller 1 star formation history (SFH; Dalessandro et al., 2022). The best-fit solution reveals that star formation was active in Liller 1 for nearly its entire existence, with three distinct episodes. The main episode started approximately 12-13 Gyr ago, with a tail extending for about 3 Gyr, and it created $\sim$ 70% of the current total mass of the system. The second episode occurred between 6 and 9 Gyr ago, contributing an additional $\sim$ 15% of the system mass. The most recent star formation event started around 3 Gyr ago and ceased

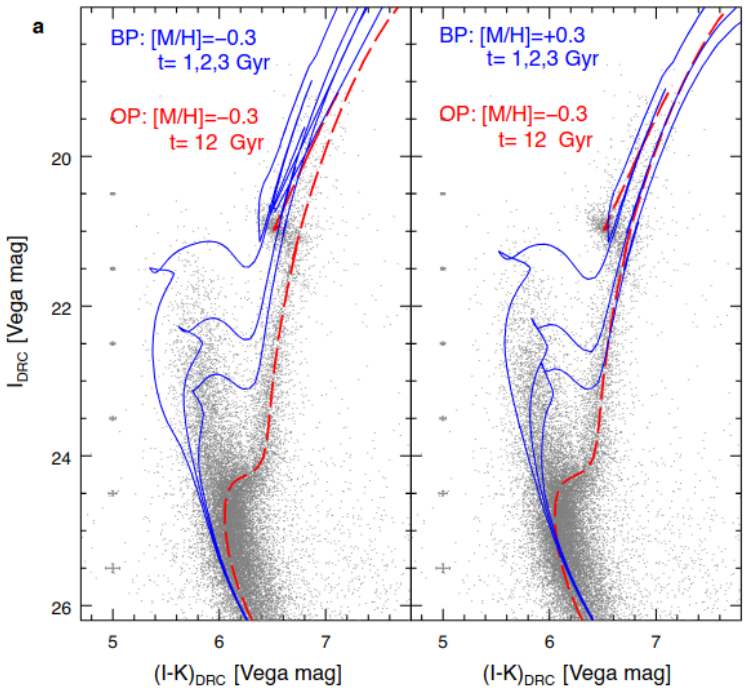

FIGURE 2.14: $(I-K), I$ CMD of Liller 1. Left panel: three isochrones of 1, 2, and 3 Gyr and with [M/H] $= -0.3$ dex are over-plotted to the young population (the blue lines), together with the best fit of the old population with an age of 12 Gyr and [M/H] $= -0.3$ dex (the red line).
Right panel three isochrones of 1, 2, and 3 Gyr but with [M/H] $= +0.3$ dex are over-plotted to the young population (the blue lines), together with the best fit of the old population (the red line). Figure from Ferraro et al. (2021).

roughly 1 Gyr ago, when a quiescent phase began. This young subpopulation constitutes $\sim 10\%$ at least of the total mass of Liller 1.

2.2.4 Spectroscopy of Liller 1

To the date, a complete chemical characterization of Liller 1 is missing. This would definitely confirm the BFF nature of Liller 1.

The chemical composition of Liller 1 is poorly known and based in a handful of stars. The first estimation of the metallicity of Liller 1 was made by Armandroff & Zinn (1988) based on the integrated-light spectroscopy at the Ca II infrared triplet. They found a corresponding [Fe/H] $= +0.20 \pm 0.30$ dex. Later on, Frogel et al. (1995) based on the slope of the RGB stars along the NIR CMD found a photometric estimation [Fe/H] $= +0.25 \pm 0.30$ dex. Origlia et al. (2002), from the analysis of high-resolution NIR spectra for two giant stars found [Fe/H] $= -0.30 \pm 0.20$ dex and [α/Fe] $= +0.30 \pm 0.20$ dex. Such values are fully compatible with the composition of the Bulge field stars and with the OP found by Ferraro et al. (2021). Stephens & Frogel (2004), from the analysis of features such Ca triplet, Na

doublet, and CO band-head in eight stars estimated an iron abundance for Liller 1 [Fe/H] $= -0.36$ dex. Recently, Horta et al. (2020) from the analysis of four likely member stars in the APOGEE catalog estimated a [Fe/H] $= -0.03$ dex and [α/Fe] $= +0.01$ dex.

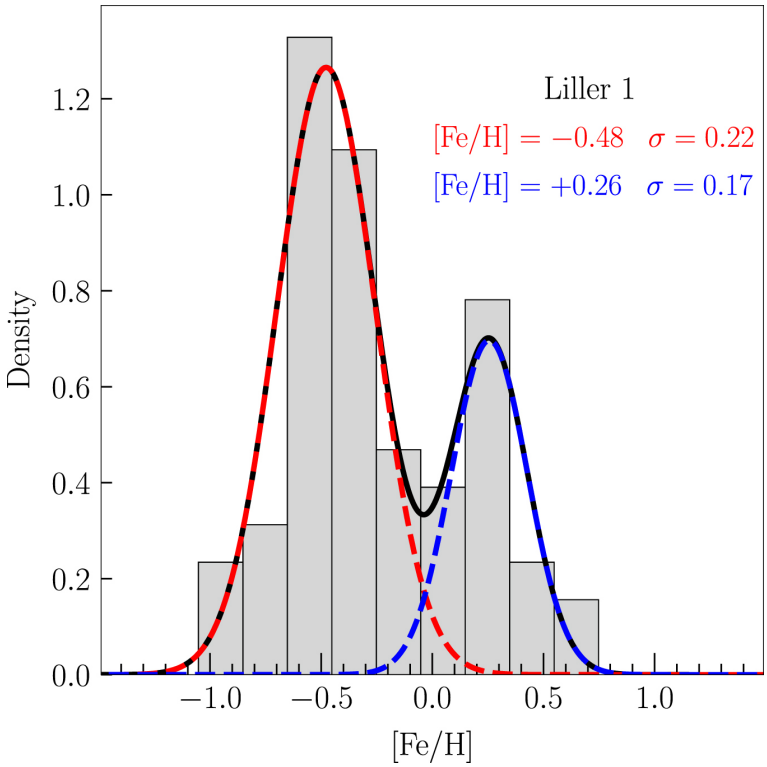

FIGURE 2.15: Metallicity distribution of Liller 1 likely members (gray histogram). The solid black line shows the best fit of the observed distribution, which is a combination of two Gaussian kernels (red and blue lines) centered at different values of [Fe/H]. The mean [Fe/H] values and the standard deviations of the two individual Gaussian components are also labeled in the panel. Figure from Crociati et al. (2023).

From all these results is clear that Liller 1 is a metal-rich stellar system. However, the spectroscopic analysis of this system is based on less than 20 stars and no systematic analysis on the two components are available. Very recently Crociati et al. (2023) analyzed the MUSE low-resolution spectra (with a resolution R $\sim$ 4000) of 64 Liller 1 member stars. This represents the largest dataset to the date for which spectroscopic analysis were performed. The authors found a multimodal Fe distribution, with the presence of two peaks of metallicity at [Fe/H] $= -0.48 \pm 0.22$ dex and [Fe/H] $= +0.26 \pm 0.17$ dex. The overall distribution can be observed in Fig. 2.15. Moreover, the metal-rich subpopulation appears to be more radially concentrated than the metal-poor one. This finding is in perfect agreement with that suggested by the photometric analysis presented in Ferraro et al. (2021) and Dalessandro et al. (2022), and is strikingly similar to that found in another Bulge stellar system, Terzan 5 (Ferraro et al., 2009).

The results by Crociati et al. (2023) provided the first spectroscopic evidence of the presence of a metal-rich component in Liller 1, adding further support to the idea that this system is the surviving relic of a massive primordial structure, a BFF as suggested also for Terzan 5, that contributed to the formation of the Galactic Bulge in early epochs and was able to survive the destruction, retain the SNe ejecta, and activate a new burst of star formation more recently. Nevertheless, currently there are no measurements available for other elements. Hence, a spectroscopic analysis of key chemical elements such iron peak, α-elements, etc., is paramount to fully reconstruct the enrichment history of Liller 1.

2.3 M 54: the Nuclear Star Cluster of Sagittarius galaxy

2.3.1 The Sagittarius dwarf galaxy

The Sagittarius dwarf spheroidal galaxy (Sgr dSph, $L \sim 2-5\times10^7$ L$_\odot$, Ibata et al., 1997) is a perfect example of a Galactic satellite that is currently undergoing disruption by the tidal field of the Milky Way (Ibata et al., 1994; Bellazzini et al., 2008). This galaxy is located behind the Galactic Bulge $\sim$ 6.5 kpc below the Galactic plane, at a distance D $=$ 26.3 $\pm$ 1.8 kpc from the Sun and at $\sim$ 18.7 kpc from the Galactic center (Monaco et al., 2004). The central component of the system is a significant elongated spheroid with low surface brightness and devoid of gas, characterized by a half-light radius (r_h) of 2.6 kpc (Burton & Lockman, 1999; Majewski et al., 2003). Moreover, the two arms of its tidal stream extend across the entire sky, reaching distances of approximately 100 kpc (e.g., Belokurov et al., 2014; Law & Majewski, 2016; Ibata et al., 2020). The main body of this system is characterized by a present-day stellar and dynamical mass, within r_h, of $M_\star \sim 2\times10^7 M_\odot$ (Ibata et al., 2004) and $M_{\rm dyn} \sim 2\times10^8 M_\odot$ (Grcevich & Putman, 2009), but it is widely accepted that the progenitor was significantly more massive, in the range of $10^{10}-10^{11}$ M$_\odot$ (Niederste-Ostholt et al., 2012; de Boer et al., 2014; Gibbons et al., 2017; Vasiliev et al., 2021).

The stellar component of the main body is dominated by an intermediate-age ($\gtrsim$ 5 Gyr) and relatively metal-rich (mean [Fe/H]~ -0.5 dex) population (Bellazzini et al., 2006; Siegel et al., 2007), with a tail of old and metal-poor population that arrives down to [Fe/H] $\leqslant -2.0$ dex. The metallicity distribution, as found by Minelli et al. (2023), for the main body of Sgr can be seen in Fig. 2.16. Similar Fe distributions are present also in the analysis by (Hayes et al., 2020; Hasselquist et al., 2021).

Finally, there are four GCs, namely Arp 2, Terzan 7, Terzan 8, and M 54, associated with the main body of the Sgr dSph (Da Costa & Armandroff, 1995; Montegriffo et al., 1998). Probably there are also many other GCs that where stripped from the main body of the galaxy and are

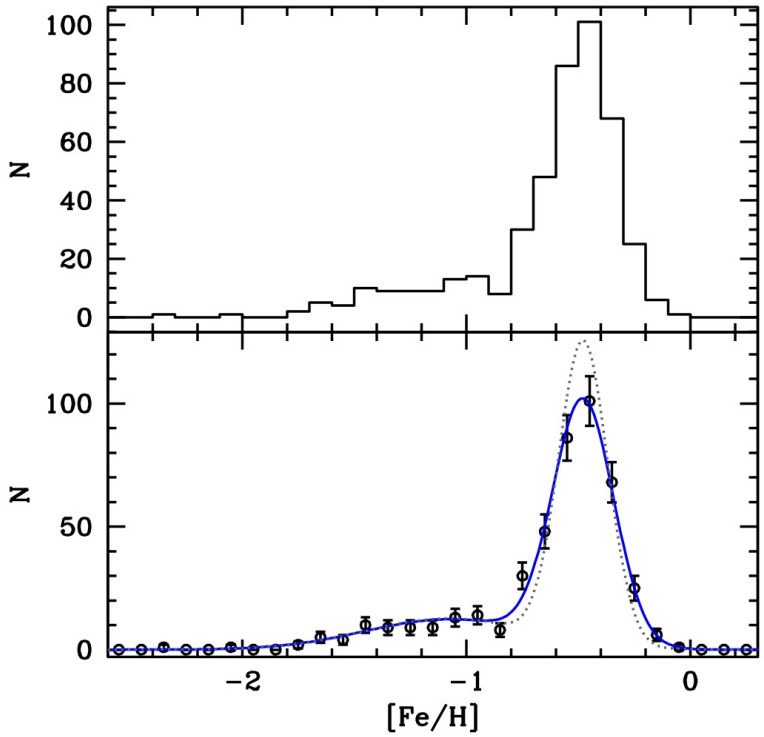

FIGURE 2.16: Top panel: Metallicity distribution for the Sgr stars.
Bottom panel: Same metallicity distribution represented with points and the associated error bars. The dotted gray curve is the best fit of the two Gaussian models with the estimated intrinsic σ values, while the continuous blue curve is the same model convolved with the mean uncertainty of individual [Fe/H] measurements. Figure from Minelli et al. (2023).

now associated with the Sgr stream (Bellazzini et al., 2003a,b; Carraro et al., 2007).
Despite its extension across several kpc, this spheroidal contains an over-density of stars on the $\leqslant$ 100 pc scale situated directly at its nucleus. The massive and metal-poor ([Fe/H] $=$ -1.56 dex, Carretta et al., 2010b) GC M 54 coincides with this nuclear region both in terms of position and radial velocity (RV). For this reason, immediately after the discovery of the Sgr dSph galaxy, it was suggested that M 54 could be the actual nucleus of the galaxy (Bassino & Muzzio, 1995; Sarajedini & Layden, 1995).
Since the mean metallicity of M 54 and of the population dominating the Sgr galaxy differ by $\sim$ 1 dex, their RGB stars can be easily distinguished from each other in a CMD. Indeed, at the same magnitude the RGB of Sgr is much redder than that of M 54. Selecting genuine Sgr stars in this way, Layden & Sarajedini (2000) and Majewski et al. (2003) found an overdensity of Sgr stars that appear concentric with M 54 and with a similar spatial scale. Using the same technique and a very large optical photometry database, Monaco et al. (2005) demonstrated that Sgr actually has a nucleus of metal-rich stars, that is independent from the GC M 54, and is usually known as SgrN.

Nowadays, it is widely recognized that Sgr dSph is a nucleated galaxy, with the presence at its center of a structure called Nuclear Star Cluster (Alfaro-Cuello et al., 2019; Neumayer et al., 2020).

2.3.2 Nuclear Star Clusters

According to Neumayer et al. (2020) *"Nuclear star clusters (NSCs) are extremely dense and massive star clusters occupying the innermost region or 'nucleus' of most galaxies. Observationally, NSCs are identified as luminous and compact sources that clearly 'stand out' above their surroundings"*. A very broad definition conveys that a NSC is a stellar excess of light above the inward extrapolation of the host galaxy's surface brightness profile on scales of $\leqslant$ 50 pc. An example of NSCs can be observed in Fig. 2.17.

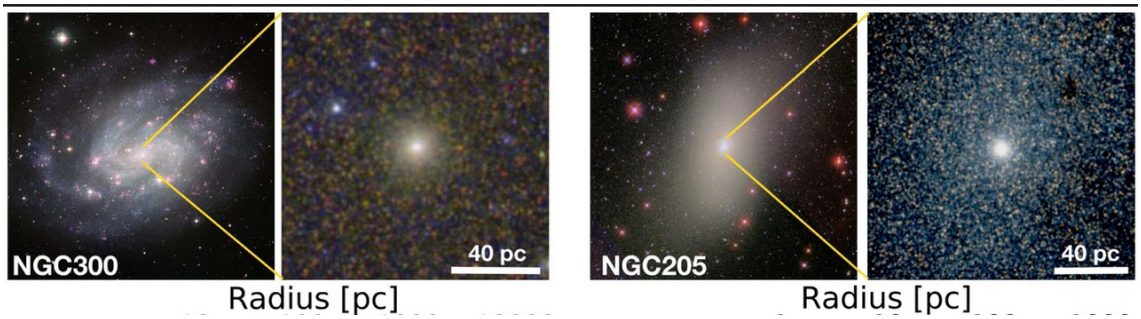

FIGURE 2.17: The NSCs in the late-type spiral NGC 300 (left) and early-type galaxy NGC 205 (M 110, right). The panels show galaxy-wide images with zoom-ins into the central regions of each galaxy. Figure from Neumayer et al. (2020).

NSCs have masses from 10^5 to 10^8 $M_\odot$ and they are on average more massive than GCs, specially in host galaxies with masses above 10^9 $M_\odot$. However, there is an overlap in terms of mass between some of the most massive GC and some of the least massive NSCs (Neumayer et al., 2020). The $r_{h,l}$ of NSCs is in the range from 1 to 40 pc, with the majority of them having $r_{h,l} < 10$ pc and a mean value of ~ 3.3 pc (Georgiev & Böker, 2014; Georgiev et al., 2016; Neumayer et al., 2020). Moreover, these systems are not spherical with value of ellipticity ϵ up to 0.6.

The analysis of high-resolution HST images of nearby galaxies revealed that NSCs are found in $\geqslant 70\%$ of galaxies across the Hubble sequence (Phillips et al., 1996; Carollo et al., 1998; Böker et al., 2004; Turner et al., 2012; Georgiev & Böker, 2014), covering a wide range of galaxy stellar masses with an occupation fraction peaking at galaxy masses in the range of $10^8 - 10^{10}$ $M_\odot$ (Ordenes-Briceño et al., 2018; Sánchez-Janssen et al., 2019).

NSCs are known to have extended star formation histories (Walcher et al., 2005; Kacharov et al., 2018), with the presence of stars with different ages and metallicities. Thus, the finding

of stellar systems with metallicity spreads coupled with age spreads are likely an indicator of a stripped NSC. Pfeffer et al. (2014) predict, via cosmological simulations of our Galaxy, that between one and three GCs with masses higher than 10^5 $M_\odot$ are tidally striped nuclei, with a high likelihood of remnants above 10^6 $M_\odot$.

An important question about these systems is how they form. The first formation scenario for NSCs was offered by Tremaine et al. (1975), who suggested that the compact nuclear structures are formed when globular clusters are 'dragged' into the nucleus by dynamical friction created as they orbit through the stellar body of their host galaxy. The strength of this dynamical friction depends linearly on the mass of the GC, and thus the most massive clusters are the most likely to inspiral into and form the NSC. Therefore, NSCs more metal-poor than their surrounding hosts are likely an expectation of dynamical friction-driven infall models. However, the cluster infall scenario alone cannot readily explain the presence of young stars in many NSCs, which is why additional mechanisms are needed to fully describe NSC evolution. Usually the presence of young stars, is explained by invoking *in situ* star formation. This scenario is well supported by a series of both observational and theoretical works. Thus, the evidence suggest that NSCs grow through both globular cluster inspiral and *in situ* formation. For a complete review on the different mechanisms of growing I refer to Neumayer et al. (2020) and all the references therein.

In the case of Sgr dSph, its NSC is composed of at least two distinct populations, a metal-poor one and a metal-rich one, with the metal-rich population having stars as young as ~ 2 Gyr, while the metal-poor population is consistent with an age of ~ 13 Gyr (Monaco et al., 2005; Siegel et al., 2007; Bellazzini et al., 2008; Mucciarelli et al., 2017; Alfaro-Cuello et al., 2019). Some authors have referred to these two components as separate objects, a massive metal-poor GC (M 54) and a metal-rich component associated with the galaxy (SgrN). Bellazzini et al. (2008) showed that the two systems have different surface density profiles and, specially, very different velocity dispersion profiles, supporting the idea that M 54 formed independently from the metal-rich nuclear component and was brought to its current position by dynamical friction. The feasibility of this scenario was demonstrated both analytically (Monaco et al., 2005) and with N-body simulations (Bellazzini et al., 2008), and it found independent support from a chemical point of view (Carretta et al., 2010b). Thus, M 54 is a very interesting object because is the only NSC for which can be obtained optical spectroscopy of individual member stars. This makes it a key object for the understanding of NSCs, specially for low-mass early-type galaxies ($M_\star \sim 3 \times 10^8$ $M_\odot$, Neumayer et al., 2020).

2.3.3 Structural properties of M 54

M 54 (see Fig. 2.18; Messier, 1781), also known as NGC 6715, is the second brightest and massive system among GCs after ω Centauri, with an absolute magnitude in the V-band $M_V = -9.53$ (Baumgardt et al., 2020) and a mass $M = (1.59 \pm 0.03) \times 10^6$ $M_\odot$ (Baumgardt & Hilker, 2018). In Fig. 2.19 is shown the position of M 54 in the distribution of absolute magnitudes and masses, demonstrating that this system has extreme properties as ω Centauri.

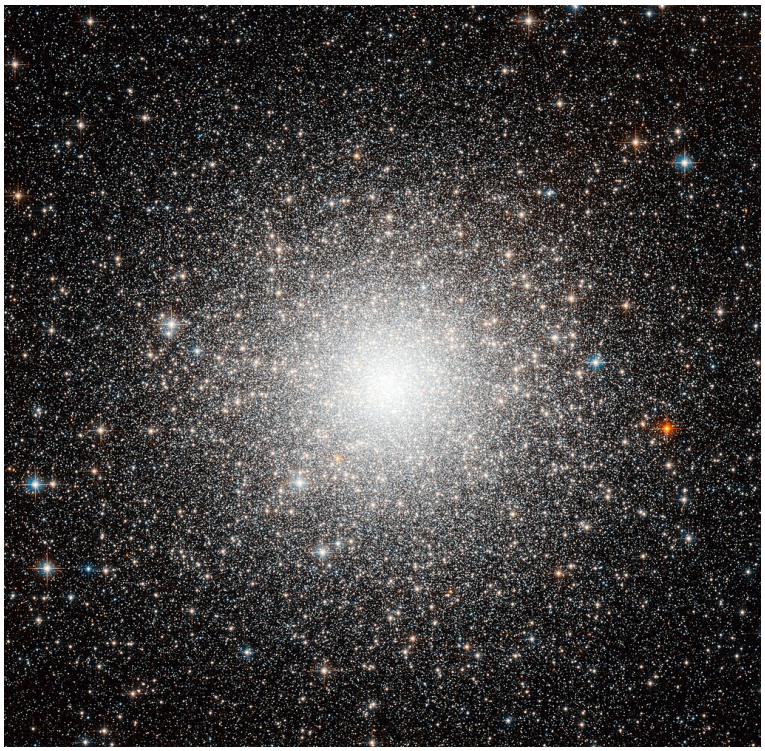

FIGURE 2.18: M 54 image acquired with HST. Credits: ESA/Hubble & NASA.

M 54 is immersed in the nucleus of the Sgr dSph, located at a distance of 26.28 ± 0.33 kpc from the Sun and at 18.51 ± 0.31 kpc from the Galactic center (Baumgardt & Vasiliev, 2021). M 54 has a $r_c = 0.55$ pc, a $r_{h,l} = 3.58$ pc, a $r_{h,m} = 5.78$ pc, and a $r_t = 279.15$ pc (Baumgardt & Hilker, 2018). The resulting concentration is $c = 2.71$. All the described properties of M 54 are reported in Table 2.4.

Moreover, M 54 is considering a non-rotating stellar system, with a rotation velocity reported by Sollima et al. (2005a) of 0.57 ± 1.11 km s^{-1} and a probability of rotation of 18.5%. This translate in an ϵ value of 0.06 (Harris, 2010). Finally, the central velocity dispersion is equal to 17.2 km s^{-1} (Baumgardt et al., 2019).

M 54 is considered to be part of the NSC of the Sgr dSph galaxy, being the old and metal-poor component of the NSC. M 54 displays a wide metallicity range, spanning almost 1 dex in

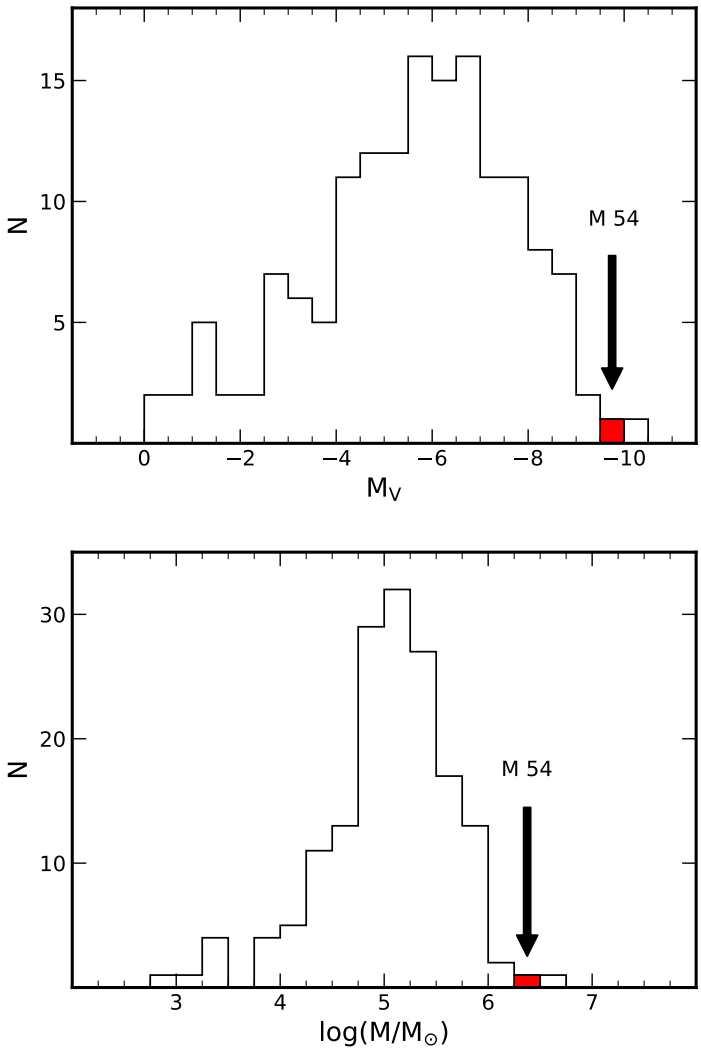

FIGURE 2.19: Histograms of absolute magnitudes, M_V (top panel), and masses, $\log(M/M_\odot)$ (bottom panel) for all the Galactic GCs. The position of M 54, at the extreme of the distributions, is marked by an arrow and a red bin. Data from Baumgardt & Hilker (2018); Baumgardt et al. (2020); Baumgardt & Vasiliev (2021).

[Fe/H] from ~ -2.0 dex up to -1.0 dex. The mean value of metallicity reported by Carretta et al. (2010b) is [Fe/H] $= -1.56$ dex with an intrinsic spread $\sigma = 0.19$ dex, making M 54 the GC-like system with the second highest spread after ω Centauri.

However, despite all its astonishing properties such as the extreme properties in terms of mass, the wide metallicity range, its proposed nature of NSC, etc., M 54 remains a poorly studied system.

Table 2.4. Main properties of M 54.

RA J2000	283.°76385	Goldsbury et al. (2010)
Dec J2000	−30.°47986	Goldsbury et al. (2010)
$\mu_\alpha \cos\delta$	-2.682 mas yr^{-1}	Vasiliev & Baumgardt (2021)
μ_δ	-1.374 mas yr^{-1}	Vasiliev & Baumgardt (2021)
Galactic latitude	5.°607	Harris (1996)
Galactic longitude	−14.°087	Harris (1996)
Distance from Sun	26.28±0.33 kpc	Baumgardt & Vasiliev (2021)
Distance from Galactic center	18.51±0.31 kpc	Baumgardt & Vasiliev (2021)
Mass M	1.59×10^6 M$_\odot$	Baumgardt & Hilker (2018)
Core radius r_c	0.55 pc	Baumgardt & Hilker (2018)
Half-light radius $r_{h,l}$	3.58 pc	Baumgardt & Hilker (2018)
Half-mass radius $r_{h,m}$	5.78 pc	Baumgardt & Hilker (2018)
Tidal radius r_t	279.15 pc	Baumgardt & Hilker (2018)
Concentration c	2.71	Baumgardt & Hilker (2018)

2.3.4 Photometry and metallicity of M 54

The first photometric study of M 54 was performed by Harris (1975), who constructed a CMD based on photographic plates. The CMD reached the cluster HB at $V \sim 17.7$, and indicated a foreground reddening of $E(B-V) = 0.17$. However, from this analysis, no other relevant information were obtained, due to the difficult going at magnitudes fainter than the level of the HB. Zinn (1980) from photoelectric photometry of the integrated light of M 54 derived a $E(B-V) = 0.15 \pm 0.03$ and a metallicity [Fe/H] $= -1.41 \pm 0.06$ dex. Then, for long time M 54 remained unexplored, until the discovery of the Sgr dSph galaxy by Ibata et al. (1994). After that date, systematic studies on M 54 started. Sarajedini & Layden (1995) performed a photometric study of this cluster presenting a $(V-I), I$ CMD and obtaining a $E(B-V) = 0.13 \pm 0.02$ and a value [Fe/H] $= -1.79 \pm 0.08$ dex. The authors found a well-populated, quite steep RGB with $V_{tip} \sim 15.2$, along with a well-defined blue HB, and a red HB at $V \sim 18.3$. From the intrinsic spread in the CMD, the authors concluded that a metallicity dispersion of 0.16 dex is present among the stars of M 54. Along with the presence of M 54 stars, Sarajedini & Layden (1995) found also the presence of the SgrN stars, for which they derived a [Fe/H] $= -0.52 \pm 0.09$ dex.

Layden & Sarajedini (1997) from a deep photometric analysis going below the MS-TO, estimated the age of M 54, finding that this system is very old with an age of $\sim$ 14 Gyr that is compatible with the ages of Galactic halo GCs. Moreover, they estimated that the SgrN is at least 3 Gyr younger than M 54.

Later on, Siegel et al. (2007) from very deep (F606W $\sim$ 26.5), high-precision HST photometry showed an unprecedentedly detailed CMD with extended blue HB and multiple MSs of the M 54 + Sgr system. The authors found that the entire system is dominated by the old ($\sim$ 13 Gyr) and metal-poor population of the GC M 54, but at the same time the multiple TO indicate the presence of at least two star formation episodes at 4 and 6 Gyr and [Fe/H] in the range -0.6 to -0.4 dex. They also showed, for the first time, a prominent, $\sim$ 2.3 Gyr old Sgr population of near-solar abundance. A trace population of even younger ($\sim 0.1-0.8$ Gyr old), more metal-rich ([Fe/H] $\sim +0.6$ dex) stars is also indicated.

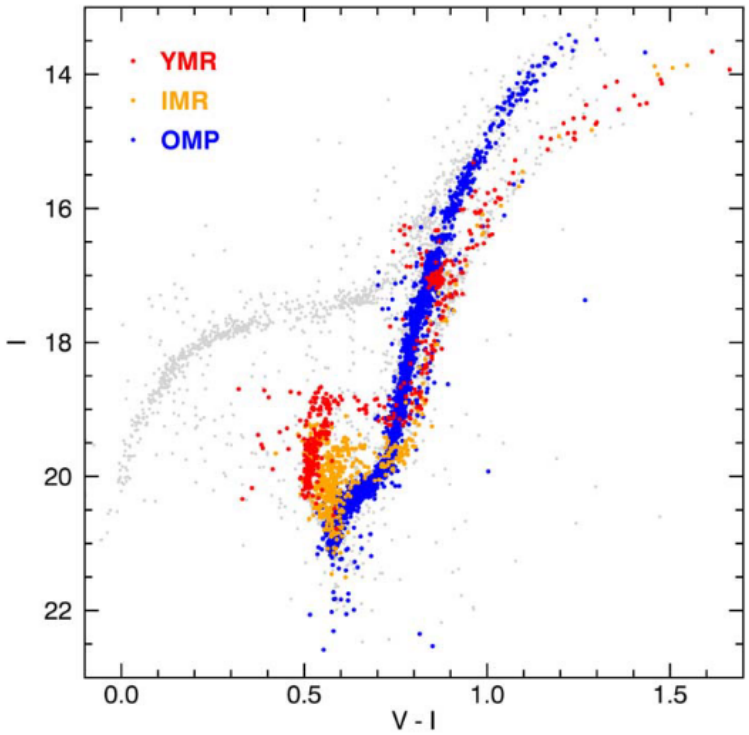

FIGURE 2.20: $(V-I), I$ CMD of the NSC of Sgr dSph. The red points represent the young and metal-rich subpopulation (2.2 Gyr, [Fe/H] $= -0.04$ dex), orange points are for the intermediate age metal-rich (4.3 Gyr, [Fe/H] $= -0.29$ dex) and blue points are for the old metal-poor (12.2 Gyr, [Fe/H] $= -1.41$ dex). Gray points show the stars with age relative error greater than 40% or for which age was not estimated. Figure from Alfaro-Cuello et al. (2019).

More recently, a combined spectroscopic and photometric analysis by Alfaro-Cuello et al. (2019) confirmed the results by Siegel et al. (2007). In particular, Alfaro-Cuello et al. (2019) found three subpopulations divided as follows: **(1)** a young metal-rich, with an age of $\sim$ 2.2

Gyr and average metallicity [Fe/H] $= -0.04$ dex; **(2)** an intermediate age metal-rich, with an age of ~ 4.3 Gyr and metallicity [Fe/H] $= -0.29$ dex; and **(3)** an old metal-poor, with an age of ~ 12.2 Gyr and metallicity [Fe/H]$= -1.41$ dex. These three subpopulations can be seen in Fig. 2.20.

The old metal-poor subpopulation constitutes M 54 and has a metallicity spread of 0.24 dex. Such spread is larger than the one reported by the high-resolution spectroscopic analysis by Carretta et al. (2010b), which corresponds to 0.19 dex. However, both agree with the fact that M 54 has a large and intrinsic spread in metallicity, which is the second largest after the one in ω Centauri.

These studies show that is not possible to ignore the SgrN when analyzing the GC M 54, even though is possible to study each component separately due to their differences in age and metallicity. These two structures constitute the NSC of the Sgr dSph, which is located at the center of the galaxy.

According to Alfaro-Cuello et al. (2019) the metal-poor component of the NSC, namely M 54, could have formed from the infall of two or more *genuine* GCs, which merged to create a single high-mass cluster with a large metallicity spread as is observed in M 54.

2.3.5 Spectroscopy of M 54

The wide Fe distribution in M 54 is well recognized also from a spectroscopic point of view. The first spectroscopic study where Fe variations were detected was made by Da Costa & Armandroff (1995), who using spectroscopic metallicities obtained with the Ca triplet technique for five M 54 members found a mean [Fe/H] $= -1.55$ dex. However, from the analysis, they found two discrepant stars with $+0.18$ and -0.13 dex with respect to the mean. The authors suggested the possibility of an intrinsic metallicity spread in M 54.

Brown et al. (1999) analyzed a sample of five M 54 member stars using high-resolution spectra, finding a mean value [Fe/H] $= -1.55$ dex but without any spread in the derived metallicity. Later studies, based on samples dedicated only to M 54 or where M 54 is well separated from SgrN and with high number of member stars demonstrated that this system has a wide Fe distribution with an intrinsic spread. Among these studies the most famous are the ones performed by Bellazzini et al. (2008); Carretta et al. (2010b); Mucciarelli et al. (2017); Alfaro-Cuello et al. (2019). Despite small differences in the derived values, all these studies are consistent with the fact that M 54 has a peak of metallicity at [Fe/H] ~ -1.50 dex and a long tail extending to higher metallicities, with a spread $\sigma_{\rm [Fe/H]} > 0.15$ dex.

Although the observational scenario clearly shows that is a complex stellar system, far from *genuine* GCs, M 54 displays the typical chemical signatures of (anti)correlations indicating

the presence of MPs.

The first hint of chemical variations among the light elements was suggested by Brown et al. (1999), who from the analysis of five stars in M 54 through high-resolution spectra found that one star was characterized by low O and high Na and Al. A second star shows a lesser degree of O depletion unaccompanied by Na and Al excesses. However, the sample was to small to conclude firmly on the existence of MPs in this cluster. The first analysis of the elements involved in the phenomenon of MPs based on large number of M 54 member stars and analyzed by using high-resolution spectra was performed by Carretta et al. (2010b). The authors analyzed a sample of 76 RGB stars belonging to M 54, together with 27 stars belonging to SgrN. It was found that M 54 displays a clear Na-O anticorrelation (see Fig. 2.21). When the stars are divided into two groups, being one more metal-poor than the mean [Fe/H] value and the other more metal-rich, an interesting feature emerges: the two groups display different extension of the Na-O anticorrelation, with the metal-rich component reaching higher degrees of processing by proton capture reaction in H burning at high temperature. The same feature was observed also in the Na-O anticorrelation of ω Centauri (Johnson & Pilachowski, 2010; Marino et al., 2011c). On the other hand, no evidence of anticorrelation is present among the stars belonging to the SgrN. Thus, a well developed, very extended Na-O anticorrelation is present only among the M 54 stars, while it is completely absent in the surrounding nucleus of the Sgr dSph galaxy.

M 54 shows also hints of the presence of chemical variations due to the activation of the extreme MgAl chain. Indeed, Carretta et al. (2010b) found a moderate Mg-Al anticorrelation, with mild Mg depletion[2] associated with large enhancements in Al abundances. This behavior is evidently not present in the SgrN stars, where, in contrast, Mg and Al abundances are possibly positively correlated with each other. Also a small Al-Si correlation is present in M 54. However, no clear evidence of a Mg-Si anticorrelation is present among the analyzed stars, signature that the temperatures reached during the H burning inside the polluter stars were not sufficiently high to efficiently produce Si. Finally, as a consequence of the activation of both the NeNa and MgAl chains, among the M 54 stars is present Na-Al correlation.

Very recently, Fernández-Trincado et al. (2021) presented the results of the analysis of 22 M 54 member RGB stars from the APOGEE survey. They derived the N abundances, finding the existence of a population N-, Al-rich coupled with moderate depletion of Mg. This confirms that M 54, share the light elements anomalies typical of the presence of SG stars in GCs, confirming the findings on the Na-O anticorrelation by Carretta et al. (2010b).

Carretta (2022) found evidence of a statistically marginal Mg-K anticorrelation in M 54, due

[2] I recall that in any case, no stars with [Mg/Fe]$<$ 0.0 dex are present in the Mg-Al anticorrelation, at odds with what is observed in ω Centauri.

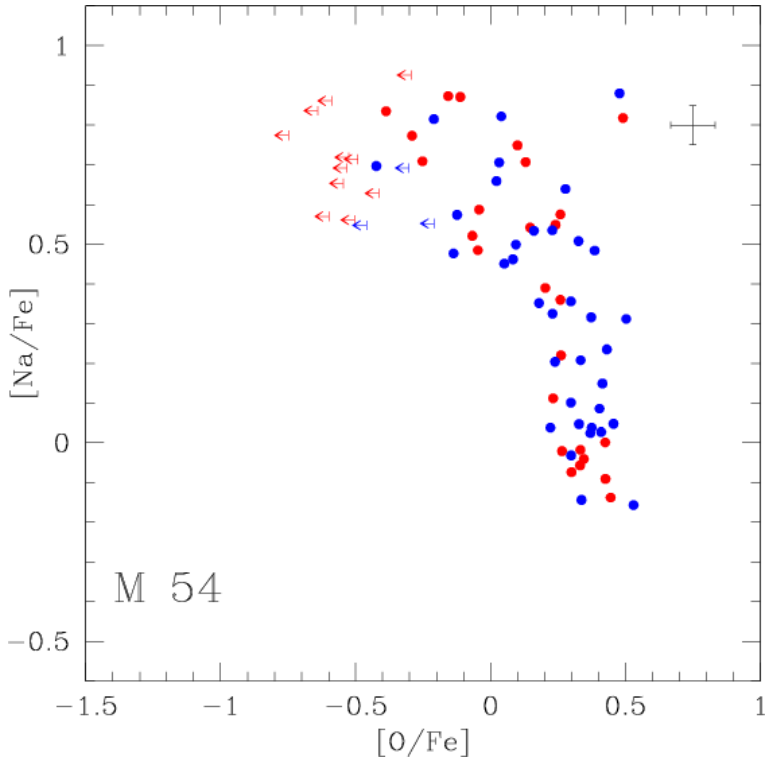

FIGURE 2.21: Na-O anticorrelation in M 54 from UVES and GIRAFFE spectra. Blue and red circles indicate stars that are respectively more metal-poor and more metal-rich than the cluster average [Fe/H] = −1.56. Upper limits to [O/Fe] are indicated by arrows. The typical star-to-star error bars are shown in the upper-right part. Figure from Carretta et al. (2010b).

to the lack of very Mg-poor stars[3]. On the other hand, they found evidence of a clear K-O anticorrelation.

To conclude, even though the presence of MPs in M 54 is evident, only a handful of spectroscopic studies based on large (N> 20) number of stars were performed among the M 54 stars. Therefore, further studies based on larger spectroscopic datasets are required, in order to shed light into the phenomenon of MPs in this peculiar system, as well to constrain its history of formation and evolution and the way in which this system is linked to the SgrN to form the NSC of the Sgr dSph galaxy. Indeed, it is well recognized that M 54 and SgrN show different patterns regarding the light elements.

[3]In the context of MPs, stars are considered Mg-poor when they have [Mg/Fe] < 0.0 dex.

2.4 Thesis layout

This Thesis is structured in the following way:

- In Chapter 3, I will present the results on the phenomenon of anticorrelations linked to the MgAl chain in ω Centauri, from optical high-resolution spectra obtained with ESO@VLT FLAMES@GIRAFFE spectrograph. The presence of MPs with variations in the elements involved in the MgAl chain (Mg, Al, Si, and K) are very useful to put further constraints on the nature of polluters responsible for the formation of the SG stars.

- In Chapter 4, I will present the results about the complete chemical characterization of Liller 1 in terms of Fe, light, α, and Fe-peak elements based on medium NIR resolution spectra obtained with the ESO@VLT X-shooter spectrograph. These results, together with the previous results by Ferraro et al. (2021), Dalessandro et al. (2022), and Crociati et al. (2023) will shed light on the true nature of the bizarre stellar system Liller 1.

- In Chapter 5, I will present the results from the analysis of a large spectroscopic dataset for M 54 member stars, observed with the ESO@VLT FLAMES spectrograph. These results combined with the findings by our group on the Sgr stars will help to understand the phenomenon of formation of MPs in M 54, as well its nature of NSC.

- Finally, in Chapter 6 I will present a summary of my findings, I will discuss the impact they had on the open issues related to these peculiar systems, and I will present a list of future steps that are the outcome of this Thesis work.

CHAPTER 3

The complete MgAl burning chain in ω Centauri

Based on the results published in:

- *Alvarez Garay, D. A., Mucciarelli, A., Lardo, C., Bellazzini, M., & Merle, T., 2022 ApJL, 928, L11*
- *Alvarez Garay, D. A., Mucciarelli, A., Bellazzini, M., Lardo, C., & Ventura, P., 2024 A&A, 681, A54*
- *Alvarez Garay, D. A, Bonifacio, P., Mucciarelli, A., in preparation*

3.1 Introduction

The detection within GCs of MPs that display chemical variations in the light elements involved in the MgAl burning chain is extremely important, because these evidence can help us to put strong constraints on the nature of the polluter stars responsible for the enrichment of the intracluster medium from which SG stars arose. Indeed, the temperatures needed for the activation of the MgAl chain are very high and are reachable only in a small subset among the proposed polluters in literature (see Sect. 1.4). Evidence of anticorrelations arising from the MgAl chain were found among the most massive and/or metal-poor stellar systems.
In this context, ω Centauri represents an ideal candidate to study the anticorrelations linked to the MgAl burning chain. Indeed, this system is the most massive among Galactic GCs and displays all the anticorrelations usually observed in GCs, including also the barely visible such the Na-Li one. Moreover, ω Centauri among its populations spanning a wide range of metallicities, hosts a dominant component of metal-poor stars.
In the following Sections I will present the results obtained by studying the complete MgAl burning chain, through the analysis of a large sample of ω Centauri member stars in order to put further constraints on the nature of polluters at the origin of the SG stars in this very intricate stellar system.

3.2 The Mg-K anticorrelation in ω Centauri

3.2.1 Observations

Observations were performed with the multi-object spectrograph FLAMES (Pasquini et al., 2002), within the ESO programme 095.D-0539 (P.I. Mucciarelli). I used FLAMES in the GIRAFFE mode that allows us to allocate simultaneously up to 132 fibers. All the targets were observed with both high-resolution (HR) HR11 and HR18 setups, covering the wavelength range from 5597 to 5840 Å and from 7648 to 7889 Å, and with a spectral resolution of 29500 and 20150, respectively. The first setup allows to measure the Mg line at 5711 Å and the Na doublet at 5682 and 5688 Å, the second the K I resonance line at 7699 Å. I checked for each target that K line was not contaminated by telluric lines. This is due to the high radial velocity of ω Centauri (232.7 ± 0.2, $\sigma = 17.6$ km s^{-1}; Baumgardt & Hilker, 2018). Also, several Fe lines are included in the considered wavelength range.

I selected targets among the member stars of ω Centauri already analyzed in previous works (Norris & Da Costa, 1995b; Johnson & Pilachowski, 2010; Marino et al., 2011c). Also I considered only stars that result to be not contaminated by neighbor stars within the size of the GIRAFFE fibers. I observed a total of 450 stars: 350 are in common with Johnson & Pilachowski (2010), 85 with Marino et al. (2011c) and 15 with Norris & Da Costa (1995b).

Four configurations of targets were defined and each of them was observed with both HR11 and HR18 setups. Due to the brightness of the targets ($10.7 < G < 14.5$), for each configuration two exposures of 1300 s and two of 300 s each were sufficient to reach a signal-to-noise ratio (SNR) ~ 70 and SNR ~ 100 for HR11 and HR18, respectively. The observation of each configuration was split in two exposures in order to get rid of the effects of cosmic rays and other transient effects. Finally, during each exposure about 15 fibers were dedicated to observe empty sky regions in order to sample the sky background.

Spectra were reduced with the GIRAFFE ESO pipeline[1], that includes bias subtraction, flat field correction, wavelength calibration and spectral extraction. For each exposure, the individual sky spectra were median-combined together and the resulting spectrum was subtracted from each stellar spectrum.

From visual inspection, I decided to exclude from the subsequent chemical analysis: four stars (179_NDC, 201_NDC, 37024_J10 and 48099_J10) with $T_{\rm eff} < 3900$ K because their spectra were contaminated by the TiO molecular bands, and one star (371_NDC) with a very low SNR with respect to other stars with similar magnitude.

[1] https://www.eso.org/sci/software/pipelines/giraffe/giraffe-pipe-recipes.html

3.2.2 Chemical analysis

3.2.2.1 Atmospheric parameters

I derived the stellar parameters from *Gaia* early Data Release 3 (eDR3) photometry (Gaia Collaboration et al., 2016, 2021). Figure 3.1 shows the CMD of ω Centauri where the position of the spectroscopic targets is marked, while Fig. 3.2 illustrates the spatial distribution of the sample relative to the cluster center.

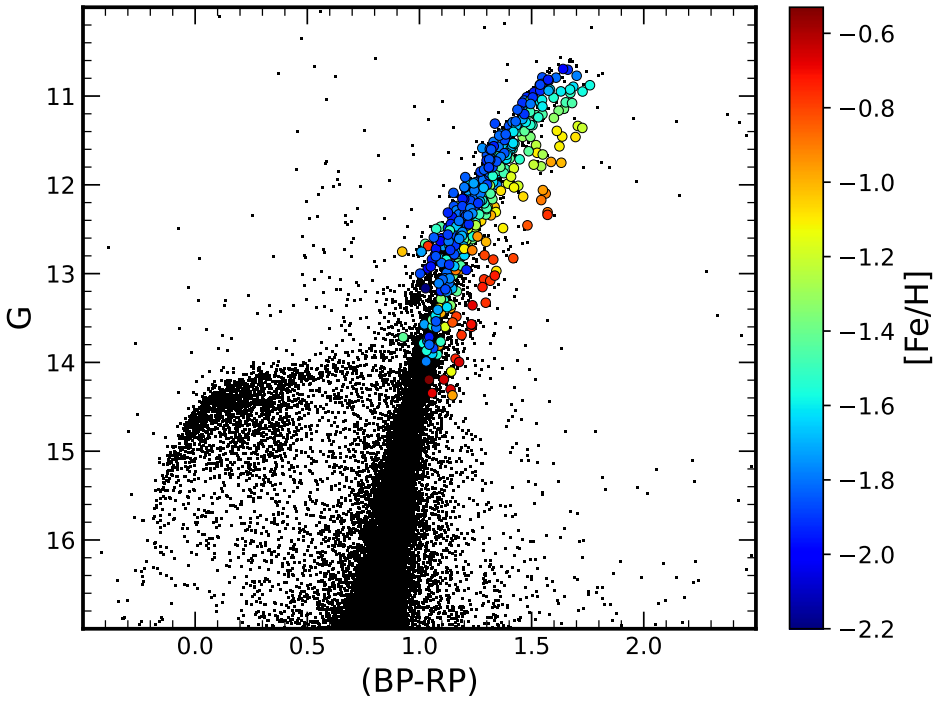

FIGURE 3.1: Color-magnitude diagram of ω Centauri. Black points represent all the targets of ω Centauri observed with *Gaia*, while the targets selected for this work are colored according with their metallicity. The color scale is shown on the right side.

Effective temperatures ($T_{\rm eff}$) were computed using the empirical $(BP-RP)_0 - T_{\rm eff}$ relation by Mucciarelli et al. (2021), based on the InfraRed Flux Method. The dereddened color $(BP-RP)_0$ was obtained by assuming a color excess of $E(B-V) = 0.12 \pm 0.02$ (Harris, 2010) and adopting an iterative procedure following the scheme proposed by Gaia Collaboration et al. (2018). Internal errors in $T_{\rm eff}$ due to the uncertainties in photometric data, reddening and $(BP-RP)_0 - T_{\rm eff}$ relation are of the order of 85-115 K.
Surface gravities ($\log g$) were obtained from the Stefan-Boltzmann relation using the photometric $T_{\rm eff}$ and assuming a typical mass of 0.80 $M_\odot$. Luminosities were computed using the dereddened G-band magnitude with the bolometric corrections from Andrae et al. (2018) and a true distance modulus $DM_0 = 13.70 \pm 0.06$ (Del Principe et al., 2006). I computed

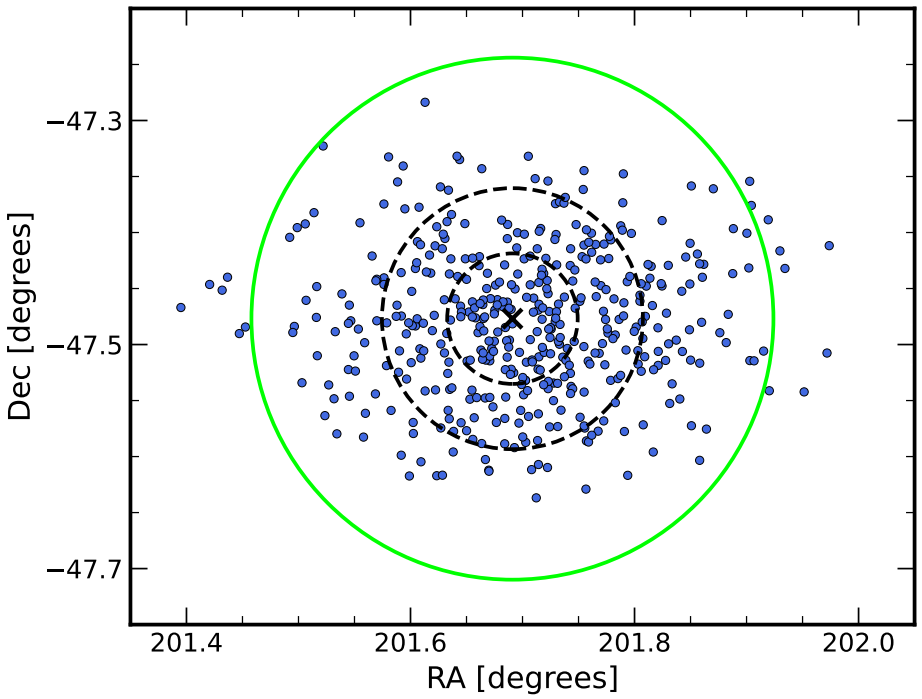

FIGURE 3.2: The coordinate positions of FLAMES targets are displayed by the red circles. The black cross denotes the cluster center (201.°6910, −47.°4769) according to van Leeuwen et al. (2000). The dashed black circles show 2.5 and 5 times the core radius ($r_c = 1.'40$; Harris, 1996). 424 out of the 439 stars that were analyzed in this work are contained within the green circle, which is 10 times the core radius.

the uncertainties in gravities by propagating the uncertainties in $T_{\rm eff}$, distance modulus and photometry. These uncertainties are of the order of 0.1 dex. I would like to point out that an incorrect attribution of the targets to an evolutionary stage (AGB stars attributed to RGB sequence) has a negligible impact on the derived abundances: indeed a difference of 0.2 $M_\odot$ in the attribution mass leads to a modification in $\log g$ of ~ 0.1, corresponding to a variation in the measured Mg, Al, Si, and Fe abundances of about 0.005 dex or less. To assess the impact of 0.1 dex change in $\log g$ on elemental abundances, I performed calculations while keeping the other atmospheric parameters fixed to their best values and only varying $\log g$ by the specified value. The results indicate that such a difference leads to an extremely small change in the measured abundance ratios, amounting to less than 0.005 dex. This negligible variation arises from the fact that all the measured elements (Fe, Mg, Al, and Si) are in their neutral stage, rendering them almost insensitive to variations in $\log g$.

Microturbolent velocities (v_t) were obtained adopting the relation between v_t and $\log\ g$ by Kirby et al. (2009). This relation provides values of v_t of about 1.6-2.0 km s^{-1}. To compute the uncertainties in v_t I assumed a conservative error of 0.2 km s^{-1}.

The derived atmospheric parameters for all the analyzed targets are listed in Table 3.1, together with some additional information.

3.2.2.2 Line lists and tools

The chemical analysis was performed using one-dimensional, Local Thermodynamic Equilibrium (LTE), plane-parallel geometry model atmospheres computed with the code `ATLAS9` (Castelli & Kurucz, 2003) that treats the line opacity through the opacity distribution functions (ODF) method. All the models are calculated using the ODFs computed by Castelli & Kurucz (2003) with α-enhanced chemical composition and without the inclusion of the approximate overshooting in the calculation of the convective flux.
A line list of relatively strong and unblended spectral features at the resolution of my GIRAFFE observations was selected from the Kurucz/Castelli line lists[2] by comparing observed spectra with synthetic ones having appropriate metallicity and $T_{\rm eff}$. Model spectra were calculated with the `SYNTHE` code in its Linux version (Sbordone et al., 2004; Kurucz, 2005).
I derived the chemical abundances of Fe, Na, Mg and K from the comparison between measured and theoretical Equivalent Widths (EWs) with the package `GALA` (Mucciarelli et al., 2013). EWs were measured with the code `DAOSPEC` (Stetson & Pancino, 2008), through the wrapper `4DAO` (Mucciarelli, 2013).
Non-LTE (NLTE) corrections for Na (at 5682 and 5688 Å) and K (at 7699 Å) were calculated by interpolating into the grids of Lind et al. (2011) and Reggiani et al. (2019), respectively. Finally, solar abundances are from Grevesse & Sauval (1998).

3.2.2.3 Error estimates

Uncertainties associated with the chemical abundances were calculated as the sum in quadrature of the error related to measurement process and the errors associated to the atmospheric parameters[3].
Error related to the measurement was calculated as the line-to-line scatter divided by the square root of the number of used lines. When only one line was present the error was calculated by varying the EW of $1\sigma_{EW}$ (i.e. the EW error provided by `DAOSPEC`).
Errors related to the adopted atmospheric parameters were calculated by varying only one parameter at time, keeping the others fixed to their best value, and recalculating each time

[2] `https://wwwuser.oats.inaf.it/castelli/linelists.html`

[3] If I add in quadrature all the possible sources of errors the uncertainties would increase from a minimum of 0.02 for Na to a maximum of 0.06 dex for K, which is the most problematic element to measure. However, the results of this work are the same even if I adopt this extremely conservative approach to estimate errors.

the chemical abundances. At the end all the error sources are added in quadrature. This approach is the most conservative in the calculation of uncertainties because it does not take into account the correlation terms between parameters. So, it should be regarded as an upper limit to the real error associated to the measurements.
Since the abundances are expressed as abundance ratios, the total uncertainties in [Fe/H] and [X/Fe] are calculated as follows:

$$\sigma_{[Fe/H]} = \sqrt{\frac{\sigma_{Fe}^2}{N_{Fe}} + (\delta_{Fe}^{T_{\rm eff}})^2 + (\delta_{Fe}^{\log g})^2 + (\delta_{Fe}^{v_t})^2} \tag{3.1}$$

$$\sigma_{[X/Fe]} = \sqrt{\frac{\sigma_X^2}{N_X} + \frac{\sigma_{Fe}^2}{N_{Fe}} + (\delta_X^{T_{\rm eff}} - \delta_{Fe}^{T_{\rm eff}})^2 + (\delta_X^{\log g} - \delta_{Fe}^{\log g})^2 + (\delta_X^{v_t} - \delta_{Fe}^{v_t})^2} \tag{3.2}$$

where $\sigma_{X,Fe}$ is the line-to-line scatter, $N_{X,Fe}$ the number of lines used to compute the abundance and $\delta_{X,Fe}^i$ are the abundance variations obtained after variation of the atmospheric parameter i.

3.2.3 Results

3.2.3.1 Mg-K anticorrelation

Potassium elemental abundances were derived for a total of 440 stars. Moreover, I obtained Fe, Na and Mg abundances for 440, 359 and 357 stars, respectively (Table 3.1).
The mean value of the [K/Fe] distribution is $+0.31$ dex ($\sigma = 0.19$ dex), with values ranging from -0.20 dex up to $+0.94$ dex. In this calculation I excluded one star showing a significant higher [K/Fe] and that I will discuss in Sect. 3.2.3.2.
The main result of my work is the presence of a clear anti-correlation between [Mg/Fe] and [K/Fe] shown in the left-hand panel of Fig. 3.3. I identified a sample of stars with [Mg/Fe]$<$ 0.0 dex that are systematically enriched in [K/Fe]. This kind of stars are rarely observed in GCs.
Also K correlates with Na (see the right-hand panel of Fig. 3.3). To quantitatively assess these results, I computed for the couples [K/Fe]-[X/Fe] (with X = Na and Mg) the Spearman's correlation coefficient (C_S) and the corresponding two-tailed probability that an absolute value C_S larger than the observed one can derive from non-correlated random variables. I found $C_S = +0.41$ and -0.52 for [K/Fe]-[X/Fe] (with X = Na and Mg) respectively, leading to null probability that the observed correlations arose by chance from uncorrelated variables.

Table 3.1. Data for the analyzed targets in ω Centauri. The adopted solar abundances are reported in the header of each element abundance column.

ID	G	v_r	$T_{\rm eff}$	$\log g$	v_t	[Fe/H]	[Na/Fe]	[Mg/Fe]	[K/Fe]
	[mag]	[km s^{-1}]	[K]	[dex]	[km s^{-1}]	7.50	6.33	7.58	5.12
48_NDC	10.7035	220.6	4041	0.44	2.03	-1.92 ± 0.07	-0.01 ± 0.06	0.42 ± 0.04	0.56 ± 0.15
74_NDC	11.0120	215.7	4273	0.72	1.96	-1.93 ± 0.10	0.21 ± 0.04	0.44 ± 0.03	0.41 ± 0.11
84_NDC	10.9489	220.3	3971	0.49	2.02	-1.57 ± 0.07	0.08 ± 0.09	...	0.31 ± 0.17
161_NDC	11.2326	247.3	4301	0.82	1.94	-1.74 ± 0.10	-0.26 ± 0.07	0.42 ± 0.02	0.29 ± 0.11
182_NDC	11.3292	207.3	4247	0.83	1.94	-1.53 ± 0.07	-0.06 ± 0.05	0.51 ± 0.05	0.25 ± 0.14
357_NDC	11.7420	230.9	4153	0.93	1.92	-0.97 ± 0.06	...	...	0.39 ± 0.18
480_NDC	12.2484	226.7	4503	1.35	1.82	-1.02 ± 0.11	...	...	0.48 ± 0.13
27048_J10	11.8638	242.0	4529	1.21	1.85	-1.59 ± 0.10	0.37 ± 0.06	-0.07 ± 0.05	0.53 ± 0.11
27094_J10	12.8344	237.9	4778	1.73	1.73	-1.83 ± 0.11	0.24 ± 0.06	0.44 ± 0.06	0.14 ± 0.08
29085_J10	12.3903	226.7	4730	1.53	1.78	-1.75 ± 0.10	0.21 ± 0.06	-0.37 ± 0.07	0.52 ± 0.10

Note. — This is a portion of the entire table. This table is available in its entirety in machine-readable form at: https://vizier.cds.unistra.fr/viz-bin/VizieR?-source=J/ApJ/928/L11

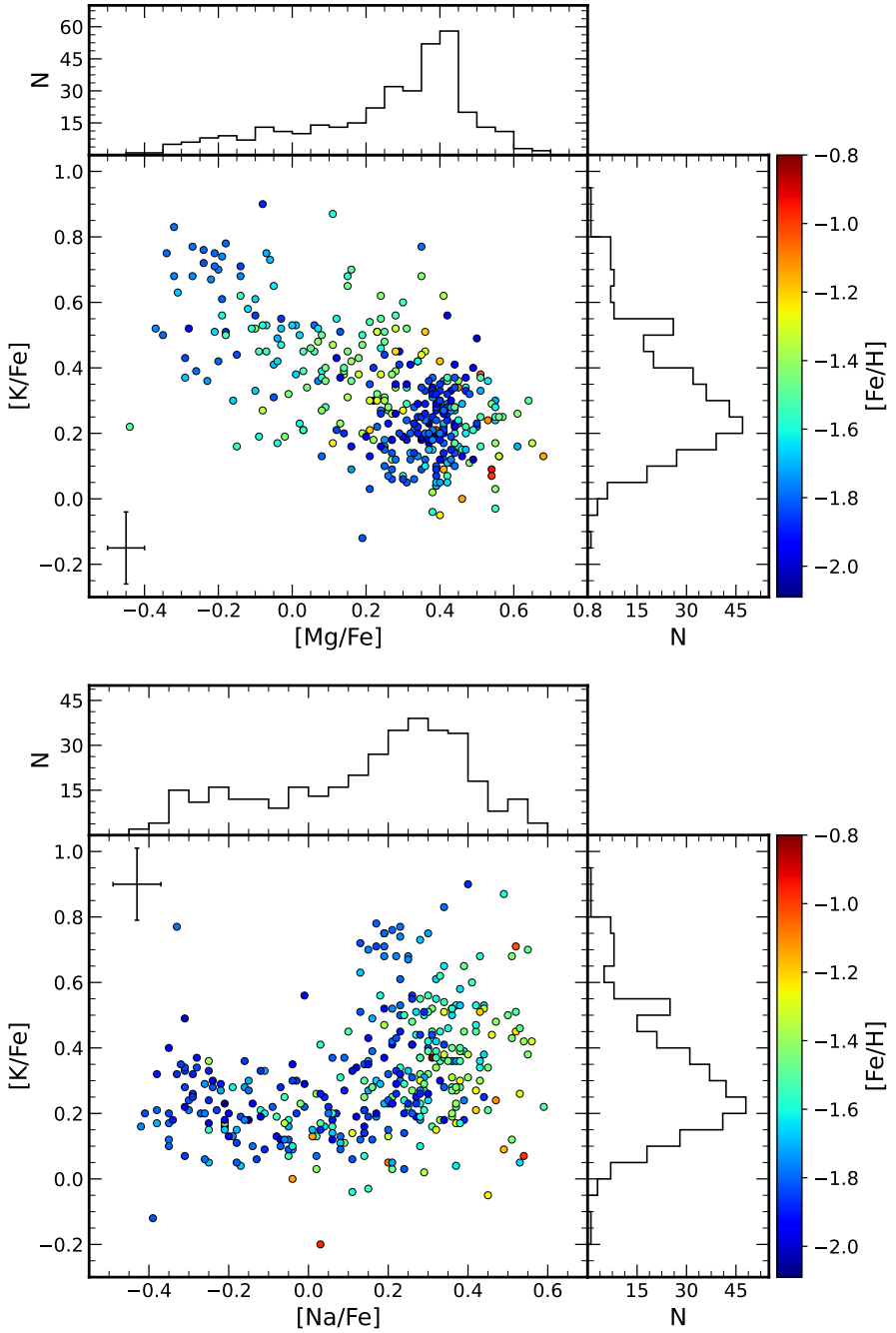

FIGURE 3.3: Top panel: behavior of [K/Fe] as a function of [Mg/Fe]. Each star is color coded according to its value of [Fe/H] and the color scale is shown on the right side. The error bar represents the typical error associated to the abundance ratios. The distribution of [K/Fe] and [Mg/Fe] are shown as marginalized histograms.
Bottom panel: the same as the left panel, but for [K/Fe] and [Na/Fe] abundance ratios.

A hint of the presence of a Mg-K anticorrelation in ω Centauri was firstly detected by Mészáros et al. (2020). They found seven stars with [Mg/Fe]$<$ 0.0 dex (out of a total sample of 898 stars) in which [K/Fe] seems to be enhanced with respect to stars with [Mg/Fe]$>$ 0.0

dex (see their Fig. 10). Unfortunately, the K lines in H band measured by Mészáros et al. (2020) are weak and blended with other lines. Therefore, the authors concluded that it is not possible to claim convincingly the presence of a K enhancement in the Mg-poor stars of ω Centauri. Hence, this is the first time that the presence of a strong Mg-K anti-correlation is undoubtedly established in ω Centauri.

3.2.3.2 A super K-rich star

In the analyzed sample I identified a peculiar star, named 43241_J10, that clearly stands out from the mean locus of other ω Centauri members in the [Mg/Fe] vs [K/Fe] distribution, as can be seen in the left-hand panel of Fig. 3.4. Indeed, this star has [K/Fe]= +1.60 dex.
I compared its spectrum with that one of a reference star (41375_J10), with similar atmospheric parameters and [Fe/H] and [Mg/Fe] abundance ratios. In the right-hand panel of Fig. 3.4 the observed K lines of the two stars are directly compared, showing the obvious difference in line depth, implying intrinsic difference in the [K/Fe] abundance.

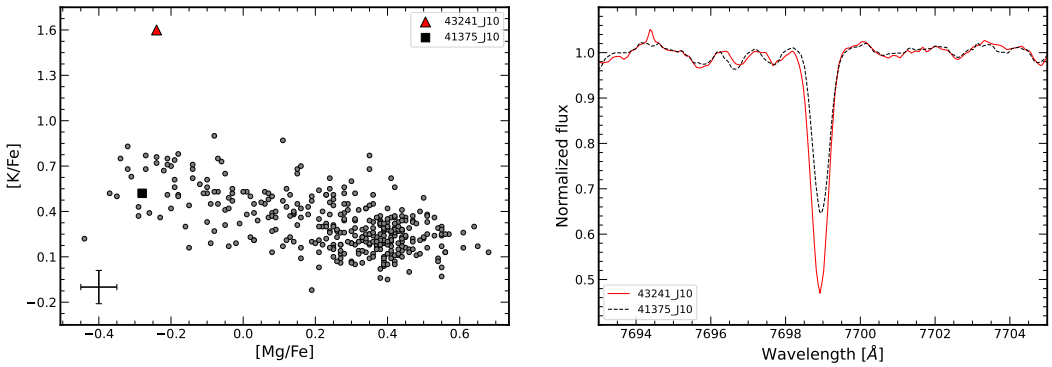

FIGURE 3.4: Left panel: behavior of [K/Fe] as a function of [Mg/Fe] with the inclusion of the K-rich star 43241_J10 (red triangle). The black square represents the reference star 41375_J10 with similar atmospheric parameters as the K-rich star.
Right panel: comparison between the GIRAFFE spectra of the two stars around the strong K line at 7699 Å. The large K enhancement of 43241_J10 is clearly visible from this comparison.

This star was also included in the sample studied by Johnson & Pilachowski (2010). For the stars in common between the two studies I found that my temperatures are on average (140 ± 94 K) higher than those computed by Johnson & Pilachowski (2010). Thus, the difference of +185 K computed for 43241_J10 in this work with respect to Johnson & Pilachowski (2010) is well within the mean difference between the two temperature scales. Even if I adopt the temperatures by Johnson & Pilachowski (2010), the difference in K abundance of 43241_J10 with respect to the other stars remains. Therefore, I can conclude that the high [K/Fe] abundance of this star is real and not an artifact of the analysis.

3.2.4 Discussion

The analysis of a large sample of 450 giants in ω Centauri has revealed the presence of **(1)** a large intrinsic spread in the [K/Fe]; **(2)** a correlation between the K abundances and other light elements (i.e. Na and Mg) which are observed to vary in GCs showing MPs. In particular, I detected the presence of a prominent Mg-K anticorrelation. This finding makes ω Centauri the third stellar system after NGC 2419 (Mucciarelli et al., 2012; Cohen & Kirby, 2012) and NGC 2808 (Mucciarelli et al., 2015) in which a subpopulation of stars with [Mg/Fe]$<$ 0.0 dex and enriched in K is present (Fig. 3.5).

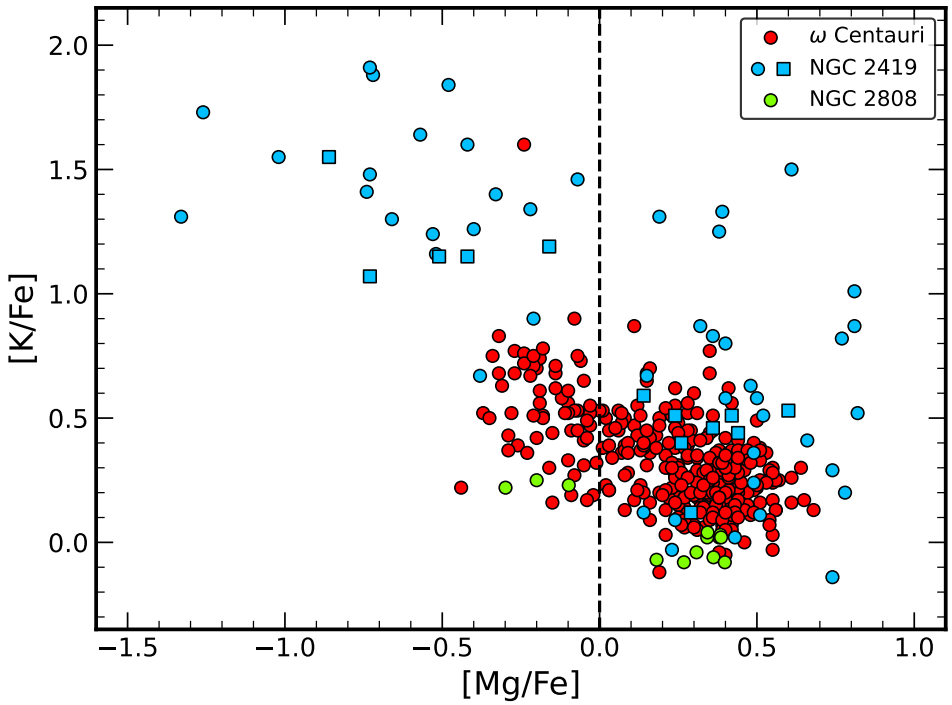

FIGURE 3.5: Run of the [K/Fe] abundance against [Mg/Fe] for stars in GCs. ω Centauri stars are shown as red circles. Stars in NGC 2808 are plotted as green circles (Mucciarelli et al., 2015), whereas stars in NGC 2419 are in blue (data from Mucciarelli et al. (2012) and Cohen & Kirby (2012) are shown as circles and squares respectively). The dashed line splits the Mg-poor from the Mg-rich stars.

The amplitude of the [K/Fe] spread in ω Centauri is intermediate between those of NGC 2419 and NGC 2808. Carretta (2021) suggested the presence of a weak (but statistically significant) Mg-K anticorrelation in NGC 4833. In this cluster the stars showing the highest Mg depletion exhibit a typical overabundance in K of 0.1 dex with respect to the most Mg-rich stars. However, this cluster does not harbor stars with [Mg/Fe]$<$ 0.0 dex at variance to NGC 2419, NGC 2808 and ω Centauri.

The chemical complexity of the stellar populations of ω Centauri deserves further discussion

of the measured [K/Fe] abundance ratios and their correlations with other light elements for the different groups of stars with distinct metallicities. The extent of the Mg-K anti-correlation is mainly driven by the metal-poor ([Fe/H]$\leqslant -1.70$ dex) component which exhibits a bimodal distribution both in [K/Fe] and in [Mg/Fe]. In particular, the group of metal-poor stars with [Mg/Fe]< 0.0 dex has a mean value of [K/Fe] ~ 0.4 dex higher than that of the Mg-rich, metal-poor stars. On the other hand, an evident but less extended Mg-K anticorrelation is detected also among the stars with intermediate [Fe/H] ($-1.70 <$[Fe/H]$\leqslant -1.30$ dex). Finally, for the most metal-rich population ([Fe/H]> -1.30 dex) I cannot conclude for the presence of a Mg-K anti-correlation. For this group of stars I do not have objects with [Mg/Fe]< 0.0 dex and the spread in [K/Fe] is less extended than that of the other subpopulations.

The evidence of a correlation between K and the other light elements involved in MPs phenomenon supports the idea that the spread in [K/Fe] can be ascribed to the self-enrichment process typical of GCs.

The detection of an intrinsic variation in K abundances in the most massive clusters represents a serious challenge for theoretical models for the MPs. In the model proposed by Ventura et al. (2012) to explain the Mg-K anticorrelation in NGC 2419 and based on AGB and SAGB stars, the production of K occurs during the HBB phase, by proton capture reaction on Argon nuclei at temperatures $T \sim 10^8$ K. Even if AGB yields discussed by Ventura et al. (2012) are qualitatively able to explain a Mg-K anticorrelation, the observed [K/Fe] abundance ratios in the extreme case of NGC 2419 can be reproduced only with an increase **(1)** in the cross section of the reaction $^{38}\mathrm{Ar}(p,\gamma)^{39}\mathrm{K}$ by a factor 100 with respect to literature or **(2)** in the temperature at the base of envelope up to $1.5 \cdot 10^8$ K during the HBB. Moreover, Ventura et al. (2012) also predicted that Mg-poor stars would show normal Na abundances, if the Mg-K anticorrelation was indeed produced by AGB and SAGB stars. This is not observed in ω Centauri, where the Mg-poor stars are also enhanced in Na.

On the other hand, Prantzos et al. (2017) discuss the possible production of K from FRMS and supermassive stars, ruling out both the classes of polluters because not able to reach the temperature of K-burning. Therefore, the existence of MPs in GCs remains largely unexplained.

Another interesting result that I found is the presence of a peculiar star with a [K/Fe]~ 1 dex higher than the abundances of Mg-poor, metal-poor stars. Even if the origin of this extraordinary overabundance of [K/Fe] is unclear, it is worth noting that the Mg and K abundances of this star are very similar to those of NGC 2419 (see Fig. 3.5) for which Ventura et al. (2012) proposed that the K enhanced subpopulation was born from the AGB and SAGB ejecta without dilution process.

The metal-poor population of ω Centauri exhibits the usual light element anticorrelations typical of GCs with MPs. Assuming a scenario where the K enhancement in Mg-poor stars is due to pollution by the first generation of AGB and SAGB stars, the ejected gas undergoes a dilution process with the pristine GC gas before forming new generations of stars (D'Ercole et al., 2008, 2010). In this scenario is possible that a small fraction of stars will form directly from the ejecta of polluters without dilution with pristine material. In this framework, I can suppose that the super K-rich star I discovered formed directly from the pure ejecta of AGB stars before dilution, while the other Mg-poor stars show a lower [K/Fe] due to a level of dilution with pristine material. Further inspections of this star are necessary to understand its origin. In particular, it would be useful to study other light elements involved in the proton-capture reactions (C, N, O, etc.).

In conclusion, with the present analysis I support the idea that the observed spread in [K/Fe] in ω Centauri stars is associated to a self-enrichment process typical of GCs. So far a clear Mg-K anticorrelation was found only in three GCs, namely ω Centauri, NGC 2808 and NGC 2419. Those clusters are among the most massive stellar systems of the Milky Way, so I suggest that this anomaly is a manifestation of an extreme self-enrichment process that occurs only in the most massive and/or metal-poor clusters.

3.3 MgAl burning chain in ω Centauri

3.3.1 Observations

In this work I present the chemical abundances of those elements (Mg, Al, and Si) participating in the MgAl cycle, in order to study the role of this extreme burning cycle in the formation of MPs among the different subpopulation of ω Centauri.
This work is a continuation of the work published in Alvarez Garay et al. (2022) (see Sect. 3.2), in which I analyzed the extension of the Mg-K anticorrelation among the RGB stars of ω Centauri (see Fig. 3.1). The data-set is the same described in Sect. 3.2.1, and consists of high-resolution spectra collected with the multiobject spectrograph FLAMES (Pasquini et al., 2002), mounted on UT2 (Kueyen) at the ESO-VLT Observatory in Cerro Paranal, within the ESO program 095.D-0539 (P.I. Mucciarelli). The adopted setups HR11 and HR18 allowed to measure up to five lines of Si, while the second Al doublet at 7835 and 7836 Å.

3.3.2 Abundance analysis

In this work I adopted Fe and Mg abundances from Alvarez Garay et al. (2022), while I derived abundances for Al and Si. In Table 3.2 all the obtained elemental abundances are reported, including the Fe and Mg abundances derived in Alvarez Garay et al. (2022).
Si abundances were derived through the comparison between measured and theoretical equivalent widths (EWs) using the code `GALA` (Mucciarelli et al., 2013). I measured the EWs of selected lines with the code `DAOSPEC` (Stetson & Pancino, 2008) through the wrapper `4DAO` (Mucciarelli, 2013). The lines were selected in order to be unblended and not saturated at the resolution of the GIRAFFE setups. The atomic data for the transitions are from the Kurucz-Castelli linelist [4].
Al abundances were derived using the proprietary code `SALVADOR`, which performs a χ^2 minimization between the observed line and a grid of suitable synthetic spectra calculated on the fly using the code `SYNTHE` (Sbordone et al., 2004; Kurucz, 2005) in which only the Al abundance is varying. Al abundances were derived through spectral synthesis and not via an EW, as I did for Si, because the Al doublet at 7835-7836 Å is contaminated by CN lines. At low metallicities, the impact of CN contamination is negligible; however, as metallicity increases, its impact becomes more pronounced[5]. Since most of the stars in my sample do not have published C and N abundances, I fixed [N/Fe] = +1.5 dex as a reasonable N value (according to Marino et al., 2012b) and treated C as a free parameter to fit the CN affecting

[4] `https://wwwuser.oats.inaf.it/castelli/linelists.html`
[5] I would like to remark that the CN contamination does not affect the Fe, Mg, or Si at any metallicity.

Table 3.2. Abundance ratios for the GIRAFFE targets of ω Centauri. The adopted solar abundances for the measured chemical elements are from Grevesse & Sauval (1998) and they are reported in the header of each element abundance column.

ID	[Fe/H]	[Mg/Fe]	[Al/Fe]	[Si/Fe]
Sun	7.50	7.58	6.47	7.55
48_NDC	-1.92 ± 0.07	0.42 ± 0.04	0.51 ± 0.05	0.29 ± 0.10
74_NDC	-1.93 ± 0.10	0.44 ± 0.03	0.57 ± 0.06	0.41 ± 0.10
84_NDC	-1.57 ± 0.07	...	0.29 ± 0.07	0.48 ± 0.10
161_NDC	-1.74 ± 0.10	0.42 ± 0.02	0.05 ± 0.07	0.26 ± 0.09
182_NDC	-1.53 ± 0.07	0.51 ± 0.05	0.41 ± 0.04	0.34 ± 0.08
357_NDC	-0.97 ± 0.06	...	1.21 ± 0.06	0.41 ± 0.12
480_NDC	-1.02 ± 0.11	...	1.46 ± 0.06	0.44 ± 0.14
27048_J10	-1.59 ± 0.10	-0.07 ± 0.05	1.35 ± 0.05	0.57 ± 0.09
27094_J10	-1.83 ± 0.11	0.44 ± 0.06	0.43 ± 0.08	0.50 ± 0.10
29085_J10	-1.75 ± 0.10	-0.37 ± 0.07	1.16 ± 0.06	0.55 ± 0.10
31041_J10	-1.85 ± 0.10	-0.10 ± 0.05	1.14 ± 0.06	0.61 ± 0.08
31095_J10	-1.75 ± 0.10	-0.27 ± 0.08	1.22 ± 0.06	0.57 ± 0.07
31141_J10	-1.75 ± 0.11	-0.14 ± 0.05	1.10 ± 0.06	0.51 ± 0.08
31152_J10	-1.91 ± 0.11	0.31 ± 0.06	0.67 ± 0.08	0.62 ± 0.08
32169_J10	-1.01 ± 0.10	...	1.14 ± 0.04	0.46 ± 0.12
32171_J10	-1.64 ± 0.09	-0.12 ± 0.05	1.39 ± 0.04	0.62 ± 0.10
33099_J10	-1.31 ± 0.09	0.24 ± 0.05	1.70 ± 0.04	0.49 ± 0.14
33115_J10	-1.44 ± 0.11	0.27 ± 0.07	1.39 ± 0.06	0.64 ± 0.08
34075_J10	-1.65 ± 0.08	0.02 ± 0.04	1.33 ± 0.03	0.49 ± 0.08
34143_J10	-1.19 ± 0.10	0.40 ± 0.06	1.39 ± 0.05	0.51 ± 0.11

Note. — This is a portion of the entire table. This table is available in its entirety in machine-readable form at:
https://vizier.cds.unistra.fr/viz-bin/VizieR?-source=J/A+A/681/A54

the Al doublet. Taking these assumptions into account, [C/Fe] abundance ratios between -0.5 and $+0.3$ dex provide the best fits to the CN lines. Finally, all of the derived abundance ratios were referred to the solar abundances of Grevesse & Sauval (1998).
I followed the same approach described in Sect. 3.2.2.3 to estimate star-to-star uncertainties associated with the chemical abundances. Internal errors, associated with the measurement process, were estimated as the line-to-line scatter divided by the root mean square of the number of lines. For Si, when only one line was available, I calculated the internal error by varying the EW of the lines of $1\sigma_{EW}$ (i.e., the EW error provided by `DAOSPEC`). For Al, I adopted $\sigma/\sqrt{2}$ for all of the stars in which I used both lines, while for the stars in which only one line was available, I estimated the internal error by resorting to a Monte Carlo simulation.
Errors associated with the adopted atmospheric parameters were computed by recalculating chemical abundances, varying only one parameter at a time by its uncertainty and keeping the other parameters fixed to their best value. The uncertainties of the abundance ratios [Al/Fe] and [Si/Fe] were obtained following Equation 3.2.

3.3.3 Results

Depending on the metallicity range, ω Centauri exhibits (anti)correlations with different amplitudes. Given the wide range of metallicities present in the system, it is crucial to analyze the chemical anomalies not only as a whole, but also in distinct metallicity regimes. This approach provides a more comprehensive understanding of the mechanisms underlying the complex chemical patterns observed in ω Centauri.

3.3.3.1 Fe, Mg, Al, and Si abundances

According to the literature, ω Centauri hosts stars covering a broad range of metallicities. The metallicity distribution function (MDF hereafter) that I found in this investigation is shown in Fig. 3.6. In particular, to identify distinct populations in the data, I employed the `scikit-learn`[6] implementation of Gaussian mixture models (GMMs), which allowed me to identify four distinct groups corresponding to the following peaks in [Fe/H]: -1.85, -1.55, -1.15, and -0.80 dex. For comparison, I considered the analyses performed by Johnson & Pilachowski (2010) and Mészáros et al. (2021) in which they studied a total sample of 855 and 1141 stars, respectively, covering the cluster's entire metallicity range. In particular, Johnson & Pilachowski (2010) found the presence of five distinct metallicity peaks that are located at [Fe/H] = -1.75, -1.50, -1.15, -1.05, and -0.75 dex (in their distribution

[6] https://scikit-learn.org/stable/modules/mixture.html

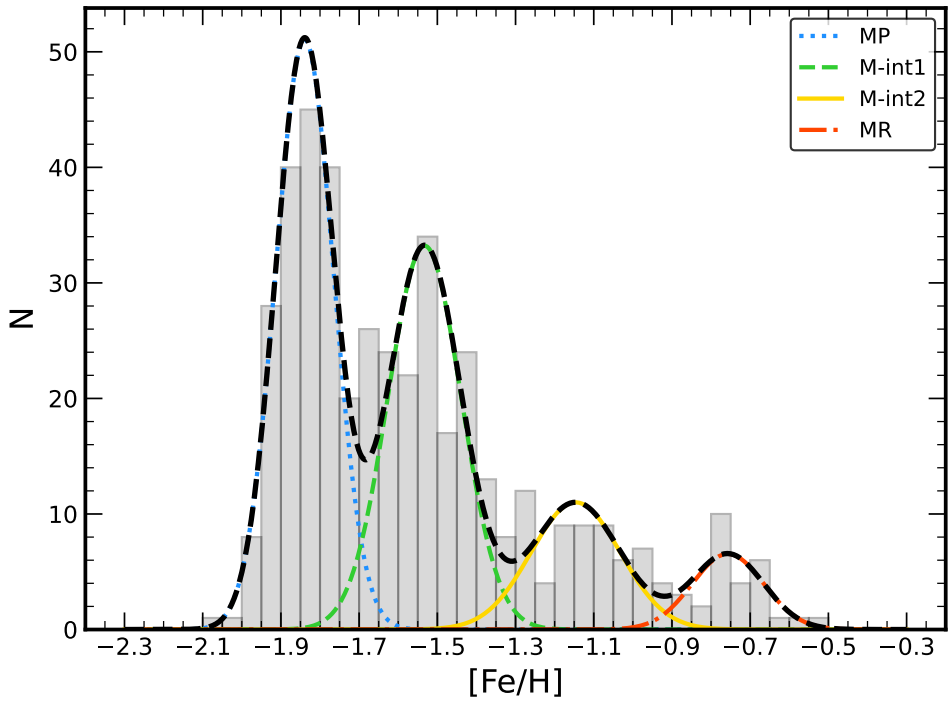

FIGURE 3.6: Histogram displaying the MDF of ω Centauri. Also shown as a dashed black line is the Gaussian kernel fit of the distribution. Four Gaussian components can be identified. They represent the MP, M-int1, M-int2, and MR subpopulations, and are plotted in the Figure as dotted, dashed, solid, and dash-dotted lines, respectively.

the peaks at -1.15 and -1.05 dex were combined due to the difficulty in separating the two populations), while Mészáros et al. (2021) found four peaks at [Fe/H] = -1.65, -1.35, -1.05, and -0.7 dex. The three MDFs exhibit a good agreement with each other, in terms of [Fe/H] extension and the relative position and intensity of the peaks.

With the exception of the peak at -1.15 dex, my measurements of the metallicity peaks are slightly lower (by about 0.05-0.1 dex) compared to those reported by Johnson & Pilachowski (2010). On the other hand, the metallicity peaks in this work are systematically lower by about 0.1-0.2 dex than the ones from Mészáros et al. (2021). These discrepancies are likely to be attributed to the very different method and set of lines used to calculate the metallicities from the H band (Mészáros et al., 2021) and optical spectra.

Finally, following the results obtained from my distribution and a nomenclature similar to the one adopted by Sollima et al. (2005a), I divided the population into the following four subpopulations: metal-poor (MP, [Fe/H]$\leqslant -1.69$ dex), metal-int1 (M-int1, $-1.68 \leqslant$ [Fe/H] $\leqslant -1.34$ dex), metal-int2 (M-int2, $-1.33 \leqslant$ [Fe/H] $\leqslant -0.94$ dex), and metal-rich (MR, [Fe/H]$\geqslant -0.93$ dex). The main information for the four subpopulations is reported in Table 3.3.

Table 3.3. Mean metallicity ⟨[Fe/H]⟩, its associated dispersion (σ), the sample size (N), and number fraction of the four metallicity subpopulations identified in ω Centauri (see text for details).

Group	⟨[Fe/H]⟩ (dex)	σ (dex)	N number	fraction
Metal-poor (MP)	-1.85	0.08	193	0.44
Metal-int1 (M-int1)	-1.55	0.10	153	0.35
Metal-int2 (M-int2)	-1.15	0.13	63	0.14
Metal-rich (MR)	-0.80	0.11	30	0.07

In Fig. 3.7 can be observed the behavior of [Mg/Fe], [Al/Fe], and [Si/Fe] as a function of [Fe/H] for the stars that I analyzed in this work. In the left panel, can be seen that the [Mg/Fe] distribution is split into two different branches, with the upper branch that covers a [Fe/H] range from ~ -2.1 dex up to ~ -1.3 dex and is characterized by enriched values of [Mg/Fe]. On the other hand, the lower branch covers a range of [Fe/H] from ~ -1.9 dex up to ~ -0.5 dex, with Mg abundances ranging from subsolar values up to the highest values [Mg/Fe] $\sim +0.6$ dex at the highest metallicities. For the [Al/Fe] distribution, the behavior is completely different. In the MP subpopulation, there is indeed a large spread in [Al/Fe] with abundances from [Al/Fe] ~ -0.15 dex up to [Al/Fe] $\sim +1.3$ dex. At higher metallicities ([Fe/H] > -1.7 dex), there is the presence of a branch that reaches its maximum extension in the Al abundance at [Fe/H] ~ -1.3 dex and then there is a clear decrease in the Al abundances down to [Al/Fe] $\sim +0.6$ in the MR subpopulation. Finally, a minor group of stars with [Al/Fe] < 0.9 dex is in the M-int1, M-int2, and MR subpopulations. The number of stars in this latter group significantly diminishes at the highest metallicities, with only three stars present in the MR subpopulation. Finally, the behavior of [Si/Fe] as a function of [Fe/H] is bimodal at [Fe/H]< -1.3 dex, even though the separation between the two branches is not so evident (they are separated by ~ 0.2 dex). At higher metallicities, all of the stars are characterized by enhanced [Si/Fe] with a spread fully compatible with the typical uncertainties.

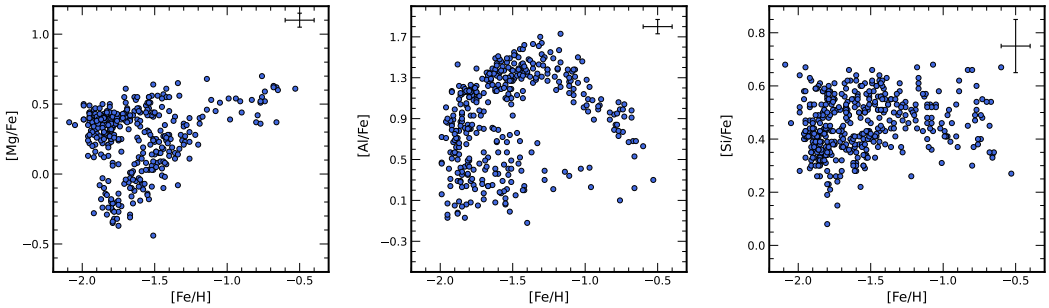

FIGURE 3.7: Distribution of [Mg/Fe] (left panel), [Al/Fe] (middle panel), and [Si/Fe] (right panel) as a function of [Fe/H] for the stars belonging to my sample. The error bar in the top-right corner represents the typical error associated with the measurements.

3.3.3.2 Mg-Al anticorrelation

A large spread is observed in both [Mg/Fe] and [Al/Fe] abundances ratios, with [Mg/Fe] ranging from 0.70 dex down to subsolar values (the minimum abundance value is -0.44 dex) with a mean value [Mg/Fe] $= +0.26$ dex ($\sigma = 0.23$ dex), while [Al/Fe] ranges from $+1.70$ dex down to -0.15 dex with a mean value [Al/Fe] $= +0.93$ dex ($\sigma = 0.44$ dex). For the 323 stars for which both Mg and Al abundances are available, a discrete Mg-Al anticorrelation can be detected, as can be seen in Fig. 3.8. In particular, groups of stars with a different metallicity exhibit different Mg-Al distributions. Especially, the MP and M-int1 subpopulations show a clear Mg-Al anticorrelation (see top panels of Fig. 3.8), whereas the other two subpopulations show a chemical anomaly that is either less clear or not present at all (see bottom panels of Fig. 3.8).

In the 144 stars that make up the MP subpopulation, I recognize the presence of a distinct Mg-Al anticorrelation, with all of the Mg-poor ([Mg/Fe] $<$ 0.0 dex) stars having [Al/Fe] $\sim +1.15$ dex. On the other hand, the Mg-rich stars ([Mg/Fe]$>$ 0.0 dex) are distributed from [Mg/Fe] $\sim$ 0.15 up to [Mg/Fe] $\sim +0.5$ dex and they cover a wide range of [Al/Fe] (from ~ -0.15 up to $\sim +1$ dex). Finally, I observe that the two groups of stars are clearly separated by a sort of gap in [Mg/Fe] between -0.1 and $+0.1$ dex. For the Mg-rich group (112 out of 144 stars), I ran a Spearman correlation test and calculated the correlation coefficient (C_s) and the corresponding two-tailed probability that an absolute value C_s larger than the observed one can be obtained starting from uncorrelated variables, in order to better quantify the amplitude of this anticorrelation. In this instance, I found $C_s = -0.70$, which resulted in zero chance that the observed anticorrelation could have come from uncorrelated data.

A clear Mg-Al anticorrelation is present also in the M-int1 subpopulation (135 stars). Two principal groups of stars can easily be distinguished in this metallicity class, which have similarities with the previous group. The first subgroup has high [Mg/Fe] values (ranging from

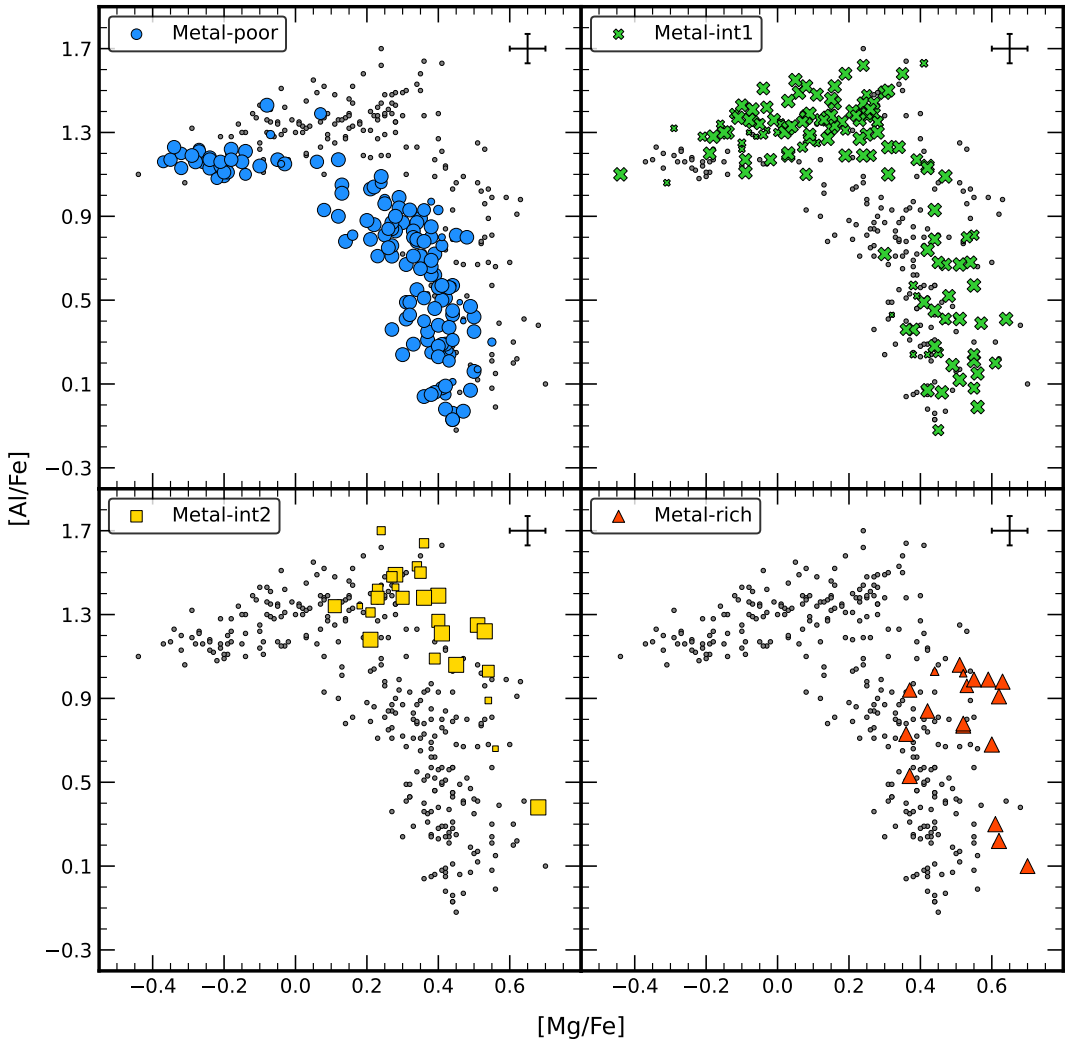

FIGURE 3.8: Trend of [Mg/Fe] as a function of [Al/Fe] for the MP, M-int1, M-int2, and MR subpopulations (from top to bottom, left to right). The size of each point indicates its probability of belonging to that particular metallicity subpopulation – the larger the symbol, the higher the probability – while gray dots represent the entire sample. The error bar in the top-right corner represents the typical measurement error associated with the data.

$\sim +0.4$ to $\sim +0.6$ dex) and a wide range of [Al/Fe] values (from $\sim +0.3$ to $\sim +1.0$ dex). The second group, however, has a smaller range of [Al/Fe] (from $\sim +1.3$ up to $\sim +1.7$ dex) but a wider range of [Mg/Fe] (from $\sim +0.35$ down to ~ -0.2 dex). There are a considerable number of Mg-poor stars in this latter group. The Spearman test was also run in this instance, and the results show that $C_s = -0.60$ and a p value that is consistent with zero. From the top panels of Fig. 3.8, it is clear that all the stars in the Mg-poor group of the MP subpopulation have lower Al abundances ([Al/Fe] ~ 0.2 dex lower) than the stars in the same

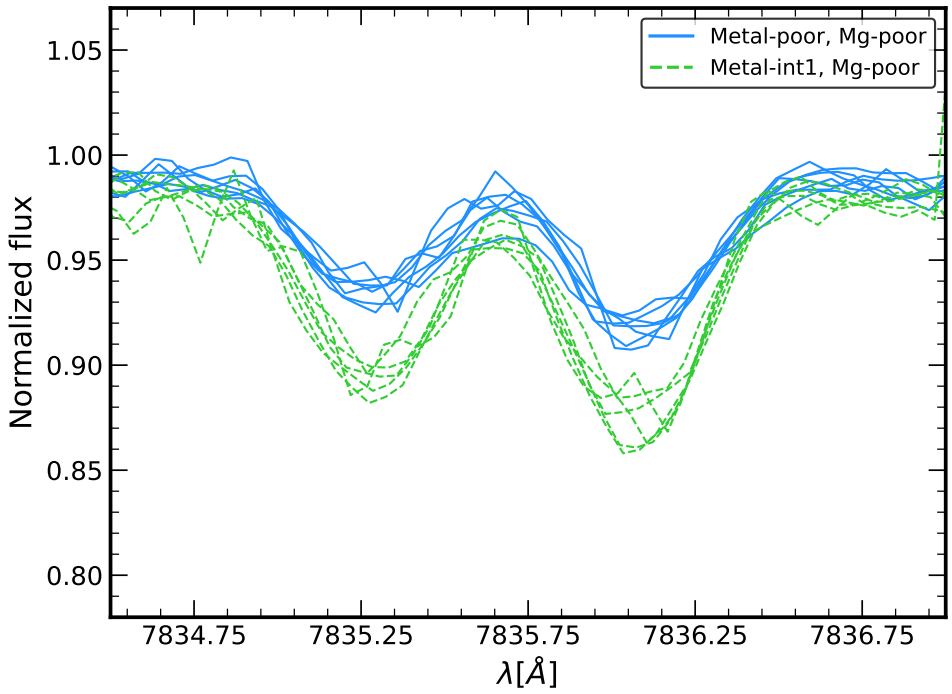

FIGURE 3.9: Spectral region around the Al doublet at 7835-7836 Å for sample stars with similar atmospheric parameters. The solid blue lines denote stars belonging to the Mg-poor group in the MP subpopulation, whereas the dashed green lines represent again Mg-poor stars but in the M-int1 subpopulation. A clear difference in the strength of the Al lines can be appreciated between the two metallicity subgroups.

Mg-poor group belonging to the M-int1 subpopulation. I investigated whether this effect is artificial or not, but neither the stellar parameters nor the evolutionary state were found to be related. Additionally, the spectra of some stars from the MP and M-int1 subpopulations can be seen in Fig. 3.9 around the Al doublet. Even though they are members of different subpopulations, all stars share similar atmospheric parameters and metallicity. In particular, stars were selected to have metallicities between $-1.78 \leqslant$ [Fe/H] $\leqslant -1.69$ dex and $-1.68 \leqslant$ [Fe/H] $\leqslant -1.63$ dex for the MP and the M-int1 subpopulations, respectively. The Figure undoubtedly demonstrates that Al lines are weaker in the Mg-poor stars corresponding to the MP subpopulation.

The existence of the Mg-Al anticorrelation in the 26 stars that make up the M-int2 subpopulation is less certain. The abundances of the stars range from $\sim +0.1$ to $\sim +0.6$ dex for [Mg/Fe] and from $\sim +1$ to $\sim +1.7$ dex for [Al/Fe], with Mg abundances that are between those of the Mg-rich stars in the previous two subpopulations. Only one star stands out among these values, having much lower Al and greater Mg abundances than the other stars in the same group. I cannot determine if there are discrete star groups in this subpopulation.

Finally, for the MR subpopulation (18 stars), there is no evidence of an anticorrelation, with the stars that have [Mg/Fe] $>\sim +0.35$ dex and [Al/Fe] $<\sim +1.1$ dex. This result is not surprising since the presence of the Mg-Al anticorrelation is detected in almost all GCs more metal poor than [Fe/H] $\lesssim -1$ (Shetrone, 1996; Mészáros et al., 2015; Pancino et al., 2017).
In summary, an anticorrelation between the abundance of Mg and Al has been observed in ω Centauri, with the strength of the correlation being dependent on the metallicity of the individual stars being considered. A clear anticorrelation can be detected, in particular, for all stars with [Fe/H] $\lesssim -1.3$ dex. However, for stars in the range between $-1.3 <$ [Fe/H] < -0.9 dex, the anticorrelation is less obvious and, ultimately, for stars more metal-rich than [Fe/H] $\gtrsim -0.9$ dex, there is no sign of the Mg-Al anticorrelation.
Different studies carried out by Norris & Da Costa (1995b), Smith et al. (2000), and Mészáros et al. (2021) found evidence of a significant spread in the Mg and Al abundances in ω Centauri. In particular, Mészáros et al. (2021) found evidence of an extended Mg-Al anticorrelation among the stars with [Fe/H] < -1.2 dex. However, this work represents the first clear detection of a discrete Mg-Al anticorrelation, specifically within the MP and M-int1 subpopulations, with different Mg and Al distributions at different metallicities. Furthermore, 73 % of my stars have [Al/Fe] > 0.5 dex. The existence of a such fraction of stars with high values of Al indicates that the majority of stars in my sample belong to the so-called SG, which was born from material processed in the polluter stars by the MgAl chain at high temperatures (Ventura et al., 2016; Dell'Agli et al., 2018).

3.3.3.3 Mg-Si anticorrelation and Al-Si correlation

For a total of 370 stars, the abundances of Mg and Si were simultaneously measured. With a mean value of +0.45 dex ($\sigma = 0.10$ dex), [Si/Fe] varies from +0.68 dex down to +0.08 dex. A Mg-Si anticorrelation is present in this sample, which is mostly contributed by the population's MP subgroup (see Fig. 3.10). In fact, the Mg-poor and the Mg-rich stars may be clearly distinguished from one another in this subpopulation. The first group is distinguished by a mean value of [Si/Fe] = +0.55 dex, whereas the second group has a mean value of [Si/Fe] +0.35 dex, even if there are certain stars (the minority) with [Si/Fe] $>$ +0.5 dex. In comparison to the Mg-rich group, the Mg-poor group is therefore increased by roughly +0.2 dex, which is significantly larger than the typical error associated with the [Si/Fe] measurements (0.1 dex). It is worth noting that the Si enhancement (Al depletion) in ω Centauri is primarily observed in stars with low Mg abundances, particularly in the most metal-poor population.
I used the Spearman correlation test to examine the Mg-Si anticorrelation in the MP subpopulation, much like I did for the Mg-Al anticorrelation. The results show that $C_s = 0.45$ and

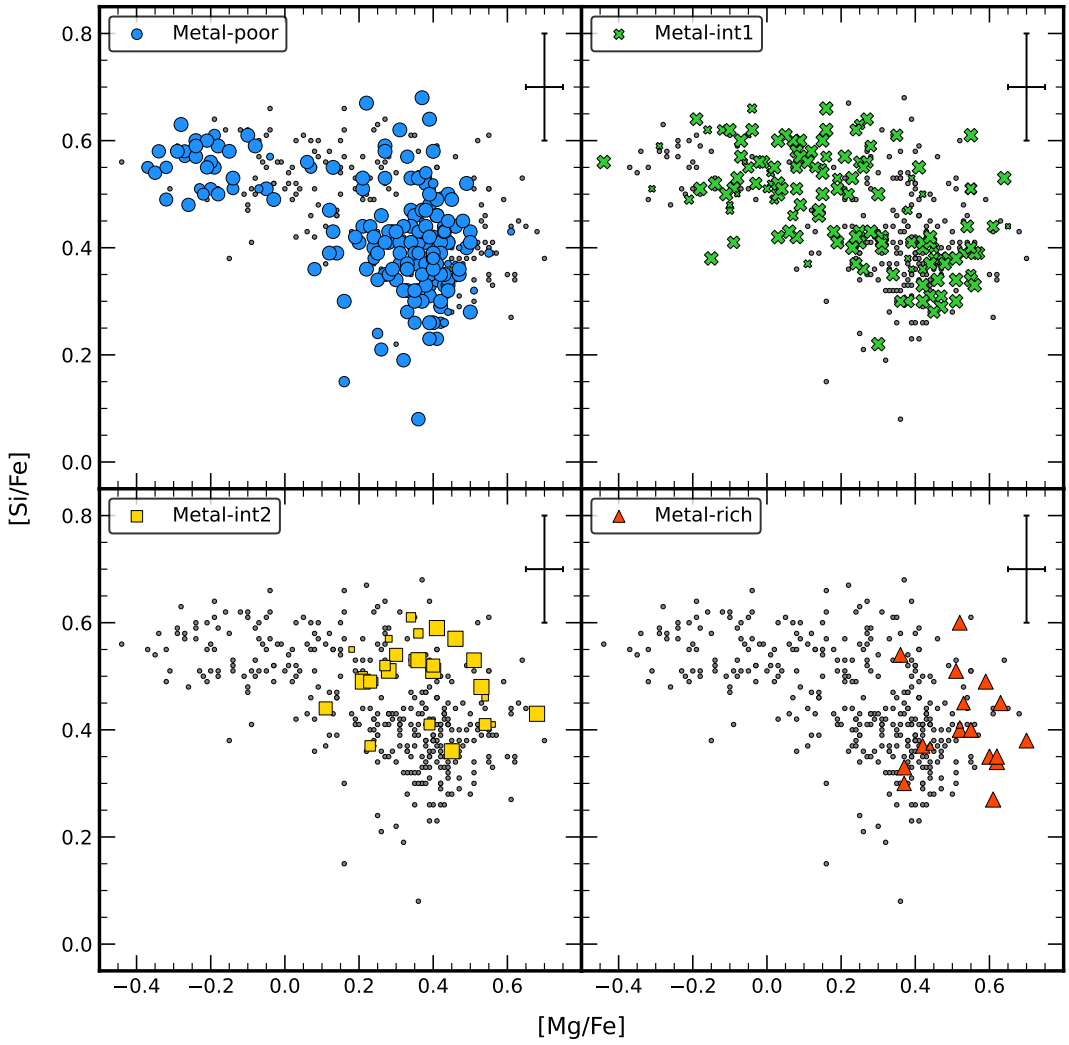

FIGURE 3.10: As for Fig. 3.8, but for [Mg/Fe] and [Si/Fe].

the p value is consistent with zero. This suggests that the presence of a Mg-Si anticorrelation in the MP subpopulation of ω Centauri is real. Besides the MP subpopulation, only the M-int1 subpopulation displays a clear anticorrelation between Mg and Si abundances, despite the challenge of distinguishing between the various subgroups within this population.

An Al-Si correlation is present in ω Centauri, as can be appreciated in Fig. 3.11. In this case, Si and Al are available at the same time for a total of 381 stars. Numerous previous studies have theorized that the Al-Si correlation in GCs is the result of a leakage from the MgAl chain into ^{28}Si via proton capture reaction at extremely high temperatures (e.g., Yong et al., 2005; Mészáros et al., 2015; Masseron et al., 2019).

All of the (anti)correlations associated with the MgAl chain are seen in the MP and M-int1

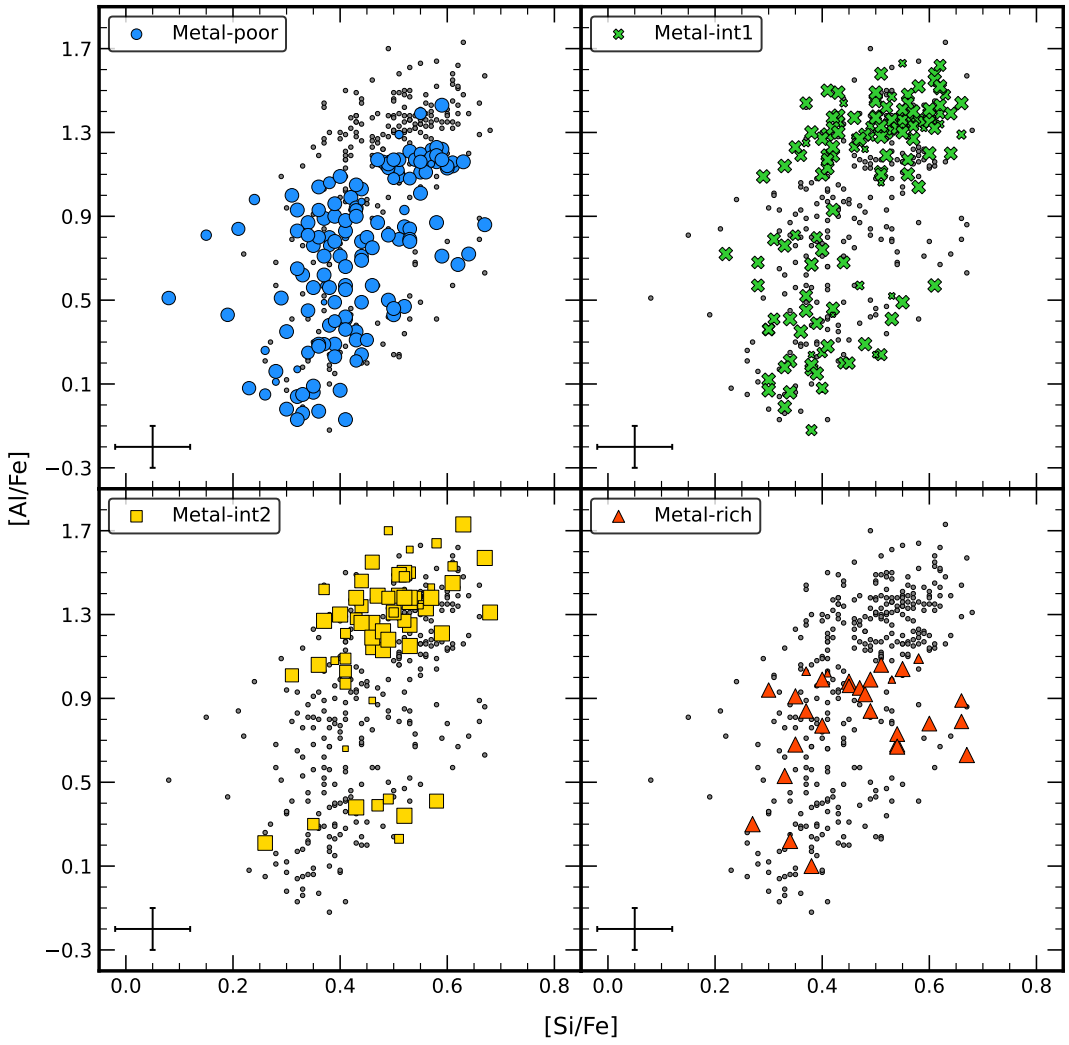

FIGURE 3.11: As for Fig. 3.8, but for [Si/Fe] and [Al/Fe].

subpopulations of ω Centauri when Mg, Al, and Si are analyzed together while taking the various metallicity groups into account. In particular, the Mg-depleted and Al (mildly) enhanced stars, which are assumed to be the product of the extreme MgAl processing in the polluter stars, correspond to the majority of Si-enhanced stars. The proton capture processes in these stars took place at temperatures greater than 10^8 K. Contrarily, only a (weak) Mg-Al anticorrelation is found in the M-int2 subpopulation, whereas the other two anticorrelations are either nonexistent or just weakly confirmed. Finally, there is no indication of any chemical anomaly linked to the MgAl chain in the MR subpopulation. This result is expected given that the polluter stars are unable to attain the temperatures required to begin the Mg destruction through proton capture at those metallicities ([Fe/H] $\gtrsim -0.9$ dex).

3.3.4 Comparison with Mészáros et al. (2021)

A large spectroscopic analysis measuring Mg, Al, and Si abundance variations in ω Centauri was performed by Mészáros et al. (2021). In particular, they studied a total sample of 982 stars with a high SNR (SNR $>$ 70), observed by the SDSS-IV/APOGEE-2 survey (Majewski et al., 2017). Mészáros et al. (2021) found behaviors of the three abundance ratios qualitatively similar to mine. They found a Mg-Al anticorrelation, the shape of which clearly depends on the metallicity of the considered stars (see their Fig. 4). In particular, at high metallicities ([Fe/H] > -1.2 dex), the presence of a Mg-Al anticorrelation is less evident, but with a bimodal distribution in the Al abundances; on the other hand, at the highest values of [Fe/H], the Mg-Al anticorrelation disappears and the Al abundances are nearly constant. These findings are well in agreement with my results and indicate a weakening of the Mg-Al anticorrelation extension toward higher metallicities. Despite the similarities in the morphology, some relevant differences between my results and those by Mészáros et al. (2021) are present (see top panel of Fig. 3.12).

- *Differences in the Mg-Al anticorrelation in the MP subpopulation:* if I consider the MP subpopulation in both samples [7] (see bottom panel of Fig. 3.12), I can observe some interesting differences. In both samples I can detect a clear gap between the Mg-poor and Mg-rich stars. However, at variance with me, in the subgroup of stars with [Mg/Fe] > 0.0 dex, Mészáros et al. (2021) did not detect a clear Mg-Al anticorrelation. They did indeed observe almost a constant [Mg/Fe], with a large spread in [Al/Fe] (from [Al/Fe]~ -0.25 dex up to [Al/Fe] $\sim +1.25$ dex).

- *Discreteness of the Al-rich group:* if I consider the MP and M-int1 subpopulations, I can observe that Al-rich stars are well separated by a gap. To test whether this observed discreteness is real or not, in my sample I considered the most Al-rich stars ([Al/Fe] $> +1.$ dex) in both MP and M-int1 subpopulations, and I measured if they are compatible in having the same Al. I found a mean value [Al/Fe] $= +1.16 \pm 0.01$ dex ($\sigma = 0.08$ dex) for the MP subsample, and [Al/Fe] $= +1.33 \pm 0.01$ dex ($\sigma = 0.11$ dex) for the M-int1 subsample (see Fig. 3.13). These values indicate that these two subsamples are compatible at a level of 8.54 σ, thus strongly suggesting that they do not display the same Al abundances. On the other hand, this discreteness is not observed in the dataset of Mészáros et al. (2021). This difference could be due to my higher precision in the abundance measure that allowed to distinguish different abundance substructures.

[7] I note that Mészáros et al. (2021) define their MP subpopulation at [Fe/H] $\leqslant -1.5$ dex.

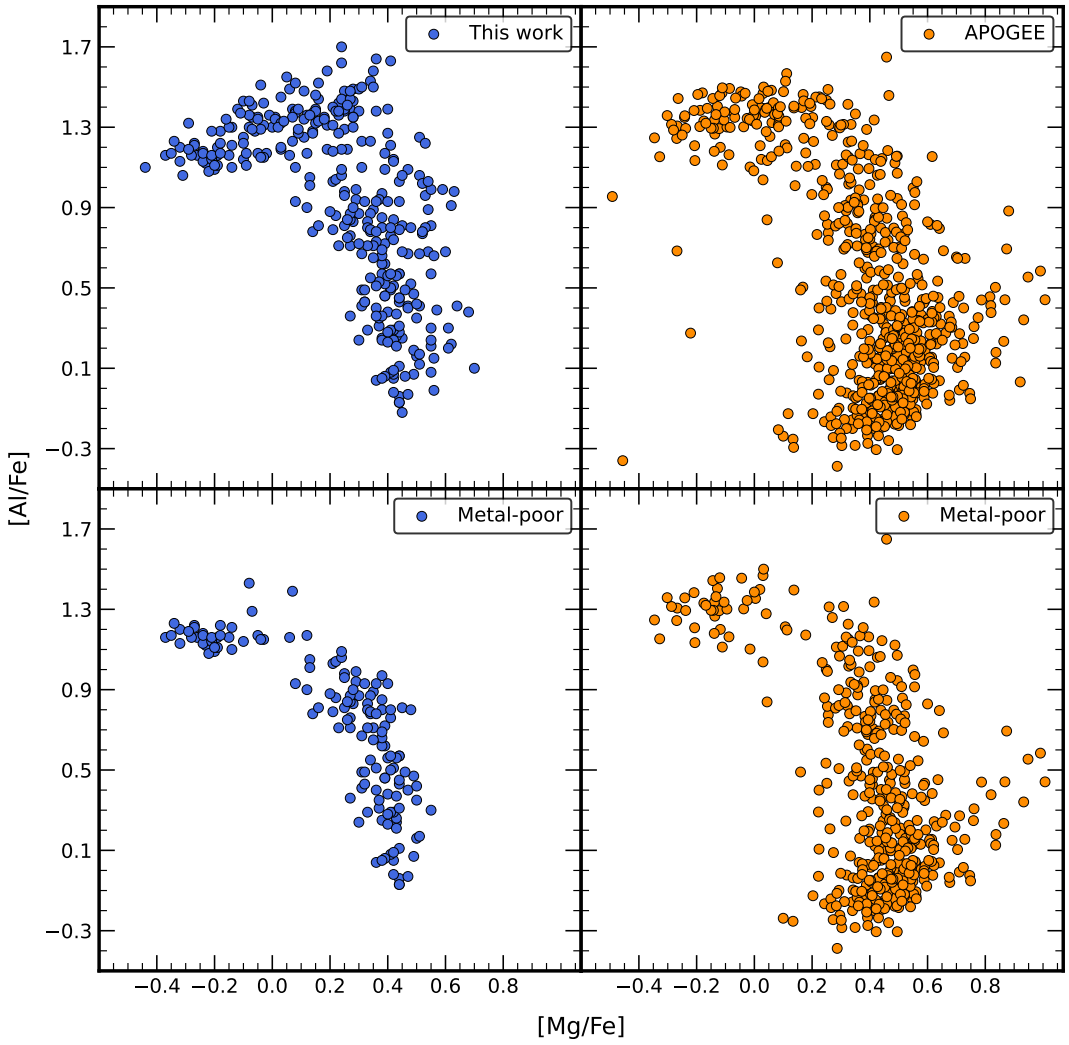

FIGURE 3.12: Trend of [Mg/Fe] as a function of [Al/Fe] for the stars analyzed in this work (top-left panel), and for the stars analyzed by Mészáros et al. (2021) (top-right panel). In the bottom panels, I display only the stars belonging to the MP subpopulation for each sample, respectively.

- *Differences in the SG/FG ratio:* the most striking difference is in the fraction of SG stars sampled by the two studies, with my work having two-thirds of stars belonging to SG, while Mészáros et al. (2021) have only half. I obtained these fractions of SG by performing a population analysis, on both Mg-Al anticorrelations, using the GMM algorithm. I considered the overall distributions on the Mg-Al plane for both anticorrelations, without making any division among the metallicity subpopulations. The aim of this type of analysis was not to uncover the presence of distinct subpopulations within the two distributions, but rather to separate the populations between so-called enriched (with high Al abundances) and primordial (with low Al abundances) stars. In

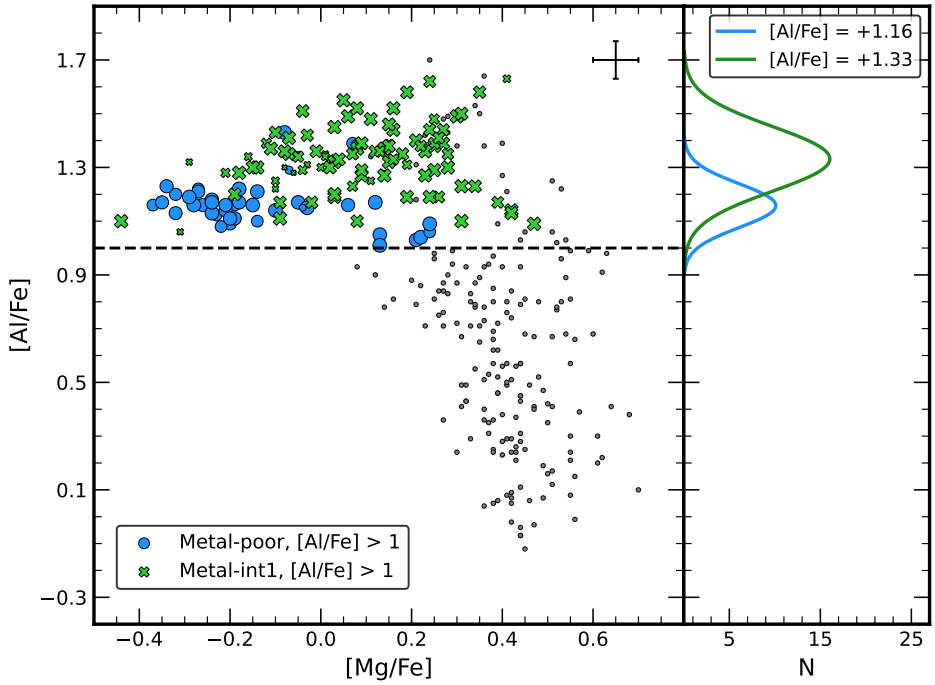

FIGURE 3.13: Trend of [Mg/Fe] as a function of [Al/Fe] for the stars analyzed in this work. The blue dots and the green crosses represent the MP and M-int1 stars with [Al/Fe] $>$ 1 dex, respectively. The gray dots represent the entire sample. The error bar in the top-right corner represents the typical measurement error associated with the data. The dashed line indicates the value [Al/Fe] = 1 dex. The distributions of the two subsamples are shown in the right panel with the corresponding colors.

the case of my Mg-Al anticorrelation, the GMM algorithm revealed that the enriched stars constitute 73% ($\sigma = 6\%$) of the entire population, while for the Mészáros et al. (2021) Mg-Al anticorrelation, the enriched population forms 52% ($\sigma = 3\%$) of the total sample. To further investigate this result, I repeated the GMM analysis at various distances from the cluster center, taking into account the fact that my sample is more radially concentrated relative to the stars analyzed in Mészáros et al. (2021). Specifically, my targets are located at a distance of about 15 core radii, while the stars studied in Mészáros et al. (2021) extend up to 30 core radii (as shown in the right panel of Fig. 3.14).

To investigate the radial distribution of the percentage of enriched stars, I divided my sample into three radial annuli: stars located within 3 core radii (105 stars), stars between 3 and 5 core radii (110 stars), and stars beyond 5 core radii (108 stars). In the case of Mészáros et al. (2021), I examined stars located within 5 core radii (80 stars),

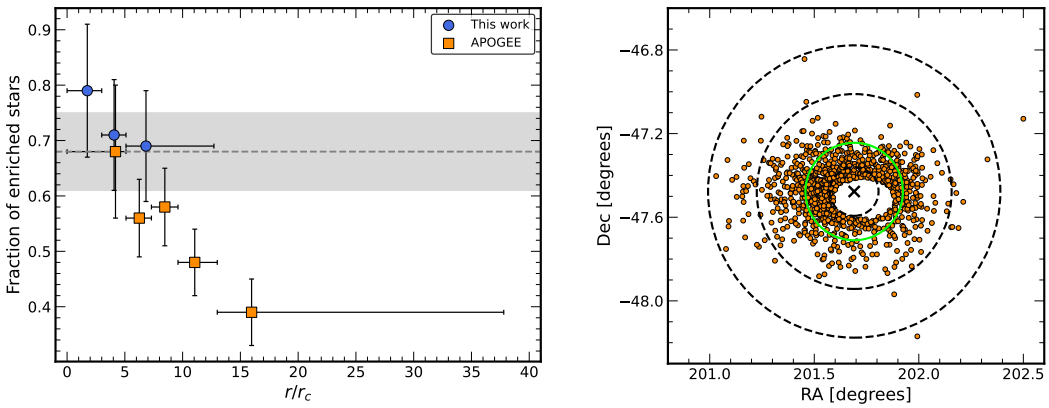

FIGURE 3.14: Left panel: Fraction of the enriched stars as a function of the distance from the cluster center, as defined by van Leeuwen et al. (2000). The blue circles represent the stars analyzed in this work, whereas the orange squares display the stars studied by Mészáros et al. (2021). In the Y axis, the error bars represent the error associated with the fraction of enriched stars, while in the X axis, they represent the extension of the stars contained in each radial ring. The dashed gray line and the gray area show the mean and the standard deviation for the genuine GCs observed so far, respectively (Bastian & Lardo, 2015).
Right panel: Coordinate positions of stars analyzed by Mészáros et al. (2021). The black cross represents the same cluster center used in Fig. 3.2. The dashed black circles show 5, 20, and 30 times the core radius ($r_c = 1.'40$; Harris, 1996). The green circle represents 10 times the core radius and it encloses 554 out of 982 stars.

between 5 and 7.3 core radii (169 stars), between 7.3 and 9.6 core radii (171 stars), between 9.6 and 13.0 core radii (174 stars), and beyond 13.0 core radii (169 stars). In the left panel of Fig. 3.14, can be observed the fraction of enriched stars in both samples. In particular, in the innermost region my value is slightly higher (but within the errors) compared to the mean value observed in other GCs (see Bastian & Lardo, 2015 for a detailed discussion). On the other hand, except for the value within 5 core radii, the fraction of enriched stars found by Mészáros et al. (2021) is constantly below the mean value observed in other GCs, even though in the overlapping regions the two distributions are consistent within the uncertainties. This may be due to the different radial distribution of the two samples, as it is well known that SG stars are more centrally concentrated than FG stars in ω Centauri (as well as in many other clusters; e.g., Bellini et al., 2009; Bastian & Lardo, 2015).

I speculate that the difference in the fraction of enriched stars between Mészáros et al. (2021) and my work may partially explain why the Mg-Al anticorrelation exhibits distinct shapes. Mészáros et al. (2021) did indeed analyze more external regions of ω Centauri, and the higher fraction of FG stars in their sample could potentially contribute to explain the observed differences in the Mg-Al anticorrelation shape.

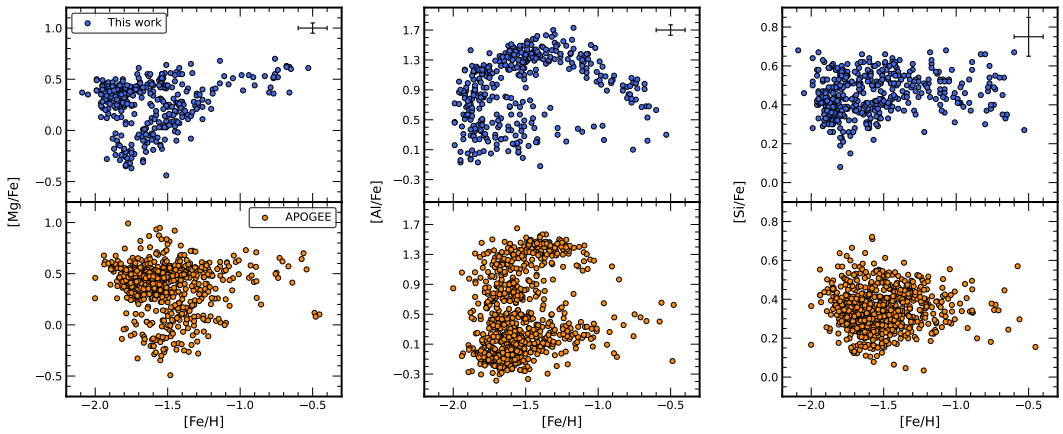

FIGURE 3.15: Distribution of [Mg/Fe] (left panel), [Al/Fe] (middle panel), and [Si/Fe] (right panel) as a function of [Fe/H]. In the top are displayed the stars here analyzed (blue dots), while in the bottom the stars analyzed by Mészáros et al. (2021) (orange dots). The error bar in the top-right corner in the top Figures represents the typical error associated with the measurements.

- *Differences in the behavior with [Fe/H]:* in Fig. 3.15 can be seen a comparison between the stars analyzed here and the ones studied by Mészáros et al. (2021) for the distributions of [Mg/Fe], [Al/Fe], and [Si/Fe] as a function of [Fe/H]. If, on the one hand, there are similar behaviors in all three elements, there are also some interesting differences. In the [Mg/Fe] versus [Fe/H] plane, the presence of the two branches in my sample is clear, while in the case of Mészáros et al. (2021), their presence is barely visible. This effect may be attributed to the predominance of Mg-rich stars in their sample, as well as potential limitations in the measurement accuracy that could prevent a clear separation of the two branches in their analysis. Regarding [Al/Fe], my distribution and the one found by Mészáros et al. (2021) cover a similar range of abundances. However, in the case of Mészáros et al. (2021), the absence of Al-rich stars at [Fe/H] > -1 dex did not allow them to observe if either is present or not a trend in the [Al/Fe] distribution against the metallicity. Moreover, their sample presents a population with [Al/Fe] $<\sim +0.5$ dex that constitutes half of the entire sample (these stars represent the FG stars) and it is distributed at almost every metallicity, with a decrease toward the highest metallicities. Finally, the [Si/Fe] distribution in the case of Mészáros et al. (2021) is characterized by a constant and enhanced [Si/Fe] abundance ratio over the entire range in metallicity, at variance with the bimodality I observe in my sample at [Fe/H] < -1.3 dex. I would like to note that for the stars analyzed by Mészáros et al. (2021), I applied their criteria, limiting the selection only to stars with SNR > 70, $T_{eff} < 5500$ K, and with errors in the single abundances < 0.2 dex. Furthermore, it

is worth mentioning that few stars were observed with [Fe/H] > -1 dex in the [X/Fe] (where X represents Mg, Al, and Si) versus [Fe/H] diagrams.

3.3.5 Discussion and conclusions

In this work, I have investigated the multiple populations of ω Centauri by evaluating the effects of the MgAl cycle in the stars of this system. I derived the Al and Si abundances from the analysis of high-resolution spectra obtained with the multi-object spectrograph VLT/FLAMES, and combined them with the Fe and Mg abundances derived in my previous work (see Sect. 3.2) obtaining a total sample of 439 stars with reliable abundances. Here I summarize the most important findings of the current work:

1. I found a multimodal MDF that is nicely reproduced by the combination of four Gaussian distributions, in good agreement with Johnson & Pilachowski (2010). My sample is dominated by a MP subpopulation that contributes 44% to the total population. The secondary peaks at higher metallicities contribute 35%, 14%, and 7%, respectively.

2. Based on the metallicity distribution, I divided the entire sample into four subpopulations (MP, M-int1, M-int2, and MR), which I used to investigate the strength of the (anti)correlations associated with the MgAl chain. My analysis revealed a clear Mg-Al anticorrelation, with the shape and extension of the correlation varying significantly with the metallicity of the stars being considered. A clear-cut and discrete Mg-Al anticorrelation is present in all stars with a metallicity lower than ~ -1.3 dex, while for higher values of [Fe/H], the anticorrelation is less evident or possibly not present at all.

3. I also detected Mg-Si and Al-Si (anti)correlations, whose extensions vary as a function of the metallicity, and as for the Mg-Al anticorrelation, their presence is evident for the stars with [Fe/H] $\lesssim -1.3$ dex. All of the observed (anti)correlations found here confirm the results found in previous works by Norris & Da Costa (1995b), Smith et al. (2000), and Mészáros et al. (2021). These results constitute a fingerprint of Mg burning at very high temperatures ($\gtrsim 10^8$ K) through the MgAl chain, at least in the MP and M-int1 subpopulations (Ventura et al., 2016).

4. The Mg-Al anticorrelation presents a discrete shape in the MP and M-int1 subpopulations. In particular, in the MP subpopulation, can be noted **(1)** a Mg-Al anticorrelation analogous to the one observed in *genuine* single-metallicity GCs (Mészáros et al., 2015; Pancino et al., 2017), with small variations in Mg abundances (~ 0.3 dex), and almost 1 dex of variation in the Al abundances; **(2)** a distinct component of Mg-poor stars that are all enriched in Al at [Al/Fe] $\sim +1.15$ dex. This kind of subpopulation has been

observed only among the most metal-poor GCs such as M 15, M 92, and NGC 5824 (Masseron et al., 2019; Mucciarelli et al., 2018b), or massive GCs such as NGC 2808 (e.g., Carretta et al., 2018). The Mg-Al anticorrelation in the M-int1 subpopulation is dominated by the most Al-rich stars, with a second group of stars at lower Al values and enhanced in Mg. The Al-rich stars in MP and M-int1 subpopulations are clearly separated by ~ 0.2 dex, with a gap not detected by Mészáros et al. (2021).

5. In the [Al/Fe] versus [Fe/H] plane, can be clearly recognized a trend as a function of the metallicity for the stars with [Al/Fe] $>\sim +0.5$ dex. Is observed that the [Al/Fe] distribution reaches its maximum at [Fe/H] ~ -1.3 dex and then there is a decrease in the Al abundances toward the highest metallicities.

6. By comparing my results with those of Mészáros et al. (2021), can be seen that the fraction of SG stars decreases from the cluster center toward the outer regions. This finding confirms that the formation of SG stars is more prevalent in the central regions of the cluster (see Marino et al., 2012b and references therein). The prevalence of SG stars in my sample can be the key factor at the origin of all the observed differences between my sample and that of Mészáros et al. (2021).

3.3.5.1 ω Centauri as a GC

ω Centauri exhibits the most extensive chemical anomalies associated with the MgAl chain, making it a unique opportunity to impose additional constraints on the potential nature of the polluters responsible for the MPs. The MgAl chain is indeed far more sensitive to temperature than the CNO and NeNa cycles (Ventura et al., 2016). Additionally, the presence of stars enhanced in Al (and Si) and depleted in Mg in the MP and M-int1 components of ω Centauri necessitates the occurrence of proton capture processes at temperatures that cannot be reached in all the polluter stars suggested in the literature.
If the polluters responsible for the observed anticorrelations are AGB and SAGB stars, then the chemical anomalies observed here and the trend of Al abundances with respect to metallicity for stars with [Al/Fe] $> +0.5$ dex can be readily explained. In the metal-poor domain, represented by the MP and M-int1 populations here, the clear Mg-Al trend is due to the strong HBB experienced by low-mass, massive AGB stars, where the ignition of proton-capture nucleosynthesis at temperatures above 10^8 K favors the depletion of the overall Mg in favor of Al (Ventura et al., 2016). In this context, the lower peak value of Al exhibited by MP stars with respect to the M-int1 counterparts is due to the activation of the full MgAlSi nucleosynthesis in the most metal-poor AGBs, with the efficient activation of the ^{27}Al proton capture reaction, which destroys part of the Al synthesized by Mg burning (Dell'Agli et al.,

2018). This understanding is confirmed by the Mg-Si and Al-Si trends detected in MP stars. In the M-int2 subpopulation, the Mg spread is shorter than in the MP and M-int1 subpopulations, since the HBB temperatures experienced by AGB stars of metallicity [Fe/H] ~ -1 are not sufficiently hot to favor an extended destruction of the Mg. The lack of a Mg-Si anticorrelation in this subpopulation is a signature of the inefficiency of the advanced MgAl chain reaction $^{26}\mathrm{Al}(p,\gamma)^{27}\mathrm{Si}(e^-,\nu)^{27}\mathrm{Al}(p,\gamma)^{28}\mathrm{Si}$ at high metallicities. High metallicities do indeed prohibit an efficient Si production. Finally, the short extension of the Mg-Al trend shown by the most metal-rich stars witnesses the action of proton-capture reactions by the two least abundant ^{25}Mg and ^{26}Mg isotopes, whereas the HBB temperatures at these metallicities are not sufficiently hot to activate the proton capture process efficiently by the most abundant ^{24}Mg isotope: the overall Mg spread is narrow in this case. Therefore, my work shows for the first time the presence in ω Centauri of the two channels of Al production and destruction (Ventura et al., 2013; Dell'Agli et al., 2018). In conclusion, at [Fe/H]$\lesssim -1.3$ dex, the Al production channel is always activated, with the destruction channel that becomes significant at the lowest metallicities. On the other hand, at [Fe/H] $\gtrsim -1.3$ dex, the Al production channel weakens as the metallicity increases, while the destruction channel is not present at all since there is no Si production through Al burning.

While the AGB model appears to qualitatively account for observed chemical anomalies, it is important to note that different levels of dilution of the AGB ejecta with pristine gas are required to reproduce the observed (anti)correlations (Dell'Agli et al., 2018). Based on their Mg and Al abundance values, SG stars with less extreme compositions may have formed from AGB ejecta mixed with up to 70% pristine gas, whereas the most extreme populations (characterized by heavy Mg depletion and Al enhancement) may have formed from AGB gas with either very limited or no dilution with pristine material. However, the precise physics and timing of the dilution process during the early evolution of the cluster remain unknown and can possibly require some degree of fine tuning.

FRMS (Krause et al., 2013) or interacting binaries (de Mink et al., 2009) are among the polluter candidates since they are able to activate the CNO cycle and the secondary chains, but they require very high masses (of the order of $\sim$ 100 $M_\odot$ or above) and some adjustment of the reaction rates in order to reproduce the observed Mg-Al anticorrelations in GCs (Prantzos et al., 2017). Supermassive stars ($> 10^3$ $M_\odot$; Denissenkov & Hartwick, 2014) have central temperatures high enough at the beginning of the main sequence to allow the simultaneous burning of He, Na, and Mg. Moreover, the models show that in these stars Si can be produced, but at temperatures where Mg is heavily destroyed. This is in contrast with what I find in ω Centauri. Also novae were suggested as polluters (Maccarone & Zurek, 2012; Denissenkov et al., 2014). The fundamental issue with stars of this type is that all the light elements that

are enhanced in SG stars (Na, Al, and Si) are regularly overproduced in quantities that are significantly greater than the reported levels. However, as nova outbursts are multiparameter phenomena, more research on the parameter space is required to determine the precise amount of light elements ejected by these stars into the intracluster medium.
Even though many different scenarios have been proposed up to this point, none of them are fully free from serious flaws (e.g., Renzini et al., 2015; Renzini et al., 2022; Bastian & Lardo, 2018, Milone & Marino, 2022). In particular, all of the self-enrichment models cannot explain that SG stars generally outnumber their FG counterparts (see Sect. 1.5 for a detailed discussion).
The available chemical evidence suggests that the ω Centauri chemical enrichment history was very complex and influenced by a simultaneous contribution of core-collapse SNe, as demonstrated by the observed spread in Fe, enhanced [α/Fe] ratios, and high [Na/Fe] and [Al/Fe] abundances (see Johnson & Pilachowski, 2010 and references therein), and likely AGB stars, which are responsible for the observed light-element variations. In contrast to regular (non nucleated) galaxies or *genuine* GCs, the ω Centauri chemical history has been controlled by its ability to retain both high- and low-velocity ejecta.

3.3.5.2 ω Centauri as a nuclear remnant

In the above discussion, I have considered my results in the perspective of the origin of the MPs in GCs (Gratton et al., 2012; Bastian & Lardo, 2018; Gratton et al., 2019), exploiting the constraints provided by the extreme chemical manifestations of this syndrome that are observed to occur in ω Centauri. I have also made some attempt to interpret general trends within the entire sample assuming that they are produced by a single chemical evolution path, driven by self-enrichment. However, the latter is just a hypothesis, since, depending on the actual nature of the system, other kinds of processes may have been involved in the origin of the present-day status of ω Centauri. In this section, I want to reconsider the observational scenario from a different perspective.
The idea that ω Centauri can be the nuclear remnant of a dwarf galaxy whose main body was completely disrupted by the interaction with the Milky Way dates back decades and was the subject of extensive literature (see, e.g., Gnedin et al., 2002; Bekki & Freeman, 2003; Bekki & Tsujimoto, 2019, and references therein). The strict analogy with the stellar nucleus of the currently disrupting Sgr dSph galaxy was firstly noted and discussed by Bellazzini et al. (2008) and Carretta et al. (2010c). In recent times the possible association of ω Centauri with a specific dwarf accretion event, Gaia-Sausage-Enceladus (GSE Helmi et al., 2018; Belokurov et al., 2014), lent further support to this hypothesis (Myeong et al., 2018; Massari et al., 2019; Limberg et al., 2022).

There is general consensus that the (widely diffused, see, e.g., Böker et al., 2004) stellar nuclei are formed by the spiral-in to the center of the host galaxy of massive star clusters, by dynamical friction, and/or by central in situ star formation, with the first channel possibly being the preferred one in M$\lesssim 10^9$ M$_\odot$ galaxies (Neumayer et al., 2020, and references therein). Such a multiple-channel formation path can greatly help in accounting for the extremely complex abundance patterns observed in ω Centauri.
In this context, I want to highlight two facts that emerge particularly clearly from my analysis and that suggest that the system may indeed be a nuclear remnant that was built up by the merging of GCs plus in situ star formation at the center of the (now disrupted) progenitor dwarf galaxy (see also Ibata et al., 2019a, 2021):

- The MDF is clearly multimodal, with the strongest peak being the most MP one. This is at odds with what is observed in local dwarfs (Kirby et al., 2011; Hasselquist et al., 2021). In these sites, where the buildup of the MDF should be dominated by the chemical evolution of a self-enriching stellar system embedded in a dark matter halo, MDFs typically have a very clean single mode toward the metal-rich side of the distribution plus an extended metal-poor tail. It is interesting to note that this is also true for the Sgr dSph when the MDF is sampled outside the nucleus (Mucciarelli et al., 2017; Minelli et al., 2021), while strong bi-modality emerges in the nuclear region (Bellazzini et al., 2008; Mucciarelli et al., 2017; Alfaro-Cuello et al., 2019, 2020).

- If I consider the different subgroups as classified by the GMM described in Sect. 3.3.3.1, I can infer the intrinsic metallicity dispersion with the maximum likelihood analysis described in Mucciarelli et al. (2012), following Pryor & Meylan (1993) and Walker et al. (2006). Doing this, I obtain mean metallicities of the various components in excellent agreement with the results of the GMM, and the intrinsic metallicity dispersions (σ_{int}) and the associated uncertainties reported in Table 3.4. It is very interesting to note that both the MP and the M-int1 components are fully consistent with null dispersion, that is, the most likely outcome of the analysis, with tiny uncertainty. Null or very small metallicity dispersion is a defining characteristic of GCs (Willman & Strader, 2012; Gratton et al., 2019). On the other hand, the M-int2 metallicity distribution is strongly incompatible with zero dispersion and nothing relevant can be said on the MR population as the uncertainty on σ_{int} is huge.

Taken at face value, these results suggest that ω Centauri may indeed be the nuclear remnant of a dwarf galaxy that was originally built up by the merging of two massive metal-poor GCs (both more massive than 10^6 M$_\odot$, according to Table 3.3 and the total mass by Baumgardt & Hilker, 2018, M $= (3.94 \pm 0.02) \times 10^6$ M$_\odot$), with each one displaying its own extended

Table 3.4. Intrinsic metallicity dispersion of the four subpopulations.

Group	σ_{int} [dex]
MP	0.00 ± 0.01
M-int1	0.00 ± 0.02
M-int2	0.08 ± 0.01
MR	0.00 ± 0.17

light elements' anticorrelations typical of GCs in this mass regime, plus some more metal-rich components, with significant metallicity dispersion, possibly formed in situ, similar to the case of the nucleus of Sgr dSph (Carretta et al., 2010b,c; Alfaro-Cuello et al., 2019, 2020). It is important to keep in mind that the reliability of the results reported in Table 3.4 depends on the accuracy of the errors on the individual [Fe/H] estimates, which is notoriously difficult to assess properly. However, there is little doubt that the intrinsic metallicity dispersion observed in my MP and M-int1 samples, if not null, is very small and compatible with that observed in other massive GCs (Carretta et al., 2010c,d; Lardo et al., 2023), and hence the hypothesis that they trace the population of ancient GCs that merged at the center of the progenitor dwarf galaxy to build the backbone of its stellar nucleus appears sustainable in any case.

It may be legitimate to ask oneself the reason why the possibility that the M-int1 and, in particular, the MP components can be single-metallicity populations has not emerged so clearly in previous studies. The comparisons between the distribution in various chemical planes suggest that my set of measures has a higher precision than comparable samples by other authors, allowing us to gain deeper insight into the trends and distributions in these planes (see, e.g., Fig. 3.15). As a quantitative test in this sense, I considered the subsamples of MP stars in common with Johnson & Pilachowski (2010, 170 stars) and with Mészáros et al. (2021, 70 stars). Since I was dealing with exactly the same set of stars, the intrinsic metallicity dispersion σ_{int} was fixed. I can compute the observed metallicity dispersion σ_{oss}, in the very reasonable hypothesis of Gaussian distribution, as $\sigma^2_{oss} = \sigma^2_{int} + \sigma^2_{err}$, where σ_{err} is the contribution of the measuring error that is different from the set of measures (mine) to set of measures (Johnson & Pilachowski, 2010 and Mészáros et al., 2021). The one having the largest

σ_{oss} necessarily also has the largest σ_{err}, and hence lower precision. For the MP stars in common with Johnson & Pilachowski (2010), I obtained $\sigma_{oss} = 0.077$ dex from my measures and $\sigma_{oss} = 0.137$ dex from their measures. For the MP stars in common with Mészáros et al. (2021), I obtained $\sigma_{oss} = 0.085$ dex from my measures and $\sigma_{oss} = 0.103$ dex from their measures. Therefore, at least for the considered samples, in both cases my [Fe/H] measures are significantly more precise than theirs. This is clearly a factor enhancing the capability to disentangle the various components of the overall MDF and to properly estimate their metallicity dispersion. The differences in the spatial distribution of the various samples may also play a role since the different components may have different radial distributions (Bellini et al., 2009; Johnson & Pilachowski, 2010) and as my sample is more centrally concentrated than those by Johnson & Pilachowski (2010) and, especially, by Mészáros et al. (2021).
In summary, the scenario outlined above seems to deserve a more thorough and deeper dedicated analysis, taking into account also different aspects of the problem not considered here, such as the age distribution and the kinematics of the various components. This is clearly beyond the scope of the present work and I postpone it to a future contribution.

3.4 The peculiar case of a K-rich star in ω Centauri

In Sect. 3.2.3.2 I described the peculiar star 43241_J10, which from the analysis of its GIRAFFE spectrum was found to have [K/Fe] = +1.60 dex, that is $\sim$ 1 dex higher than the abundances of the other stars of ω Centauri with similar parameters and abundances. Such high [K/Fe] is found only among the stars of NGC 2419, the GC with the most extended Mg-K anticorrelation.
Within the scenario where the K over-abundance is produced by AGB stars, as the result of the extreme burning of the MgAl chain, I can envisage two possible explanations: **(1)** this star formed directly from the pure ejecta of AGB and SAGB stars before that the dilution process with pristine gas occurs. This scheme was proposed by Ventura et al. (2012) to explain the huge [K/Fe] enhancement observed in the Mg-poor stars of NGC 2419. I discussed this possibility in Sect. 3.2.4. **(2)** this star was a member of a binary system together with a massive star and accreted K-rich material from the companion when the latter reached the AGB phase. In this case, the abundance that I measured is not its original one but reflects the chemical composition of the interior of the companion. To test the proposed scenarios I obtained new spectra at the VLT/ESO, which will allow to measure elements involved in the proton-capture reactions (i.e. C, N, O, Na, etc.), and to obtain a new epoch RV to establish whether the star is member of a binary system or not. Unfortunately, the spectra of this star available in the ESO archive allow us to measure only a limited number of elements (Fe, Na, Mg, Al, Si, and K) and one epoch RV preventing to establish its possible binary nature. If this star formed from the pure ejecta of a AGB star I should expect to measure also anomalous abundances of C, N and O, compared to other metal-poor *"normal"* ω Centauri stars. The same should happen if this stars formed from a mass transfer process from an AGB companion.

3.4.1 Observations

43241_J10 was observed with the high resolution UVES spectrograph (Dekker et al., 2000). The star was observed under the ESO program 109.23C2 (P.I. Mucciarelli) during the night 2022 April 06. In order to provide a complete screening over the entire optical range for the target star, I used the UVES spectrograph in the dichroic mode with different setup combinations: one exposure of 1800 s with dichroic 1 Blue Arm 346 CD#1 + Red Arm 564 CD#3, one exposure of 1800 s with dichroic 2 Blue Arm 346 CD#1 + Red Arm 760 CD#4, and one exposure of 600 s with dichroic 2 Blue Arm 390 CD#2 + Red Arm 860 CD#4. All observations were made with the 1-arcsec slit which provides a resolving power of $\sim$ 40000.

The full wavelength coverage is $\sim 3200 - 10500$ Å. However, I used the spectra in the range of $\sim 3800 - 9000$ Å because in the bluest part of the spectra the SNR is too low, while in the reddest part the spectra are heavily contaminated by telluric absorptions. The UVES spectra were reduced using the dedicated UVES ESO pipeline[8], which includes bias subtraction, flat field correction, wavelength calibration and spectral extraction.

3.4.2 Radial velocity measurements

The RV for each spectrum was determined through the standard method of cross-correlation, as implemented in the `Python` module `PyAstronomy`. In order to measure RV I cross-correlated each UVES spectrum with an appropriate synthetic template spectrum calculated with the `SYNTHE` code (Sbordone et al., 2004; Kurucz, 2005), adopting the stellar parameters derived in Sect. 3.2.2.1 and convoluted with a Gaussian profile to reproduce the observed line broadening. The final RV was calculated as the mean of the individual RV values, and the uncertainty as the dispersion of the mean RV normalized to the root mean square of the number of exposures used.

As a sanity check, I checked the accuracy of the wavelength scale for all the spectra by measuring the position of some sky emission lines or by cross-correlating some absorption telluric lines against a synthetic spectrum of the Earth atmosphere calculated with TAPAS (Bertaux et al., 2014). All these velocities shifts are compatible with zero within the uncertainties.

The target star 43241_J10 shows a RV difference of ~ 7 km s^{-1} between the GIRAFFE and UVES. Indeed, from the GIRAFFE spectra I obtained RV 220.26 ± 0.18 km s^{-1}, while from the UVES spectra RV $= 227.12 \pm 0.07$ km s^{-1}. This difference is much higher than the uncertainties associated with the RV measurements, indicating a real RV variation of this star.

Gaia DR3 (Gaia Collaboration et al., 2016, 2023) provides a RV value of 223.83 ± 2.37 km s^{-1}. This value is compatible within $\approx 1.5\sigma$ with my measures. Finally, from the SDSS-IV/APOGEE-2 survey (Majewski et al., 2017), for 43241_J10 is reported a RV value equal to 222.55 ± 0.06 km s^{-1}.

The RUWE value provided by *Gaia* DR3 is 1.15, indicating a well-behaved single star astrometric solution (but not excluding the case of a wide binary).

[8] https://www.eso.org/sci/software/pipelines/uves/

3.4.3 Photometric variability of 43241_J10

Lebzelter & Wood (2016) classified 43241_J10 as a Long Period Variable (LPV), with a variability period of 71 days. In particular, Lebzelter & Wood (2016) used the *V* band to study the light curve of 43241_J10 and derived its period. This value is perfectly in agreement with the variability period of 69.8 days given by the *Gaia* DR3 data.
Since I used the photometric information coming from *Gaia* eDR3 to derive the atmospheric parameters, I investigated the impact of the magnitude variations in the determination of the color $(BP - RP)$. In Fig. 3.16 can be observed the *Gaia* light curves for the target. From the light curves of BP and RP bands I determined the $(BP - RP)$ color at different epochs and calculated the variation in color with respect to the color I used to determine the temperature for 43241_J10. These color variations affect temperature determination at level lower than $\sim \pm 50$ K. Such kind of temperature variations have an overall impact on the abundance determination of about 0.05 dex or less. Moreover, since the light curves of the BP and RP bands have the same behavior, with the maxima and minima located at the same epochs, the errors in the abundance determinations generated by the temperature variations can be considered as a systematic errors and not as internal.

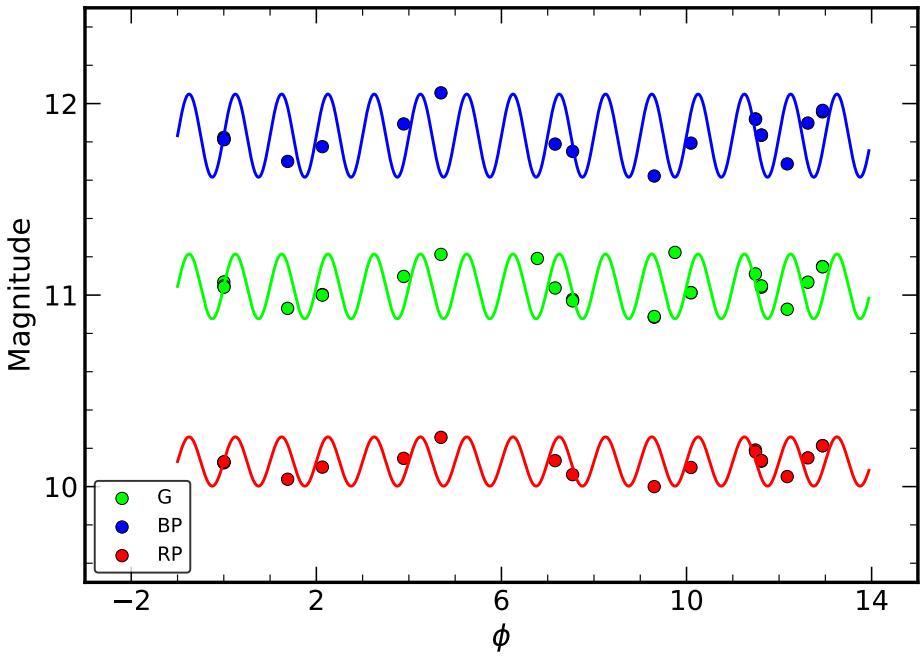

FIGURE 3.16: G, BP, and RP light curves of 43241_J10. It can be noted that the light curves have the same behavior for the three magnitudes.

Table 3.5. Chemical abundances of 43241_J10 from the UVES spectra.

Ion	Abundance [dex]
[Fe/H]	-1.82 ± 0.08
[C/Fe]	-0.93 ± 0.10
[N/Fe]	0.99 ± 0.10
[O/Fe]	-0.39 ± 0.10
[Na/Fe]	0.29 ± 0.04
[Mg/Fe]	-0.30 ± 0.04
[Al/Fe]	1.20 ± 0.05
[Si/Fe]	0.50 ± 0.09
[K/Fe]	0.62 ± 0.10
[Ca/Fe]	0.57 ± 0.04
[Sc II/Fe]	0.26 ± 0.12
[Ti/Fe]	0.56 ± 0.10
[V/Fe]	0.38 ± 0.11
[Cr/Fe]	0.17 ± 0.07
[Mn/Fe]	-0.20 ± 0.06
[Co/Fe]	0.19 ± 0.05
[Ni/Fe]	-0.17 ± 0.04
[Cu/Fe]	-0.35 ± 0.05
[Zn/Fe]	-0.15 ± 0.15
[Y II/Fe]	-0.06 ± 0.11
[Zr/Fe]	0.65 ± 0.14
[Ba II/Fe]	0.24 ± 0.13
[La II/Fe]	0.12 ± 0.10
[Ce II/Fe]	0.11 ± 0.10
[Pr II/Fe]	-0.20 ± 0.11
[Nd II/Fe]	0.19 ± 0.09
[Eu II/Fe]	0.23 ± 0.12

3.4.4 Chemical analysis

In this study I measured abundances in 43241_J10 for a total of 27 elements, including Fe, C, N, O, α- (Mg, Si, Ca, Ti), light- (Na, Al, K), iron-peak (Sc, V, Cr, Mn, Co, Ni, Cu, Zn), and neutron-capture (Y, Zr, Ba, La, Ce, Pr, Nd, Eu) elements. The derived abundances together with the associated errors are reported in Table 3.5.

To derive the abundances I performed a linelist selection over the entire optical range, by selecting lines that were unblended, not saturated, and not contaminated by telluric lines at the resolution of UVES. The atomic data for the selected lines come from the Kurucz-Castelli

linelist database[9].
I derived the abundances by using the proprietary code SALVADOR, as already described in Sect. 3.3.2. For all the abundances I adopted the solar reference from Grevesse & Sauval (1998), except for the O, where I used the solar reference from Caffau et al. (2011).

3.4.5 Results

3.4.5.1 Chromospheric diagnostics

I checked for evidence of chromospheric activity in 43241_J10, considering the classical spectral chromospheric diagnostics, i.e. H_α, H and K Ca II, Na I D lines, Ca II triplet lines (see e.g., Linsky, 2017; Carlsson et al., 2019; Hall, 2008).
In the spectra of 43241_J10 I detected emissions in the core of H and K Ca II lines at 3968.17 Å and 3933.66 Å, as can be seen in Fig. 3.17. The presence of such emission peaks in the core of Ca II lines are a good diagnostic of active chromospheres in these stars, because H and K are lines collisionally excited by electrons from the ground state (see, for example, Linsky, 2017; Carlsson et al., 2019).
The H_α Balmer line of 43241_J10 exhibits strong emissions in the wings, while the core of the line does not show signature of emission, as can be seen in fig. 3.17. This line profile is usually interpreted as the result of a optically thick chromosphere (no core emission) but with the escape of photons shifted in wavelength by anelastic diffusion processes (Dupree et al., 1984; Cacciari et al., 2004). Similar H_α line profiles are usually observed among the brightest giant stars in GCs (Cacciari et al., 2004; Meszaros et al., 2008; Mészáros et al., 2009) indicating the presence of inflow/outflow of chromospheric material.
Coreshifts and asymmetries in the chromospheric line profiles indicate outflows and inflows of material in the chromosphere. I detected in the UVES spectra of 43241_J10 coreshifts of -8.6, -5.0 and -6 km s^{-1} for Na D, H_α and Ca II triplet, respectively, indicating a slow outward motion. These coreshifts are much smaller than the escape velocity from the stellar surface ($\sim$50-60 km s^{-1}), and fully compatible with those measured in metal-poor giants stars of similar luminosities (Smith & Dupree, 1988; Bates et al., 1990, 1993; Dupree et al., 1994; Cacciari et al., 2004).
The presence of chromospheric activity in the target star 43241_J10 is not unexpected, because the majority of the stars brighter than $\log(L/L_\odot) \approx 2.7$ show the presence of active chromospheres (Mallia & Pagel, 1981; Cacciari & Freeman, 1983; Gratton et al., 1984; Cacciari et al., 2004; Meszaros et al., 2008) and this giant star in ω Centauri has $\log(L/L_\odot) = 3.22$.

[9] https://wwwuser.oats.inaf.it/castelli/linelists.html

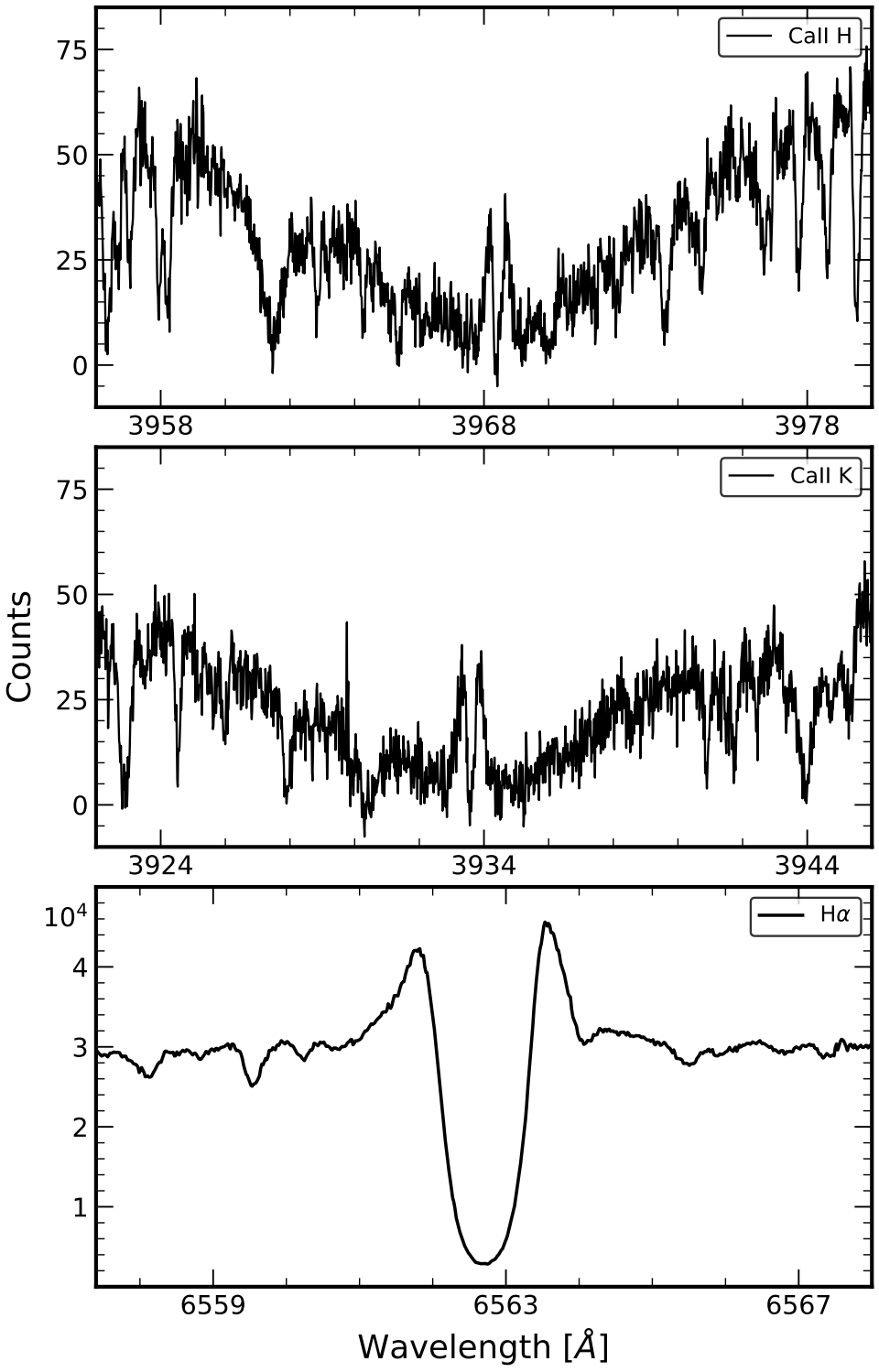

FIGURE 3.17: Portions of the UVES spectra for 43241_J10 around the H and K Ca II lines, and Hα line.

3.4.5.2 Abundance ratios

From the analysis of the new set of high resolution spectra I derived [Fe/H] $= -1.82 \pm 0.08$ for 43241_J10 from the UVES spectra. This value of [Fe/H] is in excellent agreement with the metallicity derived from the GIRAFFE spectra ([Fe/H] $= -1.86 \pm 0.08$ dex. The differences in [Fe/H] between GIRAFFE and UVES spectra can be seen in Fig. 3.18.
Regarding all the other elements, with the exception K that I will discuss in Sect. 3.4.5.3, 43241_J10 does not show any *"anomalous"* abundance ratio. Indeed, all the derived abundances are compatible with the abundances of ω Centauri at similar metallicity and with similar parameters (Johnson & Pilachowski, 2010; D'Orazi et al., 2011; Marino et al., 2011c, 2012b).

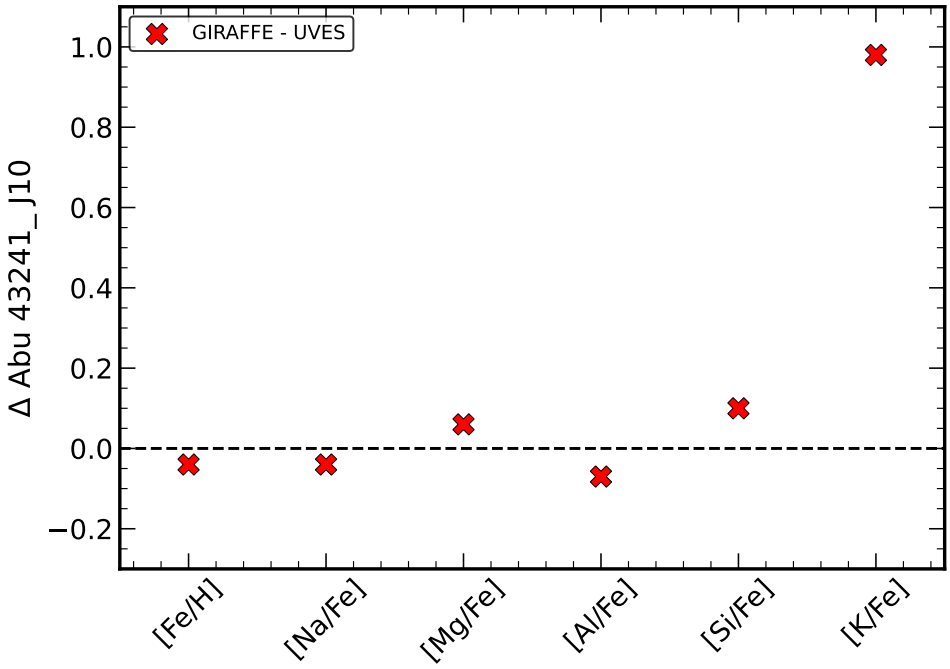

FIGURE 3.18: Differences of the abundances between GIRAFFE and UVES spectra are represented as red crosses.

3.4.5.3 Potassium

I derived K in the UVES spectra from the same K I resonance line located at 7699 Å, as already done for the GIRAFFE spectra. I applied the same NLTE corrections from the grid by Reggiani et al. (2019).
The K abundance derived from GIRAFFE and UVES spectra differs significantly (see Fig. 3.18). Indeed, the GIRAFFE spectrum provides [K/Fe] $= +1.60 \pm 0.12$ dex, while the UVES

spectrum provides [K/Fe] $= +0.62 \pm 0.10$ dex. The derived difference in [K/Fe] is significantly much higher than the typical error associated with the measures. Moreover, I checked that the K line was not contaminated by telluric lines in any of the analyzed spectra. Therefore, I can conclude that the different K abundances derived in the GIRAFFE and UVES spectra are real.

3.4.6 Discussion

The multi-epoch study of the K-rich star 43241_J10 reveals some peculiar characteristics of this star:

- 43241_J10 is a LPV, with a variability period of $\sim$ 70 days. In the G magnitude the peak to peak variations are of the order of $\sim$ 0.35 mag.
- 43241_J10 shows a RV variability suggesting that it could be member of a binary system.
- 43241_J10 exhibits clear signatures of a stellar chromosphere, i.e. emission peaks in the H and K Ca II lines and in the wings of H_α line. Also, the presence of coreshifts in several features forming in outermost stellar atmosphere (i.e., H_α, Na I D, Ca II triplet) and asymmetric profiles in Na I D lines indicate slow outflows and inflows in the chromosphere. The chromosphere of 43241_J10 seems to be variable as indicated by the strong change of the Na I D line profiles
- The line strength of the K resonance line at 7699 Å (and therefore the K abundance) significantly changes in GIRAFFE and UVES spectra. The derived [K/Fe] abundance ratios for 43241_J10 vary over 1 dex and these changes cannot be explained in light of the uncertainties. In contrast, all the other measured elemental abundances do not show any spread and their abundances are compatible with the abundances of stars with similar metallicities and parameters.

The strength variation of K is certainly the most intriguing feature of 43241_J10 and unexpected in normal, single stars. This evidence challenges the previous explanation proposed in Sect. 3.2.4, where the high K abundance of this star was suggested to be intrinsic and explainable within the complex chemical enrichment history of ω Centauri. Indeed, I found that 43241_J10 was enhanced by $\sim$ 1 dex with respect to the other ω Centauri stars at similar metallicity and Mg abundance. In the framework in which the Mg-K anticorrelation is explained by the extreme MgAl burning chain that occurs in AGB and SAGB stars, a possible explanation was that 43241_J10 could have formed from material ejected by the FG of AGB and SAGB stars without dilution with pristine material.

The new evidence collected in this study indicates that the high K abundance previously measured for this star is a transient phenomenon whose origin must be sought in the structure of the star, likely in its variable chromosphere. Indeed, the K I line at 7699 Å is a resonance line that forms around 500-600 km above the stellar surface (see e.g., Bruls et al., 1992; Bruls & Rutten, 1992; Uitenbroek & Bruls, 1992; Quintero Noda et al., 2017) in atmospheric layers between the upper photosphere and the lower chromosphere, where the temperature minimum is found. A possible explanation is that the abundance variations reflect the variability of the stellar chromosphere of this star.

In principle, a realistic calculation of line profiles for transitions that are, at least partially, formed in the chromosphere such as K, requires the inclusion of the chromosphere in the adopted model atmosphere. Standard model atmospheres (i.e. PHOENIX, MARCS, ATLAS) include only the photosphere because of the complexity to properly model the chromosphere (no radiative, hydrostatic and local thermodynamical equilibrium) and the physical processes associated to it (i.e. mass loss, stellar winds). Therefore, chemical abundances derived for these chromospheric lines could be uncorrected. An offset in the abundances of these lines when an appropriate chromosphere is included in the model atmosphere should be present.

The case of 43241_J10 is more complex because of its variable chromosphere. With the actual data, I cannot establish whether a link exist between the chromospheric variability and the photometric variability or the binary nature of the star. For this reason I will perform a time series analysis for this peculiar object, thanks a 20 observations of one hour each over a period of three months (P.I. Alvarez Garay), that will be carried out with the spectrograph VLT/ESPRESSO (Pepe et al., 2021). With this project I aim to explore the spectral variability of 43241_J10, both due to its binary nature and/or to its activity.

In conclusion, 43241_J10 represents a puzzling object that could help us to better understand the still poorly known stellar chromospheres and evaluate their impact on the line strength of some transitions partially formed in those enigmatic stellar regions.

CHAPTER 4

X-SHOOTER SPECTROSCOPY OF LILLER 1 GIANT STARS

Based on the results published in:

- *Alvarez Garay, D. A., Fanelli, C., Origlia, L., Pallanca, C., Mucciarelli, A., et al., 2024 A&A, 686, A198*

4.1 Introduction

Thanks to high-quality, deep CMD from a combination of I- and K-band images acquired with HST and the Gemini South Adaptive Optics Imager (GSAOI) camera Ferraro et al. (2021) revealed the co-existence of a 12 Gyr old and likely subsolar subpopulation, and a younger (only 1-3 Gyr old) and likely supersolar population within the stellar system Liller 1. This finding was confirmed also by the reconstructed SFH by Dalessandro et al. (2022) and by the first metallicity distribution obtained with the low-resolution MUSE spectrograph by Crociati et al. (2023), which showed that Liller 1 hosts a dominant metal-poor component at [Fe/H] ~ -0.50 dex and a metal-rich component with a peak at [Fe/H] $\sim +0.30$ dex.
These findings indicate that Liller 1 is another complex stellar system of the Bulge, hosting multi-age and multi-iron stellar subpopulations similarly to Terzan 5 (see Ferraro et al., 2009, 2016), adding further support to the idea that this system is the surviving fossil fragment of the epoch of Galactic Bulge formation. Hence, a proper spectroscopic screening of its elemental abundances is urgent in order to properly characterize its chemistry and place its subpopulations in a comprehensive evolutionary scheme, as was previously done with Terzan 5 (Origlia et al., 2011, 2013, 2019; Massari et al., 2014). In this Chapter I present a chemical analysis based on NIR X-shooter spectra of 27 stars that are likely members of Liller 1, aiming at characterize the chemical composition of this system in terms of iron, light, α-, and iron-peak elements.

4.2 Observations

I observed 34 bright giant stars in Liller 1 with the X-shooter spectrograph at the VLT under program 089.D-0306 (PI: F.R. Ferraro).
Because of the huge reddening towards Liller 1, only the spectra acquired with the NIR arm of X-shooter and the 0.6 arcsec slit (providing a resolution of R≈8,000) in the 1.15-2.37 μm range have a sufficiently high SNR to be effectively used for a chemical analysis. The X-shooter spectra were acquired by nodding on slit, with a typical throw of a few arcseconds for an optimal subtraction of the background. In particular, one AB nodding cycle was selected for a total on-source integration time ranging from 4 to 14 min, depending on the stellar brightness.
The spectra were reduced with the ESO X-shooter pipeline version 3.1.0 to obtain 2D rectified and wavelength-calibrated spectra. The 1D spectrum was extracted manually in order to optimize the location and extension on the detector of the pair of spectra corresponding to the A and B positions along the slit. An overall SNR of 30–50 per resolution element on the final spectra was measured. As an example, Fig. 4.1 shows the X-shooter spectrum in selected orders of one observed giant star. Some lines of interest for the abundance analysis are marked.
Table 4.1 lists the observed target stars, their coordinates, photometric properties, and distances from the center of Liller 1. The J and K magnitudes are taken from the compilation of NIR photometry (Valenti et al., 2010; Ferraro et al., 2021) and from the VISTA Variables in the Via Lactea (VVV, Minniti et al., 2010).

4.3 Stellar membership from proper motions

The stellar system Liller 1 is located close to the Galactic plane, and field contamination is an issue. However, the proper motion distributions plotted in Figs. 2 of Ferraro et al. (2021) and Dalessandro et al. (2022) show that the Galactic field is clearly distinguishable from the Liller 1 population, which allows a membership selection based on proper motions. The spectroscopic targets are so bright that they are saturated in the HST images that were used in these papers. Hence, I used Gaia DR3 proper motions (Gaia Collaboration et al., 2016, 2023) in the direction of Liller 1 in order to distinguish member stars from Galactic field interlopers. I found that the proper motion distribution of the likely member stars in the vector point diagram, centered on the absolute values of the system ($\mu_\alpha \cos\delta = -5.403$, $\mu_\delta = -7.431$ mas yr^{-1}; Vasiliev & Baumgardt, 2021), has a dispersion $\sigma_{\rm PM} \approx 0.5$ mas yr^{-1} in both the α and δ components. I therefore assumed that all the observed stars with proper

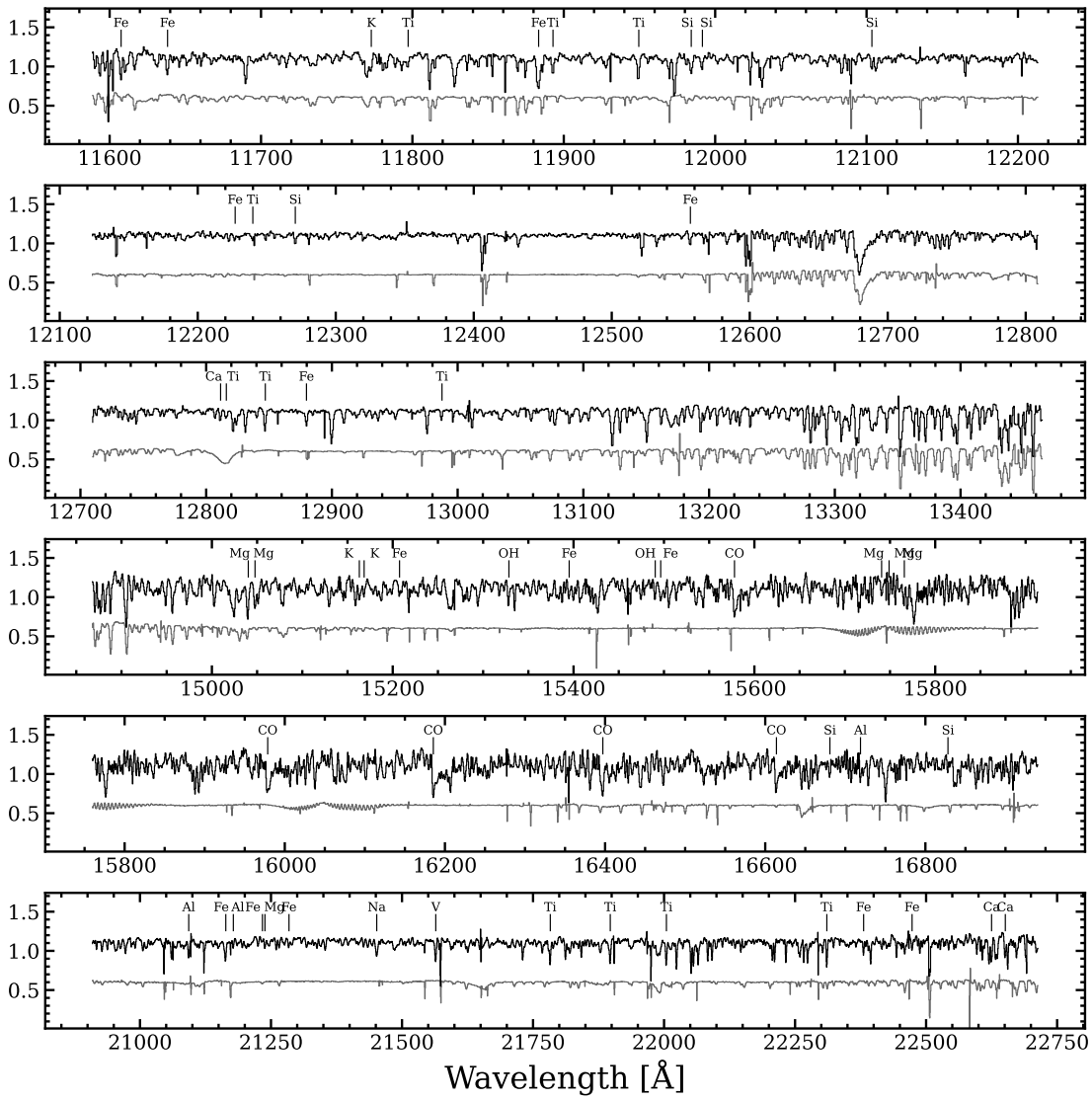

FIGURE 4.1: Portions of the X-shooter spectrum for a giant star with a temperature of 3400 K across the J, H, and K bands (featuring X-shooter orders 22, 21, 20, 17, 16, and 12 from top to bottom). Some lines of interest for the chemical analysis are also marked. In each panel, the upper spectrum in black is the stellar normalized spectrum corrected for radial velocity, and the lower gray spectrum shows the telluric absorption.

Table 4.1: Observed stars in Liller 1.

ID	RA [Deg]	Dec [Deg]	J [mag]	K [mag]	distance [arcsec]
20	263.3413160	-33.3917580	12.27	9.15	34.3
24	263.3580030	-33.3844380	12.03	9.26	25.0
27	263.3463770	-33.3867450	11.97	9.22	20.6
31	263.3386050	-33.3953320	12.10	9.29	46.4
34	263.3370940	-33.3755720	12.07	9.30	68.0
35	263.3561440	-33.3858760	12.12	9.28	17.6
37	263.3408550	-33.3894200	12.21	9.36	34.6
39	263.3619960	-33.3893320	12.20	9.26	28.9
45	263.3540437	-33.3894655	12.02	9.48	5.3
48	263.3509838	-33.3909300	12.41	8.98	6.6
62	263.3659950	-33.4061700	12.50	9.75	72.6
66	263.3614350	-33.4098700	12.50	9.78	78.3
68	263.3392510	-33.4054300	12.46	9.78	69.5
71	263.3535490	-33.3906021	12.43	9.87	5.2
74	263.3490706	-33.3910950	12.80	10.01	11.4
79	263.3491370	-33.3856470	12.65	10.02	17.4
85	263.3551136	-33.3912034	12.84	9.95	10.3
88	263.3537148	-33.3957827	12.80	10.01	22.9
98	263.3560121	-33.3878820	12.98	10.41	12.6
100	263.3440470	-33.3914300	13.00	10.38	26.2
103	263.3554470	-33.3868030	13.07	10.33	13.4
104	263.3478150	-33.3866650	13.13	10.49	17.3
108	263.3515430	-33.4021070	13.06	10.31	45.5
109	263.3548662	-33.3878013	13.08	10.60	9.8
115	263.3599230	-33.3909680	13.14	10.36	22.9
120	263.3599690	-33.3839110	13.16	10.44	30.2
121	263.3404830	-33.3814510	13.09	10.47	46.1
124	263.3421180	-33.4040030	13.11	10.49	60.6
126	263.3496644	-33.3857118	13.32	10.71	16.0
132	263.3630190	-33.4004900	13.25	10.65	50.8
136	263.3545365	-33.3861169	13.46	10.78	13.8
145	263.3499870	-33.3816380	13.45	10.83	29.3
148	263.3529737	-33.3828074	13.48	11.15	24.1
149	263.3629250	-33.4037590	13.50	10.85	60.5

motions within $3 \times \sigma_{\rm PM}$ from the absolute systemic values are bonafide members. Figure 4.2 shows the Gaia measurements for the stars with G<19 located within 80″ from the center of Liller 1(small gray circles). The 34 spectroscopic targets are superposed as large symbols. While the majority (27) of the targets satisfy the adopted membership criterion, being located within $3 \times \sigma_{\rm PM}$ in the vector point diagram, 7 stars fall beyond this limit, indicating that they are likely field interlopers. These objects were therefore excluded from the chemical analysis presented in this work. Figure 4.3 shows the location of the 27 target members in the $(J - K), K$ CMD (left panel) and on the plane of the sky (right panel) within the central 80″ (radius) from the Liller 1 center.

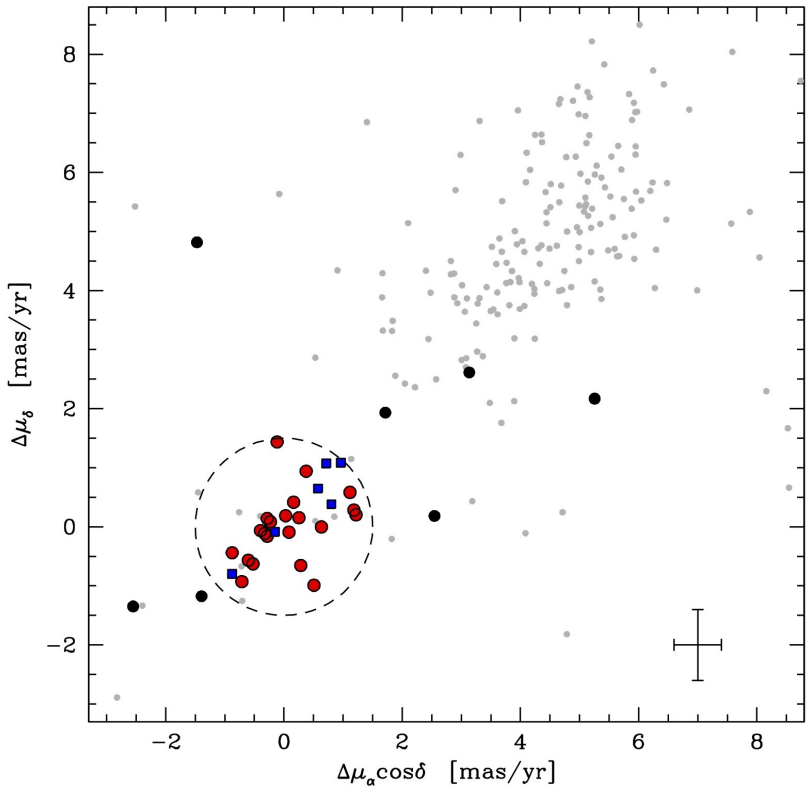

FIGURE 4.2: Vector point diagram of the stars with G< 19 in the direction of Liller 1 (small gray circles), showing the RA and Dec components of the Gaia DR3 proper motions referred to the systemic values quoted by Vasiliev & Baumgardt (2021). The large dashed circle is centered on (0,0) and has a radius equal to $3 \times \sigma_{\rm PM}$, with $\sigma_{\rm PM} = 0.5$ mas yr^{-1} being the proper motion dispersion of Liller 1 member stars. The spectroscopic targets are plotted with large symbols: Large black dots show those classified as Galactic field interlopers due to their discordant proper motions, and large red dots and blue squares show the likely metal-poor and metal-rich members, respectively. The typical error bar is reported in the bottom right corner.

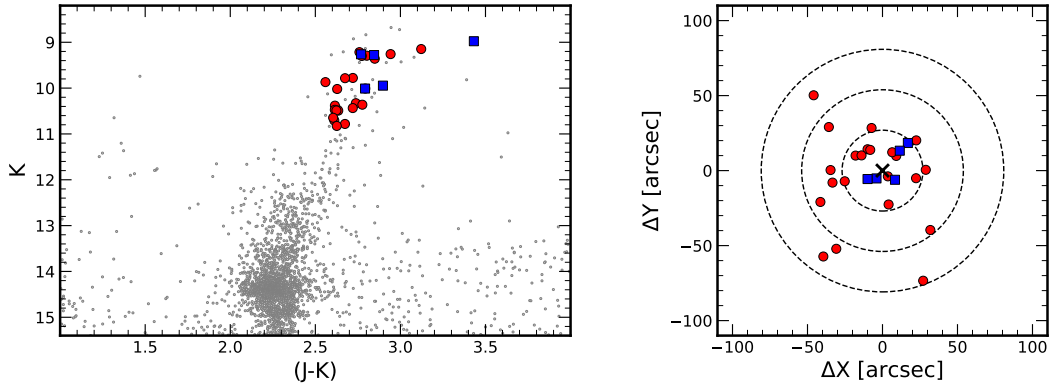

FIGURE 4.3: Left panel: $(J-K), K$ CMD of Liller 1 (gray dots). The likely metal-poor (filled red circles) and metal-rich (filled blue squares) member stars for which I measured abundances (see Sect. 4.5.2) are indicated.
Right panel: Distribution of these stars (same symbols) on the plane of the sky with respect to the cluster center, marked with the black cross and located at RA=263.°35233, Dec=−33.°38956. The radii of the dashed black circles are equal to 5, 10, and 15 times the core radius $r_c = 5.''39$ (Saracino et al., 2015).

4.4 Spectral analysis

The X-shooter NIR spectra of the 27 member stars were used to determine RVs via cross-correlation techniques. The chemical abundances were determined via spectral synthesis. For this purpose, I used the radiative transfer code `TURBOSPECTRUM` (Alvarez & Plez, 1998; Plez, 2012), along with MARCS models atmospheres (Gustafsson et al., 2008), to create grids of synthetic spectra with effective temperatures from 3200 K to 3900 K, $\log g = 0.5$ dex, $\xi = 2.0$ km s^{-1}, in a range of metallicities from [Fe/H] $= -1.0$ dex to [Fe/H] $= +0.5$ with a step of 0.1 dex, with two different [α/Fe] values, solar scaled ([α/Fe] $= 0.0$ dex) and α enhanced ([α/Fe] $= +0.4$ dex). The selected parameters are consistent with those of observed cool giants. The atomic data were sourced from the VALD3 compilation (Ryabchikova & Pakhomov, 2015), while the most recent molecular data were taken from the website of B. Plez[1]. In order to match the observed line profile broadening, the synthetic spectra were convolved with a Gaussian function at the R∼8,000 X-shooter resolution. This instrumental broadening dominates any other intrinsic broadening, such as macroturbulence and rotation. For an optimum pixel-to-pixel comparison between the observed and the synthetic spectra, the latter were also resampled to match the pixel size (0.6 Å) of the observed spectra.

[1] `https://www.lupm.in2p3.fr/users/plez/`

4.4.1 Stellar parameters

A photometric estimate of the stellar temperature and gravity was derived from suitable isochrones by Bressan et al. (2012) by matching the old (12 Gyr) and young (1,2,3 Gyr) components of Liller 1 at [Fe/H]~ -0.3 and [Fe/H]$\sim +0.3$, respectively, in the observed CMD of (Ferraro et al., 2021) corrected for differential reddening and assuming their distance modulus (m-M)$_0$=14.65 and average $E(B-V) = 4.52$ as reference. Low temperatures in the 3400-3800 K range and gravities in the 0.2-0.8 dex range were obtained. These photometric estimates of the stellar parameters were then cross-checked against the observed OH and CO molecular lines and bandheads in order to simultaneously best fit all of them. For the measured member stars, the final adopted temperatures with an uncertainty of $\pm$100 K are listed in Table 4.2, while log g=0.5$\pm$0.3 dex and a microturbulence value of 2$\pm$0.2 km s^{-1}, typical of luminous bulge giant stars with similar metallicities, were assumed for all of them. At the low temperatures and gravities of the analyzed stars, the quoted uncertainties for the adopted stellar parameters have an overall impact on the derived abundances of approximately 0.10-0.15 dex. However, it is worth mentioning that this global uncertainty can be regarded as mostly systematic, and it therefore almost canceled out when I computed abundance ratios and when I considered the abundance differences among the Liller 1 stars. For each star in the sample, I thus generated multiple grids of synthetic spectra with fixed stellar parameters (appropriate to each star) and a varying metallicity from -1.0 dex to $+0.5$ dex, in steps of 0.1 dex, with both solar-scaled and some enhancement of [α/Fe] and [N/Fe] and corresponding depletion of [C/Fe] for a proper computation of the molecular equilibria, and solar-scaled [X/Fe] values for the other elements.

4.4.2 Continuum normalization

An optimum continuum normalization of the observed spectra is crucial for determining reliable chemical abundances. Throughout the whole grid of synthetic spectra, I therefore considered a local reference continuum by selecting a few wavelength points on the left and right sides of each absorption line of interest that exhibited negligible variation with metallicity. The same wavelength points were selected on the observed spectra. I then computed the average "left" and "right" wavelengths and fluxes in the synthetic and observed spectra and performed a linear fit to these "master" points, thus obtaining the best-guess synthetic and observed local continuum.

TABLE 4.2: Temperatures, RVs and chemical abundances for the observed stars in Liller 1.

ID	T_{eff}	RV	[Fe/H]	[C/H]	[O/H]	[Na/H]	[Mg/H]	[Al/H]	[Si/H]	[K/H]	[Ca/H]	[Ti/H]	[V/H]	$^{12}C/^{13}C$
	[K]	[km s^{-1}]	7.50	8.56	8.77	6.29	7.55	6.43	7.59	5.14	6.37	4.94	3.89	89
20	3400	52	-0.28 ± 0.08	-0.42 ± 0.10	$+0.19 \pm 0.06$	$+0.32 \pm 0.07$	$+0.12 \pm 0.10$	$+0.08 \pm 0.10$	$+0.02 \pm 0.08$	$+0.14 \pm 0.10$	$+0.21 \pm 0.10$	$+0.26 \pm 0.12$	-0.05 ± 0.10	5.3 ± 1.4
24	3400	86	$+0.24 \pm 0.07$	-0.10 ± 0.03	$+0.28 \pm 0.02$	$+0.80 \pm 0.10$	$+0.27 \pm 0.06$	$+0.41 \pm 0.10$	$+0.20 \pm 0.04$	$+0.21 \pm 0.06$	$+0.25 \pm 0.06$	$+0.33 \pm 0.04$	$+0.34 \pm 0.10$	7.4 ± 1.7
27	3400	69	-0.38 ± 0.06	-0.78 ± 0.04	-0.01 ± 0.10	$+0.03 \pm 0.03$	$+0.16 \pm 0.05$	$+0.01 \pm 0.05$	-0.17 ± 0.04	$+0.02 \pm 0.05$	$+0.08 \pm 0.10$	$+0.23 \pm 0.08$	-0.33 ± 0.10	9.2 ± 1.2
31	3400	60	-0.24 ± 0.06	-0.74 ± 0.10	$+0.09 \pm 0.06$	$+0.17 \pm 0.04$	$+0.06 \pm 0.09$	$+0.03 \pm 0.06$	$+0.07 \pm 0.10$	$+0.11 \pm 0.12$	$+0.03 \pm 0.10$	$+0.31 \pm 0.05$	-0.21 ± 0.10	9.4 ± 2.0
34	3400	76	-0.28 ± 0.07	-1.04 ± 0.07	$+0.11 \pm 0.06$	$+0.29 \pm 0.11$	$+0.23 \pm 0.06$	-0.01 ± 0.10	-0.03 ± 0.01	$+0.25 \pm 0.10$	$+0.23 \pm 0.10$	$+0.13 \pm 0.07$	-0.19 ± 0.10	7.9 ± 1.3
35	3400	86	$+0.20 \pm 0.06$	-0.17 ± 0.03	$+0.19 \pm 0.06$	$+0.74 \pm 0.10$	$+0.15 \pm 0.10$	$+0.34 \pm 0.10$	$+0.17 \pm 0.06$	$+0.07 \pm 0.10$	$+0.16 \pm 0.10$	$+0.47 \pm 0.05$	$+0.30 \pm 0.10$	12.3 ± 1.8
37	3400	61	-0.33 ± 0.07	-0.58 ± 0.06	$+0.11 \pm 0.10$	-0.09 ± 0.04	$+0.18 \pm 0.05$	$+0.07 \pm 0.10$	-0.14 ± 0.05	-0.06 ± 0.03	$+0.13 \pm 0.10$	$+0.13 \pm 0.09$	-0.37 ± 0.10	6.8 ± 1.6
39	3400	55	-0.29 ± 0.09	-0.75 ± 0.07	$+0.12 \pm 0.10$	$+0.28 \pm 0.10$	$+0.19 \pm 0.09$	$+0.02 \pm 0.05$	-0.03 ± 0.06	...	$+0.02 \pm 0.10$	$+0.30 \pm 0.07$	-0.19 ± 0.10	10.5 ± 1.3
48	3400	42	$+0.13 \pm 0.08$	-0.22 ± 0.06	$+0.14 \pm 0.10$	$+0.74 \pm 0.10$	$+0.25 \pm 0.10$	$+0.25 \pm 0.06$	$+0.15 \pm 0.05$	$+0.15 \pm 0.10$	$+0.15 \pm 0.10$	$+0.22 \pm 0.07$	$+0.06 \pm 0.10$	11.3 ± 1.2
66	3500	99	-0.06 ± 0.05	-0.20 ± 0.05	$+0.09 \pm 0.06$	$+0.57 \pm 0.10$	$+0.19 \pm 0.04$	$+0.18 \pm 0.10$	$+0.14 \pm 0.06$	$+0.21 \pm 0.10$	...	...	$+0.17 \pm 0.10$	10.9 ± 1.5
68	3500	78	-0.36 ± 0.05	-0.63 ± 0.05	-0.06 ± 0.08	-0.04 ± 0.10	$+0.06 \pm 0.06$	$+0.05 \pm 0.10$	-0.19 ± 0.05	-0.12 ± 0.10	$+0.03 \pm 0.10$	$+0.18 \pm 0.09$	-0.43 ± 0.10	7.0 ± 1.6
71	3500	53	-0.40 ± 0.08	-0.87 ± 0.04	-0.17 ± 0.07	-0.18 ± 0.10	-0.13 ± 0.05	-0.13 ± 0.06	-0.07 ± 0.04	-0.12 ± 0.10	-0.05 ± 0.10	-0.05 ± 0.05	-0.53 ± 0.10	7.6 ± 1.0
74	3500	70	$+0.30 \pm 0.06$	-0.13 ± 0.03	$+0.25 \pm 0.07$	$+0.95 \pm 0.10$	$+0.32 \pm 0.10$	$+0.38 \pm 0.10$	$+0.21 \pm 0.05$	$+0.11 \pm 0.10$	$+0.31 \pm 0.10$	$+0.39 \pm 0.05$	$+0.22 \pm 0.10$	10.5 ± 1.8
79	3600	70	-0.22 ± 0.05	-0.97 ± 0.10	-0.05 ± 0.10	$+0.01 \pm 0.10$	$+0.11 \pm 0.10$	$+0.12 \pm 0.10$	$+0.06 \pm 0.08$	$+0.30 \pm 0.10$	...	$+0.19 \pm 0.08$	-0.47 ± 0.10	8.4 ± 1.0
85	3500	61	$+0.22 \pm 0.07$	-0.11 ± 0.10	$+0.12 \pm 0.06$	$+0.84 \pm 0.10$	$+0.25 \pm 0.05$	$+0.27 \pm 0.10$	$+0.18 \pm 0.04$	$+0.10 \pm 0.10$	$+0.24 \pm 0.10$	$+0.30 \pm 0.10$	$+0.14 \pm 0.10$	9.4 ± 1.9
88	3600	72	-0.34 ± 0.08	-0.67 ± 0.04	$+0.12 \pm 0.10$	$+0.02 \pm 0.10$	$+0.05 \pm 0.10$	$+0.12 \pm 0.08$	-0.05 ± 0.04	$+0.06 \pm 0.10$	$+0.02 \pm 0.07$	$+0.07 \pm 0.04$	-0.29 ± 0.10	8.2 ± 1.7
100	3700	68	-0.42 ± 0.08	-1.17 ± 0.07	-0.27 ± 0.08	$+0.13 \pm 0.10$	-0.03 ± 0.10	$+0.00 \pm 0.08$	-0.13 ± 0.05	-0.08 ± 0.06	-0.23 ± 0.10	-0.02 ± 0.08	-0.35 ± 0.10	9.2 ± 1.7
103	3700	40	-0.38 ± 0.07	-0.62 ± 0.04	$+0.03 \pm 0.06$	-0.04 ± 0.10	-0.01 ± 0.10	$+0.16 \pm 0.05$	-0.12 ± 0.05	$+0.13 \pm 0.10$	-0.05 ± 0.10	$+0.06 \pm 0.04$	-0.35 ± 0.10	11.5 ± 2.3
104	3700	57	-0.38 ± 0.06	-0.68 ± 0.05	$+0.01 \pm 0.07$	-0.04 ± 0.10	-0.08 ± 0.10	-0.07 ± 0.05	-0.16 ± 0.10	$+0.12 \pm 0.10$	-0.14 ± 0.10	-0.08 ± 0.10	-0.42 ± 0.10	9.2 ± 1.5
115	3700	57	-0.26 ± 0.09	-0.96 ± 0.10	-0.10 ± 0.10	...	$+0.15 \pm 0.05$	$+0.19 \pm 0.06$	-0.02 ± 0.09	-0.08 ± 0.10	$+0.01 \pm 0.04$	$+0.21 \pm 0.04$	-0.21 ± 0.10	8.2 ± 1.3
120	3700	68	-0.31 ± 0.07	-0.84 ± 0.10	-0.10 ± 0.05	$+0.46 \pm 0.10$	$+0.10 \pm 0.10$	$+0.18 \pm 0.10$	$+0.04 \pm 0.05$	-0.06 ± 0.10	$+0.03 \pm 0.05$	$+0.11 \pm 0.06$	-0.34 ± 0.10	10.5 ± 1.4
121	3700	62	-0.30 ± 0.07	-0.65 ± 0.04	$+0.04 \pm 0.06$	$+0.09 \pm 0.10$	$+0.03 \pm 0.10$	$+0.03 \pm 0.10$	-0.06 ± 0.04	-0.13 ± 0.10	-0.05 ± 0.05	$+0.15 \pm 0.04$	-0.34 ± 0.10	10.9 ± 2.0
124	3700	57	-0.32 ± 0.07	-0.67 ± 0.06	$+0.04 \pm 0.07$	$+0.05 \pm 0.10$	$+0.07 \pm 0.10$	$+0.02 \pm 0.05$	-0.03 ± 0.06	$+0.14 \pm 0.10$	$+0.13 \pm 0.10$	$+0.19 \pm 0.05$	-0.31 ± 0.10	10.5 ± 1.5
126	3700	72	-0.42 ± 0.05	-0.80 ± 0.05	-0.13 ± 0.08	-0.15 ± 0.10	-0.15 ± 0.05	-0.19 ± 0.10	-0.18 ± 0.10	$+0.03 \pm 0.06$	$+0.08 \pm 0.10$	$+0.09 \pm 0.10$	-0.41 ± 0.10	8.4 ± 1.1
132	3700	66	-0.26 ± 0.08	-0.70 ± 0.05	-0.03 ± 0.07	$+0.00 \pm 0.10$	$+0.13 \pm 0.05$	$+0.11 \pm 0.06$	$+0.06 \pm 0.07$	$+0.10 \pm 0.06$	$+0.11 \pm 0.06$	$+0.18 \pm 0.05$	-0.37 ± 0.10	7.6 ± 1.8
136	3800	55	-0.29 ± 0.09	-1.06 ± 0.04	-0.10 ± 0.10	$+0.37 \pm 0.10$	$+0.10 \pm 0.10$	$+0.07 \pm 0.10$	-0.10 ± 0.10	$+0.16 \pm 0.10$	$+0.03 \pm 0.10$	$+0.16 \pm 0.07$	-0.33 ± 0.10	10.0 ± 1.5
145	3800	74	-0.36 ± 0.07	-0.71 ± 0.07	-0.17 ± 0.06	-0.05 ± 0.10	$+0.11 \pm 0.05$	$+0.25 \pm 0.05$	-0.11 ± 0.06	$+0.13 \pm 0.10$	$+0.06 \pm 0.10$	$+0.08 \pm 0.10$	-0.42 ± 0.10	12.1 ± 3.1

Note: The adopted solar abundances for the measured chemical elements are from Magg et al. (2022) and they are reported in the header of each element abundance column.

The observed spectra were then normalized locally through the following formula:

$$F^{\rm obs}_{\rm norm} = F^{\rm obs} \times \frac{\text{synthetic continuum fit}}{\text{observed continuum fit}}, \tag{4.1}$$

where $F^{\rm obs}$ and $F^{\rm obs}_{\rm norm}$ are the observed fluxes before and after the normalization, respectively. The typical uncertainty in the continuum normalization around each line of interest is ∼2%, and it mostly arises from the photon noise of the few resolution elements that were used to locate it around each line and from the uncertainty in the adopted temperature.

4.4.3 Chemical analysis

For the chemical analysis, I compiled a list of suitable atomic lines over the entire J, H, K spectral range covered by the X-shooter spectra. This list included lines of Na I, Mg I, Al I, Si I, K I, Ca I, Ti I, V I, and Fe I. I was also able to use OH molecular lines and CO bandheads in order to derive O and C abundances, respectively. Each line was also scrutinized visually in order to minimize any greater risk of a potential blend with nearby stellar or telluric lines. I employed a varying number of lines, depending on the chemical element, the SNR of the spectrum, and possible telluric contamination. For Fe, between 4 to 9 lines were analyzed, while for Na, Al, Si, Ca, Ti, and V, between 1 and 5 lines were used. A few OH molecular lines and 2-4 bandheads of CO for the determination of the oxygen and carbon abundance, respectively, were used.

I derived chemical abundances by comparing the synthetic and observed spectra, the latter being optimally normalized around each line of interest, as discussed in Sect. 4.4.2. The abundance [X/H] of a given element from each line of interest was determined as the abundance of the synthetic spectrum that minimizes the difference with the observed spectrum. As figure of merit, I used the flux of the deepest pixel of each line of interest. However, I also explored solutions that used the sum of the fluxes of the three deepest pixels of each line of interest as a figure of merit, finding abundances that were fully consistent with those obtained using the central pixel alone. Hence, I ultimately decided to rely on the deepest pixel alone to minimize possible residual contamination. Random errors in the inferred chemical abundances from each line of interest in the X-shooter spectra are mostly due to the uncertainties in the placement of the continuum (2%; see Sect. 4.4.2) and to the photon noise (2-3%, according to the measured SNR of 30-50; see Sect. 4.2). The overall impact of a random error like this on the derived abundance from each line typically is 0.1-0.2 dex, and this is comparable with the typical 1σ scatter in the derived abundances from different lines. The final errors in the derived abundances, as quoted in Table 4.2, were estimated as the dispersion around the mean abundance value divided by the squared root of the number of lines used to measure each

chemical element. When only one line was available, I assumed an error of 0.1 dex, which is the typical line-to-line abundance variation.

4.5 Results

The analysis of the X-shooter spectra has provided RVs with an uncertainty of <1 km s^{-1}, chemical abundances [X/H] for eleven elements (Fe, C, O, Na, Mg, Al, Si, K, Ca, Ti, and V) with typical errors of $\leqslant$0.1 dex, and the ^{12}C/^{13}C isotopic ratios that are listed in Table 4.2. Solar reference abundances are taken from Magg et al. (2022).

4.5.1 Radial velocities

The inferred heliocentric RVs range between 40 and 100 km s^{-1}, with an average value of 65.4$\pm$2.5 km s^{-1} and a dispersion of 13.2$\pm$1.8 km s^{-1}. These values are fully consistent with the systemic velocity of 67.9$\pm$0.8 km s^{-1} quoted by Crociati et al. (2023) and within 2.5 times the velocity dispersion of $\sim$13 km s^{-1} at about 100″ from the center[2].
I therefore conclude that all the 27 proper-motion-selected stars listed in Table 4.2 are likely members of Liller 1 according to their 3D kinematics.

4.5.2 Abundances and abundance ratios

The distribution of the inferred [Fe/H] values for 27 stars, likely members of Liller 1, is reported in Fig. 4.4 (left panel). The distribution is clearly bimodal, with a main relatively metal-poor component at an average [Fe/H] $= -0.31 \pm 0.02$ and 1σ dispersion of 0.08$\pm$0.01, including 22 stars, and a metal-rich component at an average [Fe/H] $= +0.22 \pm 0.03$ and 1σ dispersion of 0.06 ± 0.02, comprising 5 stars. Interestingly, this measured bimodal distribution agrees with the prediction of Dalessandro et al. (2022). The stars belonging to the two components are highlighted with different colors in Fig. 4.3. Figure 4.4 (right panel) shows the X-shooter spectra around two iron lines in the J and K bands of a metal-poor and a metal-rich star with similar stellar parameters as an example. The metal-poor star exhibits noticeably shallower features than the metal-rich star, as expected. The inferred iron abundance dispersion of each subpopulation is consistent with the measurement errors (see Table 4.2).
The [X/Fe] abundance ratios as a function of [Fe/H] of the other chemical elements measured in the X-shooter spectra are shown in Fig. 4.5. The metal-poor subpopulation shows some

[2]Fundamental parameters of Galactic globular clusters, https://people.smp.uq.edu.au/HolgerBaumgardt/globular/

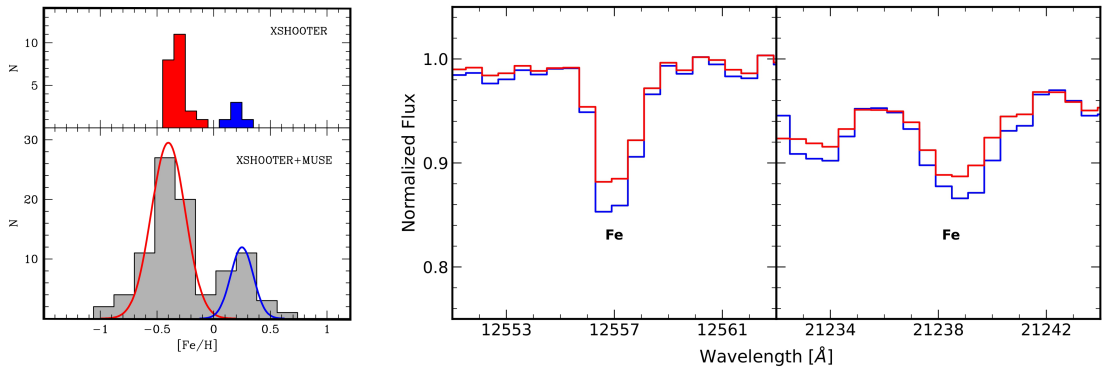

FIGURE 4.4: Histograms of the metallicity distribution of Liller 1 (left panel) for the 27 stars observed with X-shooter (top) and for the cumulative sample (from this work and the one by Crociati et al., 2023, bottom). For the sake of illustration, two Gaussian functions reproducing the subsolar and supersolar components are shown as red and blue curves, respectively. For sake of illustration, X-shooter spectra around two iron lines in the J and K bands for a metal-poor (number 39, red line) and a metal-rich (number 35, blue line) star of Liller 1, with similar stellar parameters, are also plotted (right panel).

enhanced (by a factor of 2-3 on average) [α/Fe], [Al/Fe], and [K/Fe] with respect to the solar values, while the metal-rich subpopulation shows roughly solar-scaled ratios. The dispersions in these [X/Fe] abundance ratios are consistent with the measurement errors. The [V/Fe] abundance ratio is about solar at all metallicities, with an average value of 0.01±0.01 dex and a dispersion of 0.11±0.01 dex, which is consistent with the measurement errors. [Na/Fe] is enhanced in both the metal-poor and metal-rich subpopulations, with average values of 0.42±0.04 dex and of 0.60±0.02 dex, respectively, which is consistent with measurements and model predictions for the bulge (see e.g., Johnson et al., 2014; Kobayashi et al., 2006, 2011) of some increase in the Na production at high metallicity. The metal-poor subpopulation shows a dispersion in [Na/Fe] of 0.16±0.02 dex that only marginally (by ∼10%) exceeds the measurement errors ($\leqslant$0.12 dex), while the metal-rich subpopulation has a small dispersion of 0.05±0.01 dex.

[C/H] abundances and ^{12}C/^{13}C isotopic ratios for all the observed stars (see Table 4.2) were determined by using the unsaturated ^{12}CO and ^{13}CO molecular bandheads in the H band. These bandheads are as effective as the individual lines from single roto-vibrational transitions (the latter being only barely if at all distinguishable at the X-shooter resolution) for measuring carbon abundances (see e.g., Fanelli et al., 2021). Figure 4.6 (left panels) shows the behavior of the [C/Fe] and ^{12}C/^{13}C ratios as a function of [Fe/H]. The metal-poor (red points) and metal-rich (blue points) components of Liller 1 are both significantly depleted in [C/Fe] and in the ^{12}C/^{13}C isotopic ratio (with values in the range of 5-13) with respect to the

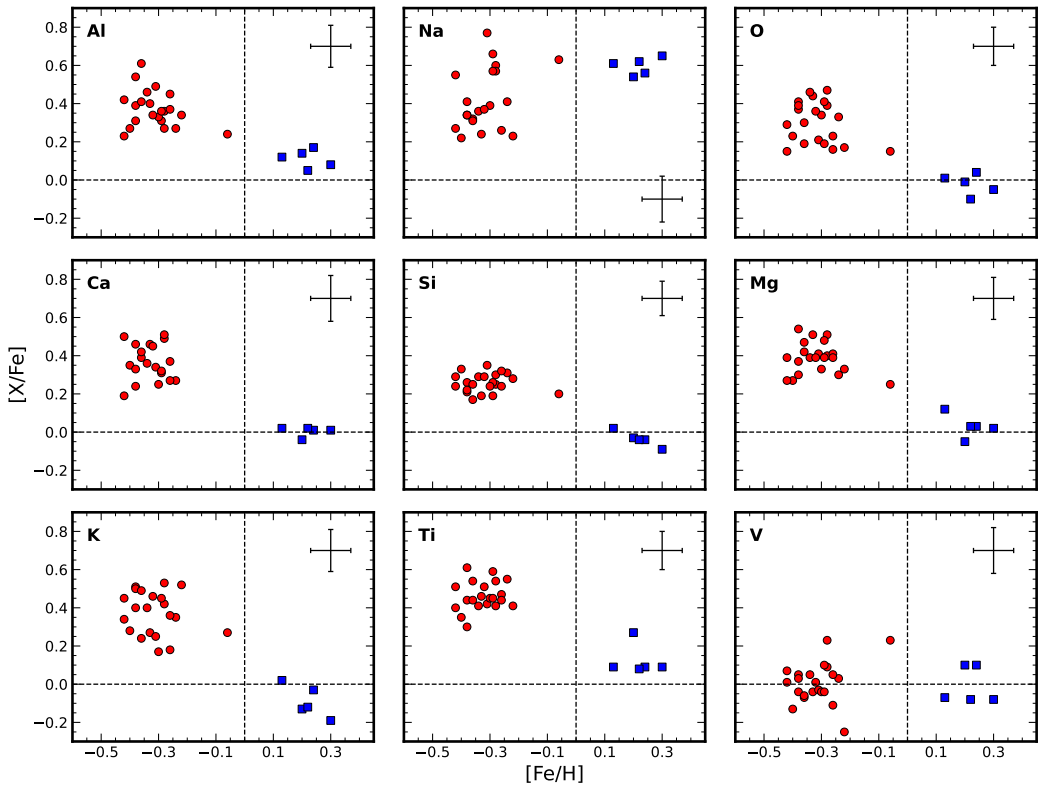

FIGURE 4.5: Behavior of [Al/Fe], [Na/Fe], [O/Fe], [Ca/Fe], [Si/Fe], [Mg/Fe], [K/Fe], [Ti/Fe], and [V/Fe] as a function of [Fe/H] for the metal-poor (filled red circles) and metal-rich (filled blue squares) subcomponents I analyzed. The typical error bars of the measurements are reported in the right corner of each panel. The dashed vertical and horizontal lines denote the corresponding zero values.

solar values, as expected because of the mixing and extra-mixing processes in the stellar interiors during the evolution along the RGB. The majority of the measured stars in Liller 1 show [C/Fe] depletion well within a factor of four and fully consistent with the values measured in other luminous giants of the Bulge and Terzan 5 (see e.g., Origlia et al., 2011; Rich et al., 2012, and references therein). Notably, however, five stars belonging to the metal-poor subpopulations of Liller 1 show an even higher [C/Fe] depletion, up to a factor of seven, while their $^{12}C/^{13}C$ isotopic ratios (between 8 and 10) are well within the range of values measured in the other Liller 1 giant stars. As an example and for the sake of clarity, Fig. 4.6 (right panels) shows two ^{12}CO and two ^{13}CO molecular bandheads that were used for measuring carbon abundances in three metal-poor stars with similar stellar parameters, iron abundances, and $^{12}C/^{13}C$. The ^{12}CO and the ^{13}CO bandheads clearly show different depths, according to the different carbon abundances of the three stars.

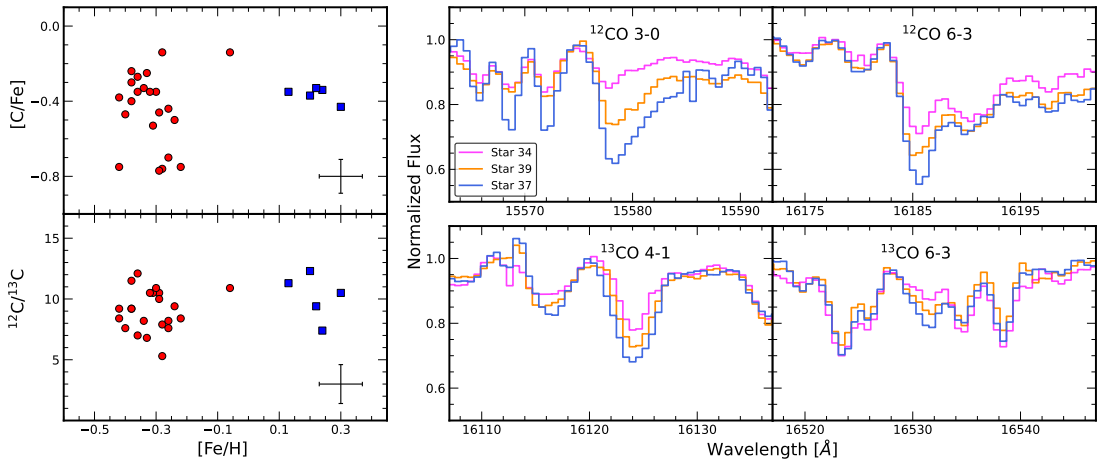

FIGURE 4.6: Carbon measurements for the observed stars. Left panel: Behavior of [C/Fe] (top) and ^{12}C/^{13}C ratio (bottom) as a function of [Fe/H] for the metal-poor (filled red circles) and metal-rich (filled blue squares) components of Liller 1. The error bars in the bottom right corners represent the typical error associated with the measurements. Right panel: ^{12}CO 3-0 and 6-3 (top) and ^{13}CO 4-1 and 6-3 (bottom) roto-vibration molecular bandheads in the H band, as observed in three metal-poor stars with similar stellar parameters, iron abundances, and ^{12}C/^{13}C isotopic ratios, but different carbon abundances.

Figure 4.7 shows the behavior of [Al/Fe] (bottom panel) and [Na/Fe] (middle panel) as a function of [O/Fe] and of [Na/Fe] as a function of [C/Fe] (top panel) for the two subpopulations of Liller 1. No specific trend (e.g., an anticorrelation) is evident in the distributions of these abundance ratios within each subpopulation. The lack of trends within the old subpopulation of Liller 1 in particular is consistent with what is measured in the Bulge field and in Terzan 5 (Origlia et al., 2011), and it is at variance with what is typically measured in other old stellar systems, such as *genuine* GCs (e.g., Carretta et al., 2009a), or in accreted stellar systems such as ω Centauri (Johnson & Pilachowski, 2010; Marino et al., 2012b), where significant spreads and some anticorrelations among light elements have been found. This evidence therefore has crucial implications for the formation scenario of Liller 1.

4.6 Discussion and conclusions

This work of Liller 1 provides the first comprehensive chemical characterization of its two distinct subpopulations: the metal-poor component with subsolar metallicity and enhanced [α/Fe], [K/Fe], and [Al/Fe] with respect to solar ratios, and the metal-rich component with supersolar metallicity and about solar scaled ratios for the same light elements. These chemical properties are consistent with an old age for the metal-poor subpopulation, which likely

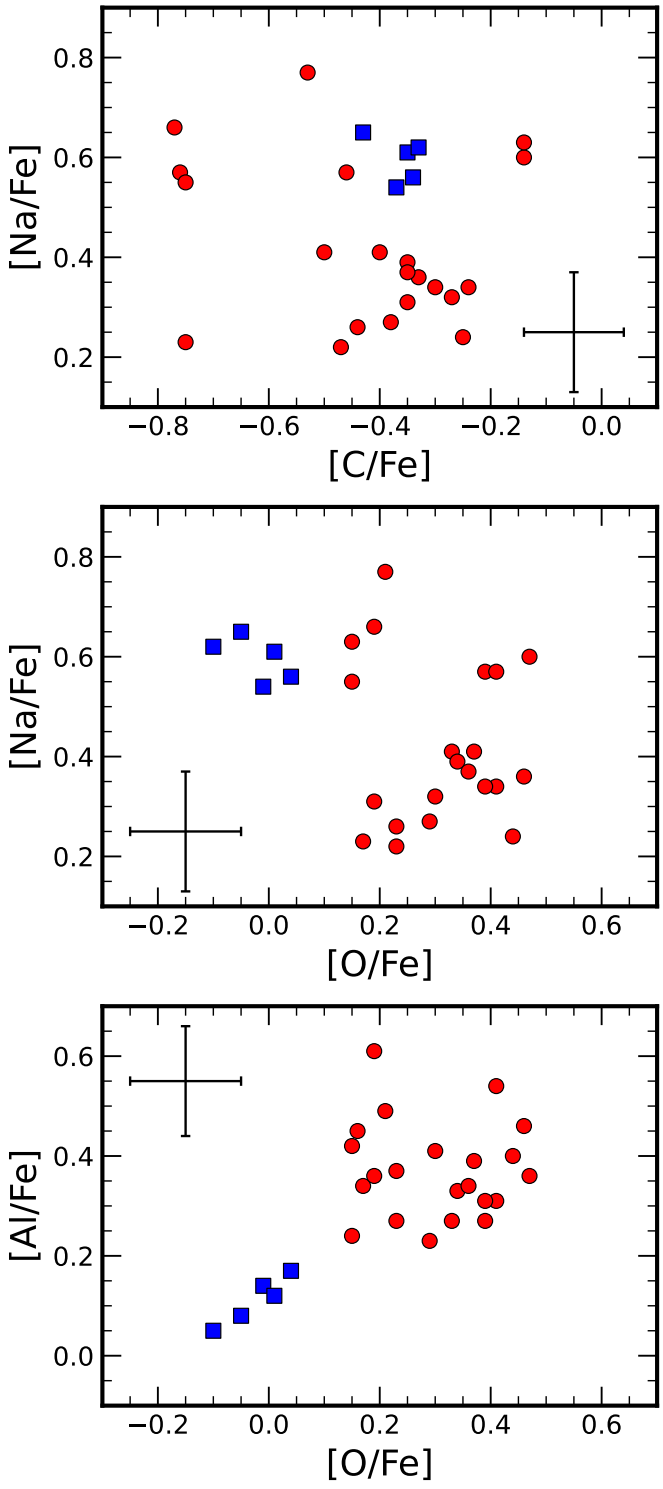

FIGURE 4.7: Behavior of [Na/Fe] vs [C/Fe] (top panel) and vs [O/Fe] (middle panel), and of [Al/Fe] vs [O/Fe] for the metal-poor (filled red circles) and metal-rich (filled blue squares) member stars of Liller 1. The typical measurement errors are reported in one corner of each panel.

formed early and quickly from gas enriched by type II SNe, and a younger age for the metal-rich subpopulation, which formed from gas that was also enriched by the ejecta of type Ia SNe on longer timescales. Interestingly, according to Fig. 4.3, (see also Dalessandro et al., 2022), the metal-rich subpopulation is also more centrally concentrated.

Liller 1 is the second complex stellar system in the bulge that, similarly to Terzan 5 (see Ferraro et al., 2009, 2016; Origlia et al., 2011, 2013, 2019; Massari et al., 2014), hosts subpopulations with different ages and metallicities, as well as different [α/Fe] abundance ratios. Both subpopulations have solar-scaled [V/Fe], thus probing the different metallicities with an additional iron-peak element, and a significantly depleted [C/Fe] and $^{12}C/^{13}C$ isotopic ratio with respect to the solar values, consistent with mixing and extra-mixing processes during the RGB evolution. They also show enhanced [Na/Fe], which is consistent with a likely formation and evolution within the Bulge. Intriguingly, no evidence of the Na-O anticorrelation that is typically observed in GCs (see, e.g., Carretta et al., 2009a) has been found. This is particular relevant for the subsolar component (shown with red circles in Fig. 4.7) since it can constrain the formation scenarios of Liller 1. This chemical fingerprint has been claimed to be so specific to GCs that it has been proposed as the benchmark to classify a stellar system as a GC (Carretta et al., 2010a).

Recently, the accretion of a giant molecular cloud by a genuine GC (McKenzie & Bekki, 2018; Bastian & Pfeffer, 2022) or the merger of two GCs (Khoperskov et al., 2018; Mastrobuono-Battisti et al., 2019; Pfeffer et al., 2021) have been proposed as possible scenarios to explain the origin of complex stellar systems such as Terzan 5 and Liller 1. However, in both these scenarios, the subsolar dominant component (tracing the accretor GC) should show the typical GC anticorrelations, which is not the case for Liller 1 (see Fig. 4.7) nor for Terzan 5 (see Fig. 3 in Origlia et al., 2011). This evidence severely challenges the scenarios that invoke an accretor GC to explain the origin of these systems. Moreover, events like this are normally very rare, and it is unlikely that they could have occurred multiple times at very specific ages and metallicities, which would be required in order to explain Liller 1 and Terzan 5 multi-iron distributions with at least three main peaks. Even if this were the case, it cannot explain the underlying continuous star formation over almost the entire lifetime of Liller 1.

The suggestion that Terzan 5 and Liller 1 could have an extragalactic origin, that is, that they are the former nuclear star cluster of an accreted dwarf galaxy (see e.g., Brown et al., 2018; Alfaro-Cuello et al., 2019; Taylor et al., 2022), has been almost discarded (see e.g., Pfeffer et al., 2021, and references therein) based on kinematic and age-metallicity considerations. Metallicity also makes it very unlikely that Liller 1 and Terzan 5 could have formed in a significantly more metal-poor Galactic environment such as the halo (Moreno et al., 2022).

All these facts thus suggest that Liller 1 and Terzan 5 are likely complex stellar systems that

have formed and evolved within the Bulge. They are both very massive, with a present-day mass exceeding 10^6 $M_\odot$ (Lanzoni et al., 2010; Ferraro et al., 2021), but they probably were more massive in the past and were thus able to retain the SN ejecta and possibly to self-enrich, as shown by the recent chemical evolution modeling of Terzan 5 presented in Romano et al. (2023). Hence, they could be fossil fragments of the pristine clumps of stars and gas that may have contributed to forming the early Bulge (e.g., Immeli et al., 2004; Elmegreen et al., 2008, and references therein). These fragments could have survived complete disruption and could have evolved and self-enriched as independent systems within the bulge. They might also have been able to experience some new events of star formation at later epochs, as probed by their younger and more metal-rich subpopulations, and consistent with the reconstructed SFH of Liller 1 (Dalessandro et al., 2022).

Given the importance of this complex but intriguing stellar systems in shedding light on the bulge formation and evolution, detailed chemical studies of Terzan 5 and Liller 1 at higher spectral resolution are ongoing. The results will be presented in forthcoming works.

CHAPTER 5

High-resolution chemical characterization of M 54 giant stars

Based on:

- *Alvarez Garay, D. A., Mucciarelli, A., et al., in preparation*

5.1 Introduction

At the center of Sgr dSph there is an over-density of stars, classified as its NSC, which consists of two different groups: **(1)** a young ($\sim$ 2 Gyr) and metal-rich component ([Fe/H] up to ~ -0.5 dex), and **(2)** an old ($\sim$ 13 Gyr) and metal-poor component ($\langle$[Fe/H]$\rangle = -1.5$ dex). Different studies classified these two groups as distinct objects, a massive and metal-poor GC called M 54 and a metal-rich component directly linked to the nucleus of the galaxy (SgrN). M 54 is an old and metal-poor GC (Layden & Sarajedini, 1997; Bellazzini et al., 2008; Carretta et al., 2010b), with a wide metallicity spread. Moreover, it displays a clear Na-O anticorrelation (Carretta et al., 2010b), together with Mg-Al and Mg-K anticorrelations (Fernández-Trincado et al., 2021; Carretta, 2022). Such anticorrelations are not detected among the stars associated with SgrN (Carretta et al., 2010b).

Due to its properties, M 54 represents an ideal target to study the connection between the most massive GCs and the NSCs of dwarf galaxies. Indeed, The presence of a large metallicity spread in M 54 could be an indicator of its capability to retain the ejecta of core collapse SNe, but at the same time M 54 presents the typical features of GCs such as the anticorrelations among light elements. Therefore, the study of systems such as M 54 can help to understand if the most massive GCs can be former nuclei of dwarf galaxies and if they differ in some properties (morphology, stellar ages, chemical composition, etc.) from less massive GCs.

In the following Sections I will present the results of the chemical characterization of M 54 likely members, based on the largest high-resolution spectroscopic dataset available so far.

5.2 Observations and target selection

This work is based on a dataset of proprietary and archival data of 243 stars likely members of M 54. In particular, the employed spectra were acquired at the Very Large Telescope UT2 (Kueyen) with the optical multi-object spectrograph FLAMES (Pasquini et al., 2000) in the GIRAFFE+UVES combined mode under the programmes 075.D-0075 (P.I. Mackey, from July to August 2005), 081.D-0286 (P.I. Carretta, from June to September 2009), and 095.D-0539 (P.I. Mucciarelli, from July to August 2015). FLAMES/GIRAFFE (Pasquini et al., 2002) was employed in the HR mode that allows to allocate up to 132 fibers simultaneously, while FLAMES/UVES (Dekker et al., 2000) allows to allocate eight high resolution fibers.
Within the programme 075.D-0075 was adopted the GIRAFFE HR21 setup (R=18000 and a wavelength coverage $\sim$ 8484 $-$ 9000Å). Under the programme 081.D-0286 were employed two GIRAFFE setups: the HR11 (R=29500 and a wavelength coverage $\sim$ 5597-5840 Å) and the HR13 (R=26400 and a wavelength coverage $\sim$ 6120-6405 Å). Finally, within the programme 095.D-0539 was used the GIRAFFE+UVES combined mode. The adopted setups are the HR18 (R=20150 and a wavelength coverage $\sim$ 7468-7889 Å), and the UVES Red Arm 580 (R=45000 and wavelength coverage $\sim$ 4800-6800 Å).
Within the observed spectral range I was able to measure Fe, Mg, Al, Si, K, Ba, and La abundances.
All the spectra were reduced using the dedicated GIRAFFE and UVES ESO pipelines[1], which include the bias subtraction, flat field correction, spectral extraction, wavelength calibration and order merging.
In order to obtain the final dataset with all the targets likely belonging to M 54, I decided to exclude some stars from the three observing programmes. In particular, to derive reliable abundances I discarded all the stars with SNR $<$ 20. The majority of the stars excluded are those ones with a magnitude *Gaia* G $>$ 17. I discarded also all the stars out of the main sequence along the RGB associated to M 54. In this case I excluded some stars from the observing programme 095.D-0539, selected from the catalog presented in Monaco et al. (2004) but for which no spectroscopic information were available. I selected the stars also according to their RVs. I considered likely M 54 members all the stars having 100 km s^{-1} $\leq$ RV $\leq$ 180 km s^{-1}, following Ibata et al. (1997) and Bellazzini et al. (2008). For the remaining stars in the final sample, I inspected also the RUWE parameter given by the *Gaia* catalog. According to the *Gaia* documentation the RUWE is expected to be around 1.0 for sources where the single-star model provides a good fit to the astrometric observations. The threshold value

[1] https://www.eso.org/sci/software/pipelines/giraffe/giraffe-pipe-recipes.html https://www.eso.org/sci/software/pipelines/uves/

that could indicate that the source is non-single or otherwise problematic for the astrometric solution is 1.4. In my sample, there are a total of 25 stars with RUWE > 1.4 and among them there are nine stars with $2.0 <$ RUWE < 4.0 . However, I decided to maintain these stars in the dataset and I will discuss them in Sect. 5.3.2 and 5.5.1.

In Table 5.1 are reported the total number of stars analyzed for the different combination of setups. A total sample of 243 stars were analyzed in this study. In particular, I analyzed a total of 207 stars from the programme 075.D-0075, 42 stars from the programme 081.D-0286, and 94 stars from the programme 095.D-0539. As can be seen from Table 5.1 many stars are in common among the three programmes.

All the stars observed within the programmes 081.D-0286 and 095.D-0539 are classified as likely M 54 members (Carretta et al., 2010b; Carretta, 2022) thanks to their RVs and metallicities ([Fe/H] < -1.0 dex). On the other hand, no information are available for the stars observed only with the HR21 setup within the programme 075.D-0075.

Table 5.1: Stars observed for different combination of setups.

Setups	N
HR11, HR13, HR18, HR21	21
HR11, HR13, HR18	11
HR13, HR18, HR21	7
HR13, HR18	3
HR18, HR21	32
HR18	15
U580, HR21	5
HR21	149
TOTAL	243

The stars observed with the setups HR11 and HR13 were already analyzed by Carretta et al. (2010b), while the stars observed with the setup HR18 and in common with Carretta et al. (2010b) were analyzed by Carretta (2022). Also, a total of 83 stars in my dataset are present among the stars analyzed by Bellazzini et al. (2008) with the multi-object spectrographs DEIMOS on the Keck 2 telescope and with the HR21 setup, and among them 37 stars are in common also with the dataset analyzed by Carretta et al. (2010b). All the other stars present in my sample were never analyzed before making this one the largest database of chemical abundances of M 54 stars based on high-resolution spectra. The entire dataset was analyzed using a homogeneous set of atmospheric parameters.

5.3 Atmospheric parameters and radial velocities

5.3.1 Atmospheric parameters

In this work I determined the atmospheric parameters by using the photometric information coming from the *Gaia* DR3 (Gaia Collaboration et al., 2016, 2023). In Fig. 5.1 is illustrated the spatial distribution of the total sample, with respect to the cluster center. I would like to note that all the selected targets are enclosed within $\sim 10'$ from the cluster center, being the tidal radius $r_t = 9'.868$ (Harris, 2010). The position of the spectroscopic targets analyzed in this work are shown in the CMD in Fig. 5.2.

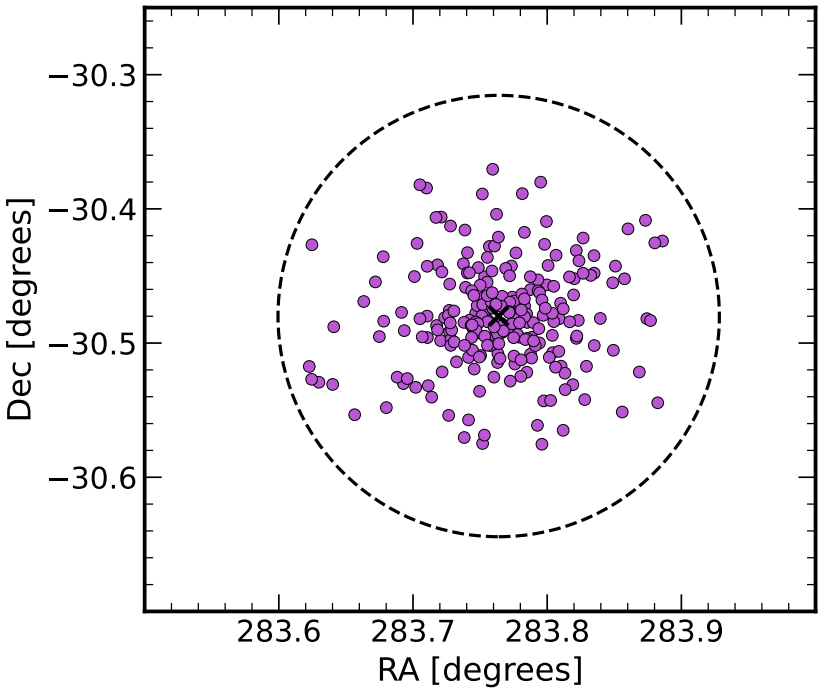

FIGURE 5.1: Coordinate positions of the observed targets are displayed by the purple circles. The black cross denotes the cluster center (283.°76385, −30.°47986) according to Baumgardt & Hilker (2018). The dashed black circle displays the tidal radius ($r_t = 9'.868$; Harris, 2010).

I derived the effective temperatures (T_{eff}) for the stars in the sample from the empirical $(BP - RP)_0$−T_{eff} relation by Mucciarelli et al. (2021), based on the infrared flux method. While deriving the $(BP-RP)_0$ color I applied the quality metric introduced by Evans et al. (2018) to determine whether the derived *Gaia* color is reliable or not. The metric is called excess factor and is defined as the ratio between the total flux in BP and RP, and the G-band flux: $C = (I_{BP} - I_{RP})/I_G$. The C value should be slightly larger than one, therefore values much larger than one are probably caused by problems in the BP or RP photometry. In Riello

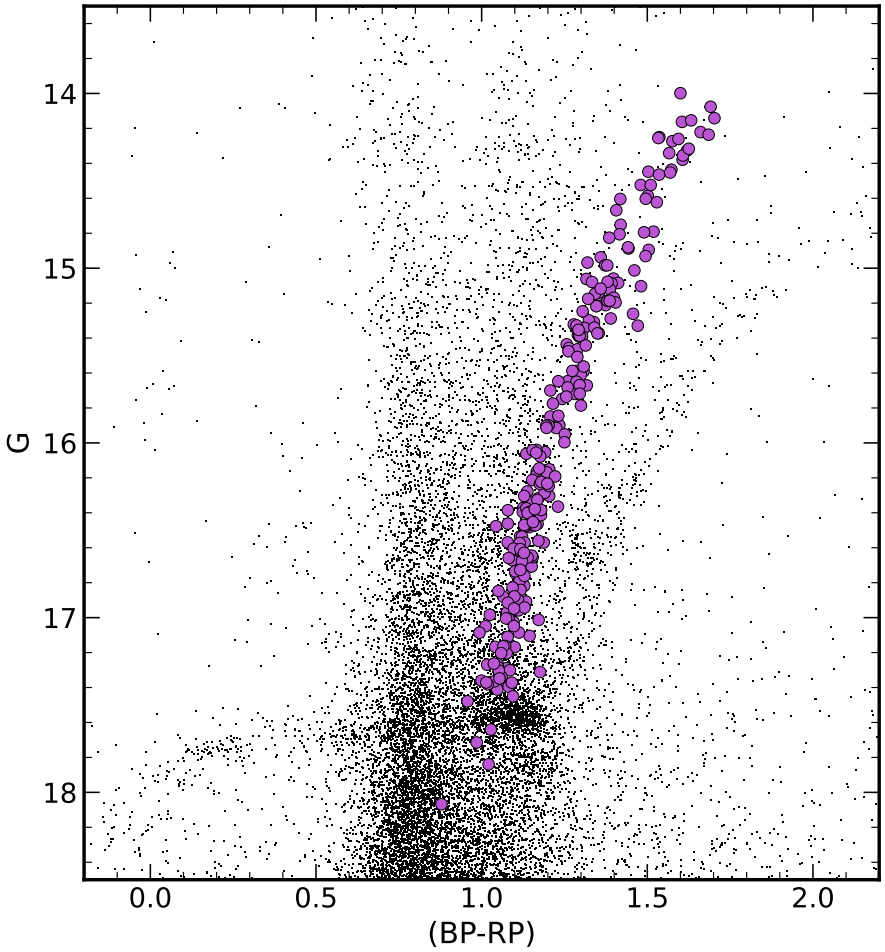

FIGURE 5.2: CMD of M 54. Black points represent all the targets of M 54 observed with *Gaia* (Gaia Collaboration et al., 2016, 2023), while the purple circles represent the target stars.

et al. (2021) is described in detail the entire procedure I used. Here I just want to highlight the fact that for all the stars for which I did not use the *Gaia* photometry, I employed the photometric catalog by Monaco et al. (2002). I used the transformations present in the *Gaia* documentation[2] to transform the $(V-I)$ in $(BP-RP)$ color. I obtained the dereddened color $(BP-RP)_0$ color by assuming a color excess factor $E(B-V) = 0.15 \pm 0.03$ (Harris, 2010) and adopting the iterative recipe proposed by Gaia Collaboration et al. (2018). I calculated the internal errors in T_{eff} as the sum in quadrature of the errors due to the uncertainties in photometric data, reddening, and $(BP-RP)_0 - T_{eff}$ relation. The errors are of the order of $\sim 90 - 130$ K.

Regarding the surface gravities ($\log g$) I adopted the Stefan-Boltzmann relation, using the photometric temperature described above and assuming a typical mass for the giants of

[2] https://gea.esac.esa.int/archive/documentation/GDR3/Data_processing/chap_cu5pho/cu5pho_sec_photSystem/cu5pho_ssec_photRelations.html

0.80 $M_{\odot}$. I computed the luminosities by using the dereddened G-band magnitude with the bolometric corrections by Andrae et al. (2018) and assuming a true distance modulus $(m - M)_0 = 17.10 \pm 0.15$ mag (Monaco et al., 2004). By propagating the uncertainties in T_{eff}, distance modulus, and photometry I obtained uncertainties in $\log g$ of the order of ~ 0.1 dex.

I derived the microturbolent velocities (v_t) from the $\log g - v_t$ relation provided by Kirby et al. (2009). In this relation, the formal error in v_t due to the uncertainties in $\log g$ is ~ 0.02 km s^{-1}, but I assumed a conservative error of 0.2 km s^{-1}.

The derived atmospheric parameters, together with additional information are reported in Table 5.2

5.3.2 Radial velocities

I determined RVs by using the standard cross-correlation technique implemented in the `IRAF` task `FXCOR`. A synthetic spectrum generated with the `SYNTHE` code (Sbordone et al., 2004; Kurucz, 2005) was employed as the template spectrum, convolved with a Gaussian profile to replicate the instrumental profile of the GIRAFFE and UVES spectrographs, accurately.

When more than one spectrum for star was available, the final heliocentric RV was calculated as the mean of the individual RV values. Table 5.2 presents the final heliocentric RVs for all targets. The uncertainties reported are calculated as the dispersion of the mean RV normalized to the root mean square of the number of exposures utilized; when only one spectrum per star was present, I used the error provided by `FXCOR`.

As a sanity check, for all the stars with RUWE > 1.4 I checked for any possible RV variation among different spectra and I found that only one star, namely #3801447, shows signs of RV variations higher than 2 km s^{-1} and a RUWE $= 3.73$. For all the other stars no signs of RV variations were found.

From the analysis of 243 stars I derived a final RV mean value of 142.4$\pm$0.5 ($\sigma = 8.4$) km s^{-1}. This value is perfectly in agreement with the mean values reported by Carretta et al. (2010b) of 143.7 ($\sigma = 8.3$) km s^{-1} for a sample of 76 stars, and with the value quoted by Bellazzini et al. (2008) of 140.9$\pm$0.4 ($\sigma = 9.3$) km s^{-1} for a sample of 425 stars.

Figure 5.3 illustrates the heliocentric RV distribution of the stars in the dataset.

5.4 Abundance analysis

In this work I measured chemical abundances by using the proprietary code `SALVADOR`, which performs a χ^2 minimization between the line under analysis and a grid of synthetic spectra

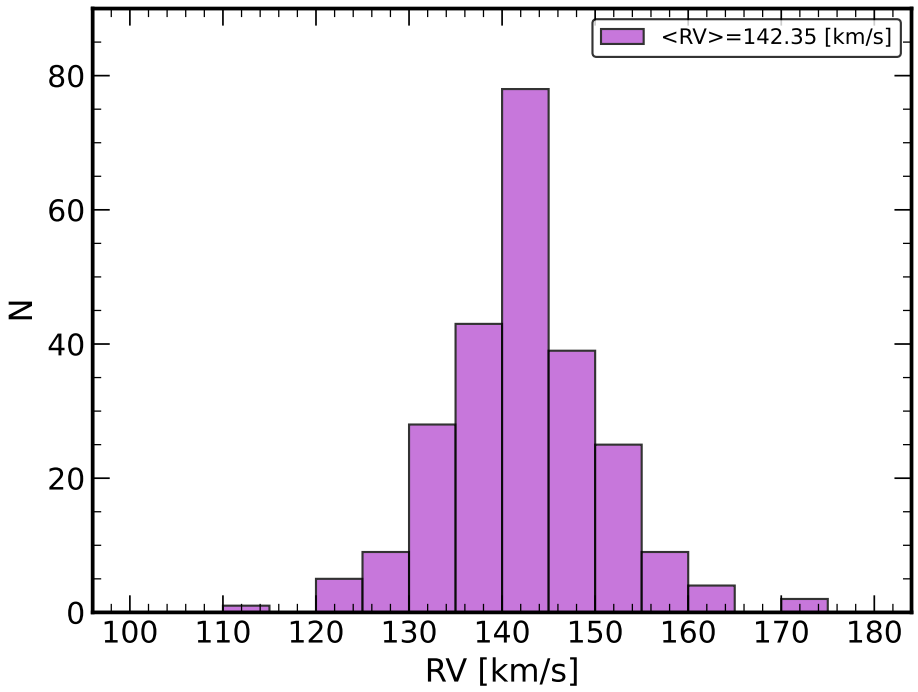

FIGURE 5.3: Histogram of the RVs for the observed targets of this work.

calculated with the appropriate atmospheric parameters and varying only the abundance of the considered element. I calculated the grids of synthetic spectra by using the `SYNTHE` code (Sbordone et al., 2004; Kurucz, 2005), and by computing one-dimensional, plane-parallel, local thermodynamic equilibrium (LTE) model atmospheres employing the `ATLAS9` code (Sbordone et al., 2004; Kurucz, 2005).

For abundance determination, I performed a thorough linelist selection across the spectral range covered by the used setups, selecting lines that are unblended, unsaturated, and not contaminated by telluric features at the resolution of selected setups, respectively. The atomic information for these chosen lines was sourced from the Kurucz-Castelli linelist database[3]. For the determination of the abundance ratios I adopted the solar reference from Grevesse & Sauval (1998).

To determine star-to-star uncertainties associated with the chemical abundances I used the same approach described in Sect. 3.2.2.3. The errors associated with the adopted atmospheric parameters were computed by recalculating chemical abundances, varying only one parameter at a time (T_{eff}, $\log g$ or v_t) by its uncertainty and keeping the other parameters fixed to their best value. Internal errors, associated with the measurement process, were estimated as the line-to-line scatter divided by the root mean square of the number of lines. When only

[3] `https://wwwuser.oats.inaf.it/castelli/linelists.html`

one line was available, such in the case of K, the uncertainties were estimated by resorting to a Monte Carlo simulation. I created synthetic spectra with representative values for the atmospheric parameters of the analyzed stars, and I injected Poissonian noise, according to the SNR of the observed spectra. For each line, I created a total of 200 noisy spectra and derived the abundance with the same procedure used for observed spectra. Finally, I calculated the internal error as the standard deviation of the abundances derived from the 200 simulations.

5.5 Results

In the following subsections, I will present in detail the results of the chemical analysis I performed within this study. The derived chemical abundances are reported in Table 5.2, together with their measurement uncertainties. Neutral element abundances are mostly affected by the uncertainty in the T_{eff}, while Ba and La mainly affected the uncertainty in the log g, being in the ionized state.

5.5.1 Iron distribution

In Fig. 5.4 can be seen the MDF for the analyzed sample of likely members of M 54. From Fig. 5.4 can be noted that there is a small fraction of stars (6) with [Fe/H] > -1.0 dex. These metal-rich stars are not present in the samples analyzed by Bellazzini et al. (2008) or by Carretta et al. (2010b). This subsample of stars is located along the RGB usually attributed to M 54, as can be seen in Fig. 5.5. For this subsample of metal-rich stars, I have only the spectra collected with the HR21 setup, from which I derived an average metallicity [Fe/H] $= -0.79 \pm 0.06$ ($\sigma = 0.15$) dex. By using a BaSTI isochrone (Hidalgo et al., 2018) I found that this subsample of stars could be actually a very young population. Indeed, they are well reproduced by an isochrone of 2 Gyr, [Fe/H] $= -0.8$ dex, and [α/Fe] $= 0.0$ dex. It is noteworthy that the SgrN stars that populate the red part of the RGB are compatible with this metallicity value, but are much older ($\sim$ 8 Gyr; Bellazzini et al., 2006). Another interesting possibility is that they are evolved BSSs, that appear rejuvenated. Indeed, BSSs are thought to form in twin systems where two stars form a tight binary. In such binary, the stars can experience a head-on collision (Leonard, 1989), combining their fuel and mass and to form a single hot more massive star or the star with lower mass can drain its larger mass companion of fresh hydrogen increasing its own mass (Collier & Jenkins, 1984).

Table 5.2. Data for the target stars belonging to M 54. The adopted solar abundances for the measured chemical elements are from Grevesse & Sauval (1998) and they are reported in the header of each element abundance column.

ID	ID *Gaia*	G [mag]	RV [km s^{-1}]	T_{eff} [K]	log g [dex]	v_t [km s^{-1}]	[Fe/H] 7.50	[Mg/Fe] 7.58	[Al/Fe] 6.47	[Si/Fe] 7.55	[K/Fe] 5.12	[Ba/Fe] 2.13	[La/Fe] 1.17
M54_1500138	6760429401842331136	14.5856	133.43 ± 0.17	4248	0.77	1.95	-1.54 ± 0.11	0.30 ± 0.03	0.74 ± 0.05	0.26 ± 0.13	0.28 ± 0.15	0.17 ± 0.11	0.23 ± 0.09
M54_1500190	6760429157003643904	14.7517	134.73 ± 0.38	4332	0.89	1.93	-1.42 ± 0.12	0.34 ± 0.03	0.55 ± 0.07	0.21 ± 0.13	0.21 ± 0.12	0.23 ± 0.11	0.25 ± 0.11
M54_1500360	6760449875922016384	15.2880	142.62 ± 0.24	4408	1.15	1.87	-1.17 ± 0.12	0.13 ± 0.03	1.30 ± 0.05	0.37 ± 0.14	...	-0.05 ± 0.11	0.03 ± 0.11
M54_2300345	6760424831996623616	16.3033	150.67 ± 0.20	4712	1.72	1.73	-1.37 ± 0.16	0.47 ± 0.09	1.05 ± 0.12	...	0.49 ± 0.13	...	...
M54_2300384	6760413046606337920	16.3751	138.84 ± 0.45	4821	1.80	1.72	-1.25 ± 0.16	0.40 ± 0.09	...	...	0.52 ± 0.11	...	...
M54_2300406	6760413080966064000	16.3376	141.51 ± 0.20	4798	1.78	1.72	-1.50 ± 0.16	0.12 ± 0.09	...	...	0.51 ± 0.09	...	...
M54_2300585	6760449807202520960	16.7071	135.31 ± 0.20	4808	1.93	1.69	-1.20 ± 0.16	...	...	...	0.28 ± 0.09	...	...
M54_2300787	6760425278673262848	17.1673	114.15 ± 2.64	5026	2.22	1.62	-1.04 ± 0.17	...	1.00 ± 0.13	...	0.58 ± 0.13	...	...
M54_2301825	6760449738495636224	18.0680	129.85 ± 0.53	5370	2.72	1.50	-1.49 ± 0.15	...	...	...	...	...	...
M54_2406717	6760423079650001408	16.3158	135.39 ± 0.48	4766	1.75	1.73	-1.37 ± 0.16	0.36 ± 0.09	...	...	0.44 ± 0.10	...	...
M54_2407142	6760423801205120256	14.4363	141.84 ± 0.25	4157	0.65	1.98	-1.48 ± 0.09	0.37 ± 0.03	0.01 ± 0.05	0.24 ± 0.12	0.09 ± 0.15	0.08 ± 0.10	0.25 ± 0.08
M54_2407725	6760424415355641728	17.1593	141.37 ± 0.20	4940	2.17	1.63	-1.05 ± 0.19	...	...	...	...	...	...
M54_2408806	6760423904283769472	15.6050	144.14 ± 0.43	4574	1.37	1.81	-1.24 ± 0.15	0.00 ± 0.09	1.15 ± 0.09	...	...	0.12 ± 0.13	0.25 ± 0.15
M54_2410051	6760424625838217344	15.3719	129.64 ± 0.23	4465	1.22	1.85	-1.38 ± 0.12	0.41 ± 0.03	-0.05 ± 0.09	0.16 ± 0.12	0.17 ± 0.12	-0.04 ± 0.12	0.16 ± 0.12
M54_2410091	6760424655873852672	16.7475	149.00 ± 0.20	4886	1.98	1.67	-1.68 ± 0.14	0.30 ± 0.09	...	...	0.26 ± 0.16	...	...
M54_2421106	6760428710323079552	14.3794	143.91 ± 0.20	4114	0.60	1.99	-1.59 ± 0.11	0.42 ± 0.04	0.10 ± 0.06	0.28 ± 0.14	...	-0.11 ± 0.12	0.21 ± 0.09
M54_2421126	6760426137650218368	14.6040	133.89 ± 0.21	4330	0.83	1.94	-1.61 ± 0.16	0.31 ± 0.09	0.59 ± 0.11	0.19 ± 0.16	0.13 ± 0.09	0.01 ± 0.13	0.22 ± 0.15
M54_2423720	6760428783366999168	14.5238	145.85 ± 0.34	4242	0.74	1.96	-1.68 ± 0.12	0.35 ± 0.03	0.50 ± 0.07	0.26 ± 0.13	0.21 ± 0.12	0.07 ± 0.13	0.31 ± 0.11
M54_3700547	6760429706759428608	16.8178	141.08 ± 0.42	4846	1.99	1.67	-1.32 ± 0.15	...	...	...	0.41 ± 0.13	...	...
M54_3700607	6760428057488002432	16.8809	142.96 ± 0.88	4977	2.08	1.65	-1.20 ± 0.18	...	0.44 ± 0.23	...	...	...	...
M54_3700670	6760426927941211520	16.9082	144.56 ± 0.87	4832	2.02	1.67	-1.36 ± 0.14	...	...	...	0.72 ± 0.10	...	...
M54_3700741	6761180677519856512	17.1099	154.44 ± 0.47	4938	2.15	1.64	-1.44 ± 0.18	...	...	...	0.50 ± 0.16	...	...

Note. — This is a portion of the entire table, which will be available in its entirety in electronic form.

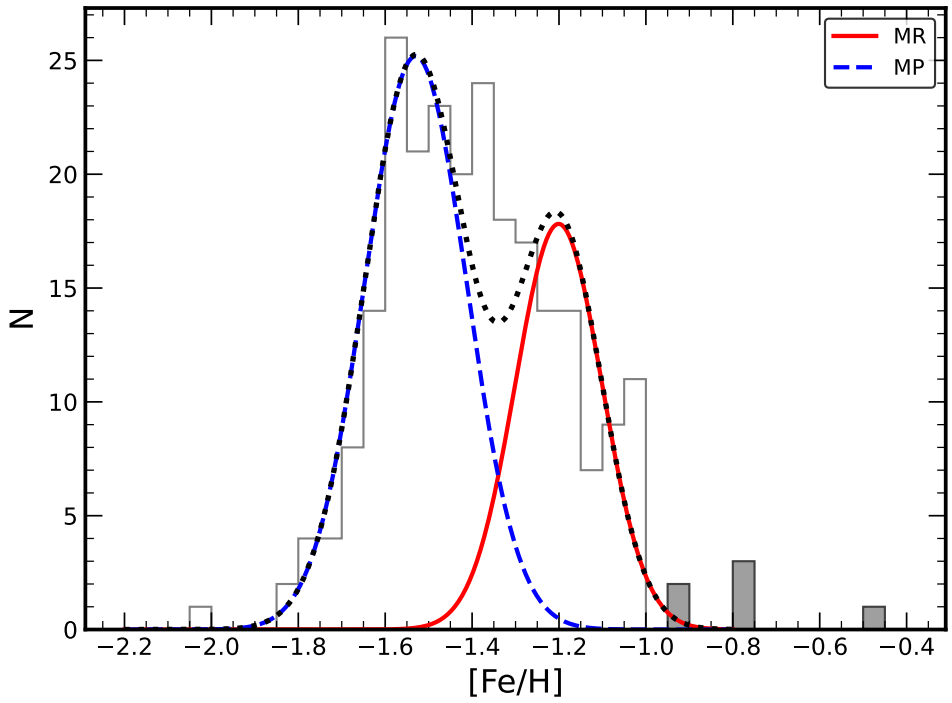

FIGURE 5.4: The histogram displays the MDF of M 54. The six stars excluded from the initial sample are shown as gray bins. The empty histogram shows the remaining 237 stars. In this sample two Gaussian components can be identified and they represent the MP (blue dashed line) and the MR (red solid line) components, respectively. Is also shown as a dotted black line the Gaussian kernel fit of the overall distribution.

The final result is a star that appears to be in a early phase of its evolution and thus seems to be younger than actually is. With the actual data I cannot state which one of the two described possibilities is the real case for these very metal-rich stars. I decided to exclude these six stars from the following analysis on the MDF.

From the remaining 237 stars I obtain an average metallicity [Fe/H] $= -1.41 \pm 0.01$ ($\sigma = 0.19$) dex. This value is in good agreement with Bellazzini et al. (2008) ($\langle$[Fe/H]$\rangle = -1.45$ dex), while is ~ 0.15 and ~ 0.10 dex higher than the values found by Carretta et al. (2010b) and Mucciarelli et al. (2017), respectively. The presence of any possible shift in the zero point of the MDF does not affect the results presented here.

Since the MDF here presented comes from different datasets obtained at different epochs and under different programmes, in which different set of lines and spectra are used is useful to check if there are differences in the [Fe/H] obtained from the different spectra. In order to check this, I considered the 21 stars for which I have spectra collected within the three observing programmes and for each star I calculated the [Fe/H] independently from the spectra of

each programme[4]. Only for two stars the difference in [Fe/H] is at level of ~ 0.1 dex among the different programmes, while for the remaining ones this difference is less than 0.05 dex indicating that the dataset is homogeneous in terms of derived metallicity. I performed the same calculation for the five stars observed with both the HR21 and UVES CD580 setups, obtaining similar results.

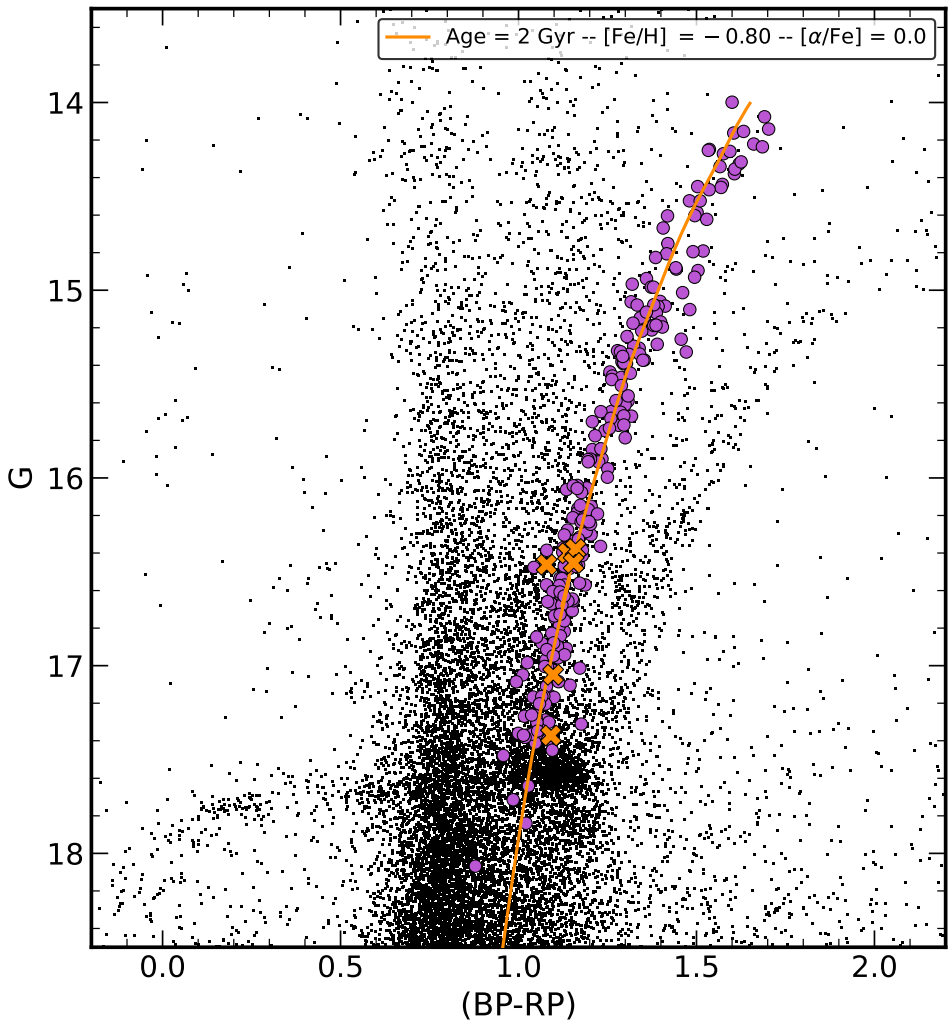

FIGURE 5.5: Same as Fig. 5.2, but with marked as orange crosses the stars with [Fe/H] > -1.0 dex. The solid orange line represents a BaSTI isochrone with an age of 2 Gyr, [Fe/H] $= -0.8$ dex, and [α/Fe] $= 0.0$ dex.

I also considered separately the [Fe/H] distribution for the stars with RUWE *Gaia* parameter > 1.4 and I found that they are distributed in the same way as the stars with RUWE < 1.4

[4]For the programme 081.D-0286 I calculated [Fe/H] from all the lines coming from HR11 and HR13 spectra since they were collected at the same epoch.

with a mean metallicity slightly lower. Indeed, if I divide the sample based on the RUWE value and at [Fe/H] < -1.0 dex, I obtain that the stars with RUWE > 1.4 have a mean [Fe/H] $= -1.49 \pm 0.03$ dex ($\sigma = 0.17$ dex, 24 stars), while the stars with RUWE < 1.4 have a mean [Fe/H] $= -1.40 \pm 0.01$ dex ($\sigma = 0.19$ dex, 213 stars).
Since M 54 displays a wide MDF, I employed the `scikit-learn`[5] implementation of GMM to study the presence of distinct populations in the distribution of stars with [Fe/H] < -1.0 dex. The GMM classification allowed to identify two different groups, corresponding to the following peaks of metallicity: [Fe/H] $= -1.53$ dex ($\sigma = 0.13$ dex) and [Fe/H] $= -1.22$ dex ($\sigma = 0.12$ dex). The first group consists of 148 stars (61%) and was defined as the metal-poor (MP) component of M 54, while the second group consists of 89 stars (39%) and was classified as the metal-rich (MR) component of M 54. The MDF together with the Gaussian kernels resulting from this investigation is visible in Fig. 5.4.

5.5.2 Mg, Al, Si, and K distributions

In this work I derived the abundances of those elements involved in the complete MgAl burning chain. In particular I derived Mg, Al, Si, and K abundances for a total of 155, 51, 45, and 78 stars, respectively. This is the largest dataset of M 54 member stars for which Mg, Al, Si, and K abundances are derived from high-resolution spectra. To derive the Mg elemental abundances, I used the Mg line at 5711 Å, the Mg triplet at 6318-6319 Å, and the line at 8806 Å, included in the HR11, HR13, HR21, and UVES CD580 setups, respectively. To derive Al abundances I used the doublets at 6696-6698 Å and at 7835-7836 Å included in the UVES CD580 and HR18 setups, respectively. To derive Si abundances I used some lines (less than 10) included in the HR11, HR13 and UVES CD580 setups. Finally, the K abundances were derived from the second K I resonance line at 7699 Å[6] present in the HR18 setup. In this work I corrected K abundances for the Non-LTE effects by interpolating into the grids of Takeda et al. (2002).
In Fig. 5.6 can be observed the distribution of [Mg/Fe], [Al/Fe], [Si/Fe], and [K/Fe] abundance ratios as a function of metallicity. I divided the dataset into the two MP and MR components, respectively.

1. In the case of [Mg/Fe] distribution, the MP component consists of 110 stars and is characterized by a high level of Mg, typical of the Galactic halo metal-poor GCs. In particular, [Mg/Fe] ranges from 0.08 to 0.80 dex with an average [Mg/Fe] $= +0.41$ dex ($\sigma = 0.14$ dex). The MR component consists of 45 stars and is characterized by

[5] `https://scikit-learn.org/stable/modules/mixture.html`
[6] The first K I resonance line at 7664 Å is heavily contaminated by telluric lines, and therefore is not possible to use this line to derive K abundances.

a decline in the Mg abundances compared to the MP component. Indeed, the [Mg/Fe] ranges from -0.11 dex up to 0.65 dex with an average [Mg/Fe] $= +0.28$ dex ($\sigma = 0.17$ dex).

2. For the [Al/Fe] distribution, the behavior is the opposite with respect to the [Mg/Fe] distribution, with the MR component having higher values of [Al/Fe] compared to the MP one. Indeed, the MP component, made by 34 stars spans a wide range of [Al/Fe], with values ranging from [Al/Fe] $= 1.38$ dex down to -0.16 dex and an average [Al/Fe] $= 0.51$ dex ($\sigma = 0.40$ dex). On the other hand, the MR component consists of 17 stars ranging from [Al/Fe] $= 1.46$ dex down to 0.12 dex and an average [Al/Fe] $= 0.91$ dex ($\sigma = 0.40$ dex).

3. The [Si/Fe] distribution is quite similar to the [Al/Fe] one. In this case, the MP component is composed by 35 stars, covering the range between [Si/Fe] $= 0.38$ dex and [Si/Fe] $= 0.09$ dex, with an average [Si/Fe] $= 0.25$ dex ($\sigma = 0.07$ dex). The MR component consists of just 10 stars, distributed from 0.43 down to 0.21 dex, with an average [Si/Fe] $= 0.30$ dex ($\sigma = 0.08$ dex). In this distribution the observed spread is smaller than the typical uncertainty in the abundance determination ($\sigma_{\rm [Si/Fe]} = 0.13$ dex).

4. The [K/Fe] distribution in the MP component consists of 52 stars. With the exception of one K-poor star that I will discuss in Sect. 5.5.5, the stars in this subsample are distributed from [K/Fe] $= 0.72$ dex down to [K/Fe] $= 0.01$ dex, with an average [K/Fe] $= 0.27$ dex ($\sigma = 0.15$ dex). The MR component is composed by 26 stars ranging from [K/Fe] $= 0.62$ dex down to [K/Fe] $= 0.05$ dex, with an average [K/Fe] $= 0.37$ dex ($\sigma = 0.14$ dex). In both the metallicity components the observed spread is slightly larger than the typical uncertainty in the abundance determination ($\sigma_{\rm [K/Fe]} = 0.13$ dex).

The run of the [Mg/Fe], [Al/Fe], [Si/Fe], and [K/Fe] as a function of metallicity here presented reflects the behavior of both [O/Fe] and [Na/Fe] as a function of [Fe/H] presented by Carretta et al. (2010b) (see their Fig. 15) for the M 54 stars. Indeed, the most metal-poor stars in Carretta et al. (2010b) sample have both low and high content of [O/Fe] and [Na/Fe], while the most metal-rich stars are characterized mainly by a high content of [Na/Fe] and low content of [O/Fe]. If I divide their sample of M 54 at [Fe/H] $= -1.56$ dex (this is the mean value found by Carretta et al., 2010b) I find that the stars more metal-poor than this value have a mean [O/Fe] $= 0.20$ dex and [Na/Fe] $= 0.36$ dex, while the stars more metal-rich than [Fe/H] $= -1.56$ dex have a mean [O/Fe] $= 0.02$ dex and [Na/Fe] $= 0.49$ dex. In

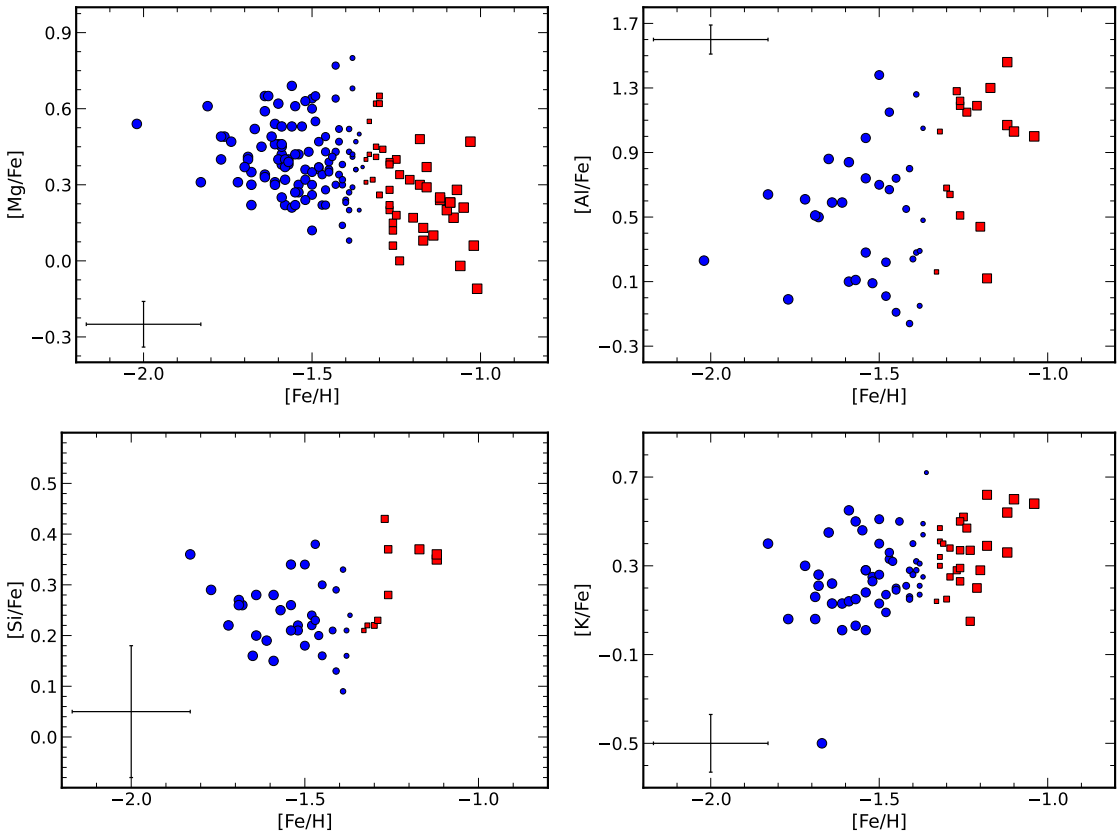

FIGURE 5.6: The four panels depict the distribution of [Mg/Fe] (top-left), [Al/Fe] (top-right), [Si/Fe] (bottom-left), and [K/Fe] (bottom-right) as function of [Fe/H] for the M 54 stars. The MP stars are shown as blue circles, while the MR stars are represented with red squares. The size of each point indicates its probability of belonging to the MP or MR subpopulation, the larger the symbol, the higher the probability. The error bar in the corner of each panel represents the typical error associated with the measurements.

the context of MPs, the metal-poor stars in Carretta et al. (2010b) are characterized by the presence of both FG and SG, respectively, while the metal-rich stars seem to be dominated by the presence of SG with high content of Na and low content of O. This seems to be the case also for the [Mg/Fe], [Al/Fe], [Si/Fe], and [K/Fe] distributions in my sample, where the MR component seems to be dominated by the presence of stars with lower (higher) content of Mg (Al, Si, and K) with respect to the MP component.

5.5.3 Mg-Al anticorrelation

From this analysis I derived Mg and Al abundances simultaneously for a total of 45 stars. These stars show a spread in both Mg and Al abundances and display a clear Mg-Al anti-correlation, as can be seen in Fig. 5.7. This is largest dataset to the date in which a Mg-Al anticorrelation is observed in M 54. Indeed, Carretta et al. (2010b) found hint of Mg-Al

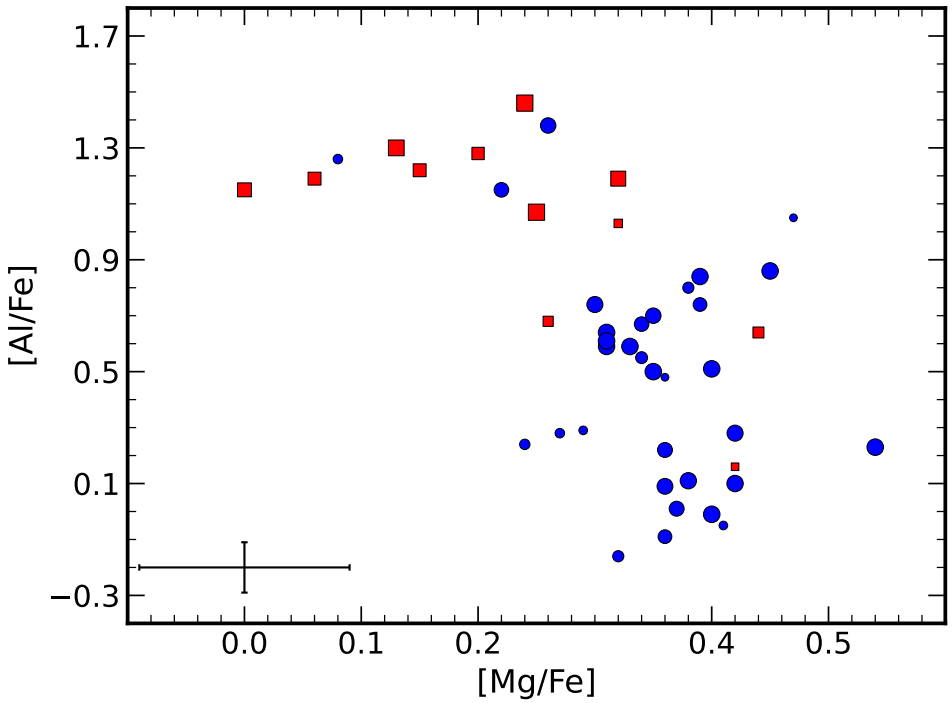

FIGURE 5.7: Mg-Al anticorrelation for the stars of M 54. The blue circles represent the MP stars of M 54, while the red squares the MR stars. The size of each point indicates its probability of belonging to the MP or MR subpopulation, the larger the symbol, the higher the probability. The error bar in the bottom-left corner represents the typical measurement error associated with the data.

anticorrelation from the analysis of six stars, while more recently Fernández-Trincado et al. (2021) detected this anticorrelation in a sample of 19 stars observed within the APOGEE survey (Majewski et al., 2017).

In the Mg-Al anticorrelation here found, 33 stars belong to the MP component. The majority of these stars are distributed in a small range of Mg abundances, between ~ 0.2 and ~ 0.45 dex in [Mg/Fe], while they cover a wide range of [Al/Fe] from ~ -0.2 up to ~ 0.9 dex. Only three stars stand out of this locus, having [Mg/Fe] < 0.25 dex and [Al/Fe] $\sim 1.2/1.3$ dex. It is important to note that none of the observed stars have [Mg/Fe] < 0.0 dex.

The MR stars composing the Mg-Al anticorrelation are 12. They are distributed from [Mg/Fe] ~ 0.0 dex up to ~ 0.4 dex, while with the exception of three stars they have a high content of Al, being all with [Al/Fe] > 1.0 dex. Of the three stars with lower Al abundance, one has [Al/Fe] ~ 0.1 dex, while the other two have [Al/Fe] ~ 0.7 dex. Also in this subsample none of the stars has [Mg/Fe] < 0.0 dex.

The existence of a clear Mg-Al anticorrelation in M 54, with stars displaying large variations in the Al abundances, is the signature of Al production through the MgAl chain at very high temperatures (Ventura et al., 2016; Dell'Agli et al., 2018). The Al variations observed cover

$\sim$ 1.5 dex, which is quite large. However, such value is not surprising, since large variations in the Al abundances are usually found in those GCs very massive and/or metal-poor (Shetrone, 1996; Mészáros et al., 2015; Pancino et al., 2017). I recall that M 54 is the second most massive GC of the Milky Way.

5.5.4 Mg-Si anticorrelation

In this work I measured Mg and Si abundances simultaneously for a total of 45 stars. All the stars cover the same range of [Mg/Fe] and [Si/Fe], ranging from $\sim$ 0.05 dex to $\sim$ 0.45 dex. In Fig. 5.8 can be seen the overall Mg-Si anticorrelation among the stars of M 54. From a run of Spearman correlation test I obtained a probability that the two abundances are non-correlated of $p = 0.049$ and a correlation coefficient $C_s = -0.29$.

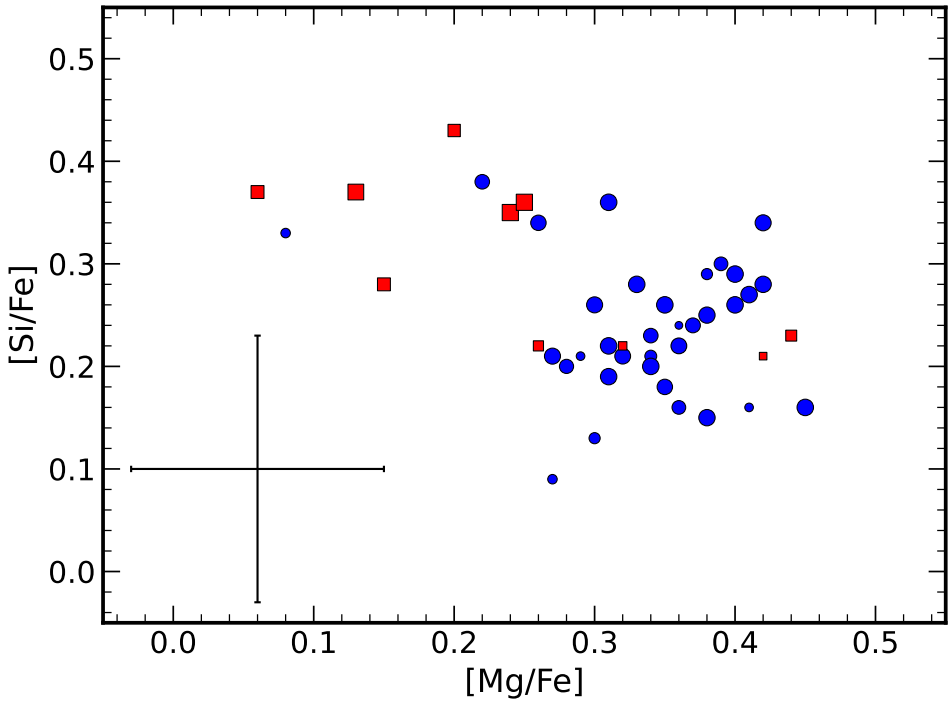

FIGURE 5.8: Same as Fig. 5.7, but for the Mg-Si anticorrelation.

If I consider the two different groups of metallicity separately, I have that the MP component consists of 35 stars, distributed in $\sim$ 0.2 dex in [Mg/Fe] from $\sim$ 0.25 dex to $\sim$ 0.45 dex, with the exception of one star that has [Mg/Fe] = 0.08 dex. [Si/Fe] is distributed from $\sim$ 0.1 dex to $\sim$ 0.4 dex. In this subsample, no anticorrelation is present. Indeed, the Spearman correlation test gives a probability that the two abundances are non-correlated of $p = 0.81$ and a correlation coefficient $C_s = 0.04$. The MR component is made by 10 stars. Six stars have a high content of Si, with [Si/Fe] $\gtrsim$ 0.3 dex, while the remaining four have a lower

content of Si, with [Si/Fe] $\sim$ 0.22 dex. For the MR component the Spearman correlation test gives a probability that the two abundances are non-correlated of $p = 8.5 \times 10^{-3}$ and a correlation coefficient $C_s = -0.77$. However, I would like to note that the four stars with lower Si content have a lower probability to belong to the MR component compared to the other six stars, due to their metallicity. Indeed, they have [Fe/H] in the range between -1.33 and -1.29 dex, which is very close to the split value given by the GMM. Finally, the errors associated with the Si measurement process are quite large, and this prevent to clearly assess on the presence of a Mg-Si anticorrelation even though the actual results are suggesting its presence.

From Fig. 5.7 and Fig. 5.8 can be observed that the stars with the higher content of Al are the same with the higher content of Si, and vice versa. The presence of such Al-Si correlation is the result of a leakage from the MgAl chain into ^{28}Si through proton capture reaction at very high temperatures (Yong et al., 2005; Mészáros et al., 2015; Masseron et al., 2019).

5.5.5 Mg-K anticorrelation

Within the analyzed dataset I was able to measure Mg and K abundances simultaneously for a total of 55 stars. In Fig. 5.9 can be observed the distribution of [K/Fe] as a function of [Mg/Fe].

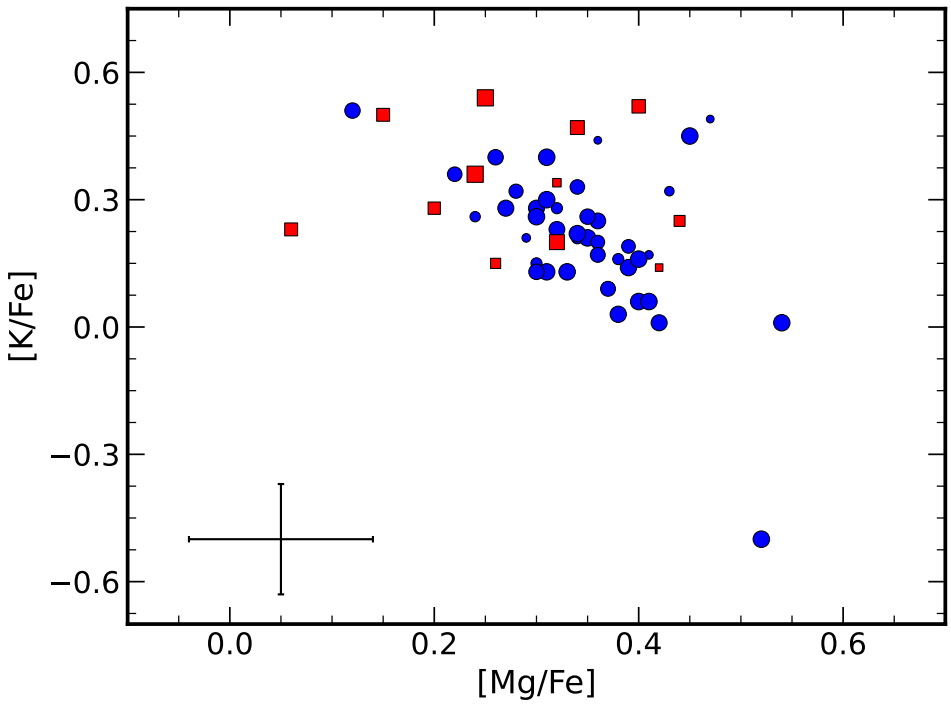

FIGURE 5.9: Same as Fig. 5.7, but for the Mg-K anticorrelation.

A Mg-K anticorrelation is present among the 55 stars of M 54, given principally by the stars belonging to the MP component (stars with [Fe/H] < -1.34 dex). The stars in the Mg-K anticorrelation belonging to the MP component are 43 and the majority are distributed from ~ 0.0 dex up to ~ 0.5 dex in both [Mg/Fe] and [K/Fe]. For this group the anticorrelation is statistically significant. Indeed, the Spearman correlation test gives a probability that the two abundances are non-correlated of $p = 3.2 \times 10^{-3}$ and a correlation coefficient $C_s = -0.44$. On the other hand, no anticorrelation is present among the 12 stars comprising the MR component. For this group the p-value is $p = 0.60$.

Among the MP component I found one star, named #3800225, having [K/Fe] $= -0.50$ dex, a value that is much lower than all the other stars making the MP component. I tested whether the derived abundance for this star is real or affected by some artifact introduced during the analysis, but I was not able to find any correlation with the adopted stellar parameters. In Fig. 5.10 can be seen the K line for the K-poor star compared with a reference star, named #2421126, having similar parameters ($T_{\rm eff}$, $\log g$, v_t, and [Fe/H]) but with [K/Fe] $= 0.13$ dex, which is compatible with the abundances of the bulk of the MP component. An obvious difference in the line depths is present, that implies a real difference in the derived K abundances. Therefore, I conclude that the derived [K/Fe] for #3800225 is real and not an artifact of the analysis.

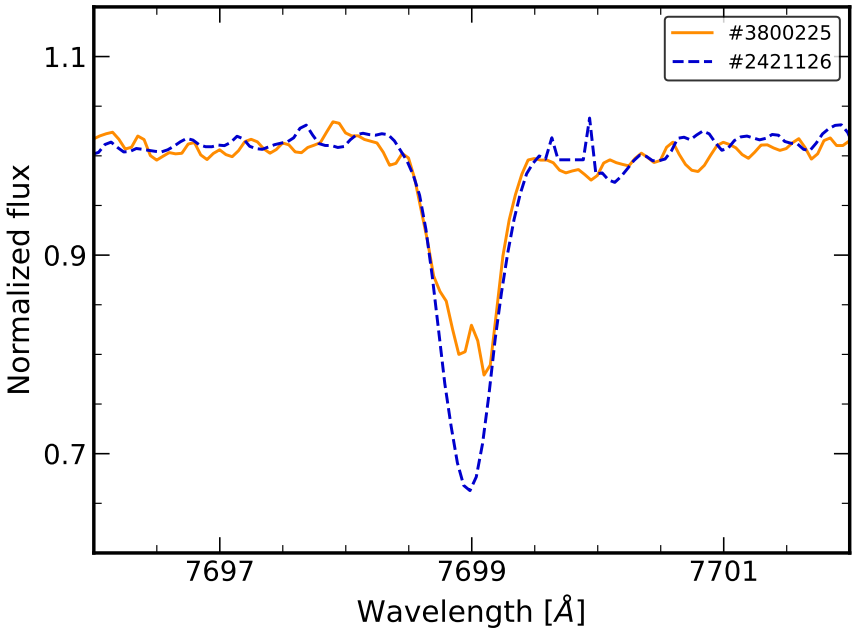

FIGURE 5.10: Comparison between the HR18 GIRAFFE spectra of #3800225 (solid orange line) and #2421126 (dashed blue line) stars around the K line at 7699 Å. The depletion of K of #3800225 compared to #2421126 is clearly visible from the comparison.

The presence of a Mg-K anticorrelation in M 54 is not surprising, since the same result was claimed by Carretta (2022). I would like to note that the entire sample of 42 stars analyzed by Carretta (2022) is included in this dataset.

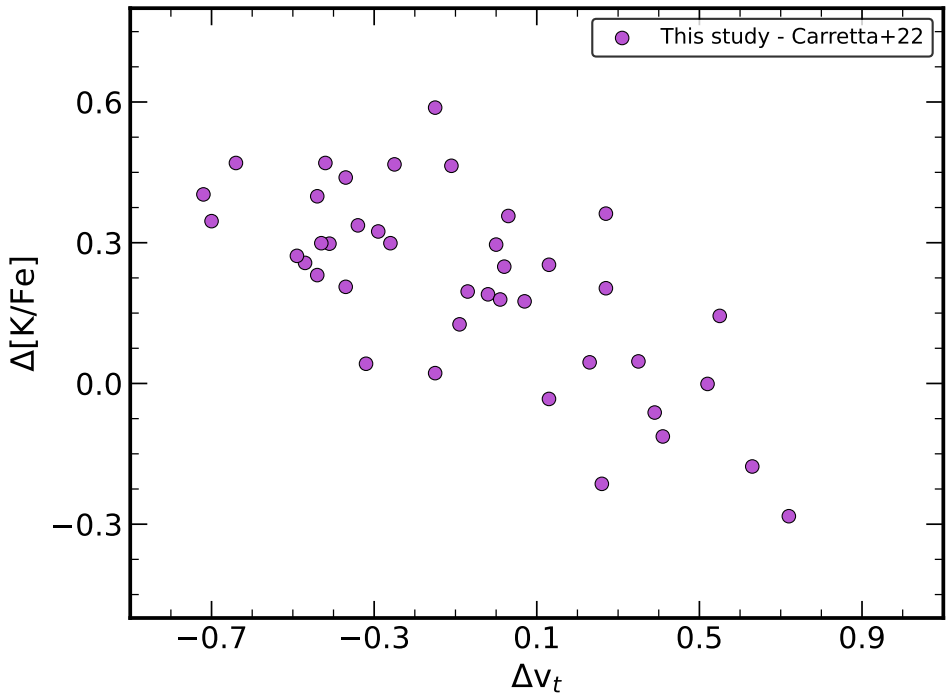

FIGURE 5.11: Difference in my [K/Fe] compared to those by Carretta (2022) as a function of the differences of my v_t compared to those by Carretta (2022). Larger differences in v_t correspond to larger differences in [K/Fe].

Nonetheless, if the Mg-K anticorrelation of this work is compared with the one by Carretta (2022) (their Fig. 4) some differences can be observed, especially regarding [K/Fe] distribution. Indeed, their [K/Fe] distribution spans a large range from ~ 0.5 dex down to ~ -0.4 dex, with a mean value [K/Fe] $= 0.02$ dex ($\sigma = 0.20$ dex). On the other hand, if I exclude the K-poor star present in my sample, I have that the [K/Fe] distribution extents in a narrower range from 0.54 dex down to 0.06 dex with a mean [K/Fe] $= 0.26$ dex ($\sigma = 0.13$ dex). For [Mg/Fe] both the samples have similar extension and values. It is interesting to note that in my sample except for #3800225 there are no stars with [K/Fe] < 0.0 dex, at odds with the result by Carretta (2022) where about half of the sample has [K/Fe] < 0.0 dex. Since the sample analyzed by Carretta (2022) is contained in my sample, I investigated the possibly origin of the observed difference in the [K/Fe] distribution and I concluded that the observed difference is mainly attributable to the different set of parameters used in the two analysis. In particular, the dominant factor seems to be the v_t, because the K line is strong enough to be very sensitive to small variations in v_t. I derived the v_t from the relation by Kirby

et al. (2009), while the v_t present in Carretta (2022) are obtained by eliminating trends in the relation between abundances from Fe neutral lines and expected line strength. The determination of v_t in the relation by Kirby et al. (2009) depends only by the $\log g$ of the stars. The v_t I obtained are distributed in the range between 1.50 and 2.04 km s^{-1}, while the v_t by Carretta (2022) are distributed in a wider range, between 1.22 and 2.95 km s^{-1}. In Fig. 5.11 can be seen the Δ[K/Fe] as a function of Δv_t. Absolute larger differences in v_t correspond to absolute larger differences in the derived K abundances. The stars with the highest values of v_t in Carretta (2022) are those ones with the lowest [K/Fe] abundance ratios and vice versa. Obviously, also the other stellar parameters and the different metallicity scales have impact on the different measured [K/Fe], but I found that the prevailing factor is v_t.

5.5.6 Neutron capture elements

Based on the photometric data collected through the HST for the Milky Way GCs, Milone et al. (2015a, 2017a) settled a new powerful photometric diagram to investigate stellar populations in GCs, based on the combination of different HST bands (F275W, F336W, F438W, and F814W). These kind of diagrams are called ChMs and allowed to discover that GCs can be classified into two different groups: type I and type II GCs. In particular, the type II GCs represent $\sim$ 15% of the total population of GCs (Milone & Marino, 2022) and are characterized by the presence of multiple sequences in their ChMs, at odds with the type I GCs. From a spectroscopic point of view, type II GCs are characterized by **(1)** significant variations in metallicity, due to Fe variation, **(2)** overall C+N+O variations, and **(3)** variations in the abundance of slow neutron capture elements (s-elements; see Milone & Marino, 2022 and references therein). In particular, the overall C+N+O content and the s-elements display an increase with the metallicity.

M 54 is classified as type II GC, according to its ChM. Moreover, it displays a wide metallicity range. However, despite being a widely studied system in the literature, very little is known about its C+N+O and s-elements (such Ba and La) abundances.

Recently, Marino et al. (2021) presented the results on the analysis of the La abundances for a total of 26 stars of M 54. The analyzed stars were selected among the stars already studied by Carretta et al. (2010b). They found that the [Fe/H] ranges from -1.9 dex up to -1.2 dex, while [La/Fe] ranges from 0.0 dex up to 0.7 dex. Marino et al. (2021) divided their dataset in two subsamples: **(1)** a metal-poor one composed by 12 stars, with a peak of [Fe/H] $= -1.70$ dex and a mean [La/Fe] $= 0.27 \pm 0.04$ dex ($\sigma = 0.15$ dex), and **(2)** a metal-rich one composed by 14 stars, with a peak of [Fe/H] $= -1.42$ dex and an average [La/Fe] $= 0.37 \pm 0.04$ dex ($\sigma = 0.15$ dex).

In this work I measured Ba and La abundances for a total of 48 stars. All the lines used to measure the abundances are present in the HR11 and HR13 setups. In Fig. 5.12 can be observed the distributions of [Ba/Fe] and [La/Fe] as a function of the metallicity.

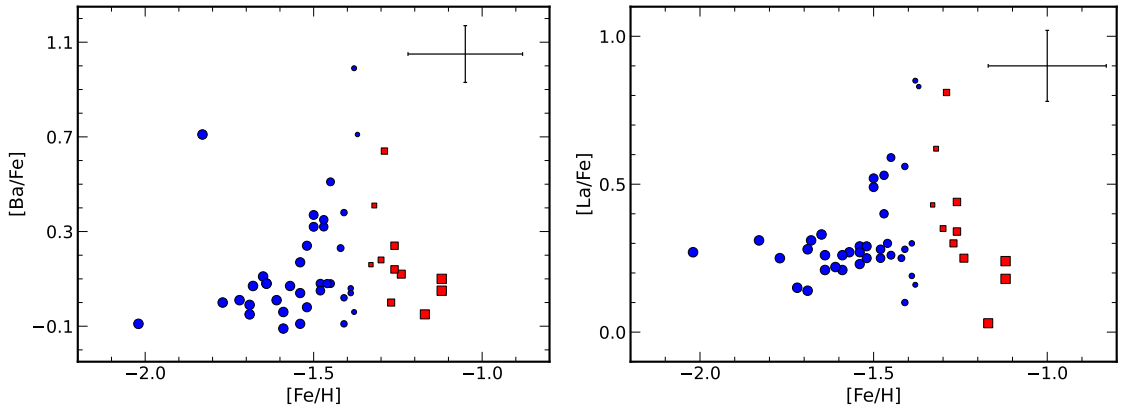

FIGURE 5.12: Same as Fig. 5.6, but for Ba (left panel) and La (right panel) abundance distributions.

For Ba, this is the first time in which its distribution in M 54 is presented. From left panel of Fig. 5.12 can be seen that, considering the overall distribution, the [Ba/Fe] is constant at ~ 0.1 dex until [Fe/H] $= -1.5$ dex with a small scatter, than from [Fe/H] $= -1.5$ up to -1.2 dex the scatter in [Ba/Fe] presents an huge increase with [Ba/Fe] reaching very high values up to 0.99 dex, and finally at [Fe/H] > -1.2 dex seems that the scatter decreases even though in this metallicity regime there are only three stars. If I consider separately the MP and MR subsample, I observe that in the MP component (37 stars out of 48) the [Ba/Fe] ranges from -0.11 dex up to 0.99 dex, with an average [Ba/Fe] $= 0.15$ dex ($\sigma = 0.25$ dex). On the other hand, in the MR component the [Ba/Fe] (11 stars out of 48) ranges from -0.05 dex up to 0.65 dex, with an average [Ba/Fe] $= 0.18$ dex ($\sigma = 0.19$ dex).

For [La/Fe] abundance ratios in the right panel of Fig. 5.12, the behavior is qualitatively the same as for [Ba/Fe]. Indeed, until [Fe/H] $= -1.5$ dex the mean value of [La/Fe] is ~ 0.25 dex with a small scatter, than at higher metallicities the scatter increases, and finally at [Fe/H] > -1.2 dex seems to decrease even though there are only three stars. Again, considering separately the MP and MR subsamples, in the MP (37 stars out of 48) the [La/Fe] ranges from 0.1 dex up to 0.85, with a mean [La/Fe] $= 0.32$ dex ($\sigma = 0.17$ dex), while in the MR component the [La/Fe] ranges from 0.03 dex up to 0.81 dex, with a mean [La/Fe] $= 0.36$ dex ($\sigma = 0.20$ dex).

In conclusion, from this analysis there is no increase in the s-element abundances going from low to high metallicities among the M 54 stars. The most interesting result is the striking scatter in both the [Ba/Fe] and [La/Fe] observed between [Fe/H] $= -1.5$ dex and -1.2 dex.

5.6 Discussion and conclusion

In this work I presented the analysis of high-resolution spectra, collected with the multiobject spectrograph FLAMES/VLT, for a total of 243 stars selected along the blue RGB usually associated to the GC M 54. In this work I derived the abundances for Fe, Mg, Al, Si, K, Ba, and La. In the following I summarize the most important findings from the analysis.

- I obtained Fe abundances for the total sample of 243 stars. This represents the largest dataset for M 54 stars obtained from high-resolution spectra. In this sample I found six stars with [Fe/H] > -1.0 dex, which can be either very young stars ($\sim$ 2 Gyr) present along the RGB of M 54 or evolved BSS that appear rejuvenated by their amount of newly fresh H. For the remaining 237 stars I found a wide metallicity distribution, ranging from [Fe/H] ~ -2.0 dex to ~ -1.0 dex and with the same spread already confirmed in other spectroscopic studies ($\sigma = 0.19$ dex, Carretta et al., 2010b).
  For the first time I found that the metallicity distribution is not symmetric. Indeed, from a GMM I found that in M 54 are present different groups of metallicity, nicely reproduced by a combination of two Gaussian distributions: a dominant MP component that contributes 61% of the total sample, with a peak at [Fe/H] $= -1.53$ dex ($\sigma = 0.13$), and a MR component that contributes 39% of the sample, with a peak at [Fe/H] $= -1.22$ dex ($\sigma = 0.12$). All the previous studies, based on both high- and low-resolution spectroscopic datasets (Bellazzini et al., 2008; Carretta et al., 2010b; Mucciarelli et al., 2017; Alfaro-Cuello et al., 2019) found that the metallicity distribution of M 54 is not mono-modal and well reproducible with one Gaussian distribution.

- I analyzed all the elements involved in the complete MgAl burning chain, namely Mg, Al, Si, and K. From the distributions of these elements as a function of the metallicity I found that along the MP subpopulation the stars are characterized by both low and high abundances, indicating that in the MP component are present both FG and SG stars. On the other hand, in the MR subpopulation seems that the dominant component are the SG stars, with low content of Mg and high content of Al, Si, and K.

- I detected a clear Mg-Al anticorrelation for a total of 45 stars. This is the largest sample for which this anticorrelation is presented in M 54. Indeed, previous studies found the presence of the Mg-Al anticorrelation from the analysis of 6 and 19 stars, respectively (Carretta et al., 2010b; Fernández-Trincado et al., 2021). The MP component is characterized by a small variation in [Mg/Fe] ($\sim$ 0.2 dex) associated with a large variation in [Al/Fe] ($\sim$ 1 dex). On the other hand, the MR component shows a larger [Mg/Fe]

variation associated with a smaller [Al/Fe] spread. In particular, the majority of the stars in this group have the highest content of Al, being at [Al/Fe] $\sim$ 1.3 dex.

- Considering the overall population of M 54 I found a hint of a Mg-Si anticorrelation, even though the quite large errors in the Si abundance determination prevent to clearly claim this finding.

- I found a Mg-K anticorrelation, given mainly by the stars making the MP component. Among the 55 stars making the anticorrelation, I found one K-poor star, namely #3800225. This stars has a [K/Fe] $= -0.50$ dex, a value that is much lower than the bulk of the [K/Fe] distribution. I checked whether this value could be affected by some bias introduced during the analysis, concluding that its low K abundance is real. Unfortunately this star is not present among the stars analyzed by Carretta (2022). The presence of Mg-K anticorrelation among the M 54 stars was already claimed by Carretta (2022). However, the main difference between the two analyses is the [K/Fe] range. In their case, the [K/Fe] covers $\sim$ 0.9 dex, while in my case $\sim$ 0.6 dex. After a careful inspection I found that this difference is mainly attributable to the different set of atmospheric parameters, and in particular to the different v_t employed.
  The presence of the Mg-K anticorrelation, coupled with the Mg-Al and Mg-Si ones is the fingerprint of Mg burning at very high temperatures (T $> 10^8$ K) through the MgAl chain (Ventura et al., 2016; Dell'Agli et al., 2018).

- I presented for the first time the distributions for both the s-elements Ba and La. In particular, I measured their abundances for a total of 48 stars. Indeed, even if M 54 is classified as type II GC, very little is known about its distribution of s-elements. The only analysis to the date was presented by Marino et al. (2021), who measured the La abundances for a total of 26 stars, finding that the stars in their metal-poor component have a [La/Fe] 0.1 dex lower than the stars in their metal-rich component. From this dataset I observed a striking increase the scatter of both [Ba/Fe] and [La/Fe] abundance ratios in the metallicity range between [Fe/H] $= -1.5$ dex and [Fe/H] $= -1.2$ dex.

The wide metallicity spread present in M 54 is factual. Indeed, previous spectroscopic analysis of this system found the same result that I presented here. This is a clear indication that M 54 is a more complex systems than *genuine* GCs. M 54 is the second most massive GC and the system with the second highest metallicity spread, being ω Centauri the first both in terms of mass and Fe spread. It is located at the center of the Sgr dSph galaxy and it is considered to be part of the NSC of this galaxy. Therefore, M 54 represents a bridge between *genuine* GCs, which show the typical anticorrelations involving light elements, and

more complex systems such dwarf galaxies, which were able to retain the fast ejecta from core collapse SNe. The observed metallicity spread in M 54 confirms this idea.

I observed the presence of all the anticorrelation arising from the MgAl chain at very high temperatures. These findings reinforce the idea that the polluter stars responsible for the formation of MPs in GCs are the AGB stars (e.g., D'Ercole et al., 2010; Ventura et al., 2013, 2016), at least in those systems where clear anticorrelations coming from the MgAl chain are present. Indeed, all the other polluters proposed in the literature are not able to activate efficiently the MgAl chain in their interiors (see e.g., Renzini et al., 2015; Bastian & Lardo, 2018, for a detailed discussion).

In M 54 there is no significant fraction of Mg-poor stars ([Mg/Fe] < 0.0 dex), at odds with other systems such as NGC 2419, NGC 2808, NGC 5824 or ω Centauri (Mucciarelli et al., 2012, 2015, 2018a; Mészáros et al., 2021). A part from ω Centauri, M 54 is more massive than the other GCs. This is an indication that even though M 54 was able to activate the complete MgAl burning chain in its polluter stars, these were not able to destroy Mg efficiently as done in other GCs where the [Mg/Fe] reaches values well below 0.0 dex.

The s-elements production is well established to occur in low to intermediate-mass thermally pulsating AGB stars (1 to 4 $M_{\odot}$, see Travaglio et al., 2004 and references therein). Therefore, the s-process provides a contribution to the chemical enrichment of the intracluster medium that is delayed by $\sim$ 100 to 300 Myr from the time in which these AGB stars formed. From this analysis I found that the s-elements Ba and La do not show any significant increase as a function of the metallicity. On the other hand, Marino et al. (2021) found just a small variation of [La/Fe] as a function of metallicity. These findings suggest that the chemical enrichment driven by low-mass AGB stars seems to be poorly efficient despite the significant [Fe/H] spread driven by core collapse SNe.

In conclusion, M 54 emerges to be a very complex system, where different mechanisms contributed to its chemical enrichment history. **(1)** this system was massive enough to be able to retain the high-velocity ejecta coming from core collapse SNe, responsible for the observed metallicity spread; **(2)** the observed anticorrelations point out to the massive AGB to be the responsible for the phenomenon of MPs (e.g., Ventura et al., 2013, 2016); **(3)** the observed lack of significant variations in the s-elements abundances as a function of the metallicity indicates that the contribution from the low-mass AGB was poorly efficient in M 54.

CHAPTER 6

Conclusions and future perspectives

In this PhD Thesis I chemically characterized three stellar systems traditionally classified as GCs, namely ω Centauri, Liller 1, and M 54. However, these systems are known to have experienced more complex histories of formation and evolution compared to *genuine* GCs. The analysis here performed allowed to derive some important conclusions on these systems:

- From the analysis of a large high-resolution spectroscopic dataset (440 stars observed with the VLT/FLAMES spectrograph in the GIRAFFE mode) of ω Centauri stars I found for the first time a clear and extended Mg-K anticorrelation in this system, given mainly by the most metal-poor subpopulation of ω Centauri. Moreover, I found evidence of clear Mg-Al and Mg-Si anticorrelations, with their shapes and extensions varying as a function of the metallicity. In particular, at [Fe/H] > -1.3 no evidence of anticorrelation is present. These findings strongly suggest a predominant role of the AGB stars in the formation of MPs in ω Centauri. Indeed, these stars are able to explain the presence of the complete MgAl burning chain in the metal-poor regime, as well the lack of anticorrelations related to the chain in the metal-rich regime.
  From this analysis I also found a K-rich star in ω Centauri. This giant was found to have a [K/Fe] $= +1.6$ dex, ~ 1 dex higher than other stars with similar metallicity and parameters. I firstly proposed that it could have formed directly from the ejecta of AGB and super-AGB stars without dilution with pristine material. However, a subsequent analysis based on higher resolution spectra revealed a more intricate scenario. Indeed, I found that this star is a LPV, presents clear RV variations, has an active chromosphere, and has a newly derived [K/Fe] $= +0.6$ dex. I concluded that the high K abundance previously measured for this star is a transient phenomenon whose origin could be related to the structure of the star, likely its variable chromosphere.

- From the analysis of medium-resolution IR spectra (27 stars observed with the VLT/X-shooter spectrograph) of Liller 1 I performed a first complete chemical characterization

of this system. I confirmed the presence of two distinct subpopulations in Liller 1, one classified as metal-poor ([Fe/H] $= -0.3$ dex) and another as metal-rich ([Fe/H] $= +0.2$ dex). I found that the metal-poor subpopulation has a high content of α-elements, with [α/Fe] $\sim +0.4$ dex, while the metal-rich has a solar content of α-elements, with [α/Fe] $= 0.0$ dex. The behavior of these two subpopulation resembles that of the Bulge field stars, suggesting that Liller 1 formed and evolved within the Bulge. Moreover, in Liller 1 no evidence of the classical Na-O anticorrelation is present. All these chemical fingerprints, coupled with previous results based on the photometric age determination of the two subpopulations and on the SFH of this system strongly point out on the same direction: Liller 1 is a fossil fragment of the epoch of the Bulge formation that survived until now with the apparent aspect of a GC.

- I presented the analysis of the largest high-resolution spectroscopic dataset (243 stars observed with the VLT/FLAMES spectrograph in the GIRAFFE+UVES mode) obtained so far for M 54 member stars. I confirmed the presence of a wide metallicity spread among its stars, as already found in other studies. In particular, compared to the previous MDF for M 54, here I found a multimodal MDF reproducible with two Gaussian distributions separated by ~ 0.3 dex in [Fe/H]. I found evidence that the complete MgAl burning chain was active in M 54. Indeed, M 54 displays Mg-Al, Mg-Si, and Mg-K anticorrelations. However, the lack of Mg-poor ([Mg/Fe]< 0.0 dex) stars in M 54 indicates that the MgAl chain was not efficient enough to allow a wide Mg destruction, at odds with other massive GCs such as NGC 2419 or ω Centauri where a significant fraction of Mg-poor stars is present.
  I presented also the first distributions Ba and La abundances for M 54. From their distributions I did not found any significant increase as a function of the metallicity.
  All these findings suggest that in M 54 the contribution from intermediate-mass AGB stars (responsible for the light-elements anticorrelations) was efficient, while the contribution from low-mass AGB stars (responsible for the s-element enrichment) was poorly efficient.

These results demonstrate that much still needs to be done in the characterization of peculiar systems that historically are classified as GCs, due to their morphology. Indeed, despite their apparent aspect of GCs, there is growing number of systems that actually appear to be more complex than previously thought. Each one of them experienced its own history of formation and evolution, and dedicated studies are needed to characterize them.

Here I summarize the future steps arising from this PhD work:

- In ω Centauri I will explore the impact of the chromosphere in the K abundance determination, due to the extreme importance of this element in the phenomenon of MPs. To achieve this goal I secured a total of 20 hours of observation at the VLT with the ESPRESSO spectrograph (P.I. Alvarez Garay).

- In Liller 1 our group is performing studies based on high-resolution (R $\sim$ 50000) spectra collected with the VLT/CRIRES spectrograph (P.I. F. R. Ferraro) to fully describe the chemistry of this system. As a first step we already published a work based on high-resolution (R $\sim$ 25000) spectra collected with the Keck-II/NIRSPEC spectrograph (Fanelli et al., 2024).

- In M 54 I secured a total of 9 hours of observations at the VLT with the FLAMES spectrograph in the GIRAFFE mode (P.I. Alvarez Garay), which will allow to measure the C+N+O content, in order to put further constraints on the evolutionary history of M 54.

Bibliography

Adams S. M., Kochanek C. S., Gerke J. R., Stanek K. Z., Dai X., 2017, "The search for failed supernovae with the Large Binocular Telescope: confirmation of a disappearing star" MNRAS, 468, 4968 (arXiv:1609.01283)

Alcaino G., Liller W., 1987, "BVRI CCD Photometry of Omega Centauri" AJ, 94, 1585

Alfaro-Cuello M., et al., 2019, "A Deep View into the Nucleus of the Sagittarius Dwarf Spheroidal Galaxy with MUSE. I. Data and Stellar Population Characterization" ApJ, 886, 57 (arXiv:1909.10529)

Alfaro-Cuello M., et al., 2020, "A Deep View into the Nucleus of the Sagittarius Dwarf Spheroidal Galaxy with MUSE. II. Kinematic Characterization of the Stellar Populations" ApJ, 892, 20 (arXiv:2002.07814)

Alvarez R., Plez B., 1998, "Near-infrared narrow-band photometry of M-giant and Mira stars: models meet observations" A&A, 330, 1109 (arXiv:astro-ph/9710157)

Alvarez Garay D. A., Mucciarelli A., Lardo C., Bellazzini M., Merle T., 2022, "The Mg-K Anticorrelation in ω Centauri" ApJ, 928, L11 (arXiv:2203.05462)

Alvarez Garay D. A., Mucciarelli A., Bellazzini M., Lardo C., Ventura P., 2024, "MgAl burning chain in ω Centauri" A&A, 681, A54 (arXiv:2309.14603)

Anderson A. J., 1997, PhD thesis, University of California, Berkeley

Andrae R., et al., 2018, "Gaia Data Release 2. First stellar parameters from Apsis" A&A, 616, A8 (arXiv:1804.09374)

Armandroff T. E., Zinn R., 1988, "Integrated-Light Spectroscopy of Globular Clusters at the Infrared CA II Lines" AJ, 96, 92

Arnould M., Goriely S., Jorissen A., 1999, "Non-explosive hydrogen and helium burnings: abundance predictions from the NACRE reaction rate compilation" A&A, 347, 572 (arXiv:astro-ph/9904407)

Arp H. C., Baum W. A., Sandage A. R., 1952, "The HR diagrams for the globular clusters M 92 and M 3." AJ, 57, 4

Baeza I., et al., 2022, "APOGEE-2S Mg-Al anti-correlation of the metal-poor globular cluster NGC 2298" A&A, 662, A47 (arXiv:2204.09703)

Ballero S. K., Matteucci F., Origlia L., Rich R. M., 2007, "Formation and evolution of the Galactic bulge: constraints from stellar abundances" A&A, 467, 123 (arXiv:astro-ph/0702137)

Barbuy B., Bica E., Ortolani S., 1998, "Globular clusters within 5(deg) of the Galactic center" A&A, 333, 117

Bassino L. P., Muzzio J. C., 1995, "Is M54 the nucleus of the Sagittarius galaxy?" The Observatory, 115, 256

Bastian N., Lardo C., 2015, "Globular cluster mass-loss in the context of multiple populations" MNRAS, 453, 357 (arXiv:1507.05634)

Bastian N., Lardo C., 2018, "Multiple Stellar Populations in Globular Clusters" ARA&A, 56, 83 (arXiv:1712.01286)

Bastian N., Pfeffer J., 2022, "Star cluster ecology: revisiting the origin of iron and age complex clusters" MNRAS, 509, 614 (arXiv:2110.10616)

Bastian N., Cabrera-Ziri I., Davies B., Larsen S. S., 2013, "Constraining globular cluster formation through studies of young massive clusters - I. A lack of ongoing star formation within young clusters" MNRAS, 436, 2852 (arXiv:1309.5092)

Bates B., Catney M. G., Keenan F. P., 1990, "High Resoltuion Interstellar and Stellar Line Profiles of the Stars in the Globular Cluster M22" MNRAS, 245, 238

Bates B., Kemp S. N., Montgomery A. S., 1993, "High resolution NA D and H-alpha line profiles of stars in the globular clusters M 22 and omega Centauri." A&AS, 97, 937

Baumgardt H., Hilker M., 2018, "A catalogue of masses, structural parameters, and velocity dispersion profiles of 112 Milky Way globular clusters" MNRAS, 478, 1520 (arXiv:1804.08359)

Baumgardt H., Vasiliev E., 2021, "Accurate distances to Galactic globular clusters through a combination of Gaia EDR3, HST, and literature data" MNRAS, 505, 5957 (arXiv:2105.09526)

Baumgardt H., Hilker M., Sollima A., Bellini A., 2019, "Mean proper motions, space orbits, and velocity dispersion profiles of Galactic globular clusters derived from Gaia DR2 data" MNRAS, 482, 5138 (arXiv:1811.01507)

Baumgardt H., Sollima A., Hilker M., 2020, "Absolute V-band magnitudes and mass-to-light ratios of Galactic globular clusters" PASA, 37, e046 (arXiv:2009.09611)

Bedin L. R., Piotto G., Anderson J., Cassisi S., King I. R., Momany Y., Carraro G., 2004, "ω Centauri: The Population Puzzle Goes Deeper" ApJ, 605, L125 (arXiv:astro-ph/0403112)

Behr B. B., 2003, "Chemical Abundances and Rotation Velocities of Blue Horizontal-Branch Stars in Six Globular Clusters" ApJS, 149, 67 (arXiv:astro-ph/0307178)

Bekki K., 2017, "Globular cluster formation with multiple stellar populations from hierarchical star cluster complexes" MNRAS, 467, 1857 (arXiv:1705.01341)

Bekki K., Freeman K. C., 2003, "Formation of ω Centauri from an ancient nucleated dwarf galaxy in the young Galactic disc" MNRAS, 346, L11 (arXiv:astro-ph/0310348)

Bekki K., Tsujimoto T., 2019, "A New Formation Model for ω Centauri: A Complex Interplay of Astrophysical Processes" ApJ, 886, 121 (arXiv:1909.11295)

Bell R. A., Dickens R. J., 1980, "Chemical abundances in the globular clusters M 3, M 13, and NGC 6752." ApJ, 242, 657

Bellazzini M., Ferraro F. R., Ibata R., 2003a, "Building Up the Globular Cluster System of the Milky Way: The Contribution of the Sagittarius Galaxy" AJ, 125, 188 (arXiv:astro-ph/0210596)

Bellazzini M., Ibata R., Ferraro F. R., Testa V., 2003b, "Tracing the Sgr Stream with 2MASS. Detection of Stream stars around Outer Halo globular clusters" A&A, 405, 577 (arXiv:astro-ph/0304502)

Bellazzini M., Correnti M., Ferraro F. R., Monaco L., Montegriffo P., 2006, "The age of the main population of the Sagittarius dwarf spheroidal galaxy. Solving the "M giant conundrum"" A&A, 446, L1 (arXiv:astro-ph/0512109)

Bellazzini M., et al., 2008, "The Nucleus of the Sagittarius Dsph Galaxy and M54: a Window on the Process of Galaxy Nucleation" AJ, 136, 1147 (arXiv:0807.0105)

Bellini A., Piotto G., Bedin L. R., King I. R., Anderson J., Milone A. P., Momany Y., 2009, "Radial distribution of the multiple stellar populations in ω Centauri" A&A, 507, 1393 (arXiv:0909.4785)

Bellini A., Bedin L. R., Piotto G., Milone A. P., Marino A. F., Villanova S., 2010, "New Hubble Space Telescope WFC3/UVIS Observations Augment the Stellar-population Complexity of ω Centauri" AJ, 140, 631 (arXiv:1006.4157)

Bellini A., et al., 2013, "The Intriguing Stellar Populations in the Globular Clusters NGC 6388 and NGC 6441" ApJ, 765, 32 (arXiv:1301.2822)

Bellini A., Anderson J., van der Marel R. P., King I. R., Piotto G., Bedin L. R., 2017a, "The State-of-the-art HST Astro-photometric Analysis of the Core of ω Centauri. II. Differential-reddening Map" ApJ, 842, 7 (arXiv:1705.01951)

Bellini A., Milone A. P., Anderson J., Marino A. F., Piotto G., van der Marel R. P., Bedin L. R., King I. R., 2017b, "The State-of-the-art HST Astro-photometric Analysis of the Core of ω Centauri. III. The Main Sequence's Multiple Populations Galore" ApJ, 844, 164 (arXiv:1706.07063)

Belokurov V., et al., 2014, "Precession of the Sagittarius stream" MNRAS, 437, 116 (arXiv:1301.7069)

Belserene E. P., 1959, "Magnitudes and colors in omega Centauri." AJ, 64, 58

Bertaux J. L., Lallement R., Ferron S., Boonne C., Bodichon R., 2014, "TAPAS, a web-based service of atmospheric transmission computation for astronomy" A&A, 564, A46 (arXiv:1311.4169)

Böker T., Sarzi M., McLaughlin D. E., van der Marel R. P., Rix H.-W., Ho L. C., Shields J. C., 2004, "A Hubble Space Telescope Census of Nuclear Star Clusters in Late-Type Spiral Galaxies. II. Cluster Sizes and Structural Parameter Correlations" AJ, 127, 105 (arXiv:astro-ph/0309761)

Bournaud F., 2016, in Laurikainen E., Peletier R., Gadotti D., eds, Astrophysics and Space Science Library Vol. 418, Galactic Bulges. p. 355 (arXiv:1503.07660), doi:10.1007/978-3-319-19378-6_13

Bournaud F., Elmegreen B. G., 2009, "Unstable Disks at High Redshift: Evidence for Smooth Accretion in Galaxy Formation" ApJ, 694, L158 (arXiv:0902.2806)

Bragaglia A., Carretta E., D'Orazi V., Sollima A., Donati P., Gratton R. G., Lucatello S., 2017, "NGC 6535: the lowest mass Milky Way globular cluster with a Na-O anti-correlation? Cluster mass and age in the multiple population context" A&A, 607, A44 (arXiv:1708.07705)

Bressan A., Marigo P., Girardi L., Salasnich B., Dal Cero C., Rubele S., Nanni A., 2012, "PARSEC: stellar tracks and isochrones with the PAdova and TRieste Stellar Evolution Code" MNRAS, 427, 127 (arXiv:1208.4498)

Brown J. A., Wallerstein G., Gonzalez G., 1999, "Elemental Abundances in Five Stars in M54, A Globular Cluster Associated with the Sagittarius Galaxy" AJ, 118, 1245

Brown G., Gnedin O. Y., Li H., 2018, "Nuclear Star Clusters in Cosmological Simulations" ApJ, 864, 94 (arXiv:1804.09819)

Bruls J. H. M. J., Rutten R. J., 1992, "The formation of helioseismology lines. II. Modeling of alkali resonance lines with granulation." A&A, 265, 257

Bruls J. H. M. J., Rutten R. J., Shchukina N. G., 1992, "The formation of helioseismology lines. I. NLTE effects in alkali spectra." A&A, 265, 237

Burton W. B., Lockman F. J., 1999, "HI observations towards the Sagittarius dwarf spheroidal galaxy" A&A, 349, 7 (arXiv:astro-ph/9908012)

Butler D., Dickens R. J., Epps E., 1978, "Studies of RR Lyrae variable stars in the unusual globular cluster Omega Centauri. I. Spectroscopic observations." ApJ, 225, 148

Cabrera-Ziri I., et al., 2015, "Constraining globular cluster formation through studies of young massive clusters - V. ALMA observations of clusters in the Antennae" MNRAS, 448, 2224 (arXiv:1501.05657)

Cacciari C., Freeman K. C., 1983, "Survey of H-alpha emission in globular cluster red giants." ApJ, 268, 185

Cacciari C., et al., 2004, "Mass motions and chromospheres of RGB stars in the globular cluster NGC 2808" A&A, 413, 343 (arXiv:astro-ph/0309685)

Cadelano M., et al., 2023, "JWST uncovers helium and water abundance variations in the bulge globular cluster NGC 6440" A&A, 679, L13 (arXiv:2310.13056)

Cadelano M., Dalessandro E., Vesperini E., 2024, "The structural properties of multiple populations in globular clusters: The instructive case of NGC 3201" A&A, 685, A158 (arXiv:2402.09514)

Caffau E., Ludwig H. G., Steffen M., Freytag B., Bonifacio P., 2011, "Solar Chemical Abundances Determined with a CO5BOLD 3D Model Atmosphere" Sol. Phys., 268, 255 (arXiv:1003.1190)

Callingham T. M., Cautun M., Deason A. J., Frenk C. S., Grand R. J. J., Marinacci F., 2022, "The chemo-dynamical groups of Galactic globular clusters" MNRAS, 513, 4107 (arXiv:2202.00591)

Caloi V., D'Antona F., 2007, "NGC 6441: another indication of very high helium content in globular cluster stars" A&A, 463, 949 (arXiv:astro-ph/0610406)

Cameron A. G. W., Fowler W. A., 1971, "Lithium and the s-PROCESS in Red-Giant Stars" ApJ, 164, 111

Cannon R. D., Stobie R. S., 1973, "Photometry of Southern globular clusters. I. Bright stars in OME Cen." MNRAS, 162, 207

Cannon R. D., Croke B. F. W., Bell R. A., Hesser J. E., Stathakis R. A., 1998, "Carbon and nitrogen abundance variations on the main sequence of 47 Tucanae" MNRAS, 298, 601

Carlsson M., De Pontieu B., Hansteen V. H., 2019, "New View of the Solar Chromosphere" ARA&A, 57, 189

Carollo C. M., Stiavelli M., Mack J., 1998, "Spiral Galaxies with WFPC2. II. The Nuclear Properties of 40 Objects" AJ, 116, 68 (arXiv:astro-ph/9804007)

Carollo C. M., Scarlata C., Stiavelli M., Wyse R. F. G., Mayer L., 2007, "Old and Young Bulges in Late-Type Disk Galaxies" ApJ, 658, 960 (arXiv:astro-ph/0610638)

Carraro G., Zinn R., Moni Bidin C., 2007, "Whiting 1: the youngest globular cluster associated with the Sagittarius dwarf spheroidal galaxy" A&A, 466, 181 (arXiv:astro-ph/0702253)

Carrera R., Martínez-Vázquez C. E., 2013, "Searching for chemical inhomogeneities in open clusters. Analysis of the CN and CH molecular band strengths in NGC 2158, NGC 2420, NGC 2682, NGC 7789, and Berkeley 29" A&A, 560, A5 (arXiv:1308.4548)

Carretta E., 2015, "Five Groups of Red Giants with Distinct Chemical Composition in the Globular Cluster NGC 2808" ApJ, 810, 148 (arXiv:1507.07553)

Carretta E., 2021, "Potassium abundances in multiple stellar populations of the globular cluster NGC 4833" A&A, 649, A154 (arXiv:2103.10441)

Carretta E., 2022, "Multiple stellar populations in the high-temperature regime: Potassium abundances in the globular

cluster M 54 (NGC 6715)" A&A, 666, A177 (arXiv:2209.06220)
Carretta E., et al., 2009a, "Na-O anticorrelation and HB. VII. The chemical composition of first and second-generation stars in 15 globular clusters from GIRAFFE spectra" A&A, 505, 117 (arXiv:0909.2938)
Carretta E., Bragaglia A., Gratton R., Lucatello S., 2009b, "Na-O anticorrelation and HB. VIII. Proton-capture elements and metallicities in 17 globular clusters from UVES spectra" A&A, 505, 139 (arXiv:0909.2941)
Carretta E., Bragaglia A., Gratton R. G., Recio-Blanco A., Lucatello S., D'Orazi V., Cassisi S., 2010a, "Properties of stellar generations in globular clusters and relations with global parameters" A&A, 516, A55 (arXiv:1003.1723)
Carretta E., et al., 2010b, "Detailed abundances of a large sample of giant stars in M 54 and in the Sagittarius nucleus" A&A, 520, A95 (arXiv:1006.5866)
Carretta E., et al., 2010c, "M54 + Sagittarius = ω Centauri" ApJ, 714, L7 (arXiv:1002.1963)
Carretta E., et al., 2010d, "Abundances for a Large Sample of Red Giants in NGC 1851: Hints for a Merger of Two Clusters?" ApJ, 722, L1 (arXiv:1007.5301)
Carretta E., Bragaglia A., Lucatello S., Gratton R. G., D'Orazi V., Sollima A., 2018, "Aluminium abundances in five discrete stellar populations of the globular cluster NGC 2808" A&A, 615, A17 (arXiv:1801.09689)
Cassisi S., Salaris M., Irwin A. W., 2003, "The Initial Helium Content of Galactic Globular Cluster Stars from the R-Parameter: Comparison with the Cosmic Microwave Background Constraint" ApJ, 588, 862 (arXiv:astro-ph/0301378)
Cassisi S., Salaris M., Pietrinferni A., Piotto G., Milone A. P., Bedin L. R., Anderson J., 2008, "The Double Subgiant Branch of NGC 1851: The Role of the CNO Abundance" ApJ, 672, L115 (arXiv:0711.3823)
Castelli F., Kurucz R. L., 2003, in Piskunov N., Weiss W. W., Gray D. F., eds, IAU Symposium Vol. 210, Modelling of Stellar Atmospheres. p. A20 (arXiv:astro-ph/0405087), doi:10.48550/arXiv.astro-ph/0405087
Chantereau W., Charbonnel C., Meynet G., 2016, "Evolution of long-lived globular cluster stars. III. Effect of the initial helium spread on the position of stars in a synthetic Hertzsprung-Russell diagram" A&A, 592, A111 (arXiv:1606.01899)
Charbonnel C., 1994, "Clues for non-standard mixing on the red giant branch from 12C/13C and 12C/14N ratios in evolved stars." A&A, 282, 811
Charbonnel C., Chantereau W., Krause M., Primas F., Wang Y., 2014, "Are there any first-generation stars in globular clusters today?" A&A, 569, L6 (arXiv:1410.3967)
Cohen J. G., 1978, "Abundances in globular cluster red giants. I. M3 and M13." ApJ, 223, 487
Cohen J. G., 1981, "Abundances in globular cluster red giants. IV. M 22 and omega Centauri." ApJ, 247, 869
Cohen J. G., Kirby E. N., 2012, "The Bizarre Chemical Inventory of NGC 2419, An Extreme Outer Halo Globular Cluster" ApJ, 760, 86 (arXiv:1209.2705)
Cohen J. G., Briley M. M., Stetson P. B., 2002, "Carbon and Nitrogen Abundances in Stars at the Base of the Red Giant Branch in M5" AJ, 123, 2525 (arXiv:astro-ph/0112199)
Collier A. C., Jenkins C. R., 1984, "Close binary stars and old stellar populations : the blue straggler problem revisited." MNRAS, 211, 391
Colucci J. E., Bernstein R. A., Cameron S., McWilliam A., Cohen J. G., 2009, "M31 Globular Cluster Abundances from High-Resolution, Integrated-Light Spectroscopy" ApJ, 704, 385 (arXiv:0908.3899)
Combes F., Sanders R. H., 1981, "Formation and properties of persisting stellar bars." A&A, 96, 164
Conroy C., 2012, "On the Birth Masses of the Ancient Globular Clusters" ApJ, 758, 21 (arXiv:1101.2208)
Conroy C., Spergel D. N., 2011, "On the Formation of Multiple Stellar Populations in Globular Clusters" ApJ, 726, 36 (arXiv:1005.4934)
Cottrell P. L., Da Costa G. S., 1981, "Correlated cyanogen and sodium anomalies in the globular clusters 47 TUC and NGC 6752." ApJ, 245, L79
Crociati C., et al., 2023, "First Evidence of Multi-iron Subpopulations in the Bulge Fossil Fragment Candidate Liller 1" ApJ, 951, 17
D'Antona F., Bellazzini M., Caloi V., Pecci F. F., Galleti S., Rood R. T., 2005, "A Helium Spread among the Main-Sequence Stars in NGC 2808" ApJ, 631, 868 (arXiv:astro-ph/0505347)
D'Antona F., D'Ercole A., Marino A. F., Milone A. P., Ventura P., Vesperini E., 2011, "The Oxygen versus Sodium (Anti)Correlation(S) in ω Cen" ApJ, 736, 5 (arXiv:1105.0366)
D'Antona F., Ventura P., Fabiola Marino A., Milone A. P., Tailo M., Di Criscienzo M., Vesperini E., 2019, "The Lithium Test for Multiple Populations in Globular Clusters: Lithium in NGC 2808" ApJ, 871, L19

(arXiv:1901.01273)
D'Antona F., et al., 2022, "HST Observations of the Globular Cluster NGC 6402 (M14) and Its Peculiar Multiple Populations" ApJ, 925, 192 (arXiv:2201.02546)
D'Ercole A., Vesperini E., D'Antona F., McMillan S. L. W., Recchi S., 2008, "Formation and dynamical evolution of multiple stellar generations in globular clusters" MNRAS, 391, 825 (arXiv:0809.1438)
D'Ercole A., D'Antona F., Ventura P., Vesperini E., McMillan S. L. W., 2010, "Abundance patterns of multiple populations in globular clusters: a chemical evolution model based on yields from AGB ejecta" MNRAS, 407, 854 (arXiv:1005.1892)
D'Orazi V., Lucatello S., Gratton R., Bragaglia A., Carretta E., Shen Z., Zaggia S., 2010, "Lithium and Proton-capture Elements in Globular Cluster Dwarfs: The Case of 47 TUC" ApJ, 713, L1 (arXiv:1003.0013)
D'Orazi V., Gratton R. G., Pancino E., Bragaglia A., Carretta E., Lucatello S., Sneden C., 2011, "Chemical enrichment mechanisms in ω Centauri: clues from neutron-capture elements" A&A, 534, A29 (arXiv:1108.5216)
D'Orazi V., Angelou G. C., Gratton R. G., Lattanzio J. C., Bragaglia A., Carretta E., Lucatello S., Momany Y., 2014, "Lithium Abundances in Globular Cluster Giants: NGC 6218 (M12) and NGC 5904 (M5)" ApJ, 791, 39 (arXiv:1406.5513)
D'Orazi V., et al., 2015, "Lithium abundances in globular cluster giants: NGC 1904, NGC 2808, and NGC 362" MNRAS, 449, 4038 (arXiv:1503.05925)
Da Costa G. S., Armandroff T. E., 1995, "Abundances and Kinematics of the Globular Cluster Systems of the Galaxy and of the Sagittarius Dwarf" AJ, 109, 2533
Dalessandro E., Lapenna E., Mucciarelli A., Origlia L., Ferraro F. R., Lanzoni B., 2016, "Multiple Populations in the Old and Massive Small Magellanic Cloud Globular Cluster NGC 121" ApJ, 829, 77 (arXiv:1607.05736)
Dalessandro E., et al., 2022, "Clues to the Formation of Liller 1 from Modeling Its Complex Star Formation History" ApJ, 940, 170 (arXiv:2210.05694)
Dantona F., Gratton R., Chieffi A., 1983, "CNO self-pollution in globular clusters; a model and its possible observational tests." Mem. Soc. Astron. Italiana, 54, 173
Davidge T. J., 2000, "A Near-Infrared Photometric Study of the Low-Latitude Globular Clusters Liller 1, Djorgovski 1, HP 1, and NGC 6528" ApJS, 126, 105 (arXiv:astro-ph/9909408)
Decressin T., Meynet G., Charbonnel C., Prantzos N., Ekström S., 2007a, "Fast rotating massive stars and the origin of the abundance patterns in galactic globular clusters" A&A, 464, 1029 (arXiv:astro-ph/0611379)
Decressin T., Charbonnel C., Meynet G., 2007b, "Origin of the abundance patterns in Galactic globular clusters: constraints on dynamical and chemical properties of globular clusters" A&A, 475, 859 (arXiv:0709.4160)
Decressin T., Baumgardt H., Charbonnel C., Kroupa P., 2010, "Evolution of two stellar populations in globular clusters. II. Effects of primordial gas expulsion" A&A, 516, A73 (arXiv:1003.5921)
Dekel A., Tziperman O., Sarkar K. C., Ginzburg O., Mandelker N., Ceverino D., Primack J., 2023, "Conditions for clump survival in High-z disc galaxies" MNRAS, 521, 4299 (arXiv:2209.04462)
Dekker H., D'Odorico S., Kaufer A., Delabre B., Kotzlowski H., 2000, in Iye M., Moorwood A. F., eds, Society of Photo-Optical Instrumentation Engineers (SPIE) Conference Series Vol. 4008, Optical and IR Telescope Instrumentation and Detectors. pp 534–545, doi:10.1117/12.395512
Del Principe M., et al., 2006, "A Pulsational Distance to ω Centauri Based on Near-Infrared Period-Luminosity Relations of RR Lyrae Stars" ApJ, 652, 362 (arXiv:astro-ph/0608052)
Dell'Agli F., et al., 2018, "A view of the H-band light-element chemical patterns in globular clusters under the AGB self-enrichment scenario" MNRAS, 475, 3098 (arXiv:1712.04500)
Denisenkov P. A., Denisenkova S. N., 1989, "Possible Explanation of the Correlation Between Nitrogen and Sodium Over Abundances for Red Giants in Globular Clusters" Astronomicheskij Tsirkulyar, 1538, 11
Denissenkov P. A., Hartwick F. D. A., 2014, "Supermassive stars as a source of abundance anomalies of proton-capture elements in globular clusters" MNRAS, 437, L21 (arXiv:1305.5975)
Denissenkov P. A., Tout C. A., 2000, "On a physical mechanism for extra mixing in globular cluster red giants" MNRAS, 316, 395
Denissenkov P. A., et al., 2014, "MESA and NuGrid simulations of classical novae: CO and ONe nova nucleosynthesis" MNRAS, 442, 2058 (arXiv:1303.6265)
Denissenkov P. A., VandenBerg D. A., Hartwick F. D. A., Herwig F., Weiss A., Paxton B., 2015, "The primordial and evolutionary abundance variations in globular-cluster stars: a problem with two unknowns" MNRAS, 448, 3314

(arXiv:1409.1193)
Di Criscienzo M., Tailo M., Milone A. P., D'Antona F., Ventura P., Dotter A., Brocato E., 2015, "An HST/WFC3 view of stellar populations on the horizontal branch of NGC 2419" MNRAS, 446, 1469 (arXiv:1507.04152)
Dickens R. J., Bell R. A., 1976, "Enhanced abundances of nitrogen and s-process elements in red giant stars in Omega Centauri." ApJ, 207, 506
Dickens R. J., Carey J. V., 1967, "Studies of the globular cluster [omega] Centauri VI," Royal Greenwich Observatory Bulletins, 129, 335
Dickens R. J., Woolley R. v. d. R., 1967, "Studies of the globular cluster [omega] Centauri V," Royal Greenwich Observatory Bulletins, 128, 255
Dinescu D. I., Girard T. M., van Altena W. F., 1999, "Space Velocities of Globular Clusters. III. Cluster Orbits and Halo Substructure" AJ, 117, 1792
Doherty C. L., Gil-Pons P., Lau H. H. B., Lattanzio J. C., Siess L., Campbell S. W., 2014, "Super and massive AGB stars - III. Nucleosynthesis in metal-poor and very metal-poor stars - Z = 0.001 and 0.0001" MNRAS, 441, 582 (arXiv:1403.5054)
Dondoglio E., Milone A. P., Lagioia E. P., Marino A. F., Tailo M., Cordoni G., Jang S., Carlos M., 2021, "Multiple Stellar Populations along the Red Horizontal Branch and Red Clump of Globular Clusters" ApJ, 906, 76 (arXiv:2011.03283)
Dondoglio E., et al., 2022, "Survey of Multiple Populations in Globular Clusters among Very-low-mass Stars" ApJ, 927, 207 (arXiv:2201.08631)
Dondoglio E., et al., 2023, "A deep dive into the Type II globular cluster NGC 1851" MNRAS, 526, 2960 (arXiv:2309.16423)
Drake J. J., Smith V. V., Suntzeff N. B., 1992, "Sodium, Aluminum, and Oxygen Abundance Variations in Giants in the Globular Cluster M4" ApJ, 395, L95
Dunlop J., 1828, "A Catalogue of Nebulae and Clusters of Stars in the Southern Hemisphere, Observed at Paramatta in New South Wales" Philosophical Transactions of the Royal Society of London Series I, 118, 113
Dupree A. K., Avrett E. H., 2013, "Direct Evaluation of the Helium Abundances in Omega Centauri" ApJ, 773, L28 (arXiv:1307.5860)
Dupree A. K., Hartmann L., Avrett E. H., 1984, "Chromospheres and mass loss in metal-deficient giant stars." ApJ, 281, L37
Dupree A. K., Hartmann L., Smith G. H., Rodgers A. W., Roberts W. H., Zucker D. B., 1994, "Spectroscopy of Chromospheric Lines of Giants in the Globular Cluster NGC 6752" ApJ, 421, 542
Eldridge J. J., Stanway E. R., 2022, "New Insights into the Evolution of Massive Stars and Their Effects on Our Understanding of Early Galaxies" ARA&A, 60, 455 (arXiv:2202.01413)
Elmegreen B. G., Bournaud F., Elmegreen D. M., 2008, "Bulge Formation by the Coalescence of Giant Clumps in Primordial Disk Galaxies" ApJ, 688, 67 (arXiv:0808.0716)
Elmegreen D. M., Elmegreen B. G., Marcus M. T., Shahinyan K., Yau A., Petersen M., 2009, "Clumpy Galaxies in Goods and Gems: Massive Analogs of Local Dwarf Irregulars" ApJ, 701, 306 (arXiv:0906.2660)
Elson R. A. W., Gilmore G. F., Santiago B. X., Casertano S., 1995, "HST Observations of the Stellar Population of the Globular Cluster W CEN" AJ, 110, 682
Evans D. W., et al., 2018, "Gaia Data Release 2. Photometric content and validation" A&A, 616, A4 (arXiv:1804.09368)
Fanelli C., Origlia L., Oliva E., Mucciarelli A., Sanna N., Dalessandro E., Romano D., 2021, "Stellar population astrophysics (SPA) with the TNG. The Arcturus Lab" A&A, 645, A19 (arXiv:2011.12321)
Fanelli C., et al., 2024, "Multi-iron subpopulations in Liller 1 from high resolution H-band spectroscopy" arXiv e-prints, p. arXiv:2408.12649 (arXiv:2408.12649)
Fernández-Trincado J. G., et al., 2021, "APOGEE spectroscopic evidence for chemical anomalies in dwarf galaxies: The case of M 54 and Sagittarius" A&A, 648, A70 (arXiv:2102.07785)
Ferraro F. R., Bellazzini M., Pancino E., 2002, "Discovery of an Accreted Stellar System within the Globular Cluster ω Centauri" ApJ, 573, L95 (arXiv:astro-ph/0206145)
Ferraro F. R., et al., 2009, "The cluster Terzan 5 as a remnant of a primordial building block of the Galactic bulge" Nature, 462, 483 (arXiv:0912.0192)
Ferraro F. R., Massari D., Dalessandro E., Lanzoni B., Origlia L., Rich R. M., Mucciarelli A., 2016, "The Age of the

Young Bulge-like Population in the Stellar System Terzan 5: Linking the Galactic Bulge to the High-z Universe" ApJ, 828, 75 (arXiv:1609.01515)

Ferraro F. R., et al., 2021, "A new class of fossil fragments from the hierarchical assembly of the Galactic bulge" Nature Astronomy, 5, 311 (arXiv:2011.09966)

Frebel A., Norris J. E., 2015, "Near-Field Cosmology with Extremely Metal-Poor Stars" ARA&A, 53, 631 (arXiv:1501.06921)

Freeman K. C., Rodgers A. W., 1975, "The Chemical Inhomogeneity of Omega Centauri" ApJ, 201, L71

Frogel J. A., Kuchinski L. E., Tiede G. P., 1995, "Infrared Array Photometry of Metal-Rich Globular Clusters. II. Liller 1- The Most Metal Rich Cluster?" AJ, 109, 1154

Fukugita M., Hogan C. J., Peebles P. J. E., 1998, "The Cosmic Baryon Budget" ApJ, 503, 518 (arXiv:astro-ph/9712020)

Gaia Collaboration Prusti T., de Bruijne J. H. J., Brown A. G. A., Vallenari A., Babusiaux C., et al., 2016, "The Gaia mission" A&A, 595, A1 (arXiv:1609.04153)

Gaia Collaboration Babusiaux C., van Leeuwen F., Barstow M. A., Jordi C., Vallenari A., et al., 2018, "Gaia Data Release 2. Observational Hertzsprung-Russell diagrams" A&A, 616, A10 (arXiv:1804.09378)

Gaia Collaboration Brown A. G. A., Vallenari A., Prusti T., de Bruijne J. H. J., Babusiaux C., et al., 2021, "Gaia Early Data Release 3. Summary of the contents and survey properties" A&A, 649, A1 (arXiv:2012.01533)

Gaia Collaboration Vallenari A., Brown A. G. A., Prusti T., de Bruijne J. H. J., Arenou F., et al., 2023, "Gaia Data Release 3. Summary of the content and survey properties" A&A, 674, A1 (arXiv:2208.00211)

Gatto M., et al., 2020, "A search for star clusters in the outskirts of the Large Magellanic Cloud: indication of clusters in the age gap" MNRAS, 499, 4114 (arXiv:2007.00341)

Georgiev I. Y., Böker T., 2014, "Nuclear star clusters in 228 spiral galaxies in the HST/WFPC2 archive: catalogue and comparison to other stellar systems" MNRAS, 441, 3570 (arXiv:1404.5956)

Georgiev I. Y., Böker T., Leigh N., Lützgendorf N., Neumayer N., 2016, "Masses and scaling relations for nuclear star clusters, and their co-existence with central black holes" MNRAS, 457, 2122 (arXiv:1601.02613)

Gibbons S. L. J., Belokurov V., Evans N. W., 2017, "A tail of two populations: chemo-dynamics of the Sagittarius stream and implications for its original mass" MNRAS, 464, 794 (arXiv:1607.00803)

Gieles M., et al., 2018, "Concurrent formation of supermassive stars and globular clusters: implications for early self-enrichment" MNRAS, 478, 2461 (arXiv:1804.04682)

Gnedin O. Y., Zhao H., Pringle J. E., Fall S. M., Livio M., Meylan G., 2002, "The Unique History of the Globular Cluster ω Centauri" ApJ, 568, L23 (arXiv:astro-ph/0202045)

Goldsbury R., Richer H. B., Anderson J., Dotter A., Sarajedini A., Woodley K., 2010, "The ACS Survey of Galactic Globular Clusters. X. New Determinations of Centers for 65 Clusters" AJ, 140, 1830 (arXiv:1008.2755)

Gonzalez O. A., Rejkuba M., Zoccali M., Valenti E., Minniti D., Schultheis M., Tobar R., Chen B., 2012, "Reddening and metallicity maps of the Milky Way bulge from VVV and 2MASS. II. The complete high resolution extinction map and implications for Galactic bulge studies" A&A, 543, A13 (arXiv:1204.4004)

Gratton R. G., 1982, "Abundances in metal-poor stars. II. The anomalous globular cluster omega Centauri." A&A, 115, 336

Gratton R. G., Pilachowski C. A., Sneden C., 1984, "H-alpha emission in old giants." A&A, 132, 11

Gratton R. G., Sneden C., Carretta E., Bragaglia A., 2000, "Mixing along the red giant branch in metal-poor field stars" A&A, 354, 169

Gratton R. G., et al., 2001, "The O-Na and Mg-Al anticorrelations in turn-off and early subgiants in globular clusters" A&A, 369, 87 (arXiv:astro-ph/0012457)

Gratton R., Sneden C., Carretta E., 2004, "Abundance Variations Within Globular Clusters" ARA&A, 42, 385

Gratton R. G., Carretta E., Bragaglia A., 2012, "Multiple populations in globular clusters. Lessons learned from the Milky Way globular clusters" A&A Rev., 20, 50 (arXiv:1201.6526)

Gratton R. G., et al., 2014, "The Na-O anticorrelation in horizontal branch stars. IV. M 22" A&A, 563, A13 (arXiv:1401.7109)

Gratton R., Bragaglia A., Carretta E., D'Orazi V., Lucatello S., Sollima A., 2019, "What is a globular cluster? An observational perspective" A&A Rev., 27, 8 (arXiv:1911.02835)

Grcevich J., Putman M. E., 2009, "H I in Local Group Dwarf Galaxies and Stripping by the Galactic Halo" ApJ, 696, 385 (arXiv:0901.4975)

Grevesse N., Sauval A. J., 1998, "Standard Solar Composition" Space Sci. Rev., 85, 161
Grieco V., Matteucci F., Pipino A., Cescutti G., 2012, "Chemical evolution of the Galactic bulge: different stellar populations and possible gradients" A&A, 548, A60 (arXiv:1209.4462)
Grundahl F., Vandenberg D. A., Stetson P. B., Andersen M. I., Briley M., 2000, in Noels A., Magain P., Caro D., Jehin E., Parmentier G., Thoul A. A., eds, Liege International Astrophysical Colloquia Vol. 35, Liege International Astrophysical Colloquia. p. 503 (arXiv:astro-ph/9909447), doi:10.48550/arXiv.astro-ph/9909447
Grundahl F., Briley M., Nissen P. E., Feltzing S., 2002, "Abundances of RGB stars in NGC 6752" A&A, 385, L14
Guo Y., et al., 2015, "Clumpy Galaxies in CANDELS. I. The Definition of UV Clumps and the Fraction of Clumpy Galaxies at 0.5 < z < 3" ApJ, 800, 39 (arXiv:1410.7398)
Gustafsson B., Edvardsson B., Eriksson K., Jørgensen U. G., Nordlund Å., Plez B., 2008, "A grid of MARCS model atmospheres for late-type stars. I. Methods and general properties" A&A, 486, 951 (arXiv:0805.0554)
Häberle M., et al., 2024, "oMEGACat. II. Photometry and Proper Motions for 1.4 Million Stars in Omega Centauri and Its Rotation in the Plane of the Sky" ApJ, 970, 192 (arXiv:2404.03722)
Hall J. C., 2008, "Stellar Chromospheric Activity" Living Reviews in Solar Physics, 5, 2
Han S.-I., Lee Y.-W., Joo S.-J., Sohn S. T., Yoon S.-J., Kim H.-S., Lee J.-W., 2009, "The Presence of Two Distinct Red Giant Branches in the Globular Cluster NGC 1851" ApJ, 707, L190 (arXiv:0911.5356)
Harris W. E., 1975, "New color-magnitude data for twelve globular clusters." ApJS, 29, 397
Harris W. E., 1996, "A Catalog of Parameters for Globular Clusters in the Milky Way" AJ, 112, 1487
Harris W. E., 2010, "A New Catalog of Globular Clusters in the Milky Way" arXiv e-prints, p. arXiv:1012.3224 (arXiv:1012.3224)
Hasselquist S., et al., 2021, "APOGEE Chemical Abundance Patterns of the Massive Milky Way Satellites" ApJ, 923, 172 (arXiv:2109.05130)
Hayes C. R., et al., 2020, "Metallicity and α-Element Abundance Gradients along the Sagittarius Stream as Seen by APOGEE" ApJ, 889, 63 (arXiv:1912.06707)
Helmi A., Babusiaux C., Koppelman H. H., Massari D., Veljanoski J., Brown A. G. A., 2018, "The merger that led to the formation of the Milky Way's inner stellar halo and thick disk" Nature, 563, 85 (arXiv:1806.06038)
Herschel W., 1789, "Catalogue of a Second Thousand of New Nebulae and Clusters of Stars; With a Few Introductory Remarks on the Construction of the Heavens. By William Herschel, L L. D. F. R. S." Philosophical Transactions of the Royal Society of London Series I, 79, 212
Hidalgo S. L., et al., 2018, "The Updated BaSTI Stellar Evolution Models and Isochrones. I. Solar-scaled Calculations" ApJ, 856, 125 (arXiv:1802.07319)
Hopkins P. F., et al., 2010, "Mergers and Bulge Formation in ΛCDM: Which Mergers Matter?" ApJ, 715, 202 (arXiv:0906.5357)
Horta D., et al., 2020, "The chemical compositions of accreted and in situ galactic globular clusters according to SDSS/APOGEE" MNRAS, 493, 3363 (arXiv:2001.03177)
Ibata R. A., Gilmore G., Irwin M. J., 1994, "A dwarf satellite galaxy in Sagittarius" Nature, 370, 194
Ibata R. A., Wyse R. F. G., Gilmore G., Irwin M. J., Suntzeff N. B., 1997, "The Kinematics, Orbit, and Survival of the Sagittarius Dwarf Spheroidal Galaxy" AJ, 113, 634 (arXiv:astro-ph/9612025)
Ibata R., Chapman S., Ferguson A. M. N., Irwin M., Lewis G., McConnachie A., 2004, "Taking measure of the Andromeda halo: a kinematic analysis of the giant stream surrounding M31" MNRAS, 351, 117 (arXiv:astro-ph/0403068)
Ibata R. A., Bellazzini M., Malhan K., Martin N., Bianchini P., 2019a, "Identification of the long stellar stream of the prototypical massive globular cluster ω Centauri" Nature Astronomy, 3, 667 (arXiv:1902.09544)
Ibata R. A., Malhan K., Martin N. F., 2019b, "The Streams of the Gaping Abyss: A Population of Entangled Stellar Streams Surrounding the Inner Galaxy" ApJ, 872, 152 (arXiv:1901.07566)
Ibata R., Bellazzini M., Thomas G., Malhan K., Martin N., Famaey B., Siebert A., 2020, "A Panoramic Landscape of the Sagittarius Stream in Gaia DR2 Revealed with the STREAMFINDER Spyglass" ApJ, 891, L19 (arXiv:2002.11121)
Ibata R., et al., 2021, "Charting the Galactic Acceleration Field. I. A Search for Stellar Streams with Gaia DR2 and EDR3 with Follow-up from ESPaDOnS and UVES" ApJ, 914, 123 (arXiv:2012.05245)
Iben Icko J., 1964, "The Surface Ratio of N^{14} to C^{12} during Helium Burning." ApJ, 140, 1631
Iben I., Renzini A., 1984, "Single star evolution I. Massive stars and early evolution of low and intermediate mass

stars" Phys. Rep., 105, 329
Iliadis C., D'Auria J. M., Starrfield S., Thompson W. J., Wiescher M., 2001, "Proton-induced Thermonuclear Reaction Rates for A=20-40 Nuclei" ApJS, 134, 151
Immeli A., Samland M., Gerhard O., Westera P., 2004, "Gas physics, disk fragmentation, and bulge formation in young galaxies" A&A, 413, 547 (arXiv:astro-ph/0312139)
Johnson C. I., Pilachowski C. A., 2010, "Chemical Abundances for 855 Giants in the Globular Cluster Omega Centauri (NGC 5139)" ApJ, 722, 1373 (arXiv:1008.2232)
Johnson J. A., Ivans I. I., Stetson P. B., 2006, "Chemical Compositions of Red Giant Stars in Old Large Magellanic Cloud Globular Clusters" ApJ, 640, 801 (arXiv:astro-ph/0512132)
Johnson C. I., Rich R. M., Kobayashi C., Kunder A., Koch A., 2014, "Light, Alpha, and Fe-peak Element Abundances in the Galactic Bulge" AJ, 148, 67 (arXiv:1407.2282)
Johnson C. I., Rich R. M., Pilachowski C. A., Caldwell N., Mateo M., Bailey John I. I., Crane J. D., 2015, "A Spectroscopic Analysis of the Galactic Globular Cluster NGC 6273 (M19)" AJ, 150, 63 (arXiv:1507.00756)
José J., 2017, in Kubono S., Kajino T., Nishimura S., Isobe T., Nagataki S., Shima T., Takeda Y., eds, 14th International Symposium on Nuclei in the Cosmos (NIC2016). p. 010501, doi:10.7566/JPSCP.14.010501
Kacharov N., Neumayer N., Seth A. C., Cappellari M., McDermid R., Walcher C. J., Böker T., 2018, "Stellar populations and star formation histories of the nuclear star clusters in six nearby galaxies" MNRAS, 480, 1973 (arXiv:1807.08765)
Khoperskov S., Mastrobuono-Battisti A., Di Matteo P., Haywood M., 2018, "Mergers, tidal interactions, and mass exchange in a population of disc globular clusters" A&A, 620, A154 (arXiv:1809.04350)
Kirby E. N., Guhathakurta P., Bolte M., Sneden C., Geha M. C., 2009, "MULTI-ELEMENT ABUNDANCE MEASUREMENTS FROM MEDIUM-RESOLUTION SPECTRA. I. THE SCULPTOR DWARF SPHEROIDAL GALAXY" The Astrophysical Journal, 705, 328–346
Kirby E. N., Lanfranchi G. A., Simon J. D., Cohen J. G., Guhathakurta P., 2011, "Multi-element Abundance Measurements from Medium-resolution Spectra. III. Metallicity Distributions of Milky Way Dwarf Satellite Galaxies" ApJ, 727, 78 (arXiv:1011.4937)
Kobayashi C., Umeda H., Nomoto K., Tominaga N., Ohkubo T., 2006, "Galactic Chemical Evolution: Carbon through Zinc" ApJ, 653, 1145 (arXiv:astro-ph/0608688)
Kobayashi C., Karakas A. I., Umeda H., 2011, "The evolution of isotope ratios in the Milky Way Galaxy" MNRAS, 414, 3231 (arXiv:1102.5312)
Kraft R. P., 1979, "On the nonhomogeneity of metal abundances in stars of globular clusters and satellite subsystems of the Galaxy." ARA&A, 17, 309
Kraft R. P., 1994, "Abundance Differences among Globular Cluster Giants: Primordial vs. Evolutionary Scenarios" PASP, 106, 553
Krause M., Charbonnel C., Decressin T., Meynet G., Prantzos N., 2013, "Superbubble dynamics in globular cluster infancy. II. Consequences for secondary star formation in the context of self-enrichment via fast-rotating massive stars" A&A, 552, A121 (arXiv:1302.2494)
Kroupa P., 2001, "On the variation of the initial mass function" MNRAS, 322, 231 (arXiv:astro-ph/0009005)
Kruijssen J. M. D., 2015, "Globular clusters as the relics of regular star formation in 'normal' high-redshift galaxies" MNRAS, 454, 1658 (arXiv:1509.02163)
Kurucz R. L., 2005, "ATLAS12, SYNTHE, ATLAS9, WIDTH9, et cetera" Memorie della Societa Astronomica Italiana Supplementi, 8, 14
Lada C. J., Lada E. A., 2003, "Embedded Clusters in Molecular Clouds" ARA&A, 41, 57 (arXiv:astro-ph/0301540)
Lagioia E. P., et al., 2021, "Multiple Stellar Populations in Asymptotic Giant Branch Stars of Galactic Globular Clusters" ApJ, 910, 6 (arXiv:2101.09843)
Langer G. E., 1985, "Bimodal cyanogen distributions in moderately metal-poor globular clusters. II. Evidence for "mixing" and "saturation"." PASP, 97, 382
Langer G. E., Hoffman R., Sneden C., 1993, "Sodium-Oxygen Abundance Anticorrelations and Deep Mixing Scenarios for Globular Cluster Giants" PASP, 105, 301
Lanzoni B., et al., 2010, "New Density Profile and Structural Parameters of the Complex Stellar System Terzan 5" ApJ, 717, 653 (arXiv:1005.2847)

Lapenna E., et al., 2016, "Lost and Found: Evidence of Second-generation Stars Along the Asymptotic Giant Branch of the Globular Cluster NGC 6752" ApJ, 826, L1 (arXiv:1606.09256)
Lardo C., Bellazzini M., Pancino E., Carretta E., Bragaglia A., Dalessandro E., 2011, "Mining SDSS in search of multiple populations in globular clusters" A&A, 525, A114 (arXiv:1010.4697)
Lardo C., et al., 2012, "C and N abundances of main sequence and subgiant branch stars in NGC 1851" A&A, 541, A141 (arXiv:1202.6176)
Lardo C., et al., 2013, "The double red giant branch in M2: C, N, Sr and Ba abundances" MNRAS, 433, 1941 (arXiv:1305.3181)
Lardo C., Salaris M., Savino A., Donati P., Stetson P. B., Cassisi S., 2017, "Multiple populations along the asymptotic giant branch of the globular cluster M4" MNRAS, 466, 3507 (arXiv:1612.08929)
Lardo C., Salaris M., Cassisi S., Bastian N., 2022, "Confirmation of a metallicity spread amongst first population stars in globular clusters" A&A, 662, A117 (arXiv:2205.03323)
Lardo C., Salaris M., Cassisi S., Bastian N., Mucciarelli A., Cabrera-Ziri I., Dalessandro E., 2023, "High-precision abundances of first-population stars in NGC 2808: confirmation of a metallicity spread" A&A, 669, A19 (arXiv:2210.13369)
Larsen S. S., Brodie J. P., Grundahl F., Strader J., 2014, "Nitrogen Abundances and Multiple Stellar Populations in the Globular Clusters of the Fornax dSph" ApJ, 797, 15 (arXiv:1409.0541)
Latour M., Calamida A., Husser T. O., Kamann S., Dreizler S., Brinchmann J., 2021, "A stellar census in globular clusters with MUSE. A new perspective on the multiple main sequences of ω Centauri" A&A, 653, L8 (arXiv:2109.01540)
Law D. R., Majewski S. R., 2016, in Newberg H. J., Carlin J. L., eds, Astrophysics and Space Science Library Vol. 420, Tidal Streams in the Local Group and Beyond. p. 31, doi:10.1007/978-3-319-19336-6_2
Layden A. C., Sarajedini A., 1997, "The Globular Cluster M54 and the Star Formation History of the Sagittarius Dwarf Galaxy" ApJ, 486, L107 (arXiv:astro-ph/9706168)
Layden A. C., Sarajedini A., 2000, "Photometry of the Globular Cluster M54 and the Sagittarius Dwarf Galaxy: The Age-Metallicity Relation" AJ, 119, 1760
Lebzelter T., Wood P. R., 2016, "The long-period variables in ω Centauri" A&A, 585, A111
Lee J.-W., 2022, "Multiple Stellar Populations of Globular Clusters from Homogeneous Ca-CN-CH-NH Photometry. VII. Metal-poor Populations in 47 Tucanae (NGC 104)" ApJS, 263, 20 (arXiv:2210.12332)
Lee J.-W., 2023, "M92 (NGC 6341) Is a Metal-complex Globular Cluster with an Atypical Primordial Population" ApJ, 948, L16 (arXiv:2305.02983)
Lee Y. W., Joo J. M., Sohn Y. J., Rey S. C., Lee H. C., Walker A. R., 1999, "Multiple stellar populations in the globular cluster ω Centauri as tracers of a merger event" Nature, 402, 55 (arXiv:astro-ph/9911137)
Lee Y.-W., et al., 2005, "Super-Helium-rich Populations and the Origin of Extreme Horizontal-Branch Stars in Globular Clusters" ApJ, 621, L57 (arXiv:astro-ph/0501500)
Legnardi M. V., et al., 2022, "Constraining the original composition of the gas forming first-generation stars in globular clusters" MNRAS, 513, 735 (arXiv:2203.07571)
Leon S., Meylan G., Combes F., 2000, "Tidal tails around 20 Galactic globular clusters. Observational evidence for gravitational disk/bulge shocking" A&A, 359, 907 (arXiv:astro-ph/0006100)
Leonard P. J. T., 1989, "Stellar Collisions in Globular Clusters and the Blue Straggler Problem" AJ, 98, 217
Letarte B., Hill V., Jablonka P., Tolstoy E., François P., Meylan G., 2006, "VLT/UVES spectroscopy of individual stars in three globular clusters in the Fornax dwarf spheroidal galaxy" A&A, 453, 547 (arXiv:astro-ph/0603315)
Li C., et al., 2023, "Multiple Stellar Populations at Less Evolved Stages. III. A Possible Helium Spread in NGC 2210" ApJ, 948, 8 (arXiv:2302.10466)
Liller W., 1977, "Searches for the optical counterpart of the X-ray burst sources MXB 1728-34 and MXB 1730-33." ApJ, 213, L21
Limberg G., Souza S. O., Pérez-Villegas A., Rossi S., Perottoni H. D., Santucci R. M., 2022, "Reconstructing the Disrupted Dwarf Galaxy Gaia-Sausage/Enceladus Using Its Stars and Globular Clusters" ApJ, 935, 109 (arXiv:2206.10505)
Lind K., Primas F., Charbonnel C., Grundahl F., Asplund M., 2009, "Signatures of intrinsic Li depletion and Li-Na anti-correlation in the metal-poor globular cluster NGC 6397" A&A, 503, 545 (arXiv:0906.2876)

Lind K., Asplund M., Barklem P. S., Belyaev A. K., 2011, "Non-LTE calculations for neutral Na in late-type stars using improved atomic data" A&A, 528, A103 (arXiv:1102.2160)

Lindblad B., 1922, "Spectrophotometric methods for determining stellar luminosity." ApJ, 55, 85

Linsky J. L., 2017, "Stellar Model Chromospheres and Spectroscopic Diagnostics" ARA&A, 55, 159

Loup C., Forveille T., Omont A., Paul J. F., 1993, "CO and HCN observations of circumstellar envelopes. A catalogue - mass loss rates and distributions." A&AS, 99, 291

Lynn W. T., 1886, "The discovery of the star-cluster 22 Messier in Sagittarius" The Observatory, 9, 163

Maccarone T. J., Zurek D. R., 2012, "Novae from isolated white dwarfs as a source of helium for second-generation stars in globular clusters" MNRAS, 423, 2 (arXiv:1112.0571)

Magg E., et al., 2022, "Observational constraints on the origin of the elements. IV. Standard composition of the Sun" A&A, 661, A140 (arXiv:2203.02255)

Majewski S. R., Patterson R. J., Dinescu D. I., Johnson W. Y., Ostheimer J. C., Kunkel W. E., Palma C., 2000, in Noels A., Magain P., Caro D., Jehin E., Parmentier G., Thoul A. A., eds, Liege International Astrophysical Colloquia Vol. 35, Liege International Astrophysical Colloquia. p. 619 (arXiv:astro-ph/9910278), doi:10.48550/arXiv.astro-ph/9910278

Majewski S. R., Skrutskie M. F., Weinberg M. D., Ostheimer J. C., 2003, "A Two Micron All Sky Survey View of the Sagittarius Dwarf Galaxy. I. Morphology of the Sagittarius Core and Tidal Arms" ApJ, 599, 1082 (arXiv:astro-ph/0304198)

Majewski S. R., et al., 2017, "The Apache Point Observatory Galactic Evolution Experiment (APOGEE)" AJ, 154, 94 (arXiv:1509.05420)

Mallia E. A., Pagel B. E. J., 1981, "On the variation of heavy-element abundances in OME CEN giants." MNRAS, 194, 421

Marín-Franch A., et al., 2009, "The ACS Survey of Galactic Globular Clusters. VII. Relative Ages" ApJ, 694, 1498 (arXiv:0812.4541)

Marino A. F., Villanova S., Piotto G., Milone A. P., Momany Y., Bedin L. R., Medling A. M., 2008, "Spectroscopic and photometric evidence of two stellar populations in the Galactic globular cluster NGC 6121 (M 4)" A&A, 490, 625 (arXiv:0808.1414)

Marino A. F., Milone A. P., Piotto G., Villanova S., Bedin L. R., Bellini A., Renzini A., 2009, "A double stellar generation in the globular cluster NGC 6656 (M 22). Two stellar groups with different iron and s-process element abundances" A&A, 505, 1099 (arXiv:0905.4058)

Marino A. F., et al., 2011a, "The two metallicity groups of the globular cluster M 22: a chemical perspective" A&A, 532, A8 (arXiv:1105.1523)

Marino A. F., Villanova S., Milone A. P., Piotto G., Lind K., Geisler D., Stetson P. B., 2011b, "Sodium-Oxygen Anti-correlation Among Horizontal Branch Stars in the Globular Cluster M4" ApJ, 730, L16 (arXiv:1012.4931)

Marino A. F., et al., 2011c, "Sodium-Oxygen Anticorrelation and Neutron-capture Elements in Omega Centauri Stellar Populations" ApJ, 731, 64 (arXiv:1102.1653)

Marino A. F., et al., 2012a, "The double sub-giant branch of NGC 6656 (M 22): a chemical characterization" A&A, 541, A15 (arXiv:1202.2825)

Marino A. F., et al., 2012b, "The C+N+O Abundance of ω Centauri Giant Stars: Implications for the Chemical-enrichment Scenario and the Relative Ages of Different Stellar Populations" ApJ, 746, 14 (arXiv:1111.1891)

Marino A. F., et al., 2014, "Helium enhanced stars and multiple populations along the horizontal branch of NGC 2808: direct spectroscopic measurements" MNRAS, 437, 1609 (arXiv:1310.4527)

Marino A. F., et al., 2015, "Iron and s-elements abundance variations in NGC 5286: comparison with 'anomalous' globular clusters and Milky Way satellites" MNRAS, 450, 815 (arXiv:1502.07438)

Marino A. F., et al., 2021, "Spectroscopy and Photometry of the Least Massive Type II Globular Clusters: NGC 1261 and NGC 6934" ApJ, 923, 22 (arXiv:2106.15978)

Martell S. L., Smith G. H., 2009, "CN Variations in High-Metallicity Globular and Open Clusters" PASP, 121, 577 (arXiv:0905.3175)

Martell S. L., Smolinski J. P., Beers T. C., Grebel E. K., 2011, "Building the Galactic halo from globular clusters: evidence from chemically unusual red giants" A&A, 534, A136 (arXiv:1109.3916)

Massari D., et al., 2014, "Ceci N'est Pas a Globular Cluster: The Metallicity Distribution of the Stellar System Terzan 5" ApJ, 795, 22 (arXiv:1409.1682)

Massari D., Koppelman H. H., Helmi A., 2019, "Origin of the system of globular clusters in the Milky Way" A&A, 630, L4 (arXiv:1906.08271)
Masseron T., et al., 2019, "Homogeneous analysis of globular clusters from the APOGEE survey with the BACCHUS code. I. The northern clusters" A&A, 622, A191 (arXiv:1812.08817)
Mastrobuono-Battisti A., Khoperskov S., Di Matteo P., Haywood M., 2019, "Mergers, tidal interactions, and mass exchange in a population of disc globular clusters. II. Long-term evolution" A&A, 622, A86 (arXiv:1811.07907)
McKenzie M., Bekki K., 2018, "A new model for the multiple stellar populations within Terzan 5" MNRAS, 479, 3126 (arXiv:1806.04824)
McWilliam A., Matteucci F., Ballero S., Rich R. M., Fulbright J. P., Cescutti G., 2008, "The Evolution of Oxygen and Magnesium in the Bulge and Disk of the Milky way" AJ, 136, 367 (arXiv:0708.4026)
Messier C., 1781, Catalogue des Nébuleuses et des Amas d'Étoiles (Catalog of Nebulae and Star Clusters), Connoissance des Temps ou des Mouvements Célestes, for 1784, p. 227-267
Meszaros S., Dupree A. K., Szentgyorgyi A., 2008, "Mass Outflow and Chromospheric Activity of Red Giant Stars in Globular Clusters.I. M15" AJ, 135, 1117 (arXiv:0801.0433)
Mészáros S., Dupree A. K., Szalai T., 2009, "Mass Outflow and Chromospheric Activity of Red Giant Stars in Globular Clusters. II. M13 and M92" AJ, 137, 4282 (arXiv:0902.3367)
Mészáros S., et al., 2015, "Exploring Anticorrelations and Light Element Variations in Northern Globular Clusters Observed by the APOGEE Survey" AJ, 149, 153 (arXiv:1501.05127)
Mészáros S., et al., 2020, "Homogeneous analysis of globular clusters from the APOGEE survey with the BACCHUS code - II. The Southern clusters and overview" MNRAS, 492, 1641 (arXiv:1912.04839)
Mészáros S., et al., 2021, "Homogeneous analysis of globular clusters from the APOGEE survey with the BACCHUS code - III. ω Cen" MNRAS, 505, 1645 (arXiv:2104.12075)
Meylan G., Leon S., Combes F., 2000, in Bergeron J., Renzini A., eds, From Extrasolar Planets to Cosmology: The VLT Opening Symposium. p. 369 (arXiv:astro-ph/9912041), doi:10.1007/10720961_55
Milone A. P., Marino A. F., 2022, "Multiple Populations in Star Clusters" Universe, 8, 359 (arXiv:2206.10564)
Milone A. P., et al., 2008, "The ACS Survey of Galactic Globular Clusters. III. The Double Subgiant Branch of NGC 1851" ApJ, 673, 241 (arXiv:0709.3762)
Milone A. P., et al., 2012, "The Infrared Eye of the Wide-Field Camera 3 on the Hubble Space Telescope Reveals Multiple Main Sequences of Very Low Mass Stars in NGC 2808" ApJ, 754, L34 (arXiv:1206.5529)
Milone A. P., et al., 2013, "A WFC3/HST View of the Three Stellar Populations in the Globular Cluster NGC 6752" ApJ, 767, 120 (arXiv:1301.7044)
Milone A. P., et al., 2015a, "The Hubble Space Telescope UV Legacy Survey of galactic globular clusters - II. The seven stellar populations of NGC 7089 (M2)*" MNRAS, 447, 927 (arXiv:1411.5043)
Milone A. P., et al., 2015b, "The Hubble Space Telescope UV Legacy Survey of Galactic Globular Clusters. III. A Quintuple Stellar Population in NGC 2808" ApJ, 808, 51 (arXiv:1505.05934)
Milone A. P., et al., 2017a, "The Hubble Space Telescope UV Legacy Survey of Galactic globular clusters - IX. The Atlas of multiple stellar populations" MNRAS, 464, 3636 (arXiv:1610.00451)
Milone A. P., et al., 2017b, "The HST large programme on ω Centauri - I. Multiple stellar populations at the bottom of the main sequence probed in NIR-Optical" MNRAS, 469, 800 (arXiv:1704.00418)
Milone A. P., et al., 2018, "The Hubble Space Telescope UV legacy survey of galactic globular clusters - XVI. The helium abundance of multiple populations" MNRAS, 481, 5098 (arXiv:1809.05006)
Milone A. P., et al., 2019, "The HST Large Programme on NGC 6752 - II. Multiple populations at the bottom of the main sequence probed in NIR" MNRAS, 484, 4046 (arXiv:1901.07230)
Milone A. P., et al., 2020, "A chromosome map to unveil stellar populations with different magnesium abundances. The case of ω Centauri" MNRAS, 497, 3846 (arXiv:2006.13101)
Milone A. P., et al., 2023, "Multiple stellar populations in globular clusters with JWST: an NIRCam view of 47 Tucanae" MNRAS, 522, 2429 (arXiv:2301.10889)
Minelli A., Mucciarelli A., Romano D., Bellazzini M., Origlia L., Ferraro F. R., 2021, "A Homogeneous Comparison between the Chemical Composition of the Large Magellanic Cloud and the Sagittarius Dwarf Galaxy" ApJ, 910, 114 (arXiv:2102.04516)
Minelli A., et al., 2023, "The metallicity distribution in the core of the Sagittarius dwarf spheroidal: Minimising the metallicity biases" A&A, 669, A54 (arXiv:2211.06727)

Minniti D., et al., 2010, "VISTA Variables in the Via Lactea (VVV): The public ESO near-IR variability survey of the Milky Way" New A, 15, 433 (arXiv:0912.1056)

Moehler S., Dreizler S., Lanz T., Bono G., Sweigart A. V., Calamida A., Monelli M., Nonino M., 2007, "The hottest horizontal-branch stars in ω Centauri. Late hot flasher vs. helium enrichment" A&A, 475, L5 (arXiv:0709.2839)

Monaco L., Ferraro F. R., Bellazzini M., Pancino E., 2002, "First Detection of the Red Giant Branch Bump in the Sagittarius Dwarf Spheroidal Galaxy" ApJ, 578, L47 (arXiv:astro-ph/0208581)

Monaco L., Bellazzini M., Ferraro F. R., Pancino E., 2004, "The distance to the Sagittarius dwarf spheroidal galaxy from the red giant branch tip" MNRAS, 353, 874 (arXiv:astro-ph/0406350)

Monaco L., Bellazzini M., Ferraro F. R., Pancino E., 2005, "The central density cusp of the Sagittarius dwarf spheroidal galaxy" MNRAS, 356, 1396 (arXiv:astro-ph/0411107)

Monaco L., Villanova S., Bonifacio P., Caffau E., Geisler D., Marconi G., Momany Y., Ludwig H. G., 2012, "Lithium and sodium in the globular cluster <ASTROBJ>M 4</ASTROBJ>. Detection of a Li-rich dwarf star: preservation or pollution?" A&A, 539, A157 (arXiv:1108.0138)

Monelli M., et al., 2013, "The SUMO project I. A survey of multiple populations in globular clusters" MNRAS, 431, 2126 (arXiv:1303.5187)

Montegriffo P., Bellazzini M., Ferraro F. R., Martins D., Sarajedini A., Fusi Pecci F., 1998, "The globular cluster system of the Sagittarius dwarf spheroidal galaxy: the age of Terzan 8." MNRAS, 294, 315 (arXiv:astro-ph/9710237)

Monty S., Yong D., Marino A. F., Karakas A. I., McKenzie M., Grundahl F., Mura-Guzmán A., 2023, "Peeking beneath the precision floor - I. Metallicity spreads and multiple elemental dispersions in the globular clusters NGC 288 and NGC 362" MNRAS, 518, 965 (arXiv:2210.15061)

Moreno E., Fernández-Trincado J. G., Pérez-Villegas A., Chaves-Velasquez L., Schuster W. J., 2022, "Orbits of globular clusters computed with dynamical friction in the Galactic anisotropic velocity dispersion field" MNRAS, 510, 5945 (arXiv:2112.11589)

Moretti A., et al., 2009, "MCAO near-IR photometry of the globular cluster NGC 6388: MAD observations in crowded fields" A&A, 493, 539 (arXiv:0810.2248)

Muñoz C., Villanova S., Geisler D., Saviane I., Dias B., Cohen R. E., Mauro F., 2017, "The peculiar Na-O anticorrelation of the bulge globular cluster NGC 6440" A&A, 605, A12 (arXiv:1705.02684)

Mucciarelli A., 2013, "4DAO Cookbook" arXiv e-prints, p. arXiv:1311.1403 (arXiv:1311.1403)

Mucciarelli A., Origlia L., Ferraro F. R., Pancino E., 2009, "Looking Outside the Galaxy: The Discovery of Chemical Anomalies in Three Old Large Magellanic Cloud Clusters" ApJ, 695, L134 (arXiv:0902.4778)

Mucciarelli A., Salaris M., Lovisi L., Ferraro F. R., Lanzoni B., Lucatello S., Gratton R. G., 2011, "Lithium abundance in the globular cluster M4: from the turn-off to the red giant branch bump" MNRAS, 412, 81 (arXiv:1010.3879)

Mucciarelli A., Bellazzini M., Ibata R., Merle T., Chapman S. C., Dalessandro E., Sollima A., 2012, "News from the Galactic suburbia: the chemical composition of the remote globular cluster NGC 2419" MNRAS, 426, 2889 (arXiv:1208.0195)

Mucciarelli A., Pancino E., Lovisi L., Ferraro F. R., Lapenna E., 2013, "GALA: An Automatic Tool for the Abundance Analysis of Stellar Spectra" ApJ, 766, 78 (arXiv:1302.3618)

Mucciarelli A., Lovisi L., Lanzoni B., Ferraro F. R., 2014, "The Helium Abundance in the Metal-poor Globular Clusters M30 and NGC 6397" ApJ, 786, 14 (arXiv:1403.0595)

Mucciarelli A., Bellazzini M., Merle T., Plez B., Dalessandro E., Ibata R., 2015, "Potassium: A New Actor on the Globular Cluster Chemical Evolution Stage. The Case of NGC 2808" ApJ, 801, 68 (arXiv:1501.03161)

Mucciarelli A., Bellazzini M., Ibata R., Romano D., Chapman S. C., Monaco L., 2017, "Chemical abundances in the nucleus of the Sagittarius dwarf spheroidal galaxy" A&A, 605, A46 (arXiv:1705.03251)

Mucciarelli A., Salaris M., Monaco L., Bonifacio P., Fu X., Villanova S., 2018a, "Lithium abundance in lower red giant branch stars of Omega Centauri" A&A, 618, A134 (arXiv:1807.07582)

Mucciarelli A., Lapenna E., Ferraro F. R., Lanzoni B., 2018b, "The Chemical Composition of NGC 5824, a Globular Cluster without Iron Spread but with an Extreme Mg-Al Anticorrelation" ApJ, 859, 75 (arXiv:1803.09759)

Mucciarelli A., Bellazzini M., Massari D., 2021, "Exploiting the Gaia EDR3 photometry to derive stellar temperatures" A&A, 653, A90 (arXiv:2106.03882)

Myeong G. C., Evans N. W., Belokurov V., Sanders J. L., Koposov S. E., 2018, "The Sausage Globular Clusters" ApJ, 863, L28 (arXiv:1805.00453)

Nardiello D., Milone A. P., Piotto G., Marino A. F., Bellini A., Cassisi S., 2015, "Observing multiple stellar populations

with VLT/FORS2. Main sequence photometry in outer regions of NGC 6752, NGC 6397, and NGC 6121 (M 4)" A&A, 573, A70 (arXiv:1410.7503)
Ness M., et al., 2013, "ARGOS - III. Stellar populations in the Galactic bulge of the Milky Way" MNRAS, 430, 836 (arXiv:1212.1540)
Neumayer N., Seth A., Böker T., 2020, "Nuclear star clusters" A&A Rev., 28, 4 (arXiv:2001.03626)
Newell E. B., Rodgers A. W., Searle L., 1969, "The blue-horizontal branch stars of omega Cen." ApJ, 158, 699
Niederste-Ostholt M., Belokurov V., Evans N. W., 2012, "A tale twice told: the luminosity profiles of the Sagittarius tails" MNRAS, 422, 207 (arXiv:1201.4516)
Nitschai M. S., et al., 2024, "oMEGACat. III. Multiband Photometry and Metallicities Reveal Spatially Well-mixed Populations within ω Centauri's Half-light Radius" ApJ, 970, 152 (arXiv:2406.01688)
Noble R. G., Dickens R. J., Buttress J., Griffiths W. K., Penny A. J., 1991, "Main-sequence CCD photometry of the globular cluster omega Cen." MNRAS, 250, 314
Norris J., 1980, in Hanes D., Madore B., eds, Globular Clusters. p. 113
Norris J. E., 2004, "The Helium Abundances of ω Centauri" ApJ, 612, L25
Norris J. E., Da Costa G. S., 1995a, "The Sodium/Aluminum–Oxygen Anticorrelation in omega Centauri and Other Clusters" ApJ, 441, L81
Norris J. E., Da Costa G. S., 1995b, "The Giant Branch of omega Centauri. IV. Abundance Patterns Based on Echelle Spectra of 40 Red Giants" ApJ, 447, 680
Norris J., Freeman K. C., 1982, "The anticorrelation of carbon and nitrogen on the horizontal branch of 47 Tuc." ApJ, 254, 143
Norris J., Cottrell P. L., Freeman K. C., Da Costa G. S., 1981, "The abundance spread in the giants of NGC 6752." ApJ, 244, 205
Norris J. E., Freeman K. C., Mighell K. J., 1996, "The Giant Branch of omega Centauri. V. The Calcium Abundance Distribution" ApJ, 462, 241
Ordenes-Briceño Y., et al., 2018, "The Next Generation Fornax Survey (NGFS). IV. Mass and Age Bimodality of Nuclear Clusters in the Fornax Core Region" ApJ, 860, 4 (arXiv:1805.00491)
Origlia L., Rich R. M., Castro S., 2002, "High-Resolution Infrared Spectra of Bulge Globular Clusters: Liller 1 and NGC 6553" AJ, 123, 1559 (arXiv:astro-ph/0112104)
Origlia L., et al., 2011, "Spectroscopy Unveils the Complex Nature of Terzan 5" ApJ, 726, L20 (arXiv:1012.2047)
Origlia L., Massari D., Rich R. M., Mucciarelli A., Ferraro F. R., Dalessandro E., Lanzoni B., 2013, "The Terzan 5 Puzzle: Discovery of a Third, Metal-poor Component" ApJ, 779, L5 (arXiv:1311.1706)
Origlia L., et al., 2019, "Variable Stars in Terzan 5: Additional Evidence of Multi-age and Multi-iron Stellar Populations" ApJ, 871, 114
Ortolani S., Bica E., Barbuy B., 1996, "NTT V, I and Gunn Z colour-magnitude diagrams of Liller 1: a globular cluster as metal-rich as the inner bulge stellar population?" A&A, 306, 134
Ortolani S., Barbuy B., Bica E., Renzini A., Zoccali M., Rich R. M., Cassisi S., 2001, "HST NICMOS photometry of the reddened bulge globular clusters NGC 6528, Terzan 5, Liller 1, UKS 1 and Terzan 4" A&A, 376, 878 (arXiv:astro-ph/0107459)
Ortolani S., Barbuy B., Bica E., Zoccali M., Renzini A., 2007, "Distances of the bulge globular clusters Terzan 5, Liller 1, UKS 1, and Terzan 4 based on HST NICMOS photometry" A&A, 470, 1043 (arXiv:0705.4030)
Osborn W., 1971, "Two new CN-strong globular cluster stars" The Observatory, 91, 223
Pallanca C., et al., 2021, "High-resolution Extinction Map in the Direction of the Strongly Obscured Bulge Fossil Fragment Liller 1" ApJ, 917, 92 (arXiv:2106.02448)
Pancino E., Ferraro F. R., Bellazzini M., Piotto G., Zoccali M., 2000, "New Evidence for the Complex Structure of the Red Giant Branch in ω Centauri" ApJ, 534, L83 (arXiv:astro-ph/0003222)
Pancino E., Pasquini L., Hill V., Ferraro F. R., Bellazzini M., 2002, "High-Resolution Spectroscopy of Metal-rich Giants in ω Centauri: First Indication of Type Ia Supernova Enrichment" ApJ, 568, L101 (arXiv:astro-ph/0202397)
Pancino E., Rejkuba M., Zoccali M., Carrera R., 2010, "Low-resolution spectroscopy of main sequence stars belonging to 12 Galactic globular clusters. I. CH and CN band strength variations" A&A, 524, A44 (arXiv:1009.1589)
Pancino E., et al., 2017, "The Gaia-ESO Survey. Mg-Al anti-correlation in iDR4 globular clusters" A&A, 601, A112 (arXiv:1702.06083)

Pasquini L., et al., 2000, in Iye M., Moorwood A. F., eds, Society of Photo-Optical Instrumentation Engineers (SPIE) Conference Series Vol. 4008, Optical and IR Telescope Instrumentation and Detectors. pp 129–140, doi:10.1117/12.395491

Pasquini L., et al., 2002, "Installation and commissioning of FLAMES, the VLT Multifibre Facility" The Messenger, 110, 1

Pasquini L., Bonifacio P., Molaro P., Francois P., Spite F., Gratton R. G., Carretta E., Wolff B., 2005, "Li in NGC 6752 and the formation of globular clusters" A&A, 441, 549 (arXiv:astro-ph/0506651)

Pasquini L., Mauas P., Käufl H. U., Cacciari C., 2011, "Measuring helium abundance difference in giants of NGC 2808" A&A, 531, A35 (arXiv:1105.0346)

Pepe F., et al., 2021, "ESPRESSO at VLT. On-sky performance and first results" A&A, 645, A96 (arXiv:2010.00316)

Persson S. E., Frogel J. A., Cohen J. G., Aaronson M., Matthews K., 1980, "The spread in CO absorption and effective temperature among the giants in OME Cen." ApJ, 235, 452

Pfeffer J., Griffen B. F., Baumgardt H., Hilker M., 2014, "Contribution of stripped nuclear clusters to globular cluster and ultracompact dwarf galaxy populations" MNRAS, 444, 3670 (arXiv:1408.4467)

Pfeffer J., Lardo C., Bastian N., Saracino S., Kamann S., 2021, "The accreted nuclear clusters of the Milky Way" MNRAS, 500, 2514 (arXiv:2011.02042)

Phillips A. C., Illingworth G. D., MacKenty J. W., Franx M., 1996, "Nuclei of Nearby Disk Galaxies.I.A Hubble Space Telescope Imaging Survey" AJ, 111, 1566

Piotto G., 2009, in Mamajek E. E., Soderblom D. R., Wyse R. F. G., eds, IAU Symposium Vol. 258, The Ages of Stars. pp 233–244, doi:10.1017/S1743921309031883

Piotto G., et al., 2005, "Metallicities on the Double Main Sequence of ω Centauri Imply Large Helium Enhancement" ApJ, 621, 777 (arXiv:astro-ph/0412016)

Piotto G., et al., 2007, "A Triple Main Sequence in the Globular Cluster NGC 2808" ApJ, 661, L53 (arXiv:astro-ph/0703767)

Piotto G., et al., 2012a, "Hubble Space Telescope Reveals Multiple Sub-giant Branch in Eight Globular Clusters" ApJ, 760, 39 (arXiv:1208.1873)

Piotto G., et al., 2012b, "Hubble Space Telescope Reveals Multiple Sub-giant Branch in Eight Globular Clusters" ApJ, 760, 39 (arXiv:1208.1873)

Piotto G., et al., 2015, "The Hubble Space Telescope UV Legacy Survey of Galactic Globular Clusters. I. Overview of the Project and Detection of Multiple Stellar Populations" AJ, 149, 91 (arXiv:1410.4564)

Plez B., 2012, Turbospectrum: Code for spectral synthesis, Astrophysics Source Code Library, record ascl:1205.004 (ascl:1205.004)

Poveda A., Allen C., 1975, "The Mass and Tidal Radius of Omega Centauri" ApJ, 197, 155

Prantzos N., Charbonnel C., 2006, "On the self-enrichment scenario of galactic globular clusters: constraints on the IMF" A&A, 458, 135 (arXiv:astro-ph/0606112)

Prantzos N., Charbonnel C., Iliadis C., 2007, "Light nuclei in galactic globular clusters: constraints on the self-enrichment scenario from nucleosynthesis" A&A, 470, 179 (arXiv:0704.3331)

Prantzos N., Charbonnel C., Iliadis C., 2017, "Revisiting nucleosynthesis in globular clusters. The case of NGC 2808 and the role of He and K" A&A, 608, A28 (arXiv:1709.05819)

Pryor C., Meylan G., 1993, in Djorgovski S. G., Meylan G., eds, Astronomical Society of the Pacific Conference Series Vol. 50, Structure and Dynamics of Globular Clusters. p. 357

Quintero Noda C., et al., 2017, "Solar polarimetry through the K I lines at 770 nm" MNRAS, 470, 1453 (arXiv:1705.10002)

Raha N., Sellwood J. A., James R. A., Kahn F. D., 1991, "A dynamical instability of bars in disk galaxies" Nature, 352, 411

Ramírez S. V., Cohen J. G., 2002, "Abundances in Stars from the Red Giant Branch Tip to Near the Main-Sequence Turnoff in M71. III. Abundance Ratios" AJ, 123, 3277 (arXiv:astro-ph/0111572)

Reggiani H., et al., 2019, "Non-LTE analysis of K I in late-type stars" A&A, 627, A177 (arXiv:1906.08281)

Renzini A., 1983, "Current problems in the interpretation of the characteristics of globular clusters." Mem. Soc. Astron. Italiana, 54, 335

Renzini A., 2008, "Origin of multiple stellar populations in globular clusters and their helium enrichment" MNRAS, 391, 354 (arXiv:0808.4095)

Renzini A., 2013, "Rethinking globular clusters formation" Mem. Soc. Astron. Italiana, 84, 162 (arXiv:1302.0329)
Renzini A., Buzzoni A., 1986, in Chiosi C., Renzini A., eds, Astrophysics and Space Science Library Vol. 122, Spectral Evolution of Galaxies. pp 195–231, doi:10.1007/978-94-009-4598-2_19
Renzini A., et al., 2015, "The Hubble Space Telescope UV Legacy Survey of Galactic Globular Clusters - V. Constraints on formation scenarios" MNRAS, 454, 4197 (arXiv:1510.01468)
Renzini A., Marino A. F., Milone A. P., 2022, "The formation of globular clusters as a case of overcooling" MNRAS, 513, 2111 (arXiv:2203.03002)
Rich R. M., Origlia L., Valenti E., 2012, "Detailed Abundances for M Giants in Two Inner Bulge Fields from Infrared Spectroscopy" ApJ, 746, 59 (arXiv:1112.0306)
Riello M., et al., 2021, "Gaia Early Data Release 3. Photometric content and validation" A&A, 649, A3 (arXiv:2012.01916)
Romano D., Tosi M., Cignoni M., Matteucci F., Pancino E., Bellazzini M., 2010, "On the origin of the helium-rich population in ωCentauri" MNRAS, 401, 2490 (arXiv:0910.1299)
Romano D., et al., 2023, "Modeling the Chemical Enrichment History of the Bulge Fossil Fragment Terzan 5" ApJ, 951, 85 (arXiv:2305.15355)
Ryabchikova T., Pakhomov Y., 2015, "Archives of astronomical spectral observations and atomic / molecular databases for their analysis" Baltic Astronomy, 24, 453
Saha K., Gerhard O., 2013, "Secular evolution and cylindrical rotation in boxy/peanut bulges: impact of initially rotating classical bulges" MNRAS, 430, 2039 (arXiv:1212.2317)
Salaris M., Cassisi S., 2014, "Lithium and oxygen in globular cluster dwarfs and the early disc accretion scenario" A&A, 566, A109 (arXiv:1404.6123)
Salaris M., Cassisi S., Mucciarelli A., Nardiello D., 2019, "Detection of multiple stellar populations in extragalactic massive clusters with JWST" A&A, 629, A40 (arXiv:1908.02229)
Sánchez-Janssen R., et al., 2019, "The Next Generation Virgo Cluster Survey. XXIII. Fundamentals of Nuclear Star Clusters over Seven Decades in Galaxy Mass" ApJ, 878, 18 (arXiv:1812.01019)
Saracino S., et al., 2015, "GEMINI/GeMS Observations Unveil the Structure of the Heavily Obscured Globular Cluster Liller 1." ApJ, 806, 152 (arXiv:1505.00568)
Sarajedini A., Layden A. C., 1995, "A Photometric Study of the Globular Cluster M54 and the Sagittarius Dwarf Galaxy: Evidence for Three Distinct Populations" AJ, 109, 1086
Sbordone L., Bonifacio P., Castelli F., Kurucz R. L., 2004, "ATLAS and SYNTHE under Linux" Memorie della Societa Astronomica Italiana Supplementi, 5, 93 (arXiv:astro-ph/0406268)
Scannapieco C., Tissera P. B., 2003, "The effects of mergers on the formation of disc-bulge systems in hierarchical clustering scenarios" MNRAS, 338, 880 (arXiv:astro-ph/0208538)
Shapley H., Sawyer H. B., 1927, "Apparent Diameters and Ellipticities of Globular Clusters" Harvard College Observatory Bulletin, 852, 22
Shen Z. X., Bonifacio P., Pasquini L., Zaggia S., 2010, "Li - O anti-correlation in NGC 6752: evidence for Li-enriched polluting gas" A&A, 524, L2 (arXiv:1011.1718)
Shetrone M. D., 1994, in American Astronomical Society Meeting Abstracts. p. 116.02
Shetrone M. D., 1996, "Al, Mg and Eu Abundances in Globular Cluster Giants. I. Tests of Deep Mixing" AJ, 112, 1517
Shibuya T., Ouchi M., Kubo M., Harikane Y., 2016, "Morphologies of ~190,000 Galaxies at z = 0-10 Revealed with HST Legacy Data. II. Evolution of Clumpy Galaxies" ApJ, 821, 72 (arXiv:1511.07054)
Siegel M. H., et al., 2007, "The ACS Survey of Galactic Globular Clusters: M54 and Young Populations in the Sagittarius Dwarf Spheroidal Galaxy" ApJ, 667, L57 (arXiv:0708.0027)
Sills A., Glebbeek E., 2010, "Multiple populations in globular clusters: the possible contributions of stellar collisions" MNRAS, 407, 277 (arXiv:1004.4166)
Smith G. H., Dupree A. K., 1988, "A Survey of Hα Line Profiles Among Metal-Deficient Field Red Giants" AJ, 95, 1547
Smith G. H., Norris J., 1984, "Spectroscopy of clump giants in NGC 2158." AJ, 89, 263
Smith G. H., Penny A. J., 1989, "CN and CH Inhomogeneities among Red Horizontal Branch Stars in M71" AJ, 97, 1397
Smith V. V., Suntzeff N. B., Cunha K., Gallino R., Busso M., Lambert D. L., Straniero O., 2000, "The Chemical Evolution of the Globular Cluster ω Centauri (NGC 5139)" AJ, 119, 1239

Sneden C., Kraft R. P., Prosser C. F., Langer G. E., 1992, "Oxygen Abundances in Halo Giants. III. Giants in the Mildly Metal-Poor Globular Cluster M5" AJ, 104, 2121

Sollima A., Ferraro F. R., Pancino E., Bellazzini M., 2005a, "On the discrete nature of the red giant branch of ω Centauri" MNRAS, 357, 265 (arXiv:astro-ph/0411546)

Sollima A., Pancino E., Ferraro F. R., Bellazzini M., Straniero O., Pasquini L., 2005b, "Metallicities, Relative Ages, and Kinematics of Stellar Populations in ω Centauri" ApJ, 634, 332 (arXiv:astro-ph/0509087)

Stephens A. W., Frogel J. A., 2004, "An Infrared Spectroscopic Study of Eight Galactic Globular Clusters" AJ, 127, 925 (arXiv:astro-ph/0312512)

Stetson P. B., Pancino E., 2008, "DAOSPEC: An Automatic Code for Measuring Equivalent Widths in High-Resolution Stellar Spectra" PASP, 120, 1332 (arXiv:0811.2932)

Sukhbold T., Ertl T., Woosley S. E., Brown J. M., Janka H. T., 2016, "Core-collapse Supernovae from 9 to 120 Solar Masses Based on Neutrino-powered Explosions" ApJ, 821, 38 (arXiv:1510.04643)

Suntzeff N. B., Kraft R. P., 1996, "The Abundance Spread Among Giants and Subgiants in the Globular Cluster Omega Centauri" AJ, 111, 1913 (arXiv:astro-ph/9601013)

Suntzeff N. B., Smith V. V., 1991, "Carbon Isotopic Abundances in Giant Stars in the CN-bimodal Globular Clusters NGC 6752 and M4" ApJ, 381, 160

Szécsi D., Mackey J., Langer N., 2018, "Supergiants and their shells in young globular clusters" A&A, 612, A55 (arXiv:1711.04007)

Tailo M., Di Criscienzo M., D'Antona F., Caloi V., Ventura P., 2016, "The mosaic multiple stellar populations in ω Centauri: the horizontal branch and the main sequence" MNRAS, 457, 4525 (arXiv:1602.02535)

Takeda Y., Zhao G., Chen Y.-Q., Qiu H.-M., Takada-Hidai M., 2002, "On the Abundance of Potassium in Metal-Poor Stars" PASJ, 54, 275 (arXiv:astro-ph/0110165)

Tautvaišienė G., et al., 2022, "Gaia-ESO Survey: Detailed elemental abundances in red giants of the peculiar globular cluster NGC 1851" A&A, 658, A80 (arXiv:2111.10684)

Taylor D. J., et al., 2022, "Is Terzan 5 the remnant of a building block of the Galactic bulge? Evidence from APOGEE" MNRAS, 513, 3429 (arXiv:2204.01753)

Tenorio-Tagle G., Muñoz-Tuñón C., Silich S., Cassisi S., 2015, "Supernovae and Their Expanding Blast Waves during the Early Evolution of Galactic Globular Clusters" ApJ, 814, L8 (arXiv:1511.02918)

Tenorio-Tagle G., Muñoz-Tuñón C., Cassisi S., Silich S., 2016, "The Realm of the Galactic Globular Clusters and the Mass of Their Primordial Clouds" ApJ, 825, 118 (arXiv:1605.02802)

Tolstoy E., Hill V., Tosi M., 2009, "Star-Formation Histories, Abundances, and Kinematics of Dwarf Galaxies in the Local Group" ARA&A, 47, 371 (arXiv:0904.4505)

Travaglio C., Gallino R., Arnone E., Cowan J., Jordan F., Sneden C., 2004, "Galactic Evolution of Sr, Y, And Zr: A Multiplicity of Nucleosynthetic Processes" ApJ, 601, 864 (arXiv:astro-ph/0310189)

Tremaine S. D., Ostriker J. P., Spitzer L. J., 1975, "The formation of the nuclei of galaxies. I. M31." ApJ, 196, 407

Tsujimoto T., Bekki K., 2012, "Two-component Galactic Bulge Probed with Renewed Galactic Chemical Evolution Model" ApJ, 747, 125 (arXiv:1201.1019)

Turner M. L., Côté P., Ferrarese L., Jordán A., Blakeslee J. P., Mei S., Peng E. W., West M. J., 2012, "The ACS Fornax Cluster Survey. VI. The Nuclei of Early-type Galaxies in the Fornax Cluster" ApJS, 203, 5 (arXiv:1208.0338)

Uitenbroek H., Bruls J. H. M. J., 1992, "The formation of helioseismology lines. III. Partial redistribution effects in weak solar resonance lines." A&A, 265, 268

Valcarce A. A. R., Catelan M., 2011, "Formation of multiple populations in globular clusters: another possible scenario" A&A, 533, A120 (arXiv:1106.6082)

Valenti E., Ferraro F. R., Origlia L., 2007, "Near-Infrared Properties of 24 Globular Clusters in the Galactic Bulge" AJ, 133, 1287 (arXiv:astro-ph/0612280)

Valenti E., Ferraro F. R., Origlia L., 2010, "Near-infrared properties of 12 globular clusters towards the inner bulge of the Galaxy" MNRAS, 402, 1729 (arXiv:0911.1264)

Vasiliev E., Baumgardt H., 2021, "Gaia EDR3 view on galactic globular clusters" MNRAS, 505, 5978 (arXiv:2102.09568)

Vasiliev E., Belokurov V., Erkal D., 2021, "Tango for three: Sagittarius, LMC, and the Milky Way" MNRAS, 501, 2279 (arXiv:2009.10726)

Ventura P., D'Antona F., 2009, "Massive AGB models of low metallicity: the implications for the self-enrichment scenario in metal-poor globular clusters" A&A, 499, 835 (arXiv:0903.0896)
Ventura P., D'Antona F., 2011, "Hot bottom burning in the envelope of super asymptotic giant branch stars" MNRAS, 410, 2760
Ventura P., D'Antona F., Mazzitelli I., Gratton R., 2001, "Predictions for Self-Pollution in Globular Cluster Stars" ApJ, 550, L65 (arXiv:astro-ph/0103337)
Ventura P., D'Antona F., Di Criscienzo M., Carini R., D'Ercole A., vesperini E., 2012, "Super-AGB-AGB Evolution and the Chemical Inventory in NGC 2419" ApJ, 761, L30 (arXiv:1211.3857)
Ventura P., Di Criscienzo M., Carini R., D'Antona F., 2013, "Yields of AGB and SAGB models with chemistry of low- and high-metallicity globular clusters" MNRAS, 431, 3642 (arXiv:1303.3912)
Ventura P., et al., 2016, "Evidence of AGB Pollution in Galactic Globular Clusters from the Mg-Al Anticorrelations Observed by the APOGEE Survey" ApJ, 831, L17 (arXiv:1610.03243)
Ventura P., Dell'Agli F., Tailo M., Castellani M., Marini E., Tosi S., Di Criscienzo M., 2022, "Nucleosynthesis, Mixing Processes, and Gas Pollution from AGB Stars" Universe, 8, 45
Vesperini E., McMillan S. L. W., D'Antona F., D'Ercole A., 2010, "The Fraction of Globular Cluster Second-generation Stars in the Galactic Halo" ApJ, 718, L112 (arXiv:1007.1668)
Villanova S., et al., 2007, "The Multiplicity of the Subgiant Branch of ω Centauri: Evidence for Prolonged Star Formation" ApJ, 663, 296 (arXiv:astro-ph/0703208)
Villanova S., Piotto G., Gratton R. G., 2009, "The helium content of globular clusters: light element abundance correlations and HB morphology. I. NGC 6752" A&A, 499, 755 (arXiv:0903.3924)
Villanova S., Geisler D., Gratton R. G., Cassisi S., 2014, "The Metallicity Spread and the Age-Metallicity Relation of ω Centauri" ApJ, 791, 107 (arXiv:1406.5069)
Walcher C. J., et al., 2005, "Masses of Star Clusters in the Nuclei of Bulgeless Spiral Galaxies" ApJ, 618, 237 (arXiv:astro-ph/0409216)
Walker M. G., Mateo M., Olszewski E. W., Bernstein R., Wang X., Woodroofe M., 2006, "Internal Kinematics of the Fornax Dwarf Spheroidal Galaxy" AJ, 131, 2114 (arXiv:astro-ph/0511465)
Wallerstein G., Leep E. M., Oke J. B., 1987, "High-Resolution CCD Spectra of Stars in Globular Clusters. III. M4, M13, and M22" AJ, 93, 1137
Wang S., Chen B., Ma J., 2021, "Estimating ages and metallicities of M31 star clusters from LAMOST DR6" A&A, 645, A115 (arXiv:2011.11853)
Willman B., Strader J., 2012, ""Galaxy," Defined" AJ, 144, 76 (arXiv:1203.2608)
Wilson O. C., Aly M. K., 1956, "The Possible Occurrence of λ5876 of He I in Absorption in the Spectra of Certain Late-Type Stars" PASP, 68, 149
Wirth H., Jerabkova T., Yan Z., Kroupa P., Haas J., Šubr L., 2021, "How many explosions does one need? Quantifying supernovae in globular clusters from iron abundance spreads" MNRAS, 506, 4131 (arXiv:2107.06240)
Woolley R. V. D. R., 1966, "Studies of the globular cluster [omega] Centauri I," Royal Observatory Annals, 2, 1
Yaron O., Prialnik D., Shara M. M., Kovetz A., 2005, "An Extended Grid of Nova Models. II. The Parameter Space of Nova Outbursts" ApJ, 623, 398 (arXiv:astro-ph/0503143)
Yong D., Grundahl F., 2008, "An Abundance Analysis of Bright Giants in the Globular Cluster NGC 1851" ApJ, 672, L29 (arXiv:0711.1394)
Yong D., Grundahl F., Nissen P. E., Jensen H. R., Lambert D. L., 2005, "Abundances in giant stars of the globular cluster NGC 6752" A&A, 438, 875 (arXiv:astro-ph/0504283)
Yong D., Grundahl F., Johnson J. A., Asplund M., 2008, "Nitrogen Abundances in Giant Stars of the Globular Cluster NGC 6752" ApJ, 684, 1159 (arXiv:0806.0187)
Yong D., Grundahl F., D'Antona F., Karakas A. I., Lattanzio J. C., Norris J. E., 2009, "A Large C+N+O Abundance Spread in Giant Stars of the Globular Cluster NGC 1851" ApJ, 695, L62 (arXiv:0902.1773)
Yong D., et al., 2014, "Iron and neutron-capture element abundance variations in the globular cluster M2 (NGC 7089)*" MNRAS, 441, 3396 (arXiv:1404.6873)
Youakim K., Lind K., Kushniruk I., 2023, "Tidal debris from Omega Centauri discovered with unsupervised machine learning" MNRAS, 524, 2630 (arXiv:2307.03035)
Ziliotto T., et al., 2023, "Multiple Stellar Populations in Metal-poor Globular Clusters with JWST: A NIRCam View of M92" ApJ, 953, 62 (arXiv:2304.06026)

Zinn R., 1980, "The globular cluster system of the galaxy. I. The metal abundances and reddenings of 79 globular clusters from integrated light measurements." ApJS, 42, 19

Zoccali M., Valenti E., 2016, "The 3D Structure of the Galactic Bulge" PASA, 33, e025 (arXiv:1601.02839)

Zoccali M., Pancino E., Catelan M., Hempel M., Rejkuba M., Carrera R., 2009, "The Radial Extent of the Double Subgiant Branch in NGC 1851" ApJ, 697, L22 (arXiv:0901.4476)

de Boer T. J. L., Belokurov V., Beers T. C., Lee Y. S., 2014, "The α-element knee of the Sagittarius stream" MNRAS, 443, 658 (arXiv:1406.3352)

de Mink S. E., Pols O. R., Langer N., Izzard R. G., 2009, "Massive binaries as the source of abundance anomalies in globular clusters" A&A, 507, L1 (arXiv:0910.1086)

di Criscienzo M., et al., 2011, "NGC 2419: a large and extreme second generation in a currently undisturbed cluster" MNRAS, 414, 3381 (arXiv:1103.0867)

van Leeuwen F., Le Poole R. S., Reijns R. A., Freeman K. C., de Zeeuw P. T., 2000, "A proper motion study of the globular cluster ω Centauri" A&A, 360, 472